MIDLATITUDE CIRRUS CLOUD STRUCTURAL PROPERTIES ANALYZED FROM THE EXTENDED FACILITY FOR ATMOSPHERIC REMOTE SENSING DATASET

A

THESIS

Presented to the Faculty

of the University of Alaska Fairbanks

in Partial Fulfillment of the Requirements

for the Degree of

DOCTOR OF PHILOSOPHY

By

Likun Wang, B.S., M.S.

Fairbanks, Alaska

June 2004

ABSTRACT

The knowledge on cirrus inhomogeneous structural properties is important not only in radiation calculations, but also in deeply understanding the dynamics mechanism including the formation, development, and dissipation of cirrus clouds. The midlatitude cirrus inhomogeneous structural properties have been evaluated by analyzing the 10-year high cloud datasets obtained at the University of Utah, Facility for Atmospheric Remote Sensing in Salt Lake City, UT. Three goals have been reached in this research. First, the means to analyze lidar data using wavelet analysis, an advanced approach to obtain information on the structure of cirrus clouds, has been successfully developed. And then, typical cirrus structures including Kelvin-Helmholtz instabilities, cirrus mammata, and the uncinus cells have been analyzed by case studies and statistical survey. Their dynamical mechanisms, environmental characteristics, and vertical and horizontal length scale have been studied. Thirdly, using the method based on the wavelet transform and other methods, a climatology of midlatitude cirrus horizontal inhomogeneous properties is developed from the FARS lidar backscattered power data, the proxies of real cirrus clouds.

TABLE OF CONTENTS

LIST OF FIGURES

LIST OF TABLES

LIST OF ACRONYM

2D	Two Dimensional
AMS	American Meteorological Society
ARM	Atmospheric Radiation Measurement
CART	Cloud and Radiation Testbeds
CAT	Clear Air Turbulence
CBDI	Cloud Base Detrainment Instability
COI	Cone of Influence
CPL	Cloud Polarization Lidar
CPU	Central Processing Unit
CRYSTAL	Cirrus Regional Study of tropical Anvil and Cirrus Layers
CRYSTAL-FACE	CRYSTAL – Florida Area Cirrus Experiment
CWT	Continuous Wavelet Transform
DIAL	Differential Absorption Lidar
DOE	Department of Energy
DWT	Discrete Wavelet Transform
FARS	Facility for Atmospheric Remote Sensing
FFT	Fast Fourier Transform
FIRE	First ISCCP Regional Experiment
PMT	Photomultiplier Tubes
GCM	General Circulation Model
GCSS	GEWEX Cloud System Study

GEWEX	Global Energy and Water Cycle Experiment
GMT	Greenwich Mean Time
GOES	Geostationary Operational Environmental Satellites
ICE	International Cirrus Experiment
IDWT	Inverse Discrete Wavelet Transform
IOP	Intensive Operational Period
IPA	Independent Pixel Approximation
ISCCP	International Satellite Cloud Climatology Project
ITCZ	Intertropical Convergence Zone
IWC	Ice Water Content
IWP	Ice Water Path
KH	Kelvin-Helmholtz
LDR	Linear Depolarization Ratios
LIRAD	Combined Lidar and Infrared Radiometer
LWC	Liquid Water Content
LWP	Liquid Water Path
MSL	Mean Sea Level
MUC	Mesoscale Unicinus Complexes
NASA	National Aeronautics and Space Administration
NCEP	National Centers for Environmental Prediction
NWS	National Weather Service
PDL	Polarization Diversity Lidar
PMT	Photomultiplier Tubes

PPH	Plane parallel, horizontally homogeneous assumption
PRF	Pulse Repeat Frequency
RH	Relative Humidity
Ri	Richard Number
SGP	Southern Great Plains
SLW	Supercooled Liquid Water
SUCCESS	Subsonic Clouds and Contrails Effects Special Study
TKE	Turbulent Kinetic Energy
TOGA/COARE	Tropical Ocean Global Atmosphere/Coupled Ocean Atmosphere Response Experiment
UT	Utah
UTC	Coordinated Universal Time
WFT	Windowed Fourier Transform
WMO	World Meteorological Organization
WT	Wavelet Transform

ACKNOWLEDGMENTS

I would like to sincerely thank my advisor, Professor Kenneth Sassen, for his never ending support, enthusiasm, and thoughtfulness for the past 5 years. Thanks also go out to the other members of my supervisory committee, Drs. David O'C Starr, Nicole Mölders, Cathy Cahill, and Glenn Shaw, for their comments and suggestions. Thanks to previous and current group members including Jiang Zhu, Zhien Wang, Jennifer Comstock, Sally Benson, James Campbell, Diana Daneva, and Ramaswamy Tiruchirapalli for their helps.

This dissertation is finished based on the work done in University of Alaska Fairbanks and the University of Utah. Therefore, I also would like to thank the faculty and staff members in Department of Meteorology at the University of Utah for their help with my graduate studies and research there. I am grateful to Professors Ed Zipser, Gerald Mace, and Steven Krueger.

Special thanks to my family for their understanding, support, and inspiration, especially my wife, Yaping Li, who is always there for me in good times and bad.

Acknowledge grants National Science Foundation Grants ATM-0296190 and ATM-9528287, and Department of Energy Grant DE-FG02-03ER63530 from the Atmospheric Radiation Measurement Program.

CHAPTER 1

INTRODUCTION

1.1 Cirrus Clouds: General Knowledge

Clouds, one of the most important components in the climate system, may be the key to understand climate change and predict future climate using numerical climate models (Stephens and Webster 1981; Ramanathan et al. 1989). While clouds reflect solar radiation back towards space that reduces the solar energy available to the Earth (albedo effect), they also trap some of the outgoing infrared radiation emitted by the Earth, thereby warming the surface of the Earth (greenhouse effect). Which of these two opposing processes dominates depends on many parameters including cloud particle composition, cloud structure, cloud fraction, and cloud location. Changes to only one of these parameters can have significant implications for climate. It has been generally believed that low-level and middle-level clouds have a net cooling effect because they reflect more solar radiation and have a relative small effect on infrared radiation, and cold clouds reduce the emission of long wave radiation flux to space, and thereby tend to warm the surface and lower atmosphere. Since clouds play a critical role in the energy balance of the climate system, they have been treated as the highest priority issue by many major research programs such as the First International Satellite Cloud Climatology Project (ISCCP) Regional Experiment (FIRE), the International Cirrus Experiment (ICE), the Department of Energy (DOE) Atmospheric Radiation Measurement (ARM) Program, the Global Energy and Water Cycle Experiment (GEWEX) Cloud System Study (GCSS),

the CloudSat project, and the Cirrus Regional Study of tropical Anvil and Cirrus Layers (CRYSTAL) (Cox et al. 1987; Starr and Cox 1987; Raschke 1988; Rossow and Schiffer 1991; Stokes and Schwartz 1994; Browing et al. 1993; Ackerman et al. 2000; Stephens et al. 2002).

Cirrus clouds, which cover about 20-30% of the globe, have been identified as one of the major unsolved cloud types. According to the definition from the World Meteorological Organization (WMO), cirrus clouds are referred to layer, hook, band, or filament clouds composed principally of ice crystals and classified into three kinds: cirrus, cirrocumulus, and cirrostratus (WMO 1965). However, based on morphology rather than on the physical contents or dynamics of clouds, this classification scheme does not include subvisual or contrail cirrus (Sassen and Chou 1992; Lynch 2002; Lynch and Sassen 2002; Schumann 2002).

Conventionally, in light of a physical view, cirrus clouds are thought as high level, cold, and optically thin clouds composed principally of non-spherical ice crystals. Generally being located high in the troposphere and extending to the lower stratosphere in some occasion where temperature somewhat below ~40^{o}C, the height of cirrus clouds varies from 4 to 20 km with the mean altitude 9 km (Dowling and Radke 1990; Sassen and Campbell 2001). Cirrus clouds predominantly contain non-spherical ice crystal of various shapes, such as bullet rosette, plates, and columns despite the fact that some cirrus clouds may contain patches of supercooled liquid water (SLW) clouds or even form with the aid of transient SLW (Sassen et al. 1989; Heymsfield et al. 1990; Sassen et al. 1990; Hattett et al. 2002; Sassen 2002). Another term used in identifying high cirrus

clouds is cloud transparency, which is related to the visible optical thickness τ. For instance, Sassen and Chou (1992) found that a visual classification of local high-cloud feature can be approximately correlated to ranges in τ. As values of $\tau \leq 3$ are considered to categorize cirrus clouds, the range between $0.3 \leq \tau \leq 3$ defines opaque (bluish sky not visible above) cirrus, $0.1 \leq \tau \leq 0.3$ is a thin (bluish-colored) cirrus, and $\tau \leq 0.1$ sub visual or threshold-visible cirrus (where lighting condition and spatial cloud uniformity have large influences). Sassen and Comstock (2001) found that τ ($\leq$3.0) has a strong peak frequency located at around 0.1 for midlatitude cirrus clouds using the combined lidar and infrared radiometer (LIRAD) method by checking seven-year high cloud data at the University of Utah Facility of Atmospheric Remote Sensing in Salt Lake City .

Wylie and Menzel (1999) survey the global distribution of cirrus clouds using the 8-year HIRS satellite data. They found that cirrus clouds frequently are found in the Intertropical Convergence Zone (ITCZ) both over land and ocean, the midlatitude storm belts from 30^{o} -50^{o}N, and the mountain regions.

From the view of the dynamical mechanism, cirrus clouds have been characterized as a highly coupled microphysical-radiative-dynamical system (Gultepe and Starr 1995). The background flow with a significant wind shear and a stable thermal stratification is the typical environmental characteristics. Nucleation process and ice crystal growth and habit are intrinsically governed by the local temperature and humidity that, in turn, are strongly regulated by the intensity and duration of local updrafts and downdrafts. Radiative properties are determined by microphysical properties and affect on the cooling or heating rate that, finally, impacts on the dynamical processes and

microphysical properties. Dynamical processes within cirrus provide an important coupling between microphysical and radiative processes. These processes interact with each other and then compose a complicated cirrus cloud system in particular due to non-linear dependence of radiative characteristics on microphysical properties of cirrus clouds (Kondratyev 1999). Many attempts have been made to develop numerical models to investigate the role of various processes in the life cycle of cirrus clouds. In their pioneering work, Starr and Cox (1985a, b) developed a two-dimensional (2D) model and showed that the effects of radiative processes and vertical transports are both significant in cirrus cloud formation and maintenance. Khvorostyanov and Sassen (1998a, b) have incorporated explicit microphysical schemes in 2D models to simulate the devolvement of a midlatitude cirrus cloud including interaction with radiation. Gu and Liou (2000) used a two-dimensional cirrus cloud model to investigate the interaction and feedback of radiation, ice microphysics, and turbulence, and their influence on the evolution of cirrus clouds.

Several conceptual models of cirrus clouds formation and dynamical structures have been presented with advancement in understanding of cirrus clouds and their life cycle. In his early work, Heymsfield (1975a, b, and c) developed an empirical model of cirrus uncinus by the observation of radar and aircraft and the calculation of a parcel model (shown in Fig. 1.1a). According to his model, the head of an uncinus element occurs in a dry adiabatic region bounded by stable layers above and below. The positive or negative wind shear decides the shape of uncinus. Ice particles are generated and carried up to the top of the updraft possibly initially caused by the wave motion below the

head region. The fallstreak contains downdraft associated with evaporation and drag of the falling ice particles, which finally destabilizes the stable layer below. Two mechanisms on how new cirrus uncinus elements can be trigged by the older cirrus have been proposed, which include the cooling by evaporation and the convergence due to the shear environment. Lilly (1988) developed another concept model on cirrus outflow plumes from deep convection. As shown in Fig. 1.1b, these mechanisms can be understood as the air intruding into the environment from the anvil to be laden with ice, uniform buoyant, isotropic turbulence, and flowing into a stable stratified environment. And then the outflow undergoes a collapse as moving through a stratified fluid. In the second stage of the development of the outflow plume, a mixed layer can probably be maintained through turbulence generated by a strong radiative heat flux curvature in dense cirrus anvil clouds.

Cirrus clouds, because of their unique characteristics, represent a relatively significant component of the planet's radiation balance (Baker 1997; IPCC 1996; Liou 1986, 1992; Stephens 2002). The influence of cirrus clouds on the climate system is thought to be more complex than the other clouds due to the variety of macrophysical and microphysical properties. Many researchers using numerical models have recognized the influence of the optically thin and non-black cirrus on the radiation balance of the earth-atmosphere system. These radiative properties depend on both the solar and the thermal IR radiative characteristics, which, in turn, are modulated by their macrophysical properties such as cloud heights and fractional cloud cover, and their microphysical properties like ice water content (IWC) and ice crystal size distribution, shape and

a)

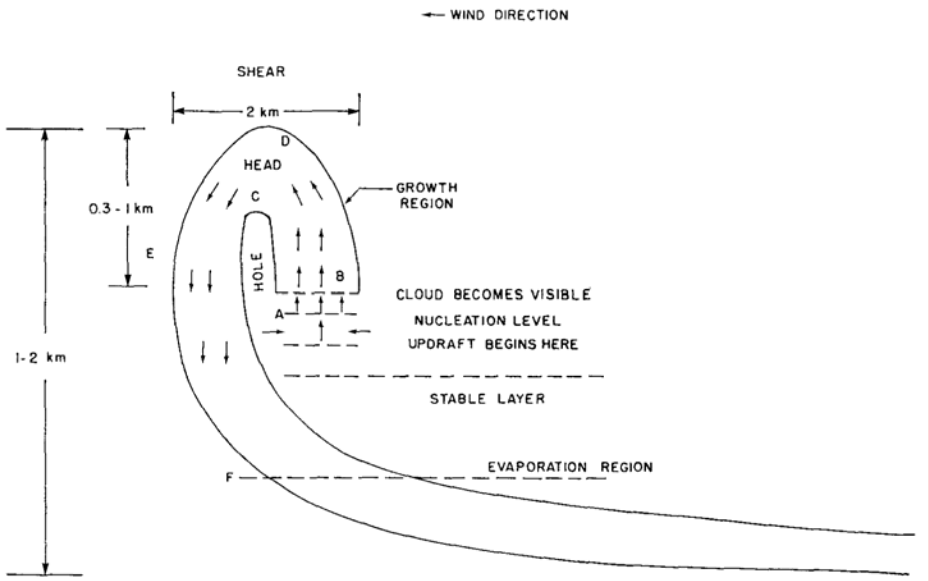

b)

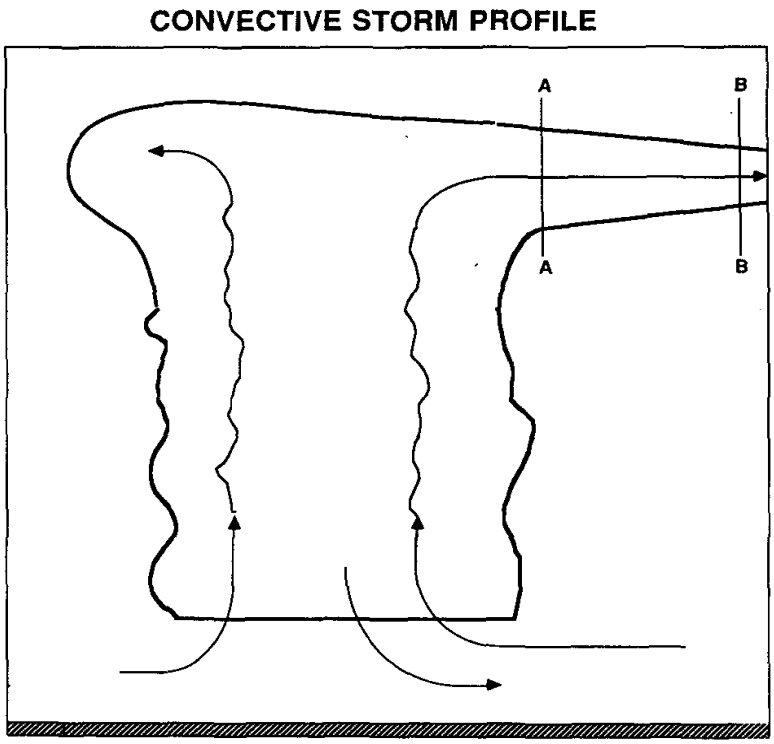

FIG. 1.1. Typical cirrus clouds conceptual models proposed by Heymsfield (1975b) and Lilly (1989): a) cirrus uncinus cloud with positive wind shears and b) outflow cirrus from anvil.

orientation (Stephens et al. 1990; Suzuki and Tanaka 1993; Ou and Liou 1995; Sinha and Shine 1994). Secondly, besides the importance of cirrus ice clouds to global warming, they are also important in the chemistry of the upper troposphere. Recent field and laboratory work has shown that cirrus ice clouds can perturb chlorine chemistry and contribute to upper tropospheric ozone depletion (Borrman et al. 1996; Kley et al. 1996; Solomon et al. 1997; Roumeau et al. 2000). Finally, thin, persistent, and tropical cirrus clouds are also thought to be an important factor for water budget of the upper troposphere and lower stratosphere, which in turn effects on the chemistry and radiative process in the stratosphere (Potter and Holton 1995; Jensen et al. 1996, 2001; Rosenfield et al. 1998; McFaquar et al. 2000; Hartmann et al. 2001).

Therefore, cirrus clouds play a significant role in the atmosphere and are required to be further studied. In the following sections, the importance of inhomogeneous structural properties of cirrus clouds will be reviewed and discussed from both dynamical and climatic view.

1.2 Importance of Inhomogeneity of Cirrus Clouds on Radiation Transfer

In the current General Circulation Models (GCM), cloud processes are incorporated implicitly by using parameterizations, since the spatial scale of typical cloud (kilometer to tens kilometer) is less than the size of a GCM grid box (a few hundred kilometers). The cloud amount and microphysical properties might be predicted from grid-box average relative humidity, stability, and wind velocity. Then radiative process is linked to predicted cloud physical quantities such as liquid and ice water contents. This method, nevertheless, assumes clouds as plane-parallel, horizontally homogeneous sheets

(PPH). While simple and practical, it does not represent the realistic state due to the existence of the nonlinear relationship between cloud optical properties and radiative quantities. Many early studies (Harshvardhan and Randall 1985; Stephens 1985) and recent research (Cahalan 1994; Cahalan et al. 1994a, b; Barker 1996a, b; Liou and Rao 1996; Marshak et al. 1998; Cairns et al. 2000; Fu et al. 2000; Pomroy et al. 2000; Gu and Liou 2001; Los and Duynkerke 2001; Carlin et al. 2002) have pointed out that significant bias can occur in radiative flux calculation without considering cloud subgrid-scale variability.

Furthermore, the same uncertainties also exist for remote sensing cloud properties from space platform (Marshak et al. 1995; Loeb and Davies, 1996; Oreopoulos and Davies 1998a, b; Loeb and Coakley 1998; Chambers et al. 2001; Várnai and Marshak 2001; Iwabuchi and Hayasaka 2002; Várnai and Marshak 2002). Cloud remote sensing techniques are generally based on one-dimensional radiative transfer theory, in which clouds are assumed to be horizontally homogeneous. Actual clouds, however, possess horizontal inhomogeneity. Efficient algorithm to retrieve parameters of inhomogeneous cloud is not well understood at present due to the lack of knowledge of the cloud inhomogeneous properties, especially with respect to the angular distribution of reflected intensities.

No matter for the direct or inverse problem, as suggested by Várnai and Devies (1999), the radiative effects of cloud horizontal inhomogeneity may be divided into two parts : 1) the heterogeneity effect due to optical property variability, and 2) the horizontal transport effect of photons moving between neighboring columns (see Fig. 1.2).

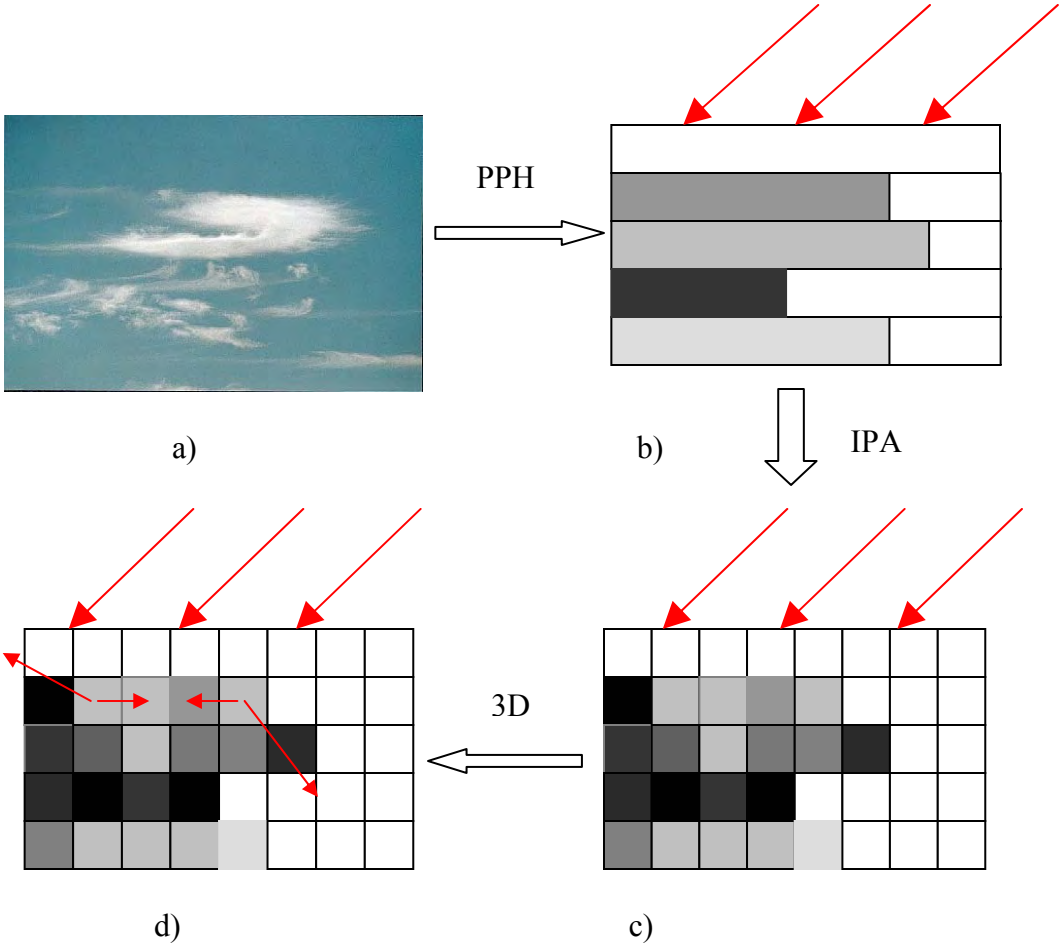

FIG. 1.2. Schematic illustration of real cloud field, PPH, IPA, and 3D radiation calculation: a) real cloud field; b) PPH; c) IPA; and d) 3D.

Facing the first problem, Cahalan et al. (1994b) proposed a scheme named "independent pixel approximation" (IPA), in which the grid box is divided into independent pixels with their own optical or microphysical properties. Computation of the albedo and other radiative properties of individual cloud pixels in a digital scene can be done using only the physical properties of clouds and/or other features within each given pixel under PPH scheme, neglecting any influence of the physical properties associated with neighboring pixels. The domain-averaged radiative properties can be calculated as following:

$$\langle \alpha \rangle = \frac{1}{N} \sum_{i=1}^{N} \alpha_{PPH}(\tau_i) \tag{1.1}$$

where $<\alpha>$ means the average radiative properties in the domain and τ_i the optical properties of every independent pixel. Due to the neglect of the horizontal radiation transportation, the IPA just requires knowledge of the one-point probability distribution function (*pdf*) of the cloud optical depth, which needs to parameterize the mean and the variance of the optical depth (Cahalan 1994). Recently, there are many efforts for parameterization of optical depth variability based on cloud type (Pincus et al. 1999), cloud fraction (Barker et al. 1996), mean optical thickness (Oreopoulos and Davies 1998b), ice water path and optical depth (Carlin et al. 2002), and cloud layer thickness and layer mean temperature (Mace 2002).

Compared with the results of Monto Carlo or other radiation transport simulation, several studies have showed that IPA is a good approximation by examining different cloud systems, including tropical mesoscale convective clouds (Barker 1998; Fu. et al.

2000), subtropical marine boundary clouds (Cahalan 1994b; Barker 1996; Zuidema Evans 1998; Fu et al. 2000), and midlatitude cirrus clouds (Liou and Rao 1996). However, there are still many arguments that great errors may exist under the IPA due to the side illumination caused by the slant pathlengths of photons and diffusion of photons in a multiple scattering process (Welch and Wielicki 1984; Marshak et al. 1995; Byrne et al. 1996; Várnai and Devies 1999). Therefore, in the present situation, there still remains the question if the IPA is adequate to predict domain average radiation flux for GCMs. If not, how important is the difference between the IAP and three-dimension effects in real cloud fields?

To address the above questions we need to apply the three dimensional radiation transfer scheme in real cloud fields, especially which would be expected to have finite cloud effects including spatial pattern, fractal fine structure, and geometry ratio. Some methods have been employed to generate the real cloud field, for example the bounded cascade model (Cahalan 1994; Cahalan et al. 1994b), spectral model (Barker and Davies 1992; Evans 1993; Titov 1998; Evan and McFarlane 2001), cloud resolve model (Fu et al. 2000), large eddy simulation (Bäuml et al. 1999), and retrieval observed field (Liou and Rao 1996). However, the fundamental question is whether these model or retrieval outputs can represent real cloud fields. Can we provide valid, effective and statistical observational facts of cloud inhomogeneous structural properties by a long-term and high- resolution dataset?

Especially, cirrus clouds, as one of the major unsolved cloud types in the climate system, have the complicated structures, irregular geometric shapes, and various spatial

patterns (Lynch 2002; Sassen 2002). While there are many efforts toward estimation of statistical properties of cirrus cloud optical properties and microphysical properties (Mace et al. 2001; Sassen and Comstock 2001; Sassen and Benson 2001; Mace 2002; Wang and Sassen 2002), their inhomogeneous structural properties still are poorly understood and have not be evaluated carefully using a long-term dataset of radar or lidar remote sensor measurements. Since cirrus clouds are an important element in modulating the energy budget of the earth-atmosphere system as discussed in the previous section, their spatial inhomogeneities must be carefully studied.

1.3 Review of Inhomogeneous Structures in Cirrus Clouds

Cirrus cloud structures strongly depend on the dynamics of the environment and its interaction with physical and radiative processes as shown in Fig. 1.3 (Quante and Starr 2002). Dynamic processes with different scale always interact including mesoscale organization, gravity waves, and turbulence so it is not easy to extract them from whole cirrus system (Sassen et al. 1989; Gultepe and Starr 1995; Demoz et al. 1998). The dynamical structures of cirrus clouds have been studied carefully during all kinds of cloud field experiments. On the basis of the larger sample of ground and aircraft observations in cirrus clouds, many case studies have found that the complexity of internal structure ranging from meters to hundreds of kilometers exist in cirrus clouds, such as turbulence, Kelvin-Helmholtz (KH) instabilities, small scale cellular structure, convective cells, gravity waves, and Mesoscale Unicinus Complexes (MUC), and mammata (Heymsfield 1975; Auria and Campistron 1987; Sassen et al. 1989; Starr and Wylie 1990; Sassen et al. 1990; Grund and Eloranta 1990; Smith et al. 1990; Gultepe and

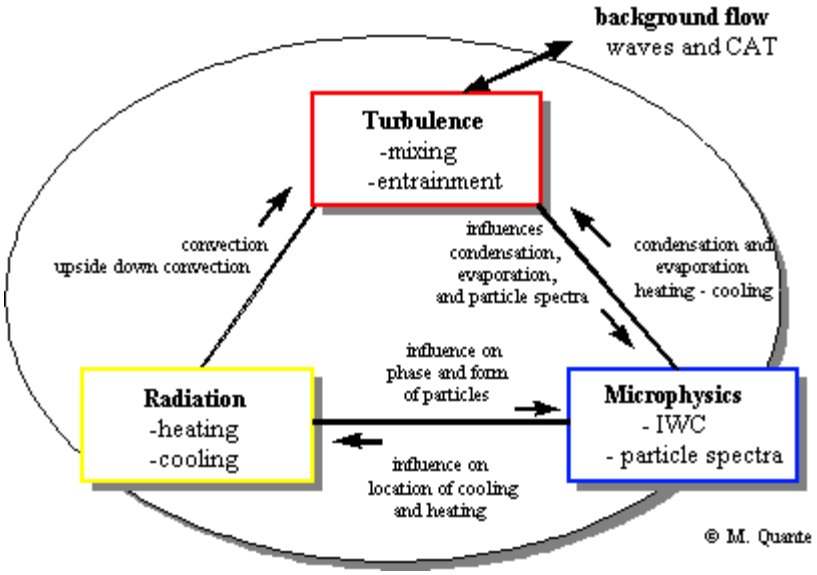

FIG. 1.3. Schematic illustration of the complex interactions within cirrus clouds among turbulence and other dynamical, microphysical and radiative processes (Quante and Starr 2002).

Starr 1995; Gultepe et al. 1995; Sassen 1995; Sassen et al. 1995; Smith and Jonas 1996; Demoz et al. 1998; Sassen et al. 1998; Quante et al. 2002; Quante and Starr 2002; Sassen 2002; Sassen et al. 2002; Starr and Quante 2002). Early and recent results of case studies are presented in Table 1.1. In the following discussion, we will review main structures that occurred frequently in cirrus clouds including the turbulence, mammata, KH instabilities, gravity wave, and MUC.

1.3.1 Turbulence

A general review of turbulence in cirrus clouds has been given by Quante and Starr (2002) as well as field experiment measurements by Smith et al. (1990), Gultepe and Starr(1995), Smith and Jonas(1996, 1997), and Demoz et al. (1998).

The turbulence in cirrus clouds tends to occur intermittently in patches, which is generated by the sporadic wind shear with the existence of KH instabilities (shear mechanism) or associated with radiative and latent heating (buoyancy mechanism) (Smith and Jonas 1996; Quante and Starr 2002). The observations of the mesoscale flow field in the cirrus clouds revealed a typical spectral slope of $-5/3$ for wave number energy spectra of the horizontal wind component. The k^{-3} dependence is also found at some scales in cloud systems, which is generally thought as the existence of two-dimensional turbulence due to suppressed vertical motion in the stable environment (Smith et al. 1990; Gultepe and Starr 1995; Demos et al. 1998; Quante and Starr 2002).

1.3.2 Mammata

TABLE 1.1 Inhomogeneous structures of cirrus clouds observed from cases study

Author	Inhomogeneous structure	Length Scale (km)	Instruments	Comments
Heymsfield (1975b)	Uncinus top generating cell	1-2	Radar, aircraft observation	Minnesota, Illinois, Colorado, Wyoming.
Auria and Campistron (1987)	Cirrus generating cell	1.3 and 0.7	Radar	PEP [a] project, in Spain, 1987.
Sassen et al. (1989)	Mesoscale Unicinus Complexes (MUC) Cirrus uncinus cell	~15- ~100 ~1	Lidar, radar and aircraft observation	FIRE data, Colorado,(1983), Utah(1985), Wisconsin(1986).
Starr and Wylie (1990)	MUC Small scale cellular structure	20-500	Rawinsonde and satellite observation	FIRE data, Wisconsin, 1986
Sassen et al. (1990)	MUC Cirrus uncinus cell	~120 ~1	Lidar and aircraft observation	FIRE data, Wisconsin, 1986
Grund and Eloranta (1990)	MUC	4-12	Lidar	FIRE data, Wisconsin, 1986
Smith et al. (1990)	Two-dimensional eddies		Aircraft observation	FIRE data, Wisconsin, 1986
Starr et al. (1992)	Gravity wave	40	Aircraft DIAL [b] and sounding	New Jersey, 1985
Gultepe and Starr (1995)	Small scale convective cells Gravity waves Quasi-two-dimensional waves Larger two-dimensional mesoscale wave	 2-9 10-20 100	Aircraft observation	FIRE data, Wisconsin, 1986
Gultepe et al. (1995)	Coherent Structure	0.2-10	Radar and Aircraft observation	FIRE II data, Kansas, 1991
Sassen (1995)	Kelvin-Helmholtz wave	3.1	Airborne Lidar	TOGA/COARE[c], 1993
Sassen et al. (1995)	Mammata Fall streaks		Lidar	FIRE IFO II, Kansas, 1991

Smith and Jonas (1996)	Convective cell Gravity waves Turbulence	2 2 0.05-0.6	Aircraft observation	EUCREX [d], England, Scotland, Iceland, 1993
Smith and Jonas (1997)	Turbulence		Aircraft observation	EUCREX [d], England, Scotland, Iceland, 1993
Demoz et al. (1998)	Convective cell Gravity waves MUC	1.2 2-40	Aircraft observation	SUCCESS [e], Oklahoma, 1996
Sassen et al. (1998)	Fallsteaks Cloud-top-generating cell		Lidar, radar and aircraft observation	ARM SGP CART [f], Oklahoma,1994
Quante et al. (2002)	Fall streaks Generating cell Mammata		Lidar and radar	Gessthart, Germany,1997 SUCCESS, Oklahoma, 1996
Sassen (2002)	Mammata MUC Orographic waves		Lidar	SUCCESS, Oklahoma, 1996
Sassen et al. (2002)	Kelvin-Helmholtz wave	2.45	Lidar	ARM SGP CART, Oklahoma, 1997

[a] Notes to Precipitation Enhancement Project of the World Metrological Organization.
[b] Notes to differential absorption lidar.
[c] Notes to Tropical Ocean Global Atmospheres/Coupled Ocean Atmosphere Response Experiment
[d] Notes to European Cloud and Radiation Experiment project
[e] Notes to SUbsonic Contrail and Cloud Effect Special Study.
[f] Notes to the U.S. Southern Great Plains (SGP) Cloud and Radiation Testbed (CART) site of DOE's Atmospheric Radiation measurement (ARM) Program.

Mammata (also named mamma) are composed mainly of cloud particles falling from an anvil cloud or downward thermals produced as a result of the subsidence of an anvil cloud. Mammata may also occur from snow or rain falling below cloud base or from streaks of falling ice crystals (Scorer 1972). According to the early hypotheses of the processes leading to the development of mammata, three related processes are identified: subsidence of a cloud interface layer, fallout of cloud particles, and evaporation of fallout (Ludlam and Scorer 1953; Scorer 1958; Ludman 1980; Scorer 1997). These three processes render the stable subcloud layer slightly unstable and result in downward convection with smooth, usually less sharply outlined surfaces. Clark (1962), Martner (1995), Windsread et al. (2001) also suggested that gravity wave in the environment or parent cloud may play in an important role in initiation of mammatus. Furthermore, Stith (1995) and Windstead et al. (2001) even observed positive temperature perturbation inside clouds, which questioned the early theory.

The observation of mammata is generally associated with cumulus, stratocumulus, cumulonimbus, and hailstorms (Hlad 1944; Clark 1962; Warner 1973; Stith 1995; Martner 1995; Sassen et al. 2001; Windstead et al. 2001). As a pioneer, Scorer (1953; 1973; 1997) firstly discussed the mammata generated in cirrus clouds. Unlike the most delicate and beautiful shapes of anvil mammata, the mammata in cirrus generally have sharp outlines. While the crystals falling out from generating head into unsaturated air, the weight of the fallout added to the cooling effect of the evaporation may produce mammata, especially when there is slightly more wind shear at that level.

Recently, some observations of mammata in cirrus were made by using modern high-resolution active remote sensors. While focusing on the influences of volcanic aerosol on cirrus clouds during the FIRE Intensive Operational Period (IOP) II field experiment, Sassen et al. (1995) first showed a highly dense cloud region above mammatus-like structures by the Facility for Atmospheric Remote Sensing (FARS) Polarization Diversity Lidar (PDL) observation. Besides showing an observation of mammata in a transitional case from a cirrostratus to fibratus, Sassen (2002) also presented a high-resolution lidar return power display of a particularly intense mammatus protruding from the base of a dense cirrus fibratus cloud from the DOE Cloud And Radiation Testbed (CART) site during the NASA Subsonic Clouds and Contrails Effects Special Study (SUCCESS) field campaign. This was the first display of a cross-section of a mammatus in cirrus clouds using high-resolution lidar. For the same observational data, Quante (2002) disclosed the apparent turbulent eddies around the mammatus edges using the two-dimensional wavelet method. According to the local sounding data he speculated that ice crystal sedimentation from a high layer, or secondary generating cell driven by strong evaporation, may be the reason for the turbulent eddies.

1.3.3 KH instabilities

KH instabilities, named after Lord Kelvin and Herman Von Helmholtz (Helmholtz 1868; Kelvin 1871) who first developed the mathematics of this type of instability in the late nineteenth century, are produced by vertical velocity shear at the interface between two fluids with different physical properties (typically different density). They appear as amplifying billow waves oriented perpendicular to the shear

vector, into which the vorticity is concentrated, and which eventually breaks into turbulent flow in a range of smaller scale (for general discussion , see Scorer 1972; Beer 1974; Gossard and Hooke 1975; Acheson 1990; Houze 1993). This distinguishes them from gravity waves from an outside disturbance such as a displacement in the boundary, or violent convection (Scorer 1997).

KH instabilities are one of several dynamical processes in cirrus. From the early observations of KH instabilities associated with cirrus clouds (Scorer 1972; Reiss and Corona 1977; Browning et al. 1978; James and Browning 1981) to recent case studies that used lidar or instrumented aircraft to discover fine structures of KH instabilities (Sassen et al. 1990; Sassen 1995; Demoz et al. 1997; Sassen et al. 2002), the results have shown that KH waves occur fairly frequently in cirrus clouds. This is because cirrus clouds are often associated with wind shear in the upper troposphere. As one of the mechanisms to generate turbulence in cirrus clouds, developed KH waves can break into turbulence (Smith and Jonas 1996; Quante and Starr 2002).

1.3.4 Cloud-scale convective and organized uncinus complexes

It is not uncommon that many early observations revealed the existence of the convective and uncinus generating cells at the cirrus cloud top (Ludlam 1980, p366; Heymsfield 1975b; Auria and Champistron 1987). Based on these observations, Sassen et al. (1989) first put forth the concept of the Mesoscale Uncinus Complex (MUC). They reported that characteristic mesoscale structures of cirrus cloud system with dimensions ranging from ~15km, in the case of narrow cirrus clouds bands, up to ~100 km in deep cirrostratus, are composed by individual uncinus cells described by Ludlam (1980),

Heymsfield (1975b), and Auria and Champistron (1987). In the following FIRE II field experiment (Starr 1987), mesoscale structures similar to the MUC were also found by high-resolution active remote sensors and in-situ measurements (Grund and Eloranta 1990; Sassen et al. 1990; Smith et al. 1990; Starr and Wylie 1990; Gultepe et al. 1995). Using the SUCCESS field data and wavelet analysis method, Demos et al. (1998) showed that within the lower cirrus cloud layer, the episodic occurrence of patches of high frequency activity at a length scale of 1.2 km assemble together into the MUC described by Sassen et al. (1989). Quante and Starr (2002) speculated that the MUC may be the results of interaction between waves and turbulence.

Moreover, some model results also support these observational results about the MUC. Using a two-dimensional (x, z) model of cirrus clouds, Starr and Cox (1985a and 1985b) found that embedded cellular development was prevalent in their simulation of a cirrostratus cloud layer. These cells developed at horizontal scales of ~1 km or less, consistent with the depth of the cloud-generating layer, in association with dynamical features (i.e., updrafts). Dobbie and Jonas (2001) showed that radiation could have an important effect on cirrus clouds inhomogeneity and lifetime. The simulation including radiation showed strong cellular structure, more turbulent activity within the cloud, greater IWC inhomogeneity, and a longer lifetime.

1.3.4 Gravity waves

Gravity waves exist in the atmosphere due to the combined forces of gravity and buoyancy acting on vertically-displaced air parcels (Beer 1974). (In fact, Gravity Waves are more correctly called buoyancy waves as suggested by Gossard and Hooke

(1975)).The restoring forces make air parcels oscillate up and down and from side to side at some nonzero angle to the horizontal plane. Generally, gravity waves propagate most readily in a stably stratified layer where potential temperature increases with height in the layer in order for a gravity wave to propagate within that layer. Gravity waves may be produced by numerous mechanisms (Einaudi et al. 1989) including: 1) wind shear; 2) synoptic-scale weather disturbances in the jet stream and frontal area (e.g., Pavelin and Whiteway 2002); 3) thunderstorm convections (e.g., Horinouchi et al. 2002); and 4) orographic effects.

Gravity waves may enter the cirrus from other levels or be produced in the region of the cirrus clouds. In his pioneering work of the formation and maintenance of cirrus clouds, Heymsfield (1975b) speculated that wave activities occurring below the uncinus head area, including gravity waves and KH waves, played an important role for formation of cirrus. In an analysis of the first study, Sassen et al. (1989) presented a highly variable structure of thin cirrus cloud dominated by the orographic produced gravity wave (also named lee wave, see Holton (1992)). Starr et al. (1992) employed airborne observations using a downward-looking, dual-frequency, near-infrared, differential absorption lidar (DIAL) system to provide the first measurements of height-dependent pressure-perturbation field associated with a strong mesoscale gravity wave with dimension of ~40km linked to upper-tropospheric cirrus cloud. Smith and Jonas (1996) have shown that gravity waves forced by convective cells at the lower level were observed in the upper regions of cirrus by aircraft observation. Using the wavelet method, Demoz et al.

(1998) found that intermittent small groups of apparent gravity waves ranged from 2 km to greater than 40 km in cirrus clouds.

1.3.5 Other mesoscale organizations

Besides the above typical cirrus cloud structures, there are still some other kinds of cirrus cloud structures that are common. For example, cirrus fibratus exists aloft in the sky with irregular cloud bands, which do not have consistent spatial structures. We put all the irregular cirrus clouds without fixed cloud band spatial frequency into this category. In addition, the stratiform cirrus (cirrostratus) clouds that resemble homogeneous cloud layers are also classified into this group.

1.4 The Goal of This Research

As discussed in the above sections, the knowledge on inhomogeneous structural properties is important not only in radiation calculation, but also for understanding of dynamical mechanisms including the formation, development, and dissipation of cirrus clouds. Hence, it is necessary to evaluate these properties by the high-resolution and long-term datasets. Lidar, as one of the modern effective remote sensors, is ideally suited to research cirrus because of the great sensitivity of light scattering to the presence of aerosols, and hydrometeors and the variety of optical techniques that can be applied (Sassen 1991; Platt 1994; Sassen and Mace 2002). Fortunately, at the University of Utah FARS, Sassen and his colleagues have collected high cloud data from 1987 to 2002 using lidar and other groundbased instruments (Sassen et al. 2001). Because of the long time series and high resolution of the dataset, it is suitable to derive the climatological

characteristics of midlatitude cirrus clouds. Using uniquely extensive FARS high cloud dataset, Sassen and Campbell (2001) examined the macrophysical properties of high clouds by developing a climatology of cirrus cloud heights and temperatures and characterized the synoptic weather patterns responsible for the cirrus; Sassen and Benson (2001) analyzed the linear depolarization ratios (LDR) in term of cirrus cloud microphysical content and revealed fundamental distinctions in cirrus cloud particle properties that vary with temperature and probably geographical location; Sassen and Comstock (2001) used the combined lidar and infrared radiometer (LIRAD) method to derive the radiative properties of cirrus clouds including the visible optical depths and infrared layer emittance; and Sassen et al. (2003) characterized the occurrence of optical displays including halo, arc, and corona according to their appearance, longevity, and the meteorological source of the cirrus.

As an additional part of this series of research using the extended time observations of cirrus clouds at FARS, an examination of the cirrus cloud structural properties and their relation to the physical mechanism will be made. This research will be composed in two parts. First, typical cirrus structures including mammata, KH instabilities, and the cloud top convection and organized uncinus cells occurring will be analyzed. The object of this part is to extend our knowledge about cirrus typical structures. Secondly, the statistical properties of several hundred 3-hour polarization lidar cases of midlatitude cirrus clouds obtained over 10 years from the FARS (1992-2001) will be analyzed to develop a midlatitude cirrus climatology characterizing the cloud structural properties. The primary focus of this dissertation is to explore the behavior of

the inhomogeneous properties of midlatitude cirrus clouds by analyzing the variations of the lidar backscattered power using wavelet transform, Fourier transform and other methods.

In the following chapters, first review the FARS cloud high datasets used in this research is given. In Chapter 3, the methods employed to detect the inhomogeneous structural properties of cirrus clouds will be introduced. Beginning from Chapter 4, the structures including the KH instabilities, mammatus, and convective uncinus cells will be examined. Then the statistical results of cloud inhomogeneous structures derived from 10 years data will be evaluated in the Chapter 7. The summary and recommendations for future work will be given in the final chapter.

CHAPTER 2

THE FACILITY FOR ATMOSPHERIC REMOTE SENSING: INSTRUMENTS AND DATASETS

The Facility for Atmospheric Remote Sensing (FARS) is located in the campus of University of Utah in Salt Lake City of Utah (40°49'00''N, 111°49'38"W) at an elevation of 1.52 km above sea level. The location overlooks the Salt Lake Valley and Great Salt Lake from a northwestern bench of the Wasatch Mountain as shown in Fig 2.1. Located at 40º 46' 48" N and 111º 57' 36" W and 12 km away to the west of the FARS site, the Salt Lake City National Weather Service station can provide upper air profiles twice a day.

The FARS was established in 1987 with joint funding from National Sciences Foundation and University of Utah. The FARS was equipped with a suit of visible, infrared, and microwave radiometers; photographic and video all-sky imagery; and two channel cloud polarization lidar (CPL), 3.2-mm Doppler radar, and the state-of-the-art dual-wavelength scanning polarization diversity lidar (PDL). The radar and PDL are mobile and have participated in several aircraft-supported cloud research programs at the FIRE field experiment, Southern Great Plains (SGP) ARM CART site and Florida region (CRYSTAL-FACE). A complete list of FARS active and passive remote sensing instruments is presented in Table 2.1 (Sassen et al. 2001).

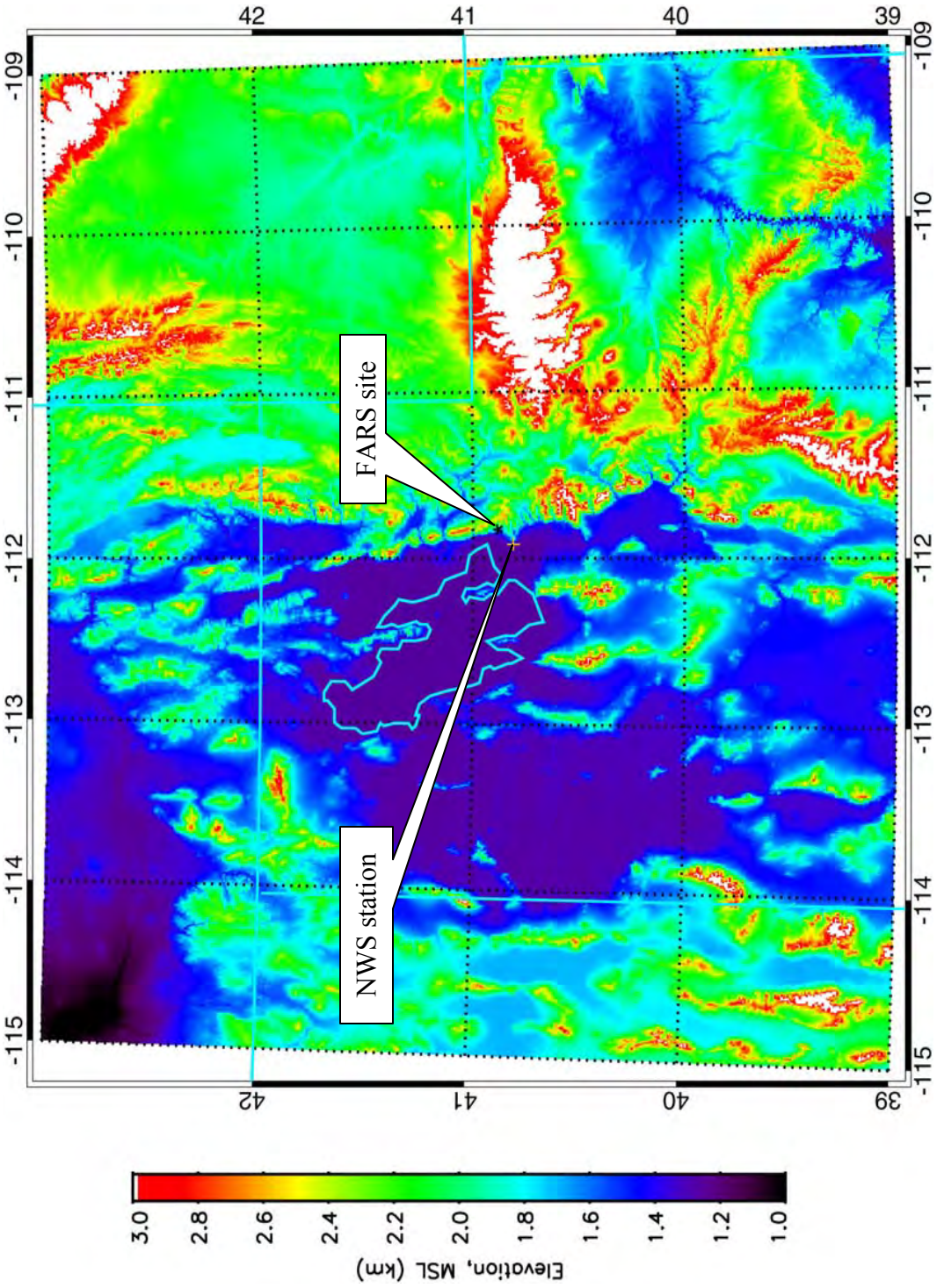

FIG. 2.1. The locations of the FARS site and NWS station shown on a topographic map.

TABLE 2.1. List of instruments operating at FARS

Passive Remote Sensors
Net flux pyradiometers
Narrow-beam (0.14°) 9.5-11.5μm radiometer (co-aligned with lidar)
Precision infrared radiometer
Pyradiometer, 0.3-2.8μm broadband visible
Rotating shadowband radiometer (0.63-2.5μm)
Pyrheliometer (0.63-2.8μm) with solar tracker
All-sky 35mm photography
All-sky video time-lapse imagery
Active Remote Sensors
Cloud polarization lidar (CPL)
-Two channels
-Vertical polarization transmitted
-Manually "tiltable" ± 5° from zenith
-0.1 Hz PRF, 7.5 m maximum range resolution
-Maximum 2K per channel data record length
-1-3 mrad receiver beamwidths
-25 cm diameter telescope
-0.694 μm wavelength, 1.5J maximum output
Polarization diversity lidar (PDL)
-Four channels
-Vertical (0.532 μm) + horizontal (1.06 μm) polarizations
-Fully scannable, 5°/s
-10 Hz PRF, 1.5 m maximum range resolution
-2-8K per channel data record length
-0.2-3.8 mrad variable receiver beamwidths
-35 cm diameter telescopes (two)
-Simultaneous 0.532 and 1.06 μm wavelengths, 0.45 J outputs
95 GHz polarimetric Doppler Radar
-Six channels (two Doppler)
-Vertical + horizontal polarizations transmitted
-Fully scannable, 5°/s
-10Hz-80KHz PRF, 7.5 m maximum range resolution
-600 range gates
-0.25° beamwidth
-90 cm diameter dish, 57 dB gain
-3.2 mm wavelength, 1.2 KW peak power

Since December of 1986, FARS has collected over 3,200 hours of ruby lidar backscattering data, which are mainly composed of typical 3-hour observations. These data include observations of various types of cirrus clouds that are important for studying the climatic impact of high clouds. Because of their tendency to be attenuated in clouds layers consisting predominately of liquid cloud droplets, a lidar system is more suitable for studying higher, colder ice clouds than water clouds. Thus, the FARS dataset in primary is composed of cirrus clouds that are independent of lower water clouds.

In this study, the FARS high cloud data used to examine the dynamical, inhomogeneous structures of cirrus clouds are mainly produced by CPL measurements. In addition, in order to detect some fine structures with small scale in cirrus, some high-resolution PDL observation at SGP ARM CART site and other field experiments is also used by this research. The upper air observations are used to diagnose the environmental conditions and provide the temperature and horizontal wind speed profiles for the lidar observation periods. In this chapter, a complete description of the instrumentation and the high-cloud dataset is presented.

2.1 Cloud Polarization Lidar

2.1.1 Instrument description

The FARS CPL is a dual-channel polarization lidar that operates at a maximum pulse repletion frequency (PRF) of 0.1 Hz and transmits a 1-3 mrad beamwidth pulse that is vertically polarized. The receiver telescope is 25 cm in diameter and directs the energy into two photomultiplier tubes that detect the vertically and horizontally polarized energy

separately. The backscattered signal from each channel is digitized into an eight-bit signal using a two-channel digital oscilloscope and recorded with a PC. The maximum vertical resolution is 7.5 m. A picture of CPL is shown in Fig 2.2 and the specification of the instrument can be referred in Table 2.1.

2.1.2 Lidar equation

The backscattered power detected by a lidar system is described by the lidar equation (for general discussion, see Measures 1984; Stephens 1994; Liou 2001). The received power P(R) by lidar is related to the strength of the scattering in a volume by

$$P(R) = P_0\left(\frac{ctA_r}{2R^2}\right)(\beta_m(R) + \beta_c(R))\exp[-2\int_{R_0}^{R}(\sigma_m(R) + \sigma_c(R))\eta(R)dR] \quad (2.1)$$

where P_0 is the power output (J), c speed of the light (m s^{-1}), t the pulse length (m), A_r the receiver collecting area (m^2), β the volume backscatter coefficient (m $sr)^{-1}$, σ the volume extinction coefficient area (m^{-1}), and η the multiple forward-scattering correction factor. For a cloudy atmosphere, the subscripts m and c denote contributions from molecules and cloud particles, respectively. P(R) is measured for both the parallel $P_{\|}(R)$ and perpendicular $P(R)_{\perp}$ planes of polarization with respect to the incident polarization plane.

Principally, since the scattering and extinction due to air molecules is predicted by Raleigh theory with known air density (known to sufficient accuracy from local balloon-borne radiosonde profiles), it is possible to calibrate lidar backscattering profiles by evoking the pure molecular scattering assumption (Sassen 1994). A common assumption is that a relationship between β and σ exists, which is usually referred to as the backscatter-to-extinction ratio k (Klett 1981). The ratio is represented as

a)

b)

FIG. 2.2. a) Interior view of the FARS site showing the zenith-pointing cloud polarization lidar (CPL) and coaligned midinfrared radiometer beneath the observation skylight, along with some of the computer controller and video systems; b) Photograph of the polarization diversity liar (PDL) deployed at the FARS for scanning operations on the mobile platforms real tailgate, depicting the laser transmitter, dual telescope receiver, and safety radar unit dish (from Sassen et al. 2001).

$$\beta = const \cdot \sigma^{k} \tag{2.2}$$

If one assumes this relationship is valid, the range square corrected backscattered power $P(R)\bullet R^2$ can be transformed into the equation that just includes β. From the fundamental of light scattering theory, β is determined by the microphysical properties of cirrus cloud ice crystal habit, distribution and IWC. Therefore, under the Taylor's hypothesis (Taylor 1938), it is possible to derive the information on inhomogeneous cirrus properties by analyzing $P(R)\bullet R^2$.

The linear depolarization ratio δ is defined as the ratio of the perpendicular to the parallel polarized lidar signals as the following (Sassen 2000):

$$\delta = \frac{P_{\perp}(R)}{P_{\parallel}(R)} \tag{2.3}$$

The depolarization ratio can be used to distinguish the shape and the orientation of non-spherical ice crystals. Sassen (1976, 1991) presented the depolarization ratio for various types of ice crystals and water droplets derived from laboratory and field studies. Sassen and Benson (2001) have analyzed the linear depolarization ratios (LDR) in term of cirrus cloud microphysical content using the FARS high cloud dataset.

2.1.3 CPL high cloud dataset

Since FARS was established in 1987, it has been applied to the regular study of high-level clouds in support of basic cirrus clouds. As of April 2002, nearly 3200 h of CPL lidar data have been collected. It is noted that a new laser transmitter was replaced during the end of 1991, which caused the change of the data resolution from 30 s to 10 s

(Campbell 1997). In order to keep the consistency of the data, in this research, we just use the data from 1992 that include 2,208 hour observations.

A yearly, monthly, and hourly breakdown of the accumulation of FARS CPL observations from 1992 to 2002 is shown in Fig. 2.3. Examining Fig. 2.3a, in 1995 we have the maximum observation hours up to 321 hours and in 2002 the minimum 16 hours, whereas most show slightly nearly 200 hours, on average. Fig. 2.3b shows that the monthly totals of measurement hours, which indicate that the highest relative amounts of cirrus clouds visible from the ground over the eastern Great Basin occur in the seasonal transition month of March and October (James 1997). This may reflect the seasonal variability of the atmosphere. Concentrating on cirrus clouds, the monthly distributions of measurements agree well with the local NWS reports of high cloud amounts (Sassen and Campbell 2001). From Fig. 2.3c, most measurements have involved around 1800 to 0300 UTC (11:00am to 8:00pm at local time). During this period, the NWS weather station has upper air sounding on 0000 UTC that can provide the environmental profile for the FARS CPL observations.

In light of generating mechanisms, the cirrus clouds observed at FARS could be classified into four different types (Sassen 2002). A list of these cirrus cloud types and their generating mechanisms can be found in Table 2.2. The midlatitude synoptic cirrus category includes all the usual cirrus clouds that form in situ in the upper troposphere due to all kinds of weather disturbance, for example jet stream and front. As discussed in the early observation and model study, typically, these cirrus clouds form from the top generating region and then ice particles slowly sediment (Heymsfield 1975b; Starr and

a)

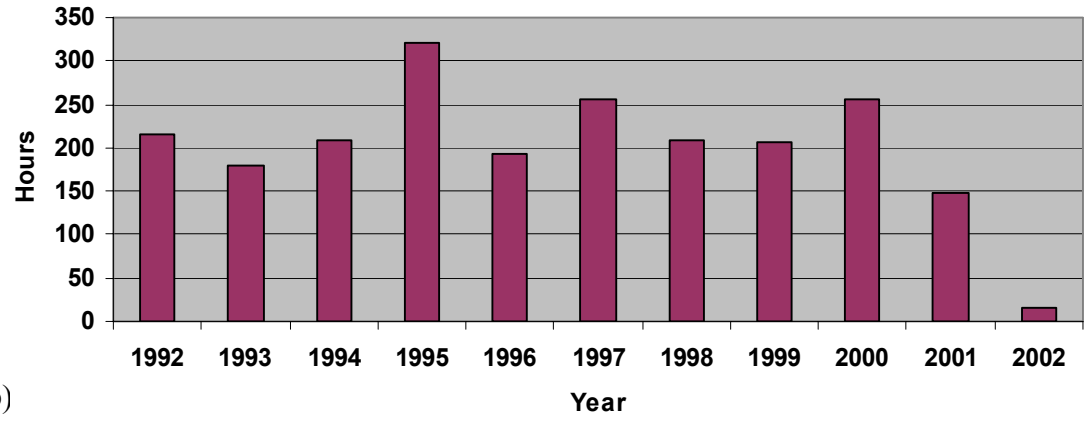

b)

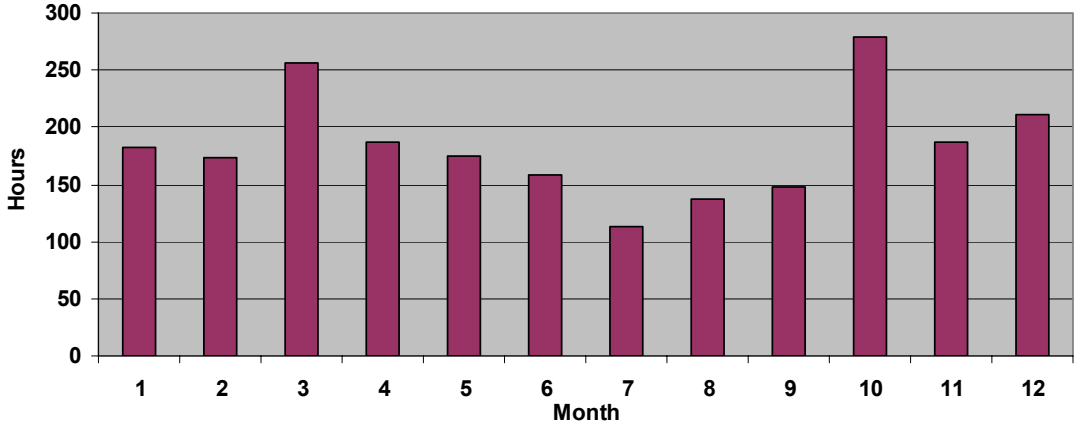

c)

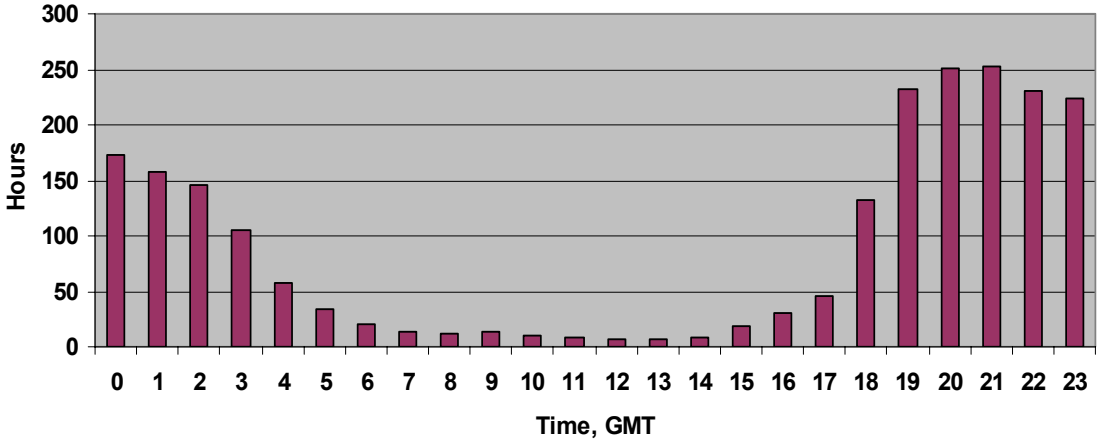

FIG. 2.3. Temporal breakdown of the accumulation of FARS CPL observation from 1992 to 2002: a) yearly; b) monthly; and c) hourly.

TABLE 2.2. Cirrus clouds type and their mechanisms

Cirrus clouds type	Mechanism
Midlatitude synoptic cirrus	Top-down generation, associated with all kinds of synoptic systems including jet stream, front, etc.
Anvil cirrus	Injection mechanism, generated from outflow of thunderstorms
Orographic cirrus	Orographic
Tropical/subtropical cirrus	Associated with tropical systems including storms and hurricanes.

Cox 1985b; Khvorostyanov and Sassen 1998), which would involve evaporation process and trigger the new cloud formation. Anvil cirrus could be understood as the "injection mechanism" (Lilly 1989). The air intrudes into the environment from the anvil to be laden with ice, uniformly buoyant, isotropically turbulent, and flowing into a stable stratified environment. This kind of cirrus is produced from the outflow of the collapsed anvil. The orographic type refers to the cirrus that there is apparent lee wave actually at the time of the observation. If the moisture source of cirrus event is noted as being subtropical, tropical, or the result of a Pacific hurricane event, then the cirrus will be classified as tropical/subtropical cirrus.

2.2 Polarization Diversity Lidar

2.2.1 Instrument description

Based on a commercial Nd:YAG laser, the PDL was designed to be the test bed of lidar polarization techniques for cloud and aerosol research (Sassen 1994; Sassen et al. 2001). Mounted on a truck, this unit provided a mobile tool for field experiments. As shown in Fig. 2.2, the lidar table can be either pointed out of a roof hatch for zenith measurements and ±10º zenith scans, or positioned on a real tailgate for range-height indicator scans. This 10-Hz PRF lidar has four simultaneous channels, two-color (0.532 and 1.06 μm) linear polarization capabilities at resolutions down to 1.5 m. The reader is referred to the Table 2.1 for the technological specification for the PDL.

2.2.2 PDL high cloud dataset

As a mobile high-resolution instrument, the PDL was mainly involved in all kinds of field experiments for cloud research. Therefore, the PDL dataset is mainly composed by the field experiment observations. It was used for the first time in the 1991 FIRE II Intensively Field Observing Campaign in Coffeyville, Kansas (Sassen et al. 1995), a study that focused on cirrus research. In the following field experiments including ARM 94' Remote Cloud Sensing (RCS) Field Evaluation IOP, '97 cloud IOP, '98 cloud physics in ARM SGP CART site, and CRYSTAL FACE in Florida area, the PDL played an important role as the high-solution active remote sensor (Sassen et al. 1998; Ackerman et al. 2001; Sassen and Mace 2002; Sassen et al. 2002).

CHAPTER 3

PRELIMINARY DATA ANALYSIS METHODS AND WAVELET TRANSFORM

Cirrus clouds have been characterized as a highly coupled microphysical-radiative-dynamical system (Quante and Starr 2002). The complex dynamical processes will affect the vertical and horizontal variability in the ice crystal size distribution and IWC in cirrus clouds. The radiative properties respond to the inhomogeneous microphysical properties and then impact the dynamic processes (Starr and Cox 1985a, b; Dobbie and Jonas 2001). Different scale processes often coexist in the same cloud system. The goal of this research is to identify and isolate such scale-dependent processes and explore their characteristic structure and behavior. In this chapter, selecting the CPL data as the example, we will mainly discuss the data preliminary processing and wavelet transform research method used in this dissertation.

3.1 The Procedure of Data Preliminary Processing

3.1.1 Lidar signal record errors and data rejection scheme

As discussed in chapter two, when clouds exist (in this situation, one can ignore the backscattered power contribution from aerosols), the back scattered power detected by lidar can be described as:

$$P(R) = P_0\left(\frac{ctA_r}{2R^2}\right)(\beta_m(R) + \beta_c(R))\exp[-2\int_{R_0}^{R}(\sigma_m(R) + \sigma_c(R))\eta(R)dR], \quad (3.1)$$

where P_0 is the power output (J), c is speed of light (m s^{-1}), t is the pulse length (m), A_r is the receiver collecting area (m^2), β is the volume backscatter coefficient (m $sr)^{-1}$, σ is the volume extinction coefficient area (m^{-1}), and η stands for the multiple forward-scattering correction factor. For a cloudy atmosphere, the subscripts m and c denote contributions from molecules and cloud particles, respectively. P(R) is measured for both the parallel $P_{\|}(R)$ and perpendicular $P(R)_{\perp}$ planes of polarization with respect to the incident polarization plane.

In real-time operation, there are some types of data recording errors due to the complicated control procedure. In order to keep the measurements as precise as possible, we have to fully consider all kinds of situations that caused mistakes for our observations, and "reject" the bad signals from the correct data. Benson (1999) and Barnett (2002) have described the main data recording errors for the CPL system. Next a brief review will be given for these possible occurrences of errors.

For each lidar profile, except the energy backscattering from aerosols, molecules, and cloud particles, the ambient scattered radiation from the sun also enters the telescope receiver, which should be removed from the measurements. Especially, for the CPL system, the power of the first 100 points is recorded as the background noise for the lidar profile. To avoid the leakage of laser fire, we choose the mean value of the first 75 ones of 100 points as the background signal. Normally, the background signal should act like a white noise. Three types of errors could be caused when the background signals

are not like the white noise: a noisy background signal, an offscale setting error, and a pretrigger error. If the standard deviation of 75 points is greater than the preset threshold value, the background signal will be identified as a noise background signal and the profile associated with it will be thrown away. If too many points of the recorded background power are falling outside of the limitation range, the offscale setting error will arise. The third error is a pretrigger error and is identified by a large drift in the background signal. Numerically, a pretrigger error is detected by averaging every ten background points up to 80 points and rejecting the lidar profile if the largest average value is greater than or equal to 1.1 times the smallest average value.

When the backscattered photons come back into the telescope, photomultiplier tubes (PMT) convert the incident photons into the electrical current pulse large enough to be detected by the oscilloscope and saved as the digital backup data. The PMT voltage is recorded for every operation of the lidar. If the PMT high voltage is less than 500 V, the transformed electrical signal cannot represent the real backscattered power and the relevant lidar profile has to be rejected.

There are some other lidar errors that are associated with the laser output. For CPL system, if the laser output power is less than 0.5 J, it will cause the output error. Another error that can be detected from the lidar profile is when no data are recorded. A lidar profile with this type of error will be rejected if the standard deviation of the entire signal is less than 1.0.

3.1.2 Lidar data preliminary processing

Although the lidar profiles with recording errors have been rejected, the white noise still coexists and overlaps on the normal lidar data due to the basic properties of the laser. Fig.3.1 presents a typical example of lidar power return plots dated on December 14 1994 (signal strength represented by the grayscale). Inspecting both of the vertical and horizontal signals extracted from the lidar backscattered power image after range square correction, one can find that the apparent white noise overlaps the normal signal. In order to filter out it, but still keep the fine structures of cirrus clouds, it is necessary to average the data in the vertical direction. Fig.3.2 shows the same vertical signal as shown in Fig.3.1 as well as the results after three, five, seven, and nine point averaging. One can find that the noise still overlaps the signal by checking the plot of the three-point average. For the seven and nine point average, although the noise disappears, the cirrus cloud fine structures located around 10.5 km are also filtered out. Compared with them, five-point average is a good choice. Fig.3.3 presents the whole image including the extracted vertical and horizontal signal after five-point averaging. The noise points have been filtered out but the cloud structures including the ice crystal fallstreaks and cloud top convective cells are still visible in the new image.

In addition to denoise the data, one also needs to interpolate the missing lidar profiles due to the data recording errors because the continuous wavelet method in this research requires the indiscrete signal as the input. The linear interpolation method is used to fill in the missing data at every horizontal layer. Fig.3.4 shows the same image after filling in missing points. All the “holes” in the original image have been filled in successfully, but the cloud structures remain unchanged. It should be noted that one has

to divide the data into two parts or throw them off for those with large area of missing shots.

3.1.3 Transforming the time series to spatial series

The time series of lidar backscattered power not only reflect the variance of the cirrus clouds with time, but also include the variance with space. On one hand, the cirrus clouds move with the predominant flow from the west (240^o-300^o) with typical wind speed around 20-30 m/s in the FARS area (Sassen and Campbell 2001). On the other hand, the inner microphysical properties of cirrus clouds will also change synchronously with time as the clouds are advected. It is a complicated process. The question is: under what conditions are the time series of one point measurements enough to be transformed into the spatial series of cloud structures?

As his pioneer research work on turbulence measurements addressing this problem carefully, Taylor (1938) proposed "Taylor's hypothesis" or the "frozen turbulence concept". If U_m and U is, respectively, the speed of the mean flow and the target structures, temporal measurements at a point can be transformed to spatial patterns with the transformation $x = U_m T$ if the condition $U_m >> U$ is satisfied and the direction of the mean flow does not change during the sample time. The characteristics of mean flows at FARS fulfill this condition. In other words, under Taylor's hypothesis one can assume that the entire cirrus clouds are frozen in time and then horizontally transported passing the lidar at a speed of U_m. Although the internal cloud structures are never really frozen, the duration of the structures is long enough in comparison with the time that they take to

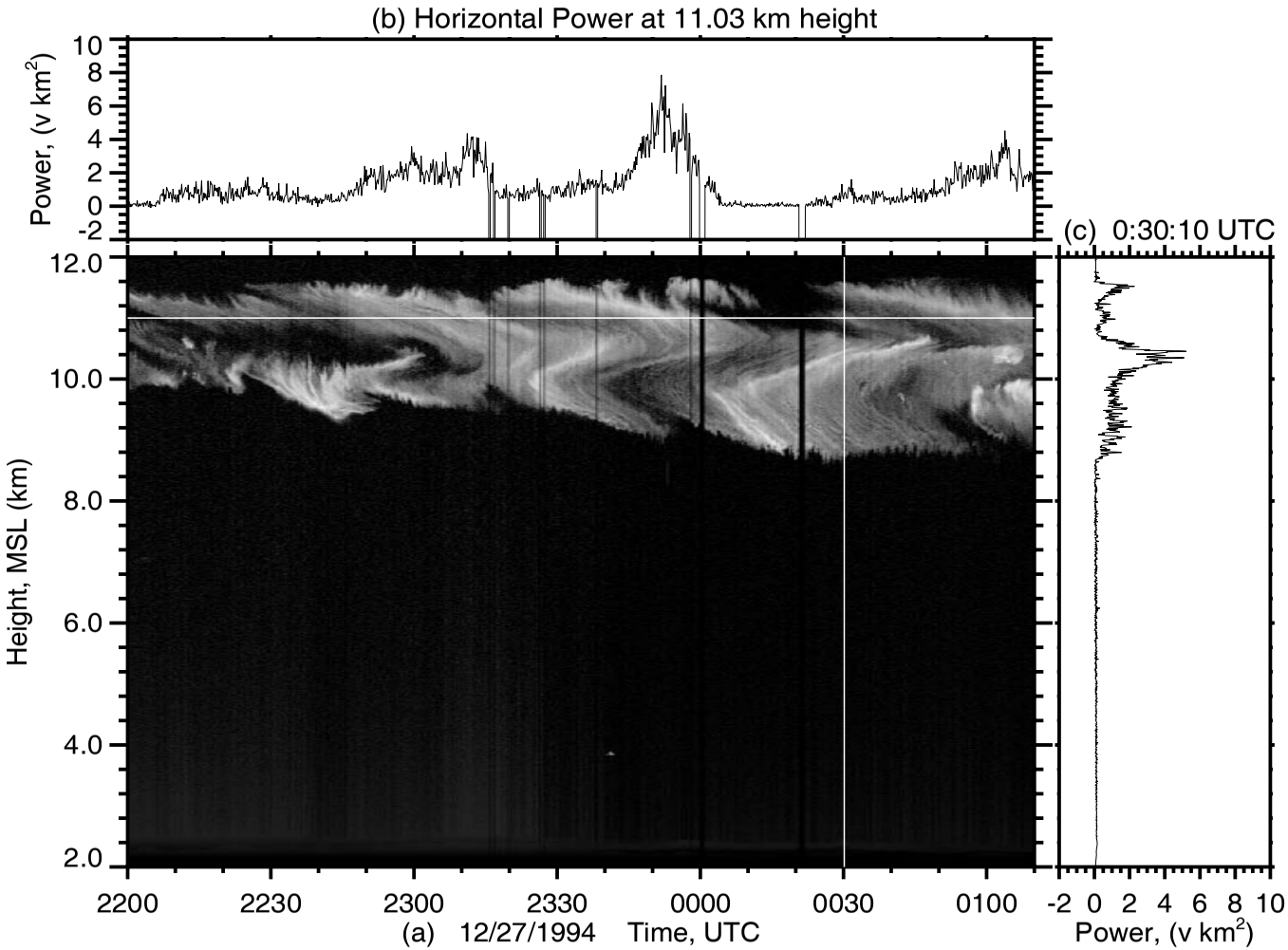

FIG. 3.1. Illustration of CPL system backscattering power return after range square correction: a) power represented by gray scale, where white means strong backscattering power; b) the extracted horizontal power at 11.03 km; and c) the extracted vertical power at 00:30:10 UTC. From b) and c), the white noise can be found superimposed on the normal signal.

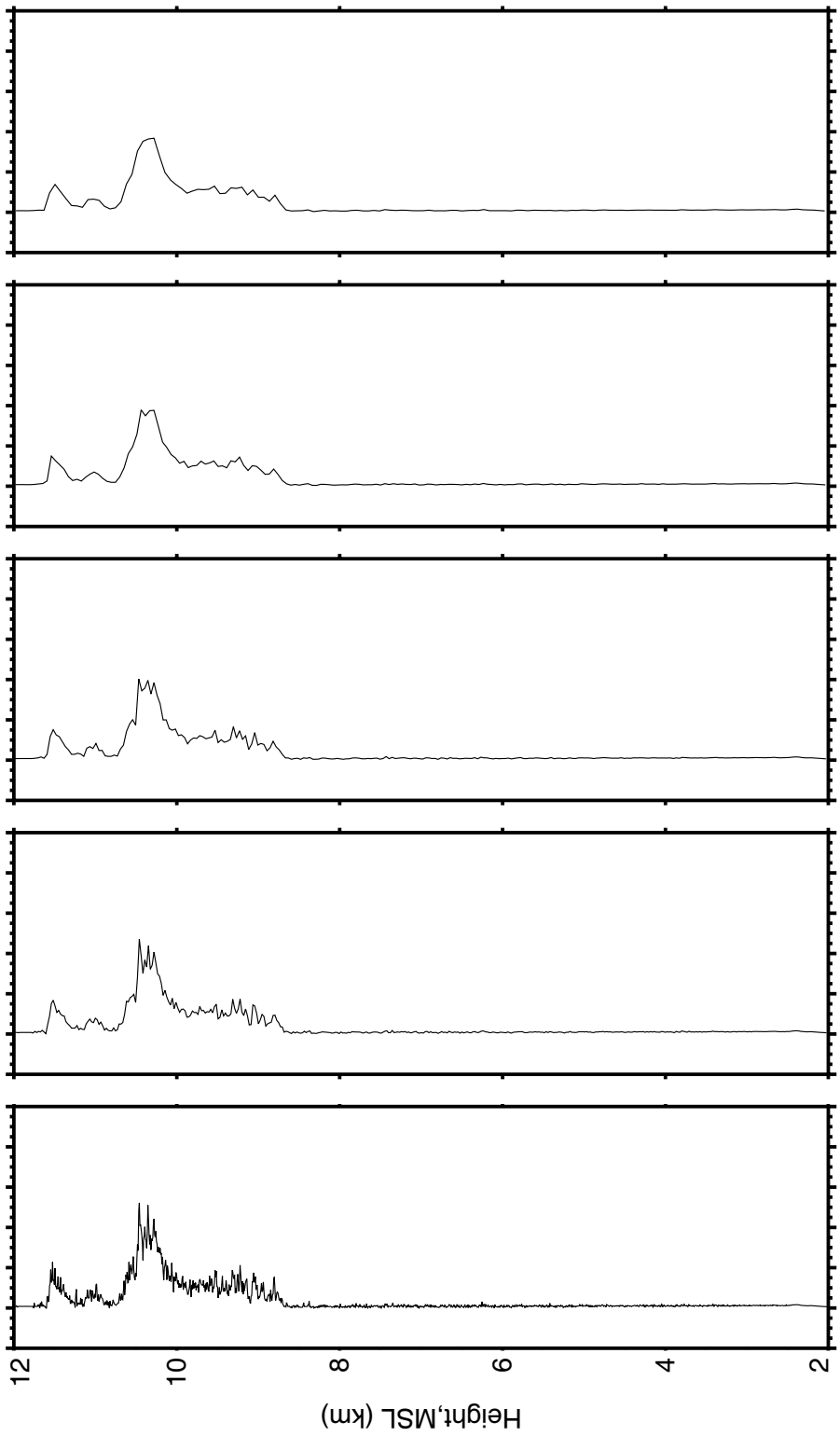

FIG 3.2. a) The same vertical signal as shown in Fig. 3.1 and after b) three-point; c) five-point; d) seven-point; and e) nine-point average. b) still shows the white noise. However, the fine structures around 10.5 km have been filtered out in d) and e).

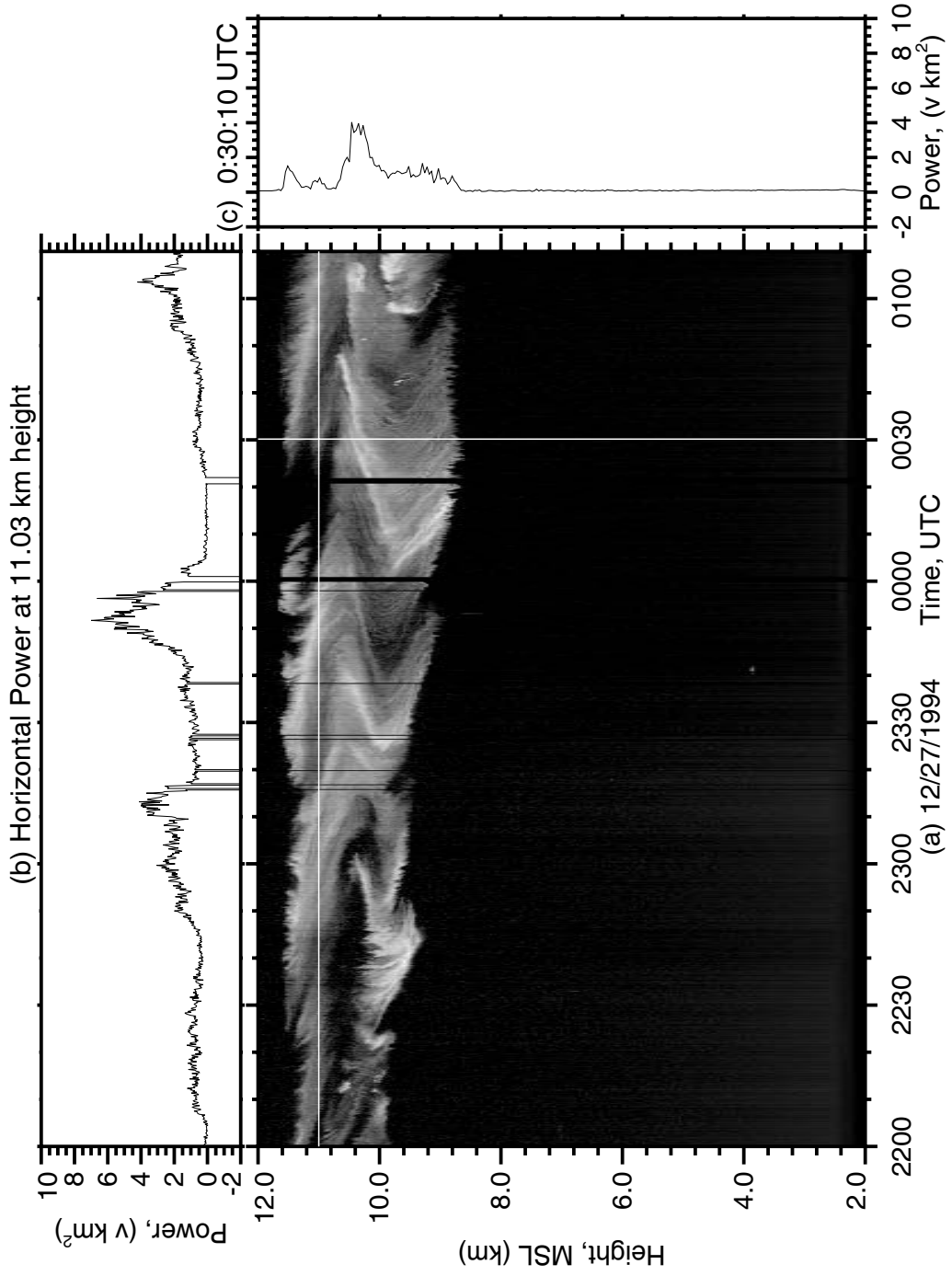

FIG. 3.3. The same data as the Fig.3.1 but after 5-ponit average.

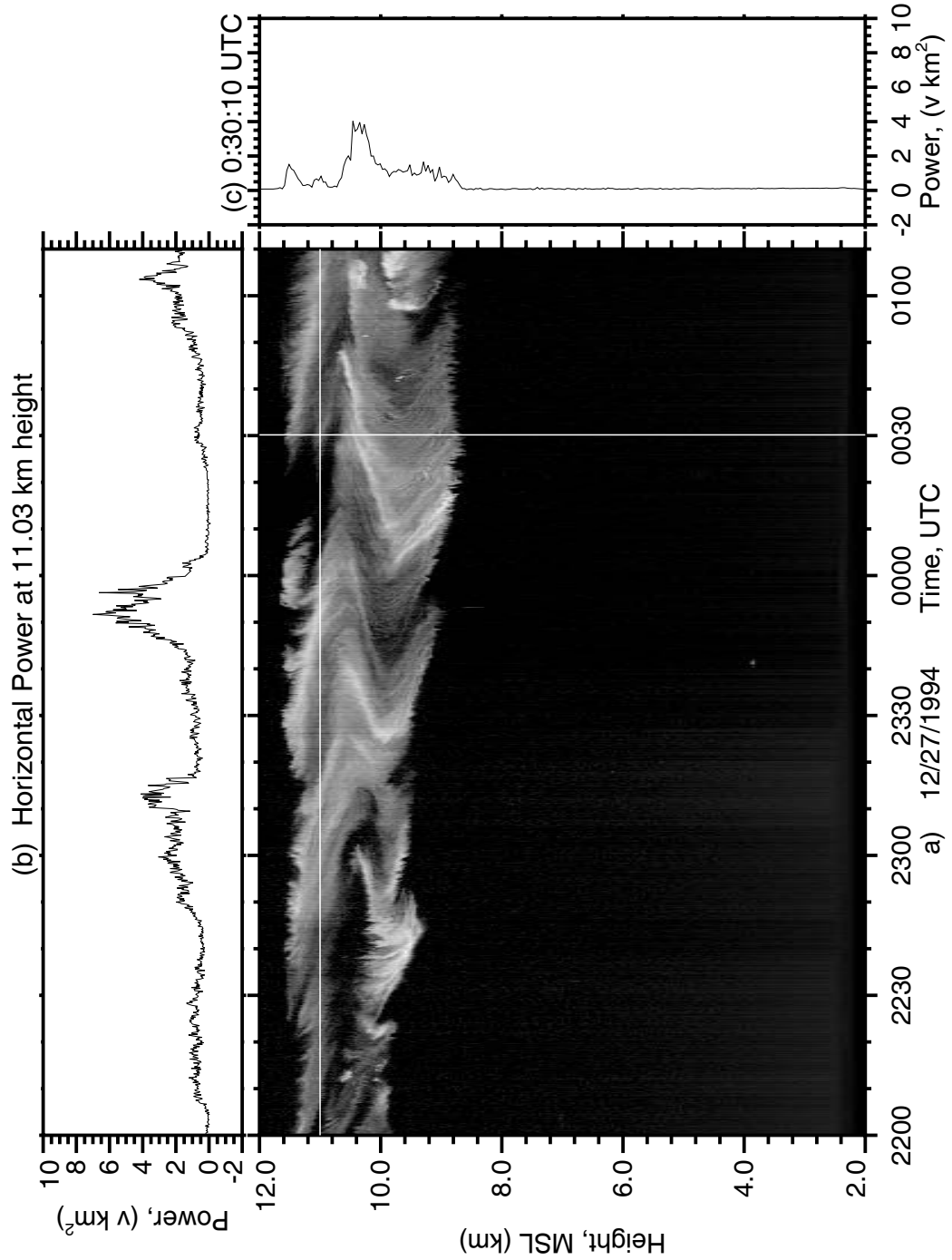

FIG. 3.4. The same data as the Fig.3.3, but after filling missing profiles using linear intepolation .

pass the lidar. Hence, this transformation can well be applied to examine the spatial structure of the cirrus clouds occurring in the FARS site. In this research, horizontal wind velocity from the radiosonde at the specified height is used to convert the time series of lidar backscattered signal to spatial series. However, it should be noted that real situations are complicated because sometimes the wind speed cannot keep the same direction that will introduce the uncertainness in the analysis.

3.1.4 Detectable length scale range

Since every instrument in FARS has its own pulse repeating frequency (PRF), it will keep us from detecting the structures with small scale when transferring the time series data into spatial series data by multiplying the mean horizontal wind velocity. On the other hand, the data are mainly composed of the typical 3-hour observations. Thus, for the large-scale structures, the observations are not long enough to grasp their features. Investigating the synoptic conditions of cirrus cloud occurrence at the FARS site, Sassen and Campbell (2001) found that the mean flow overhead the FARS site had the typical velocity around 20-30 m/s with the direction of 240^{o}-300^{o} during the cirrus occurrence. By using this value as the mean characteristic flow and considering the effects of Nyquest frequency, Table 3.1 lists the detectable scale range for every instrument in FARS. One can find that due to the high-resolution of PDL system, it can detect the small scale eddies that reach to 2-3 m while CPL and the W-band radar system just can capture the structures with the scale 200-300 m. As for the upper scale limitation, the instruments just can observe the process with the dimension around 100-150 km. In other words, this research just can concentrate on the cloud structures with the scale range of 0.5-150 km

TABLE 3.1 Detectable horizontal distance of CPL, PDL, and W-band radar.

	CPL	**PDL**	**W-band radar**
Transmitter	Ruby	Nd:YAG	Klystron
Maximum PRF (*Hz*)	0.1 Hz	10 Hz	10-80K
Wavelength (*μm*)	0.694	0.532 , 1.06	3.2×10^4
Range resolution (*m*)	7.5	1.5	75
Time resolution (*s*)	10	0.1	5
Return measurements	Backscattered power, linear depolarization ratio	Backscattered power, linear depolarization ratio	Effective reflectivity, Doppler velocity , and spectral width
Detectable smallest distance (km)	0.40~0.60	0.004~0.006	0.20~0.30
Detectable largest distance* (km)	100 ~150	100 ~150	100 ~150

* Calculated from the typical 3 hour observations.

using the 14-year FARS high cloud dataset. The turbulence and large scale gravity waves will be out of range of this research. Since the horizontal wind velocity and observational duration change case by case, this issue will be revisited in Chapter 7.

3.2 Wavelet Transform Methods

Wavelet transform (WT) method is a popular technique within the meteorological community for data analysis including atmospheric turbulence, climate time series, convective organizations, and cloud inhomogeneous structures (Farge 1992; Meyers et al. 1993; Weng and Lau 1994; Gollmer et al. 1995; Lau and Weng 1995; Mak 1995; Liu and Miller 1996; Torrence and Compo 1998; Torrence and Webster 1999; Fournier 2002). By decomposing a signal using a particular wavelet function, one can construct a picture of the energy within the signal as a function of both spatial dimension (or time) and wavelet scale (or frequency). The WT method is an effective analysis tool well suited to study multiscale, nonstationary process occurring over finite spatial and temporal domains. Recently, the WT method has also been used for analyzing dynamical and turbulent processes in cirrus clouds for the remote sensor's data or instrumental aircraft measurements (Demoz et al. 1998; Smith and Jonas 1997; Quante et al. 2002).

3.2.1 Why wavelet? From Fourier transform to wavelet transform

As discussed above, the returned backscattered lidar power is a signal that reflects the microphysical process within cirrus clouds. More often than not these processes are nonstationary, consisting of a variety of frequency regimes that may be localized in time (relative to the entire time series) or may span a large portion of the data

record. The traditional studies of dynamical processes in cirrus have relied on direct inspection of observed time series and on analysis using spectral methods by Fourier transform (FT) or windowed FT (WFT) (Gabor 1946). The FT method use sine and cosine base functions that have infinite span and are globally uniform in time. The FT does not contain any time dependence of the signal and therefore cannot provide any local information regarding the time evolution of its spectral characteristics. In a WFT, a time series is examined under a fixed time-frequency window constant in time and frequency domains. When a wide range of frequencies is involved, the fixed time window of the WFT tends to contain a large number of high-frequency and a few frequency cycles or parts of cycles. This often results in an overrepresentation of the high-frequency components and the under-representation of low components.

A WT uses generalized local base functions (wavelets) that can be stretched and translated with a flexible resolution in both frequency and time. The flexible windows are adaptive to entire time-frequency domains, known as the wavelet domains, which narrow while focusing on high-frequency signals, and widen while searching for the low-frequency background. Because of the "Heisenberg uncertainty principle", the width and height of a time-frequency window cannot be arbitrary (Chui 1992; Kumar and Foufoula –Georgiou 1994; Wickerhauser 1994; Ogden 1997). As a result, high precision in time frequency can be achieved at the expense of reduced frequency resolution, and vice versa for low frequency. This property is a unique characteristic of wavelet transformation.

In the following a simple example, given in Fig. 3.5, illustrates why WT method is more effective in data analysis than FT analysis. The signals with two different periods

of 1 and 1/4 second are shown in Fig. 3.5a and b, one of which has two frequencies mixed together and superimposed on the entire time domain and the other has 1 second time period applied on the first half domain and 1/4 second on the last half. Their FT results (shown in Fig. 3.5c and d) both have the two peaks at the 1 and 0.25 second, thus one cannot distinguish them just from the Fourier spectrum. In other words, the FT results cannot tell us the real frequency distribution of the signal, especially for the nonstationary signal. But the WT can show the spectrum both at the time and frequency frame (see Fig. 3.5e and f) so we can clearly see the real distribution characteristics of the signal.

3.2.2 The mathematical view of WT algorithms

The main features of the continuous WT will be reviewed from a mathematical view, though the strict complete description of wavelet theory is not the intent of this section. (see Daubechies (1990), Chui (1992), Orgden (1997), Holschneider (2000), and Liu (2000)). Just as FT decompose stationary signals canonically into linear combination of sines and cosines waves, the continuous WT decompose nonstationary signals into linear combinations of wavelets. Therefore, the discussion will start from FT analysis.

Given a function or data signal $X(t)$, which is assumed to be square integrable, its FT, $\widehat{X}(\omega)$, is given by:

$$\widehat{X}(\omega) = \int_{-\infty}^{+\infty} X(t) e^{-i\omega t} dt \,, \tag{3.2}$$

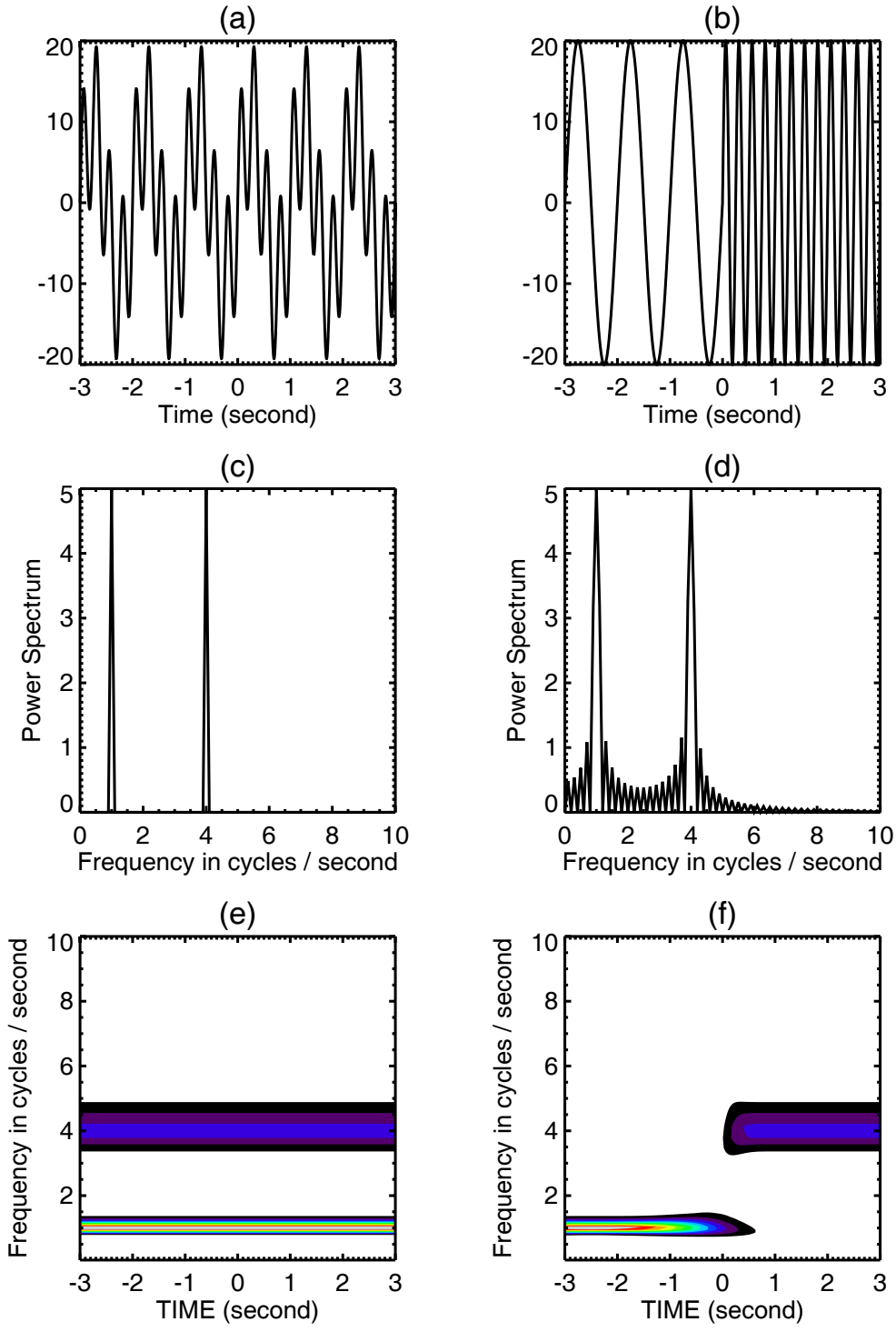

FIG. 3.5. Fourier and wavelet transform of two signals. The first signal a) consists of superposition of two frequencies (1/4 and 1 seconds), and the second b) consists of the same two frequencies each applied separately over half of the signal duration. c) and d) show the Fourier transform of signal a) and b) respectively, and e) and f) show the wavelet spectrum (using Morlet wavelet function), respectively.

which transforms the function in the time domain to frequency domain. In order to examine the characteristics of the signal in the time-frequency domain, the direct method can be obtained by including a time window function $g(t)$ such as:

$$\widehat{X}(\omega,\tau)=\int_{-\infty}^{+\infty}X(t)g(t-\tau)e^{-i\omega t}dt\,. \tag{3.3}$$

Eq. (3.3) is known as the windowed or short-time FT (Gabor 1946), as discussed before which cannot adjust the box size of time-frequency windows as time τ and frequency ω change, while succeeding in the goal of localizing the frequency information of the signal in time, and also localizing the time information in the frequency domain (Kumar and Foufoula –Georgiou 1994; Ogden 1997).

Analogically, if $X(t)$ belongs to the square-integrable function, the continuous wavelet transform (CWT) is defined to be (Kumar and Foufoula–Georgiou 1994; Holschneider 2000):

$$\widehat{W}(\tau,s)=\frac{1}{(s)^{1/2}}\int_{-\infty}^{+\infty}X(t)\,\psi^{*}(\frac{t-\tau}{s})dt\,, \tag{3.4}$$

where $\psi(t)$ is the element transformed wavelet function named "mother wavelet" defined by the translation and scale parameters, respectively, τ and s:

$$\psi_{\tau,s}(t)=\frac{1}{(s)^{1/2}}\psi(\frac{t-\tau}{s})\,. \tag{3.5}$$

As seen in the above equation, the transformed spectrum is a function of two variables, τ and s, the translation and scale parameters, respectively. ψ is the complex conjugate of

ψ^* on the open "time and scale" real (τ, s) half plane and *X(t)* the signal to be analyzed. The normalization factor $s^{1/2}$ in Eq.(3.5) ensures that $\psi_{\tau,s}$ has a constant norm

$$\| \psi_{\tau,s}(t) \|^2 = \int_{-\infty}^{+\infty} |\psi_{\tau,s}|^2 dt = 1 \tag{3.6}$$

in the space of square integrable functions. Essentially in order for function ψ to be a mother wavelet, it needs to satisfy the following admissibility conditions

$$C_\psi = \int_{-\infty}^{+\infty} \frac{|\psi(\omega)|^2}{|\omega|} d\omega < \infty, \tag{3.7}$$

so that a function or data signal, $X(t)$, can be reconstructed from wavelet $\psi_{\tau,s}$ and its corresponding wavelet transform as:

$$X(t) = \frac{1}{C_\psi} \int_{-\infty-\infty}^{+\infty+\infty} \widehat{W}(\tau,s) \psi_{\tau,s}(t) \frac{d\tau ds}{s^2}. \tag{3.8}$$

The simplest CWT method is direct numerical integration, but the drawback of this technology is that it is time consuming in practice. If one integration over $0<s\leq I$ and $0<\tau\leq J$, the integration time goes $I J^2$ (Meyer et al. 1993). An alternative is to exploit the convolution theorem and perform the WT in spectral space:

$$W(\tau,s) = s^{1/2} \int \hat{f}(\omega) \hat{g}^*(s\omega) e^{ib\omega} d\omega \tag{3.9}$$

This method allows the use of optimized fast Fourier transform (FFT) routines such as the Cooley-Tukey algorithm and results in a much faster transformation, with CPU time going as $IJ \log_2 J$. To use this method, one has to deal with finite-length time series as

the periodic one assumed by equation (3.9). Therefore errors will occur at the beginning and the end of wavelet power spectrum $|W(\tau,s)|^2$ (Meyer et al. 1993; Torrence and Compo 1998). Two solutions used to avoid this are zero padding and cosine damping. In this study, the time series are padded with sufficient zero to bring the total length N up to the next-high power of two, thus limiting the edge effects and speeding up the Fourier transform. However, padding with zero introduces discontinuity at the end and beginning of the signal. The cone of influence (COI) is defined to indict the region where the wavelet power spectrum is falsely distorted due to the edge effects.

3.2.3 The choice of the wavelet function

One of the characteristics of WT is the arbitrary choice of the wavelet function using one of more traditional transforms such as the Fourier, Bessel, Legendre, etc. There are several discussions that the following factors have to be considered when choosing the wavelet function including 1) orthogonal or nonorthogonal; 2) complex or real; 3) resolution in time and frequency space; and 4) shapes of wavelet function (Farge 1992; Torrence and Compo 1998). This research mainly focused on the wavelet spectrum of different cirrus cloud structures. I choose the Morlet wavelet function because it is commonly used for spectrum analysis, more easily interpreted due to the complex form, easily applied, and looks like a wave. For the Morlet wavelet transform, a sine and cosine function modulated by a Gaussian function is shown in Fig. 3.6., where the mother wavelet is:

$$\psi_0(\eta) = \pi^{-1/4} e^{i\omega_0\eta} e^{-\eta^2/2}. \tag{3.10}$$

First the wavenumber w_0 has to be chosen, which gives the number of oscillations within the wavelet itself. One condition of the wavelet transform is that the average of the wavelet itself must be zero. In practice, if one chooses $w_0=6$, then the errors due to non-zero mean are smaller than the typical computer round-off errors (Farge 1992). The detailed information about algorithms can be referenced from Torrence and Compo (1998) and the relevant codes in IDL or FORTRAN language can be downloaded from website http://paos.colorado.edu/research/wavelets/.

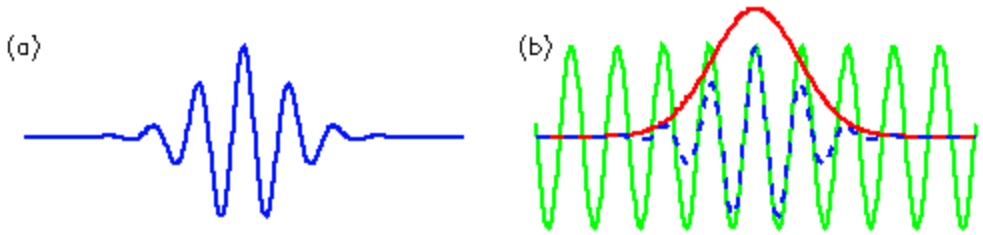

FIG. 3.6. (a) Morlet wavelet of arbitrary width and amplitude with time along the x-axis. (b) Construction of the Morlet wavelet (blue dashed) as a Sine curve (green) modulated by a Gaussian function (red). (From Torrence's wavelet website: http://paos.colorado.edu/research/wavelets/)

CHAPTER 4

KELVIN-HELMHOLTZ INSTABILITIES

4.1 Introduction

Kelvin–Helmholtz (KH) instabilities, named after Lord Kelvin and Herman Von Helmholtz (Helmholtz 1868; Kelvin 1871) who first developed the mathematics of this type of instability in the late nineteenth century, are produced by vertical velocity shear at the interface between two fluids with different physical properties (typically different density). The vertical velocity difference is a measure of the intensity of the vorticity locally. The physical property differences can be measured quantitatively by static stability. When the vorticity associated with the velocity difference across the interface is strong enough for the perturbation in the interface to overcome the static stability, the surface of the density discontinuity can become dynamically unstable and then KH Waves will form (for general discussion, see Scorer 1972; Beer 1974; Gossard and Hooke 1975; Acheson 1990; Houze 1993). They appear as amplifying billow waves oriented perpendicular to the shear vector, into which the vorticity is concentrated, and which eventually breaks into turbulent flow on a range of smaller scales. This distinguishes them from gravity waves from outside disturbance such as a displacement in the boundary, or violent convection (Scorer 1997).

KH instabilities have been the subject of numerous observational and theoretical studies over many years because of their role in the wide range of atmospheric processes. Areas in which KH instabilities play an important role include: 1) excitation of large

scale internal gravity waves vertically propagating to the mid- and upper atmosphere via vortex pairing or two KH mode interaction (Drazin and Howard 1966; Jones 1968; Lindzen 1974; Acheson 1974 ; Grimshaw 1976; Lalas and Einaudi 1976; Fritts 1982, 1984; Chimonas and Grant, 1984 a, b; Bühler and McIntyre 1999; Scinocca and Ford 2000); or 2) the vertical transport of mass, momentum and atmospheric constituents by producing the turbulence accompanying KH growth and breakdown (Lindzen 1981; Thorpe 1987; Scinocca 1995; Fritts et al. 1996; Palmer et al. 1996). Therefore, KH instabilities are thought to be one of the important sources of generating internal gravity waves as well as being mainly responsible for most occurrences of clear air turbulence (e.g., Ludman 1967; Glover et al. 1969; Hicks 1969; Atlas and Metcalf 1970; Reed and Hardy 1972; see a review paper by Fritts and Rastogi (1985)).

KH instabilities occur fairly frequently in the atmosphere, generally with wavelengths up to a few kilometers. Photographs, radar, lidar, radiosonde, and instrumented aircraft have been used to detect KH instabilities in order to compare with the results of laboratory and theoretical studies since the early 1960s. Such observations discovered that KH instabilities usually occur in a boundary layer (Atlas et al. 1970; Merrill 1977; Busack and Brummer 1988; Nielsen 1992 ; Blumen et al. 2001; Newsom et al. 2001; see review paper by Gossard 1990), the free atmosphere or cloud billow located in the upper troposphere or close above the tropopause (Ludlam 1967; Hicks and Angell 1968; Hicks 1969; Browning 1971; Axford 1973; Browning et al. 1973; Reiss and Corona 1977; Browning et al. 1978; James and Browning 1981; Klostermeyer and Rüster 1980; Sassen 1995; Chilson 1997; Singh et al. 1999; Sassen et al. 2003; see a review

paper by Gage 1990), and the middle atmosphere in connection with the polar noctilucent clouds (Witt 1962). The altitude of occurrence of KH instabilities ranges from near the surface up to 80 km. The synoptic environments associated with KH instabilities include frontal zones (Browning et al. 1973; Reed and Hardy 1972; Hardy et al. 1973; Nielsen 1992; Takayabu 1992; Takahashi et al. 1993; Chapman and Browning 1997, 1999), jet stream (Ludlam 1967; Browning et al. 1978; Klostermeyer and Rüster 1980; James and Browning 1981; Reiss and Corona 1977; Chilson et al. 1997; Singh et al. 1999), and orographically induced features and strong shears near the surface in the boundary layer (Ludlam 1967; Merrill 1977; Busack and Brummer 1988). The observational instruments, occurrence height, associated environment, and wavelength of KH instabilities from early and present studies are presented in Table 4.1.

These observations agree well with linear theoretical analysis results: e.g., the local Richard Number is less than 0.25 somewhere in the shear layer, the relationship between the depth of the shear layers and the largest growth rate of KH instabilities. There are three patterns including billow, braid, and cat's eyes that can be revealed by visual observations, as expressed by Gossard and Hooke (1975). These features are pictured schematically in Fig. 4.1. In addition, some interesting phenomena also were disclosed by the above observations. By using X-band radar, Reed and Hardy (1972) discovered that more than one wave located at a different height with a different horizontal wavelength often coupled together. Sassen et al. (1990) also found cirrus layers at times containing closely spaced (~0.5 km) grouping of cells (< 0.4 km in depth), which, as shown by airborne lidar power return, suggested KH waves superimposed on a

TABLE 4.1 KH instabilities observed from prior and recent studies

Author	Instruments	Occurrence height (km)	Wavelength (km)	Associated environment
Witt (1962)	Photograph	83	5~10	Noctilucent cloud
Ludlam (1967)	Photograph	6.9~12 (mean 7.5)	1.6~6.2 (mean 2.7)	Jet stream or orographic feature
Hicks and Angell (1968)	Radar (3.2, 10.7, 71.5 cm)	0.6~7.3 (mean 3.9)	0.9~2.2 (mean 1.6)	In the clear atmosphere
Hicks (1969)	Radar (3.2, 10.7,71.5 cm)	12	1.2~1.3	Clear atmosphere near tropopause
Atlas et al. (1970)	Radar (2.9 GHz)	0.35	0.228	Clear atmosphere in boundary layer
Browning (1971)	Radar(10.7 cm)	5.6~10.7 (mean 8.0)	0.8~4.0 (mean 1.8)	Clear atmosphere in upper troposphere
Reed and Hardy (1972)	Radar (10.7,71.5 cm)	7.0~9.0	1.6	Upper level frontal Zone
Axford (1973)	Aircraft	11.3	2	On the tropopause surface
Browning et al. (1973)	Rdadr(10.7 cm), aircraft	7	1.3-2.4	Billow clouds in the frontal zone
Hardy et al. (1973)	Radar (3.2, 10.2 cm), aircraft	1.7	2.7	Billow clouds in the frontal zone
Merrill (1977)	Acoustic sounder, microbargraphs	0.13	0.34~0.45	In the boundary layer
Reiss and Corona (1977)	Photograph	10.4	11	Billow cirrus associated with jet stream
Browning et al. (1978) James and Browning (1981)	Radar (10 cm)	7	4.2	Billow cirrus clouds associated with jet stream
Klostermeyer and Rüster (1980)	Radar (53.3 MHz)	6	4.6	Jet stream
Busack and Brummer (1988)	Aircraft	0.36	0.65	In a warm off-shore boundary layer
Nielsen (1992)	Aircraft	0.1~0.9	1~2	During costal front inversion
Takayanu (1992)	Photograph	2.8	2.7	Billow clouds on frontal surface
Takahashi et al. (1993)	Radar	3~4	3.5	Associated with stationary front
Sassen (1995)	Airborne Lidar (0.532 μm)	13.1	3.1	Tropical cirrus
Chapman and Browning (1997,1999)	Radar (3 GHz)	2	4	Billow clouds within precipitating warm frontal zone
Chilson et al. (1997)	VHF frequency domain interfermetry	9.1	4	Jet steam
Singh et al. (1999)	Radar (53 MHz)	17.7	7.2	Associated with easterly jet stream
Blumen et al. (2001) Newsom et al. (2001)	Lidar (2 μm)	0.056	0.032	Night-time boundary layer
Sassen et al (2003)	Lidar (0.532 μm)	11.3	2.45	Cirrus associated with tropical system

FIG. 4.1. Schematic views of three patterns commonly observed: billow (left), braids (middle), and cat's eye (right) (Gossard and Hooke 1975).

longer wave pattern. This phenomenon was also shown in the tropical cirrus clouds observed by the NASA ER2 cloud lidar system during Tropical Ocean Global Atmospheres/Coupled Ocean Atmosphere Response Experiment (TOGA/COARE), from which the multiple layer wave structures coupled together at different heights (Sassen 1995). It may be, to some extent, the theoretical evidence that shows the existence of some other modes generated by shear except the KH unstable mode (Lalas and Einaudi 1976).

The photograph of a billow cloud by Scorer (1972) showed that small billows formed on the back of a primary billow that was in the process of developing. Using a high-power 10-cm wavelength radar system, James and Browning (1981) also revealed the kinematic structure of the secondary billows with a wavelength of 350 m growing on the back of primary billows of 4.2 km wavelength. This also can be confirmed by cirrus cloud observation derived from hurricane remnants using FARS two-color polarization diversity lidar during DOE ARM IOP 97 (Sassen et al. 2002), in which the obvious secondary instability developed on the back of the large amplitude primary KH instabilities. Recent numerical simulation results also show that the secondary instabilities are generated when primary instabilities reach the maximum amplitude (e.g., Sciocca 1995; Fritts et al. 1996; Palmer et al. 1996).

KH instabilities are also one of the potentially important dynamical processes within cirrus clouds. From the early observations associated with cirrus clouds (Scorer 1972; Reiss and Corona 1977; Browning et al. 1978) to recent case studies that used lidar or instrumented aircraft to discover fine structures of KH instabilities (Sassen et al. 1990;

Sassen 1995; Demoz et al. 1997; Sassen et al. 2002), these results have shown that they happen fairly frequently in cirrus clouds. This may be because cirrus clouds are often associated with significant wind shear in a stable thermal stratification (Quante and Starr 2002). Just as important, there are still some questions. First, the onset and structure of billows occurring under ideal conditions have been studied in considerable detail using analytical, numerical and laboratory models. However, it is not always clear how these results apply to billows in the real atmosphere, especially in cirrus clouds. There have been few observations of billows in the cirrus clouds that shed light on what their detailed structure is, how they evolve with time from basic flow to generate waves, which in turn generate turbulence by cascade process, and what the interaction between the basic state, waves and turbulence is. Secondly, as referred by Lynch et al. (2002), "Dynamic features and effects of turbulence and cloud scale vertical motions influence the physical properties of clouds, which in turn affect the clouds' radiation properties. Thus, dynamics should be considered in studies addressing the explicit life cycle of cirrus." What role do KH instabilities play in forming, maintenance, and dissipation of cirrus clouds? How is turbulence generated from large-scale wave motion, and how do these processes effect the microphysical properties in cirrus clouds? There are many unknowns about KH instabilities in cirrus clouds. Finally, although high-powered radars have been used to detect the KH instabilities occurring up to the tropopause in the past, these observations are limited to sample resolution and only can provide the structures of large-amplitude KH billows. However, it would appear that small-amplitude KH billows are much more common than large-amplitude billows (Browning 1971; Gage 1991). For the fine

structures of small-amplitude KH waves that are frequent in the atmosphere, we still do not fully understand them according to the past observations.

Fortunately, modern active remote sensors with high resolution, mobility, and advanced technology provide us the opportunities to examine the fine structures of KH instabilities occurring in cirrus clouds (Sassen 1991; Platt et al. 1994; Sassen 1995; Sassen 2001; Newsom et al. 2001; Grund et al. 2001; Sassen and Mace 2002). In this chapter, the properties of KH instabilities of 19 cases including 27 wave packets from the FARS high cloud dataset will be presented. This chapter begins, in section 4.2, with a review of the basic theoretical knowledge of KH instabilities. A case study is presented in section 4.3 based on wavelet analysis of lidar backscattering. Section 4.4 inspects the statistical properties of the KH instabilities from the FARS high cloud dataset. This chapter ends with the conclusions in section 4.5.

4.2 Theoretical Background

In order to simplify the question we only consider small scale, two-dimensional disturbances. It is convenient to decompose the variables into a zonal-mean basic state, which reflects undisturbed conditions, and perturbations from it. Let

$$\mathrm{u} = \mathrm{U}_0(\mathrm{z}) + u',\ w = w',\ \rho = \rho_0(z) + \rho',$$

$$p = p_0(z) + p', T = T_0(z) + T',\ \theta = \theta_0(z) + \theta' \tag{4.1}$$

where the U_0 , ρ_0, p_0, T_0, and θ_0 are the mean state of horizontal flow, density, pressure, temperature, and potential temperature of the background atmosphere. u', w', and ρ' donate the disturbance terms of horizontal velocity, vertical velocity, pressure, density,

temperature, potential temperature, and density, respectively. By using the Boussinesq approximation and just considering the first order of perturbation, the equations of horizontal momentum and vertical momentum, conservation of mass, and the condition of incompressibility take the form:

$$\rho_0\left(\frac{\partial}{\partial t}+U_0\frac{\partial}{\partial x}\right)u'+\rho_0\frac{\partial U_0}{\partial z}w'+\frac{\partial p'}{\partial x}=0 \tag{4.2}$$

$$\rho_0\left(\frac{\partial}{\partial t}+U_0\frac{\partial}{\partial x}\right)w'+\frac{\partial p'}{\partial z}+g\rho'=0 \tag{4.3}$$

$$\frac{\partial u'}{\partial x}+\frac{\partial w'}{\partial z}=0 \tag{4.4}$$

$$\left(\frac{\partial}{\partial t}+U_0\frac{\partial}{\partial x}\right)\rho'-\frac{N^2}{g}\rho_0 w'=0 \tag{4.5}$$

,

where g is the acceleration of gravity and N is Brunt-Väisälä frequency given by:

$$N^2=\frac{g}{\theta_0}\frac{\partial\theta}{\partial z}. \tag{4.6}$$

It is reasonable to assume $(1/\rho_0)(\partial\rho_0/\partial z)$ is constant. That means ρ_0 varies experientially with height, say

$$\rho_0=\rho_s e^{-\alpha z}, \tag{4.7}$$

where ρ_S is the density at some reference level which may often conveniently be taken as the earth's surface, and where ρ_0 is the zero-order density function with height. Using the transformation by Gossard and Hooke (1975), one defines:

$$U=\left(\frac{\rho_0}{\rho_S}\right)^{1/2}u',\ W=\left(\frac{\rho_0}{\rho_S}\right)^{1/2}w',\ \ P=\left(\frac{\rho_0}{\rho_S}\right)^{-1/2}p'. \tag{4.8}$$

One can eliminate ρ' by (4.3) and (4.5). Then the equations change to:

$$\left(\frac{\partial}{\partial t}+U_0\frac{\partial}{\partial x}\right)U+\frac{\partial U_0}{\partial z}W+\frac{1}{\rho_S}\frac{\partial P}{\partial x}=0 \tag{4.9}$$

$$\left(\left(\frac{\partial}{\partial t}+U_0\frac{\partial}{\partial x}\right)^2+N^2\right)W+\frac{1}{\rho_s}\left(\frac{\partial}{\partial t}+U_0\frac{\partial}{\partial x}\right)\left(\frac{\partial}{\partial z}+\Gamma\right)P=0 \tag{4.10}$$

$$\frac{\partial U}{\partial x}+\frac{\partial W}{\partial z}=0 \tag{4.11}$$

,

where Γ is Eckart's coefficient (Eckart 1960) :

$$\Gamma=\frac{1}{2\rho_0}\frac{\partial \rho_0}{\partial z} \tag{4.12}$$

.

For most analyses of wind shear effects on gravity wave, Γ is negligible. P and U are easily eliminated and finally one obtains:

$$\left(\left(\frac{\partial}{\partial t}+U_0\frac{\partial}{\partial x}\right)^2\left(\frac{\partial^2}{\partial x}+\frac{\partial^2}{\partial z}\right)-\frac{\partial^2 U_0}{\partial z^2}\left(\frac{\partial}{\partial t}+U_0\frac{\partial}{\partial x}\right)\frac{\partial}{\partial x}+N^2\frac{\partial^2}{\partial x^2}\right)W=0 \tag{4.13}$$

.

Considering the boundary condition, one defines the solution as:

$$W=\overline{W}(z)e^{i(kx-\sigma t)} \tag{4.14}$$

.

Equation (4.13) becomes:

$$(U_0-C)^2\frac{d\overline{W}}{dz^2}+\left(N^2-(U_0-C)\frac{\partial^2 U_0}{\partial z^2}-k^2(U_0-C)^2\right)\overline{W}=0 \tag{4.15}$$

,

where $C=\sigma/k=C_r+ i\ C_i$ is phase speed. This equation is known as the Taylor-Goldstein equation.

Now set

$$F = \overline{W}/\left(\overline{U}_0 - c\right) \tag{4.16}$$

and then replace variable $\overline{W}$ by F in (4.16). This gives:

$$\frac{d}{dz}\left[\left(U_0 - C\right)^2 \frac{dF}{dz}\right] + \left[N^2 - k^2\left(U_0 - C\right)^2\right]F = 0 \ . \tag{4.17}$$

Set again:

$$G = \left(U_0 - c\right)^{1/2} F \ . \tag{4.18}$$

Equation (4.17) became:

$$\frac{d}{dz}\left[\left(U_0 - C\right)^2 \frac{dG}{dz}\right] + \left[\frac{1}{2}\frac{\partial^2 U_0}{\partial z} + k\left(U_0 - c\right) + \frac{\frac{1}{4}\left(\frac{\partial U_0}{\partial z}\right)^2 - N^2}{U_0 - C}\right]G = 0 \ . \tag{4.19}$$

Notes that the boundary condition is:

$$W|_{z=0,H} = F|_{z=0,H} = G|_{z=0,H} = 0. \tag{4.20}$$

4.2 1. Necessary condition for instability (Miles 1961; Howard 1961)

Multiplication of (4.19) by the complex conjugate G* of G and integration from (0, H), leads to:

$$\int_0^H \left\{\left(U_0 - C\right)\left(\left|\frac{dG}{dz}\right|^2 + k^2|G|^2\right) - \frac{1}{2}\frac{\partial^2 U_0}{\partial z^2}|G|^2 + \left[N^2 - \frac{1}{4}\left(\frac{\partial U_0}{\partial z}\right)^2\right]\frac{|G|}{U_0 - C}\right\}\delta z = 0 \ . \tag{4.21}$$

Note that subsequently $\int$ is used to denote the definite integral over (0, H).

The imaginary part of the above equation (4.21) is:

$$C_i \int \left\{\left|\frac{dG}{dz}\right|^2 + k^2|G|^2 + \left[N^2 - \frac{1}{4}\left(\frac{\partial U_0}{\partial z}\right)^2\right]\frac{|G|^2}{(U_0 - C)^2}\right\}\delta z = 0 \ . \tag{4.22}$$

If the wave is instable (C_i >0), this is clearly impossible if $N^2 - \frac{1}{4}\left(\frac{\partial U_0}{\partial z}\right)^2$ is non-negative throughout, so that a necessary condition for instability is that $N^2 - \frac{1}{4}\left(\frac{\partial U_0}{\partial z}\right)^2$ be somewhere negative, or, as Miles (1961) expressed it, a sufficient condition is that $N^2 - \frac{1}{4}\left(\frac{\partial U_0}{\partial z}\right)^2$ should be everywhere non-negative. If the Richard number (Ri) is defined by the Brunt-Väisälä frequency and vertical shear of horizontal wind velocity as the following:

$$Ri = \frac{N^2}{\left(\partial U_0 / \partial Z\right)^2}. \tag{4.23}$$

For a stratified fluid, it can be shown on the basis of linear theory that local Ri must be less than 0.25 somewhere in the flow.

4.2.2 Howard semicircle theorem (Howard 1961)

Returning to equation (4.17), using complex conjugate F* of F to multiply it, and integrating over (0, H) one gets:

$$\int \left\{ \left(U_0 - C\right)^2 \left(\left| \frac{dF}{dz} \right|^2 + k^2 \left|F\right|^2 \right) - N^2 \left|F\right|^2 \right\} \delta z = 0 . \tag{4.24}$$

Separating the real and imaginary parts of (4.24):

$$\int \left[\left(\left(U_0 - C_r\right)^2 - C_i \right) \left(\left| \frac{dF}{dz} \right|^2 + k^2 \left|F\right|^2 \right) - N^2 \left|F\right|^2 \right] \delta z = 0 \tag{4.25}$$

$$2C_i \int \left[(U_0 - C_r) \left(\left| \frac{dF}{dz} \right|^2 + k^2 |F|^2 \right) \right] \delta z = 0 \ . \tag{4.26}$$

For instable wave, $C_i>0$, it requires that $U_0 - C_r$ changes from positive to negative or vice versa over *(0, H)*. This means, over *(0, H)*, there must be one critical layer $z=z_c$ where $U_0 - C_r = 0$ so that energy can be transferred from mean flow to the instabilities. Let

$$Q = \left| \frac{dF}{dz} \right|^2 + k^2 |F|^2 \tag{4.27}$$

Then under the assumption $C_i>0$, equations (4.25) and (4.26) change into:

$$\int U_0 Q \delta z = C_r \int Q \delta z \tag{4.28}$$

$$\int U_0{}^2 Q \delta z = \left(C_r^2 + C_i^2 \right) \int Q \delta z + \int N^2 |F|^2 \delta z \ . \tag{4.29}$$

Suppose that $a \le U_0(z) \le b$. Then

$$\begin{aligned} 0 \ge \int (U_0 - a)(U_0 - b) Q \delta z &= \int U_0^2 Q \delta z - (a+b) \int U_0 Q \delta z + ab \int Q \delta z \\ &= [C_r^2 + C_i^2 - (a+b) C_r + ab] \int Q \delta z + \int N^2 |F|^2 \delta z \\ &= \left\{ \left[C_r - \frac{1}{2}(a+b) \right]^2 + C_i^2 - \left[\frac{1}{2}(a-b) \right]^2 \right\} \int Q \delta z + \int N^2 |F|^2 \delta z \end{aligned} \tag{4.30}$$

Thus, for any unstable mode the complex wave velocity *c* must lie inside the semicircle in the upper half-plane which has the range of U_0 for diameter. This is called Howard semicircle theorem.

4.2.3 Growth rate

The necessary conditions of instabilities and the semicircle limit the values of Ri and the complex wave velocities, which are accessible for unstable modes. It is of interest to have a similar bound on the growth rate kC_i possible for an unstable wave. From (4.22), by observing that

$$\frac{1}{\left|U_0 - C\right|^2} = \frac{1}{\left(U_0 - C_r\right)^2 + C_i^2} \le \frac{1}{C_i^2} \tag{4.31}$$

and so

$$\begin{aligned} k^2 \int \left|G\right|^2 \delta z &= \int \left(\frac{\partial U_0}{\partial z}\right)^2 \left(\frac{1}{4} - Ri\right) \frac{\left|G\right|^2}{\left|U_0 - C\right|^2} \delta z - \int \left|\frac{dG}{dz}\right|^2 \delta z \\ &\le \frac{1}{\mathrm{C_i^2}} \max_{(0.H)} \left(\frac{\partial U_0}{\partial z}\right)^2 \left(\frac{1}{4} - Ri\right) \int \left|G\right|^2 \delta z \end{aligned} \tag{4.32}$$

So one can get the growth rate of instability mode:

$$\left|k\mathrm{C_i}\right| \le \max_{(0.H)} \left|\frac{\partial U_0}{\partial z}\right| \sqrt{\frac{1}{4} - Ri} \,. \tag{4.33}$$

It is sufficient to show that C_i must approach zero as the wavelength decreases to zero, given the bound of $(\partial U_0/\partial z)$. This probably means all waves shorter than some critical wavelength are stable. Furthermore, for a shear layer with finite thickness ΔZ, the fastest growing wavelength is given by Miles and Howard (1964) as:

$$\lambda_{Max} = 7.5 \Delta Z \,. \tag{4.34}$$

The horizontal wavelength of the most rapid growing unstable waves is about 7.5 times the shear layer thickness.

4.3 A Case Study of KH Instabilities

Before evaluating the statistical properties of KH instabilities from the FARS high cloud dataset, a case study is first given to show the procedure that is dealt with data and the ability of wavelet methods to detect such cloud scale structures. This case (case 18 see Table 4.2) is a cirrostratus observed by the CPL system from 1827 to 2100 UTC on 23 January 2000. According to satellite images and the synoptic weather maps, this KH event was associated with a jet stream system, a typical winter synoptic system to generate cirrus clouds at FARS (Sassen and Campbell 2001; Sassen 2002). As shown in Fig. 4.2a, the GOES-10 infrared image at 2100 UTC at the time KH instability occurred, frontal cloud bands were approaching FARS from the east Pacific coast, in front of which the a jet stream propagated eastward from the east Pacific coast to eastern Colorado, producing the axe-shaped cirrus cloud area. A ridge extended from southern California and occupied most of Nevada and Utah. According to the visual satellite image with 1 km resolution at 2100 UTC in Fig. 4.2b, transparent jet stream-generating cirrus was passing through the Salt Lake City area, composed of several cloud streaks parallel to the wind direction. Below the cirrus clouds, the mountain snow still can be detected.

The radiosonde profile at 0000 UTC on 24 January 2001 (Fig. 4.3), three hours after the lidar observations, clearly characterizes these environmental features. The wind velocity increases from ~20 m/s at 7.0 km to ~60 m/s above 10.0 km, which generates strong wind shear within clouds, while the wind direction keeps westerly and does not change greatly from the cloud bottom to cloud top. The potential temperature profile discloses a stable thermal structure within the cloud. Some unstable areas can be found at the cloud top, which probably result in the formation of a convective cell that produced

a)

b)

FIG. 4.2. GOES-10 satellite images at 2100 UTC on Jan 23 2000 including a) 4-km infrared channel image and b) 1-km visual channel image. It clearly shows that jet stream generated cirrus was passing over the FARS site during the lidar observations.

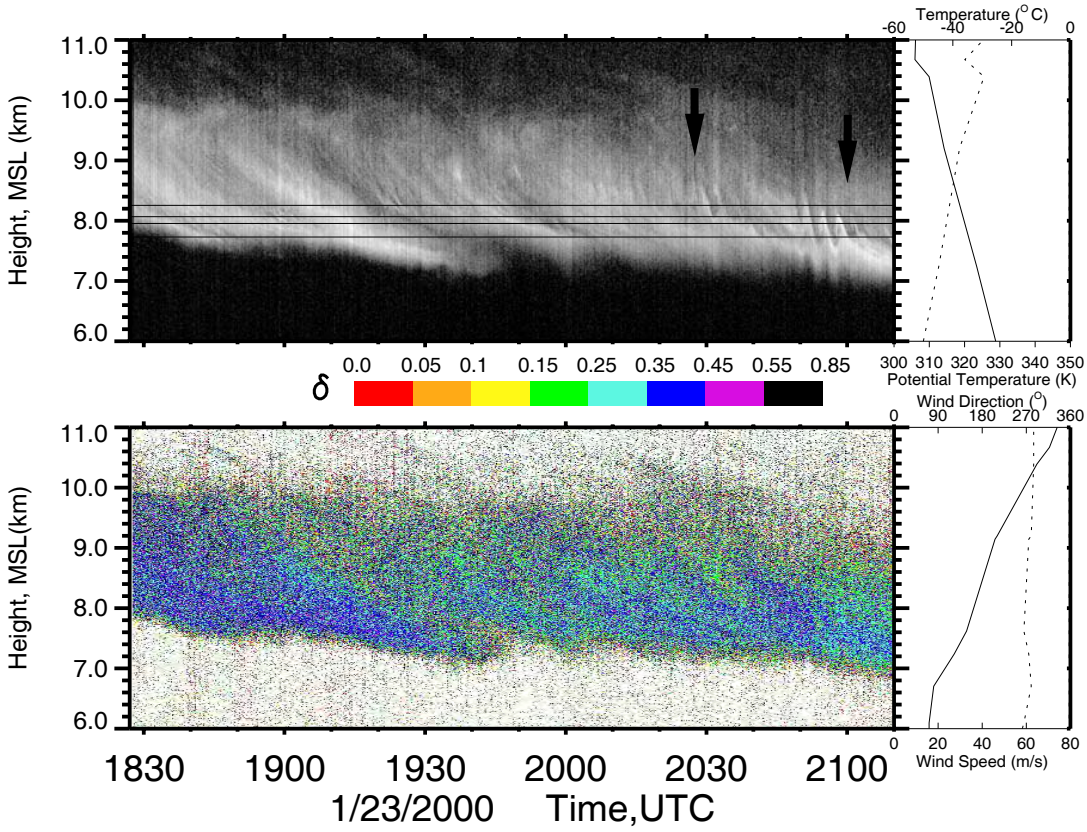

FIG. 4.3. Lidar backscattered power (top left, based on logarithmic grayscale) and linear depolarization ratio (bottom right, indicated by color table). The radiosonde profiles of temperature (top right, solid line), potential temperature (top right, dashed line), wind velocity (bottom right, solid line), and wind direction (bottom right, dashed line) at 0000 UTC on Jan 24 2000 three hours after lidar observations are shown, which disclose that cirrostratus was generated under stable thermal stratified condition with the strong wind shear. The arrows in lidar power image indicate the KH instability events, respectivly, occurring around 2030 and 2100 UTC and the dark lines represent the signals extracted to be analyzed using wavelet transform.

falling ice crystals (Heymsfield 1975b; Sassen et al. 1989; Starr and Wylie 1990). The lidar backscattering power and linear depolarization ratio profiles observed by FARS CPL system from 1827 to 2110 UTC are presented in Fig. 4.3. The backscattered power image reveals that five downdraft fallstreak cells of ice crystals are imbedded in the cirrostratus, which resemble an arc shape due to the strong wind shear. On the trailing edge of the fourth fallstreak around 2030 UTC, KH waves were generated and vanished quickly (indicated by arrow). From 2045 to 2105 UTC, another series of KH waves appear again composed of four billow wave cells. Their shapes are similar to the billows shown in Fig. 4.1. The maximum value of crest-to-trough amplitude reaches 1.1 km. The linear depolarization ratios are around 0.35-0.45 that cannot identify the KH waves except five fallstreak cells. This implies that part of the cirrus layer was composed of randomly oriented ice crystals (Sassen 2000), and that strong mixing processes occurred accompanying the growth and breakdown of the KH instabilities (Lindzen 1981; Thorpe 1987; Scinocca 1995; Fritts et al. 1996; Palmer et al. 1996).

The common parameter used to evaluate the existence of KH instabilities and turbulence is the bulk Richardson number, Ri, which is defined by the vertical gradient of potential temperature and the vertical shear of horizontal wind velocity as:

$$Ri = \frac{N^2}{\left(\frac{\partial \mathrm{U}}{\partial \mathrm{z}}\right)^2 + \left(\frac{\partial \mathrm{V}}{\partial \mathrm{z}}\right)^2}$$

where N is Brunt-Väisälä frequency defined as $N^2 = \frac{g}{\theta_0}\left(\frac{\partial \theta}{\partial z}\right)$ (Quante and Starr 2002). In order to calculate Ri, the wind velocity and direction are adjusted into the same height

in every 200 m using linear interpolation in order to compare with other results (e.g. Browning 1971). The Brunt-Väisälä frequency and the shear of the wind in north-south and west-east direction are determined by performing numerical differentiation using 3-point Lagrangian interpolation (Hildebrand 1956). In other words, the calculated bulk Ri is the average value in every 200 m layer. Fig.4.4 presents the profile of wind sheer respectively in north-south and west-east components, Brunt-Väisälä frequency, and bulk Richard number in every 200 m, where one can find that wind shear is mainly from the east-west direction and reaches the maximum value ~0.02 s^{-1} in the cloud base area. The values of N^2 are 0.0001 in the cloud area except negative values in the cloud top, which reveal the presence of the stable stratified thermal structure where KH instabilities happen (shadow area). The bulk Richard number per 200 m interval reach to 0.249 at 7.4 km and is around 1.0 in other positions where the KH instability occurred. According to the theory pf Miles' (1961) and Howard (1961), a necessary condition for KH instability is that the Richard number is less than 0.25. The results of the present study generally agree with this though the sounding profile is 3-h later than the lidar observations.

Wavelet methods have been used to extract the KH wave characteristics because of their ability to detect the localized intermittent events (see discussion in Chapter three). The 3D wavelet spectrum and the time-averaged global wavelet spectrum using Morlet wavelet function as well as the signal on 8233m are presented in Fig. 4.5. The length scale is determined from the product of the period and the horizontal wind velocity at that height. The local wavelet spectrum clearly discloses two KH instability events occurring respectively around 2030 and 2050 UTC with a power peak around 7-8 km, which are

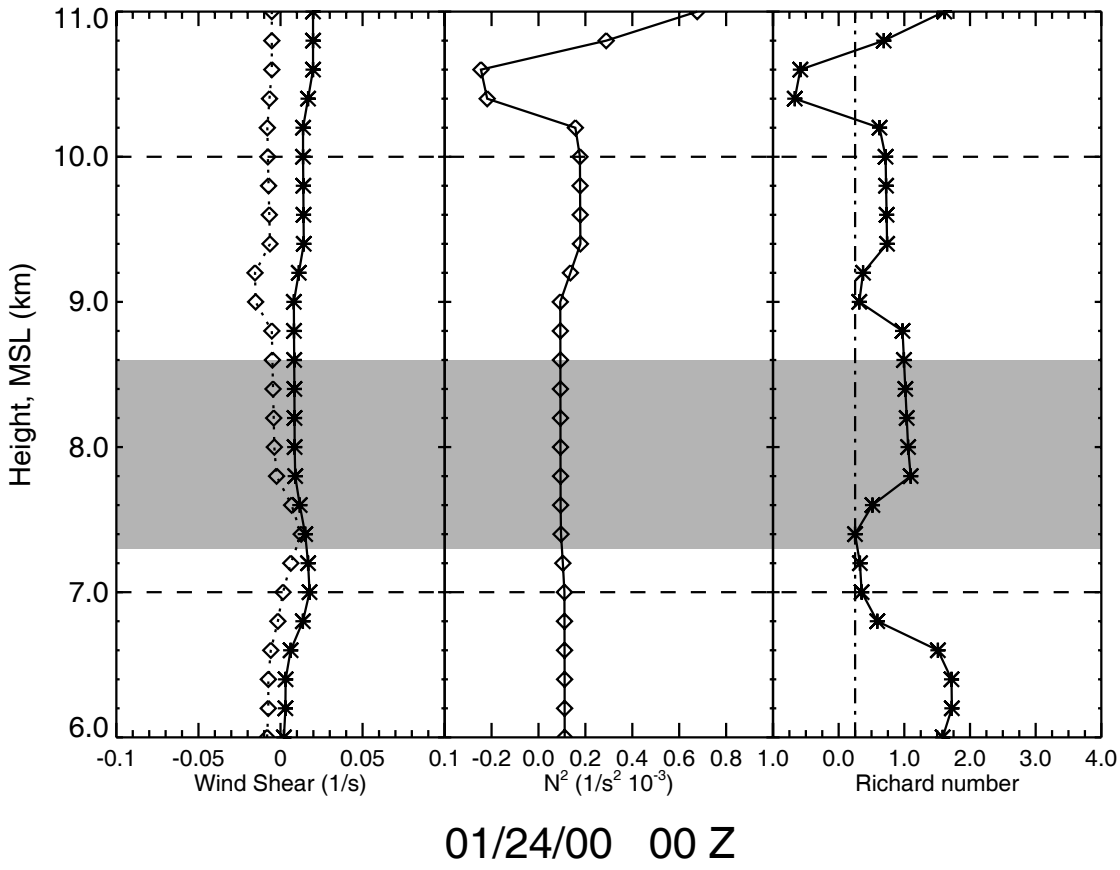

FIG. 4.4. (Left to right) Wind shear (solid line for west-east direction and dot line for north-south direction), N^2, and Richard number calculated every 200 m. The shadow area represents the position where KH instabilities occurred and the dashed line is the mean cloud top and bottom.

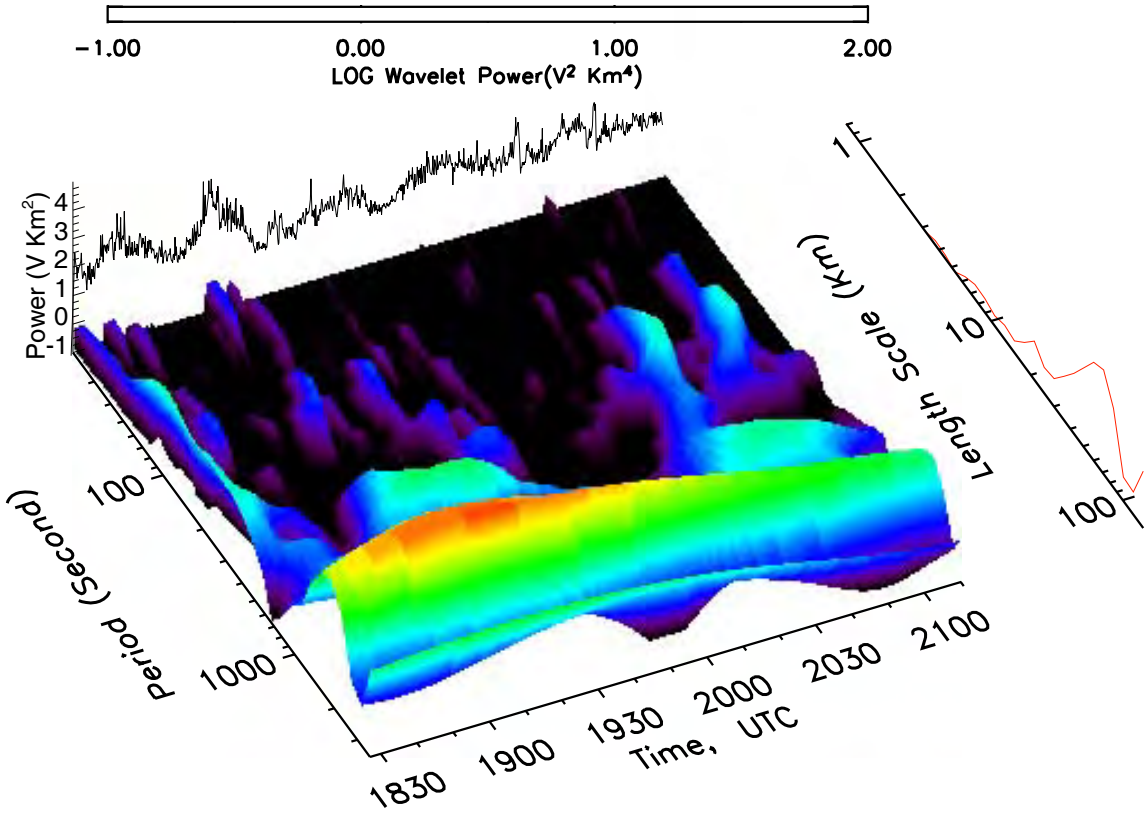

FIG. 4.5. 3D illustration of wavelet spectrum (mid) using Morlet wavelet function for the signal on the height of 8.255 km (top) as well as the time-averaged global wavelet (left). The local wavelet spectrum clearly discloses two KH instabilities occurring respectively around 2030 and 2050 UTC with a wavelength 7~8 km, which are embedded in mesoscale structures with length scales around 70~90 km.

embedded in mesoscale structures with a length scale of 70-90 km. This implies that the cloud scale structures generally interact with mesoscale processes and coexist in the same cloud system (Sassen et al. 1989; Sassen et al. 1990; Demoz et al. 1998; Quante and Starr 2002).

In order to quantitatively derive wave information, the wavelet and Fourier transform for the backscattered power at 7730, 7955, and 8067.50 m height are calculated (Fig. 4.6). The time-averaged global spectrum and Fourier spectrum are normalized into the same scale according to their inherent relationship (Torrence and Compo 1998). It should be noted that the global wavelet spectrum can be treated as the smoothed and averaged FFT spectrum (Percival 1995). In order to compare the local wavelet power at the different time period (or length scale), it is convenient to normalize the wavelet spectrum and pick the significant peak by choosing an appropriate background. For many geophysical phenomena, an appropriate background spectrum is either white noise (with a flat Fourier spectrum) or red noise (increasing power with decreasing frequency). Here, in order to simplify the question, we choose the white noise as the background spectrum, which assumes the wavelet power uniformly distribute both in chosen time and frequency domains in the background. The statistical significance testing has been carried out for the local wavelet spectrum (Torrence and Compo 1998). Shown in Fig. 4.6, 95% confidence level contour, compared with the background spectrum, indicate that the peak of the local wavelet power spectrum is significantly above the background spectrum and can be assumed to be a true feature with 95% confidence. From Fig.4.6, the power peak of three levels around 2050 UTC with the

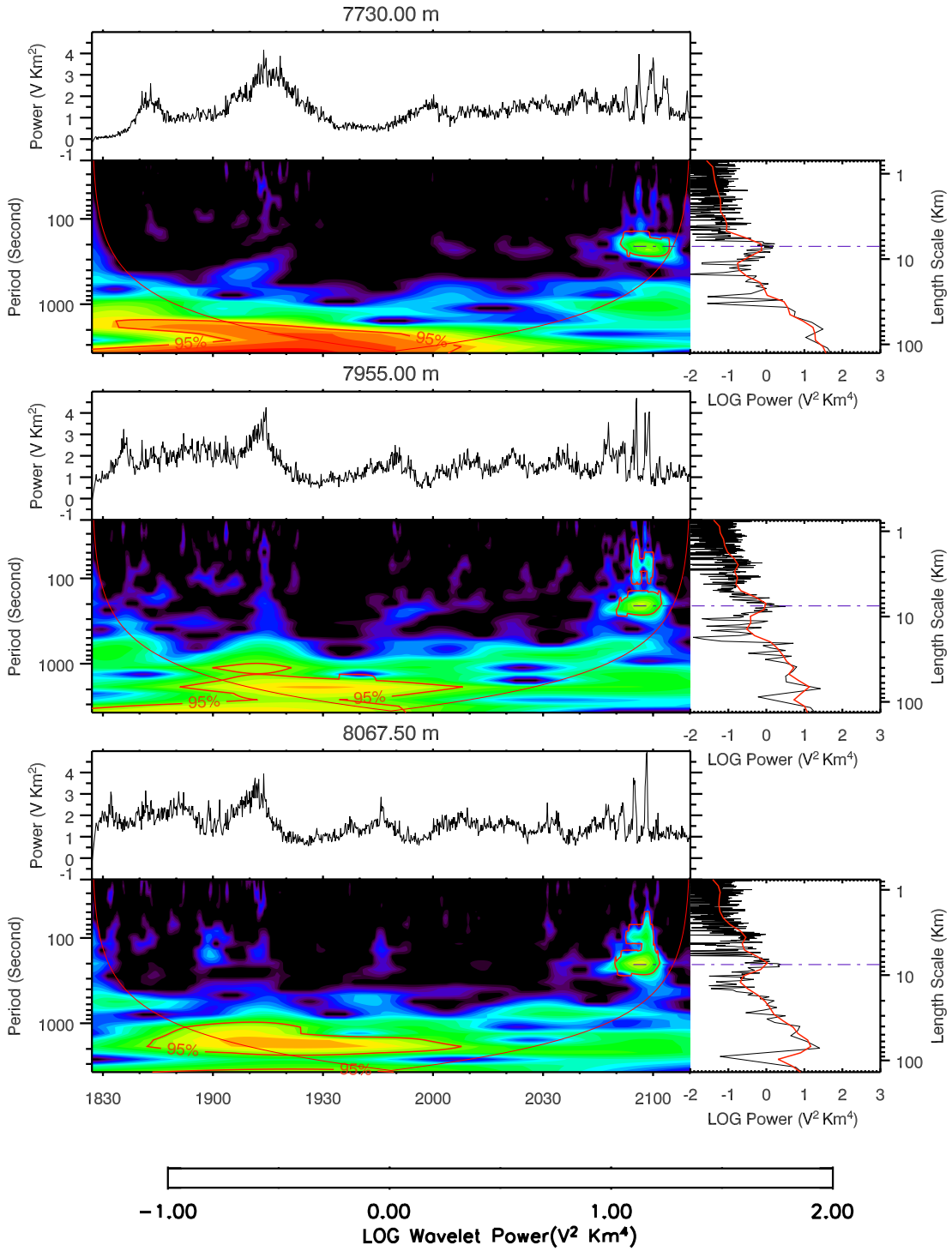

FIG. 4.6. The backscattered power used for the wavelet analysis, the local wavelet spectrum as well as the 95% confidence level compared with the white noise background spectrum, and the Fourier transform and time-averaged global wavelet on the height 7730, 7955, and 8067.5 m respectively. The red line indicates the "cone of influence", where edge effects become important. The dashed blue line indicates the peak of wavelet spectrum of the second KH instability event.

length scale 7-8 km fall in the 95% confidence level. Therefore, one can draw the conclusion that this KH wave has a wavelength of 7-8 km. In addition, the wavelet transform method also illustrates its potential ability to detect the local dynamic processes within cloud that interact with the large scale processes.

4.4 KH Instabilities Observed from FARS High Cloud Dataset

Only case study is not enough to disclose the properties of KH instabilities associated with cirrus clouds. According to three patterns presented in Fig. 4.1, the FARS high cloud datasets was visually checked for 1992-2001 and totally 27 KH instability events have been identified by the 19 lidar observation cases, which include 18 cases observed by the CPL and 1 case by the PDL during the ARM 1997 field experiment (Sassen et al. 2003). It should be pointed out that some KH instabilities (5/19) occur in groups, coupled together, and form into a series of KH waves. This phenomenon has also been reported by Reed and Hardy (1972), Sassen (1995), and Sassen et al. (1990). In this survey they were treated as different wave packets. The physical description is given in Table 4.2 including the lidar observational time, the corresponding radiosonde time, the mean cloud bottom and top, KH instability occurrence height and duration, maximum crest-to-trough amplitude, wave length, and the type of cirrus clouds according to Table 2.2.

4.4.1 Cirrus cloud type associated with KH instabilities

According to the generation mechanisms, FARS high clouds could be classified into four different types using the field notes as discussion in Chapter two (Sassen 2002).

TABLE 4.2 Cases of KH instabilities found from FARS high cloud datasets

Case #	Lidar observation	Sound file	Cloud bottom (km)	Cloud top (km)	Occurrence height (km)	Duration (s)	Wave height (km)	Wave length (km)	Cirrus type
1	92/03/25 2050~2315	92/03/25 12Z	8.6	11.5	11.0~11.5	1212	0.5	6.5~8.0	Synoptic
2	92/05/23 0121~0445	92/05/23 00Z	8.0	11.0	8.5~10.8	5440	0.4	2.0~3.0	Anvil
3	92/06/03 0052~0220	92/06/03 00Z	9.2	12.2	9.2~10.1	2750	0.9	6.0~7.0	Anvil
4	92/09/19 1857~2310	92/09/20 00Z	10.9	13.2	10.9~12.2	1932	0.4	2.0~3.0	Synoptic
5	92/10/11 0001~0134	92/10/11 00Z	10.4	12.6	11.1~12.1	1716	0.9	5.0~6.0	Contrail
					10.5~11.5	540	0.9	1.5-2.5	
6	93/04/04 0231~0430	93/04/04 00Z	8.4	11.4	10.6~11.1	630	0.5	2.0~3.0	Synoptic
					10.2~10.6	350	0.4	1.0~2.0	
					9.8~10.2	430	0.4	1.0~2.0	
7	93/12/13 2241~0040	93/12/14 00Z	10	11.4	11.2~11.4	1080	0.2	3.0~4.0	Synoptic
					10.7~10.8	780	0.1	2.0~3.0	
					10.3~10.7	1120	0.3	2.0~3.0	
8	94/10/26 2244~2359	94/10/27 00Z	6.6	10.7	6.7~8.9	1210	1.7	6.5~7.0	Synoptic
9	95/01/12 1931~2150	95/01/13 00Z	7.2	9.0	8.3~8.8	550	0.4	3.0~4.0	Synoptic
					7.2~8.9	2410	0.5	6.5~7.5	
10	95/09/18 2307~0037	95/09/19 00Z	9.0	11.1	10.5~11.1	640	0.5	1.5~2.5	Anvil
11	95/12/29 1807~2110	95/12/30 00Z	6.0	10.1	6.4~7.7	3860	0.8	3.0~5.0	Synoptic
12	96/01/16 1856~2023	96/01/17 00Z	7.0	9.2	7.5~8.8	1140	1.0	9.0~10.0	Synoptic
13	97/03/14 1705~1812	97/03/14 12Z	7.0	8.8	8.0~8.8	780	0.4	2.0~3.0	Synoptic
					7.7~8.6	1130	0.5	2.5~3.5	
			4.4	5.0	4.7~5.0	440	0.2	0.9~1.1	
14	97/09/06 0148~0323	97/09/06 00Z	9.0	12.4	11.5~12.4	2740	0.6	9.0~10.0	Anvil
15	97/09/26 1800~2000*	97/09/27 00Z	10.9	12.4	10.9~11.5	240	0.6	2.2~2.6	Tropical
16	97/11/03 1700~1920	97/11/04 00Z	7.5	13.2	9.6~10.3	816	0.3	2.0~3.0	Synoptic
17	99/07/13 0136~0436	99/07/13 00Z	10.0	13.6	10.2~11.8	1248	0.9	10.0~11.0	Anvil
18	00/01/23 1827~2110	00/01/24 00Z	7.0	10.0	7.3~8.6	2300	1.1	7.0~8.0	Synoptic
19	00/12/05 2132~0012	00/12/06 00Z	10.4	12.1	11.3~12.1	2940	0.3	6.8-7.5	Synoptic

* Notes to the observations by the high-resolution PDL system.

Sassen and Comstock (2002) surveyed a total of 860 h of cirrus cloud data between 1992 and 1999 and classified the FARS ice clouds into different types from the generation mechanisms. Synoptic cirrus, as most common cirrus cloud type in FARS site, makes up 60.6% of the total observations and the anvil cirrus clouds and subtropical cirrus, respectively, makes up 13.8% and 7.45%. By checking the cirrus cloud type associated with KH instabilities, of all 19 cases of KH instability events, the synoptic cirrus clouds makes up 63.2% (12/19) and anvil cirrus have 26.3 % (5/19). It is not surprising that most KH instabilities are associated with synoptic cirrus because the synoptic environments associated with KH instabilities generally include frontal zone (Browning et al. 1973; Reed and Hardy 1972; Hardy et al. 1973; Nielsen 1992; Takayabu 1992; Takahashi et al. 1993; Chapman and Browning 1997, 1999), jet stream (Ludlam 1967; Browning et al. 1978; Klostermeyer and Rüster 1980; James and Browning 1981; Reiss and Corona 1977; Chilson et al. 1997; Singh et al. 1999), and orographic induced features or strong shears near ground boundary layer (Ludlam 1967; Merrill 1977; Busack and Brummer 1988). However, compared with the results from Sassen and Comstock (2002), the frequency of anvil cirrus associated with KH instabilities is around 19% higher than the frequency occupied in the whole high cloud dataset. In other words, to some extent, it implies that the KH instability events occur more frequently in the environment of anvil cirrus.

Thunderstorms have long been known to be one of the most important mechanisms to generate the gravity waves (e.g., Erickson 1973; Balachandran 1980; Gedzelman 1983; Horinouchi et al. 2002). By overshooting the air from ground into the

anvil system strong convective activity can cause the wave motion around anvils. Effected by the strong wind shear in the upper troposphere, these motions can be unstable and result in KH instabilities. Thus, cirrus generated from anvil outflow is a nice tracer to detect these KH instabilities. This may be the reason why KH instabilities occur more frequently in anvil cirrus than other types of cirrus.

4.4.2 Occurrence height of KH instabilities

The height of KH instabilities was checked for all 19 cases. The relative height of KH instabilities compared to mean cloud top and bottom during the observation can been shown in Fig. 4.8a, where the yellow bars represent the cloud layer and the blues show the region where the KH instabilities happened. The results disclose that the KH instabilities in cirrus clouds occurred frequently in the three places: 1) the leading edge of cirrus cloud top; 2) the back of the trail of down-draft crystal fallstreak; and 3) cirrus cloud bottom areas. A typical example that KH instabilities occurred on cloud top can be shown in case 6 as well as Fig. 4.7a and also can be found in case 1, 6, 7, 9, 10, 13, 14, and 15. The cases that KH instabilities occur on the back of the down-draft fall streak include case 2, 4, 5, 8, 16, 17 and 18. The typical example is case 8 that can be found in Fig. 4.7b. As shown in Fig. 4.7c (case 11), case 3, 11, and 12 present those that the KH instabilities occurred around cloud base area.

It is not uncommon to observe KH instabilities on the cloud top, where there often is a discontinuity in density and wind (e.g., James and Browning 1981). On the cloud top, the generating cells of cirrus clouds are located and so conditional instability often exists which is easy for small distribution develop (Ludlam 1948; Ludlam 1956; Heymsfield

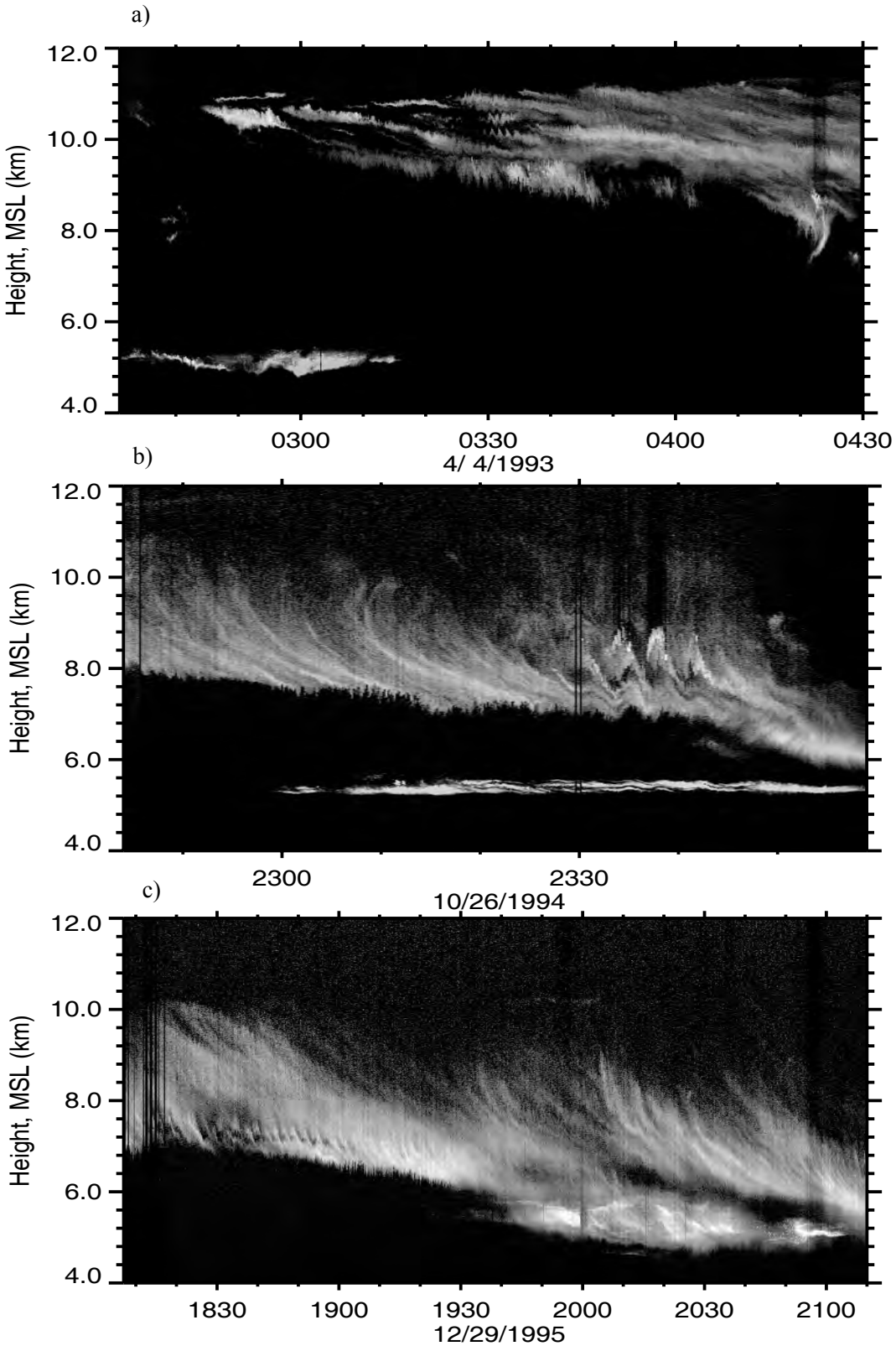

FIG. 4.7. Typical cases that show the position where KH instabilities frequently occur in cirrus: a) the leading edge of cirrus cloud top (case 6); b) the back of the trail of downdraft crystal fallstreak (case 8); and c) the cirrus cloud bottom area (case 11).

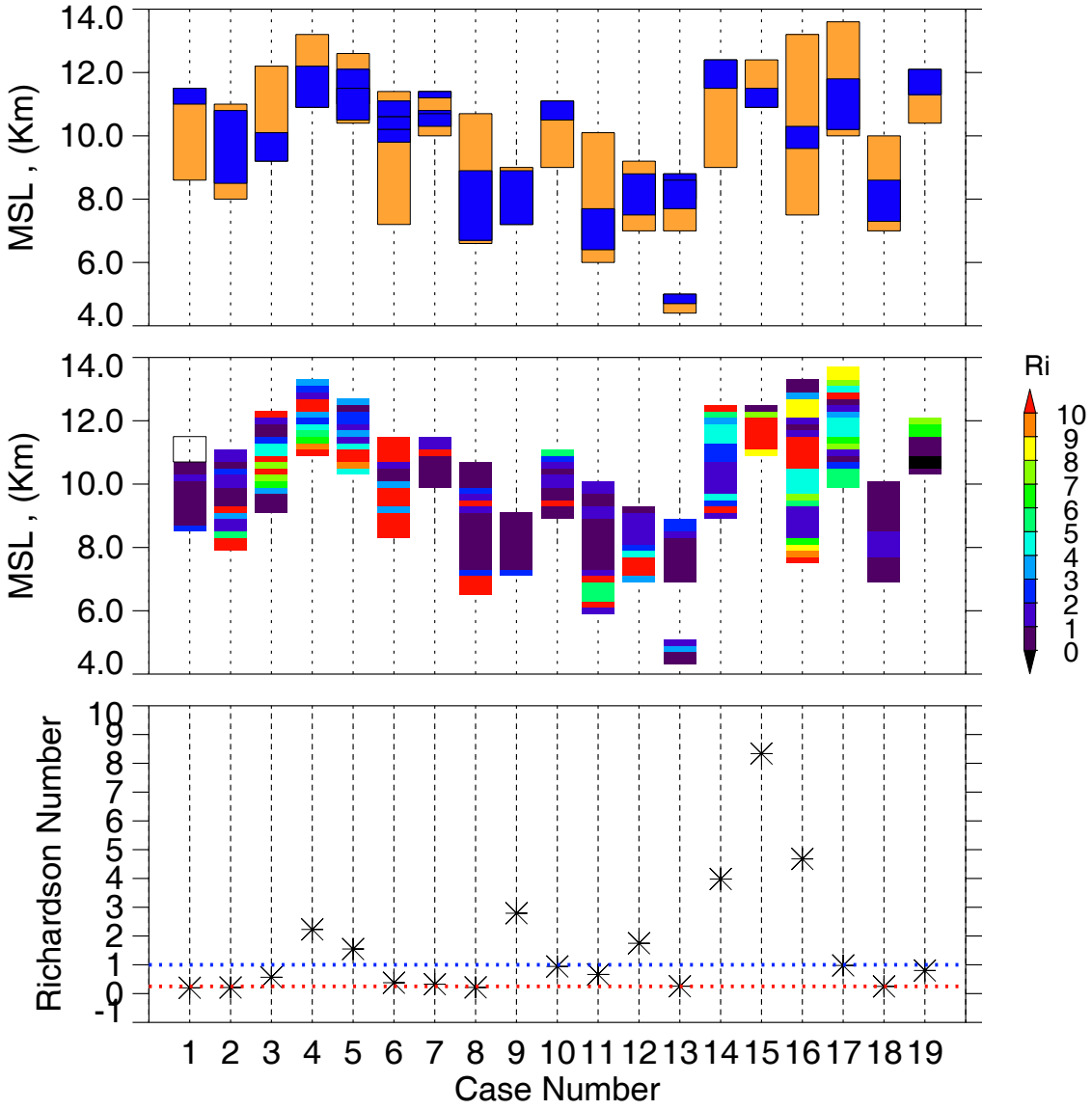

FIG. 4.8. a) The relative occurrence height of KH instabilities (blue bar) compared with mean height of cloud top and bottom (yellow bar); b) the mean bulk Richardson number of every 200 m in cloud layer; and c) minimum value of bulk Richardson number extracted from the region where KH instabilities occur. The red line presents 1/4 value and the blue one indicates 1.0.

1975a, b, c). When vertical wind shear exists in the surrounding environment, the KH instabilities will form and develop around the cloud top area.

One of mechanisms which produce KH instabilities is the intensification of shear on a titled discontinuity of density. It has been well explained theoretically by Scorer (1972; 1997) and demonstrated through lab experiment by Thorpe (1968, 1971). Cloud tops are often much colder than the air above because of the loss of heat by infrared radiation emission, thereby resulting in the apparent discontinuity of density. When the cloud top is tilted in mountain waves, enough shears are often generated to cause the layer to break into a row of vortices, and the cloud top has the appearance of KH instabilities. This mechanism also can explain why KH instabilities also often occur on the back of the 'tail' of down-draft crystal fallstreak.

Without losing any generality, one can use a simple illustration to show how the shear will be intensified when the inter-surface of the two inviscous layers with different density is tilted. The density and layer depth of two layer are defined as Fig. 4.9, where $\rho_1 < \rho_2$. They are initially horizontal and quiescent. When they are tilted with a small angle α, gravity will drive the heavy layer to the lower end. In order to keep conservation of mass, the light layer will flow up the slope. This creates an accelerating shear velocity profile with bi-direction flow. So the environmental shear will be intensified when the surface of discontinuity density is tilted.

The formation of the fallstreak begins with updraft which lifts parcels of air to the point where net condensation occurs. Then ice particles begin to form from supercooled water droplets (Heymsfield 1975b; Sassen and Dodd 1988; Roger and Yau 1989, chapter

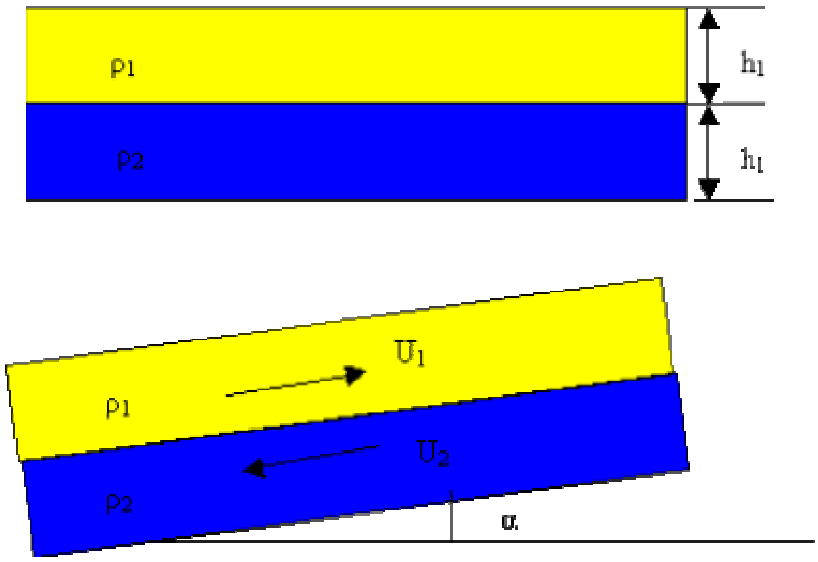

FIG. 4.9. A simple model illustrating how the shear will be intensified when the surface of discontinuity density is tilted.

9). As the crystals grow in size, they become too heavy to be supported by the updraft and they begin to fall. If one assumes the ice crystal is falling at constant from its source region, moving with the speed of wind at its level, and descending through a layer of constant shear of wind with height, then the trail produced has the shape of parabola: its local inclination to the vertical increases with distance below the source. In the real world, since falling ice crystals are distributed uniformly in size and shape, crystal fallstreaks have generally different shape though they often take the tiled arc shape (Harimaya 1968; Heymsfield 1975c; Ludlam 1989, section 9.6; Bohren and Fraser 1992). When light air is above heavy arc-like fallstreaks with ice crystals falling down, the tiled interface will intensify the shear locally. It may be the reason why KH instabilities frequently occur on the back of the trail of crystal fallstreaks.

Heymsfield (1975a, b, c) has speculated that, compared with the release of the latent heat by the evaporation of the crystal at the cloud bottom, the new cirrus uncinus head may be caused by waves forming in stable layer below the adiabatic layer causing condensation near the top of stable layer and resulting in convection in adiabatic layer. He also thought these types of waves may be a gravity wave, a critic wave, or KH wave. The results of the present study support his theory. In addition to the cloud base area, the trail region of fallstreaks is also located below the cirrus cloud head region. The lower KH instabilities will cause wave motion of the upper air. Provided with sufficient moisture in stable layer for condensation and ice nucleation to occur, the parcel ascending in the wave at the upper of the stable layer will be heated due to latent release, become positive buoyant and form generation cells. In his pioneering work, Heymsfield (1975b)

also thought that, either cooling in the trail by evaporation of crystals, which causes turbulence in the stable layer and in turn perturbs the unstable layer above, or convergence/divergence associated with downdarft of an existing cell cloud trigger the new cell of cirrus. If one speculates further, the breakdown of KH instabilities may be one of sources to produce the turbulence, which will intensify the perturbation for the former mechanism.

4.4.3 Environmental characteristics of KH instabilities

The radiosonde profiles from National Weather Services station, located 12 km west to the FARS (see in Fig. 2.1), reveal the environmental condition for the 19 cases. The sounding observation is operated two times every day at 0000 UTC or 1200 UTC. The time of the available sounding files closest to the lidar observation are shown in Table 4.2. One can find that most of the sounding data are falling in or close to the period of the lidar observation. For the case 1, since missing the data in cloud layer at 00Z on March 26 1992, it was replaced by the file at 1200 UTC on March 25 1992.

As the definition of the bulk Richardson number as the above discussion, the average Ri in every 200 m in the cloud layer was calculated. The occurrence height of KH instabilities relative to cloud top and base, the average Ri in every 200 m in cloud layer, and the minimum Ri value extracted from the areas where KH instability occurred are shown in Fig. 4.8. In Fig 4.8a the yellow bar represents the layer and the blue one means the region where the KH instabilities happened. The bars with different color in Fig. 4.8b indicate the different value of the bulk Ri ranging 0.0-10.0. Figure 4.8c shows the minimum bulk Ri extracted from the area where KH instabilities occur. The red dash

line is the value 0.25 while the blue one is 1.0. It should be noted that for the first case on March 25 92 the sounding data is missed from the height of 10.6 km so that the value from the adjacent area was chosen. The minimum bulk Ri of 5 cases (26.3%) are less than 0.25 and totally 12 cases (63.2%) are less than 1.0. There are still 7 (36.8%) cases of which the minimum Ri ranged from 1.0 to 10.0. Fig. 4.10 shows the magnitude of wind shear compared to $\Delta\theta/\Delta z$ for these minimum values of Ri number. The magnitude of the wind shear maxima varies considerably from one event to another, from as little as 0.5 m/s to nearly 6 m/s in every 200m. Most of the minimum Ri value are falling within the region less than 2.0.

According to the necessary condition which initializes the onset of KH instabilities, local Ri must be less than 0.25 somewhere in the flow (Miles 1961; Howard 1961; Miles and Howard 1964). However, some researchers pointed out that the bulk Richardson numbers calculated for entire layers are in generally larger than the critical value of 0.25 (Quante and Brown 1992; Starr et al. 1992; Quante and Starr 2002). This is because a value of bulk Ri greater than 0.25 does not ensure that local Ri less than 0.25 does not exit somewhere within the extended layer. According to the results of this study of 19 cases, generally, the value of the bulk Ri is less than 1.0 that can be treated as the critic value for the onset of the KH instabilities, though there are still some value more than 1.0.

Compared with the FARS observations, Browning's results (1971) showed that the magnitude of the wind shear maxima varied from 4-9 m/s in 200m and the minimum value of Ri over 200 m layers fell within the range 0.15-0.3, which were much closer to

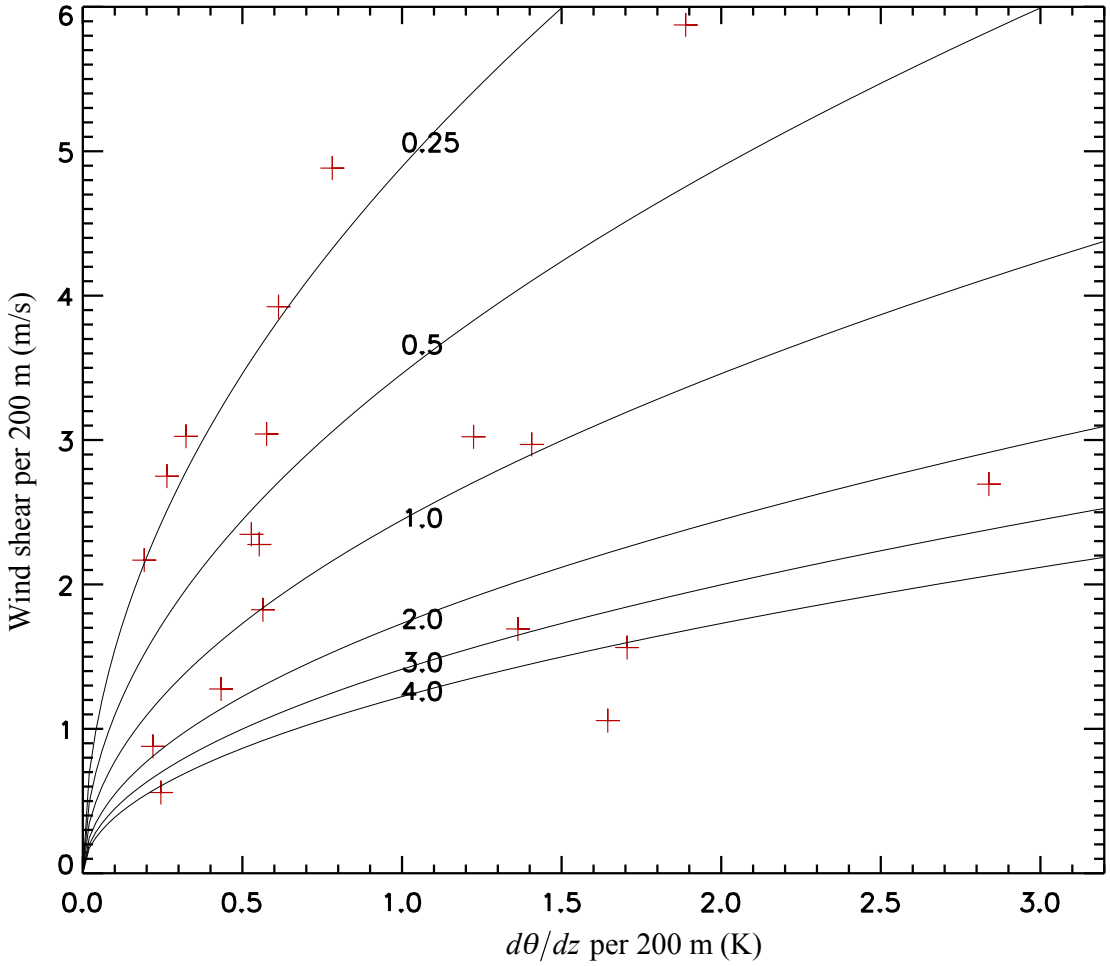

FIG. 4.10. The magnitude of wind shear and dθ/dz over 200 m deep layer of the minimum Ri number extracted from the region where KH instabilities occurred. Solid lines are isopleths of Ri over the corresponding layers.

the theoretical studies. This is because the sounding data used in the present study are not coinstantaneous with the lidar observation. In addition, they were obtained from the NWS station that is 12 km far way from FARS site. Using these data to characterize the localized intermittent KH instability event will unavoidably introduce some uncertainness.

4.4.4 Wave characteristics of KH instabilities

By visual inspection of a lidar backscatterings for all the 19 cases, it is found that they all occurred intermittently in patches, appeared sporadically in a short period, and vanished quickly. As shown in Table 4.2, the average duration of 19 KH instabilities is just 25 minutes compared to the typical observation period in FARS data is ~3 hour (180 minutes). Most of them (18/24) last around or less than 20 minutes. These results indicate that KH instabilities in cirrus are local phenomena, which were initialized locally by the wind shear. Therefore, one has to use the high-resolution remote sensors and the state-of-arts wavelet methods to detect and analyze them.

The wavelengths of all the KH instability packets are extracted using the wavelet methods introduced in the part of the case study, which are presented in Table 4.2. The wave height (maximum crest-to-trough amplitude) of KH instabilities changes from 0.1 km to 1.1 km and their wavelengths vary from 0.9 to 10 km. Because of the data resolutions (10 and 12 seconds) with typical 3 hours observation, one cannot disclose the KH instabilities with the smaller wave length. However, the results from all 19 cases reveal that the KH instabilities associated with cirrus clouds occurring in the upper troposphere generally have the wavelength between 1 and 10 km, of which 37% (10/27)

is less than 5 km and 63% (17/27) is falling between 5 to 10 km. The Fig. 4.11 shows the occurrence height and wavelength of 19 case KH instabilities as well as the previous observations from Table 4.1. Compared with the previous observations that showed the wavelengths of KH waves occurring at the altitude 7 to 10 km are mostly less than 5 km, the results disclose that their wavelengths also have the probability to range 5-10 km.

Further checking Fig.4.11, the wavelengths of KH instabilities mainly concentrate in three different regions including: 1) the boundary layer (from ground to 1 km) where the wavelengths are less than 2 km; 2) the lower troposphere (1-5 km) where the wavelengths have the average value around 2-4 km; and 3) the upper troposphere and lower stratosphere (7-13 km) at which the wavelengths vary extremely from 1 km to 11 km and the mean value is around 4-6 km. It shows that the trend of wavelength increases with the height. In other words, it implies that the closer to the ground the area is, the shorter the wavelengths. According to the study by Scorer (1969) and Browning and Watkins (1970), for a sheared layer of finite thickness, the spacing of the resulting KH billow corresponds to the maximum unstable wavelength given by

$$\lambda = (\pi/g)(\Delta u)^2 /(\Delta\theta/\theta) \tag{4.35}$$

It shows that the maximum unstable wavelength of KH instabilities will be modulated by the mean profile of potential temperature in the atmosphere. Overlapping the profiles of the average potential temperature in the winter and summer time (calculated from Salt Lake City's sounding data) in Fig.4.11 clearly discloses the reason why the wavelengths of KH instabilities increase with the height. In the boundary layer, due to the small value of the potential temperature, the KH instabilities only have the limitation value of the

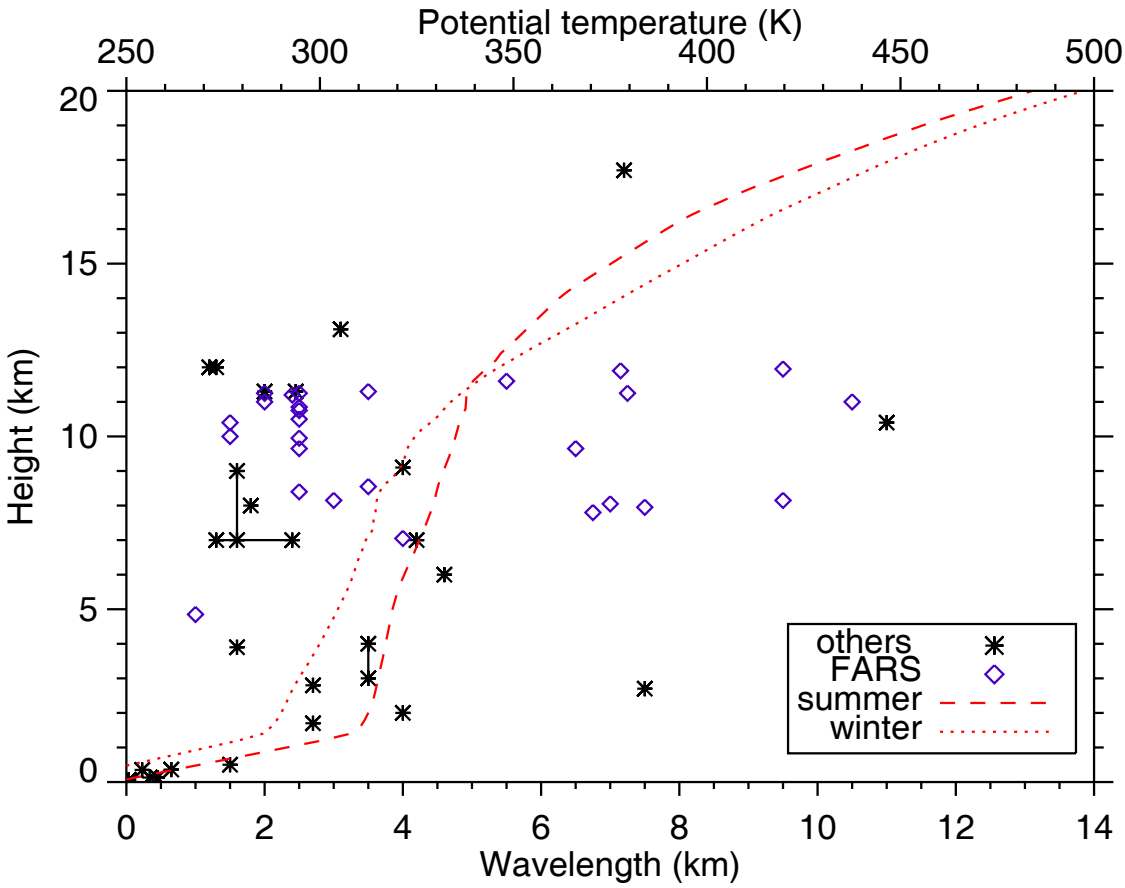

FIG. 4.11. The plot of the wavelength against the occurrence height for all 19 cases as well as the previous observations shown in Table 4.1. The profiles of average potential temperature in winter and summer (calculated from Salt Lake City's sounding data) are superimposed. It shows that the wavelength distribution of KH waves is characterized by the occurrence height.

wavelength. Beginning from the lower troposphere, the wavelengths increase with the increase of the potential temperature. At height from 7-12 km, with the variability of the tropopause, the wavelength jumps into much larger values because of the quick increase of potential temperature above the tropopause. The scattering distribution may be caused by the specific local environmental conditions.

The wave height, defined as the maximum crest-to-trough amplitude of the bellows, is another factor describing the wave. Given in Fig.4.12a is the ratio of the wave height to wavelength that can be used to measure the billow shape and reflects the wave growth rate at a specific wavelength. Their values vary from 0.04 to 0.45 and have the mean value 0.16 whereas Browning's (1971) observations give a value of 0.097-0.5. Using laboratory measurements, Thorpe (1973) found that the ratio of the maximum billow height to horizontal wavelength varied with the Richardson number, ranging from ~0.2 for Ri=0.15 to ~0.6 for Ri=0.05. This indicates that the local Richardson number can be less than 0.25 for all the 19 cases according to the wave shape, though the bulk Richardson number is sometimes larger than 0.25. In other words, measurements of the ratio of the wave height to wavelength can be another way to estimate the local Richardson number. The wave heights plotted against the wavelength, as well as the Browning's (1971) observations, are presented in Fig.4.12b, where the mean ratio value 0.16 is used for fitting. One can find that the wave heights against wavelengths tend to show a linear relation and their correlation coefficient reaches 0.6. Since the FARS observations are close to the tropopause, the wavelengths are larger than that from Browning's (1971) observation in the lower atmosphere (see the above discussion).

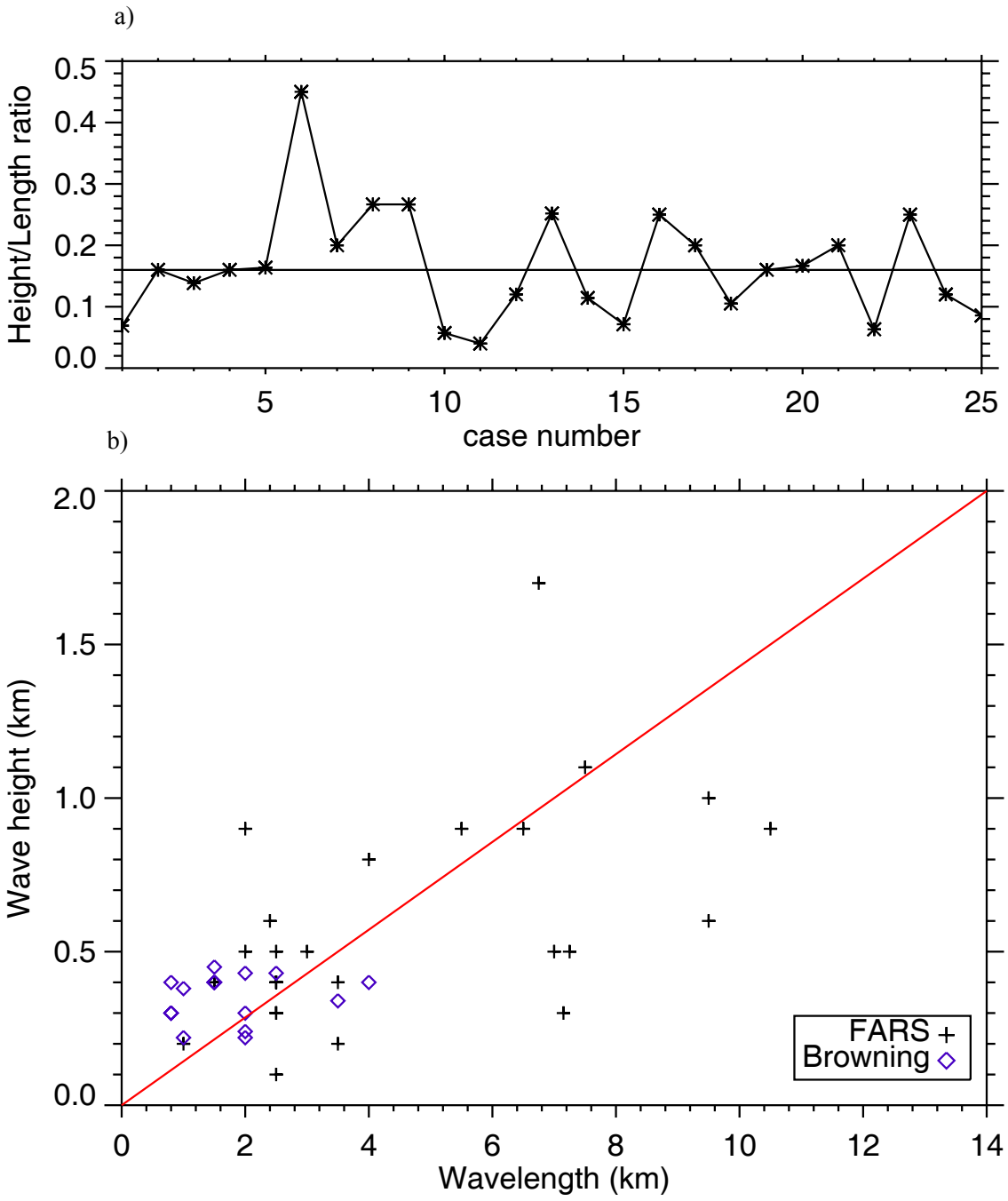

FIG. 4.12. a) The ratio of the wave height and wavelength and b) the plot of the wave height against the wave length from the FARS dataset and Browning (1971). In a), the black line indicates the value 0.16, which is used in b) as the slope value for the fit line.

4.5 Conclusion

In this chapter, all the events of KH instabilities from nearly 10 years of FARS high cloud lidar measurements were examined by using wavelet transform methods. Nineteen cases including 27 wave packets have been found. A case that occurred on 23 January 2000 was chosen to be given a detailed case study. The relative occurrence position, environmental conditions, and the wave characteristics of KH instabilities have been discussed. The following conclusions can be drawn:

1) The case study associated with jet stream cirrus showed the capability of wavelet transform methods to detect local intermittent phenomena like the KH instability. This method can successfully extract the wave information with different length scale occurring at different times while these dynamic processes coexist within a cloud system.

2) The results revealed that the KH instabilities in cirrus clouds occur basically in three regions: a) the leading edge of cirrus cloud top; b) the back of the trail of ice crystal fallstreaks; and c) the cirrus cloud bottom area. The possible reasons to account for them have been discussed. The breakdown and formation of KH instabilities may play an important role in the lifecycle of cirrus clouds.

3) Average bulk Richard numbers were calculated every 200 m in the cloud layers for all the 19 cases. Generally, the value of the bulk Ri less than 1.0 can be treated as the critical value for the onset of the KH instabilities when using the routine radiosonde data. The value of bulk Richardson number calculated for the entire layers are generally larger than the critical value of 0.25 from theoretical calculations, likely because of the drawbacks of using routine radiosonde data.

4) The wavelengths of the KH instability packets identified using wavelet methods are compared with previous observations. The results showed that the KH instabilities associated with cirrus clouds occurring in the upper troposphere generally have a wavelength between 1 and 10 km, of which 37% (10/27) is less than 5 km and 63% (17/27) is between 5 to 10 km. It is also found that some KH instabilities occur in groups, couple together, and form into a series of KH waves. This phenomenon has also been reported by Reed and Hardy (1972), Sassen (1995), and Sassen et al. (1990).

5) Combining other observations with this research, one finds that the wavelengths of KH instabilities mainly concentrate in three different regions including: 1) the boundary layer (from ground to ~1 km), where the wavelengths are less than 2 km; 2) the lower troposphere (1-5 km), where the wavelengths have the average value around 2-4 km; and 3) the upper troposphere and lower stratosphere (7-13 km), where the wavelengths vary extremely from 1 km to 11 km and the mean value is around 4-6 km. To some extent, this can be caused by the thermal structure of the vertical atmosphere distribution (e.g., air density and viscosity).

6) The ratio of the wave height to wavelength varies from 0.04 to 0.45 and has a mean value of 0.16, indicating the local Richardson number can be less than 0.25 for all 19 cases though the bulk Richardson number is sometimes larger than 0.25. It is suggested that the billow shape can be another way to estimate the local Richardson number.

CHAPTER 5

CIRRUS MAMMATA

5.1. Introduction

According to the definition of the Glossary of Meteorology published by the American Meteorological Society, mammatus (also named mamma or mammata in the plural) refers to "hanging protuberances, like pouches, on the undersurface of a cloud". "This supplementary cloud feature occurs mostly with cirrus, cirrocumulus, altocumulus, altostratus, stratocumulus, and cumulonimbus; in the case of cumulonimbus, mamma generally appear on the underside of the anvil (incus)" (Glickman 2000). Mammata are most often associated with cloud particles falling from an anvil cloud, but may also occur in snow or rain falling below cloud base or in streaks of falling ice crystals (Scorer 1972).

Both the early and recent literatures about mammata focus mainly on those associated with cumulus anvils (Hlad 1944; Clark 1962; Warner 1973; Scorer and Verkaik 1989; Stith 1995; Martner 1995; Sassen et al. 2001; Windstead et al. 2001). According to the early hypotheses of the processes leading to the development of mammata, three related processes are identified: subsidence of a cloud interface layer, fallout of cloud particles, and evaporation of fallout (Ludlam and Scorer 1953; Scorer 1958; Ludman 1980; Scorer and Verkaik 1989; Scorer 1997). During the local subsidence of a cloud layer, the cloudy air descends moist adiabatically and the dry clear air below cloud base descends dry adiabatically, producing a local instability at the cloud base. The chilling of the clear air below the cloud by evaporation of small falling

particles intensifies the temperature contrast and eventually a localized unstable lapse rate forms. Therefore, this initiates convective thermals of dry clear air that penetrate upward into the cloud base. When the cloud particles fall, dragging the immediate environment of particles with them, fallout front forms by the local rotations. These three processes render the stable subcloud layer slightly unstable and result in anvil mammata with smooth, usually less sharply outlined surfaces. In addition to the above processes, Clarke (1962), Martner (1995), Windsread et al. (2001) also suggested that gravity waves or Kelvin-Helmholtz instabilities in the environment or parent cloud may play an important role in initiation of anvil mammata. Emmanuel (1981) advanced a model based on cloud base detrainment instability that hypothesized that mammata form by entraining air through the cloud. However, studies to verify these hypotheses have been hard to come by. Some studies using modern radar observations or instrumented aircraft data even question the early theory. For example, Stith (1995) and Windstead et al. (2001) observed positive temperature perturbation between inside and outside of anvil mammata, which can not be explained by the early theory.

Although cirrus mammata are also prevalent in the atmosphere, there have been little observational facts, other than photographs, to concentrate on the mammata in cirrus. This is because cirrus clouds are located at high altitude and the normal instruments do not easily capture their fine structures. As a pioneer, Scorer (1953; 1973; 1997) first discussed the mammata generated in cirrus clouds. Unlike the most delicate and beautiful curved-shapes of anvil mammata, cirrus mammata generally have a sharp outline. He also envisioned that, in unsaturated air, the weight of the fallout added to the

cooling effect of the evaporation may produce mammata. Especially when there is slightly weak wind shear at that level, the parent cloud would grow a tail of several successive mammata in line behind it. Recently, some cirrus mammatus observations have been made by modern high-resolution active remote sensors. Whereas focusing on the influences of volcanic aerosol on cirrus clouds during the FIRE IOP II field experiment, Sassen et al. (1995) firstly showed mammatus-like protrusions in a strong attenuation region using the FARS PDL system. Sassen (2002) presented a high-resolution lidar power display of a particularly intense mammatus protruding from the base of a dense cirrus fibratus cloud at the DOE CART site during the SUCCESS field campaign. It was the first time that a cross-section of mammatus in cirrus cloud was shown using high-resolution lidar, which clearly disclosed the various scales of turbulent eddies that formed and developed around during mammatus downward penetrating into dry subcloud air. For the same observation, Quante et al. (2002) disclosed the apparent turbulent eddies around the mammatus' edges using the two-dimensional wavelet method. According to the local sounding data, he speculated that ice crystal sedimentation from the high layer or a secondary generating cell driven by strong evaporation may be the reason for the turbulence eddies. Recently, Jo et al. (2003) showed high-resolution observation of mammata in anvil cirrus with a temporal scale of 1-min and vertical scale of 0.5-0.7 km using a W-band Doppler radar during CRYSTAL-FACE. Strong downward mean Doppler velocities (4-5 m/s) were observed in the mammatus cores and compensating upward motions (1-2 m/s) were found in the mammatus peripheries.

However, quantitative research work regarding cirrus mammata has not been made until now, especially combining all kinds of modern instrumental observations together to disclose their thermodynamical and dynamical mechanism. Furthermore, many uncertainties of the knowledge about cirrus mammatus still remain. For example, are the properties and physical mechanism of cirrus and anvil mammata similar to each other? If not, what is the difference between them? Fortunately, the FARS 14-year high cloud dataset provides a unique opportunity to improve our understanding of cirrus mammatus properties. Using the FARS high cloud dataset, a quantitative evaluation of cirrus mammatus will be presented in this chapter. This chapter is composed of two parts: the first part will deal with a case study that is expected to extend our knowledge about cirrus mammatus by analyzing sounding, lidar, and Doppler radar data together. In the second part, mammatus cases found in the FARS high cloud dataset are surveyed to obtain the statistical properties of cirrus mammata.

5.2 Case Study

On 29 March 1999, a synoptic-scale arc of high- and middle-level clouds preceding a maritime Pacific storm system swept over Northern Utah. Beginning with thin cirrus, this cloud layer gradually thickened and eventually evolved into altostratus. As the deepening cloud layer penetrated into a dry layer and mixed with the aerosols from an Asian dust storm, successive cirrus mammata formed at the cloud base. The reason to choose this as case study is that it combined all the FARS remote sensors together, including the CPL, PDL, and W-band Doppler radar systems that provided an

unusual chance to look into cirrus mammata. The detailed description and specification of these instruments has been given in Chapter 2 (Table 2.1) and Chapter 3 (Table 3.1).

In addition to the data from FARS, the Salt Lake City National Weather Service station, located ~12 km to the west of the FARS site, provides upper air profiles for this case study. Although the upper air soundings are launched twice per day, fortunately, the sounding data used here is only 1-h later after the lidar and radar observation. Thus, it can well characterize the thermodynamic features. Finally, the NCEP reanalysis data and GOES-10 satellite images are used to describe synoptic environment in this case. The description and specification about the NCEP reanalysis data can be found in Kalnay et al. (1996) and Kistler et al. (2001).

5.2.1 Synoptic weather settings and environmental characteristics

As revealed by the NCEP reanalysis data and GOES-10 satellite images, this case was associated with a cold front advecting over the west coast of North America. This classic cirrus-generating mechanism at FARS associated with a subtropical jet stream has been discussed by Sassen and Campbell (2001) and Sassen (2002). According to the NCEP reanalysis at 1200 UTC on 29 March 1999 (Fig. 5.1a and b), a low pressure on the 850 mb centering at 50^{o} N and 130^{o} W was located at the east Pacific and west coast of British Columbia combined with a wet region. The anticyclonic circulation stretched from the northeast Pacific into southern California and western Nevada while a dry tongue penetrated into the inner continent from the ocean. Another high pressure system was placed over Colorado and eastern Utah. At the 300 mb, a trough extended from 51^{o}N to 33^{o}N and moved eastward while a ridge was located trough Montana, Idaho, and

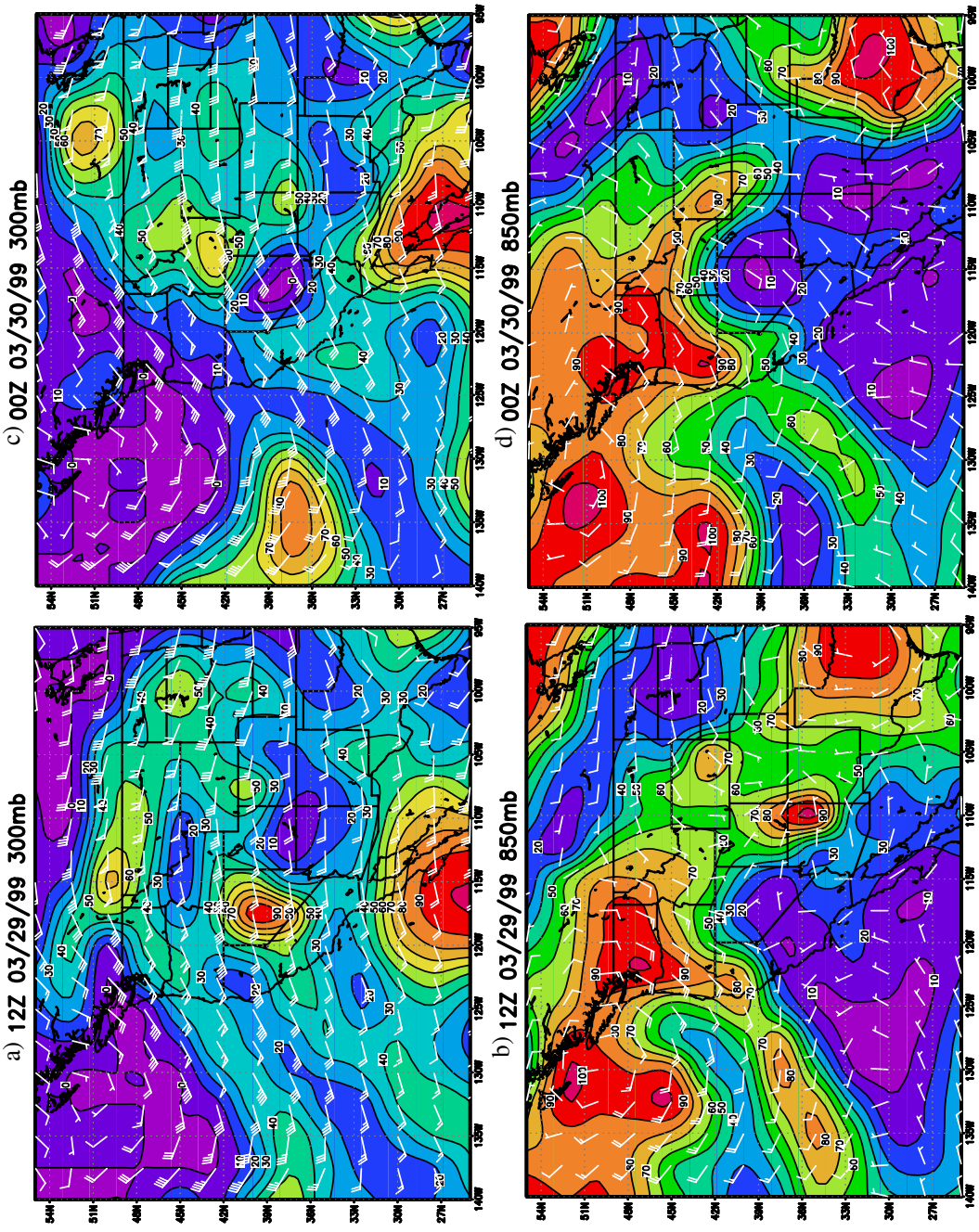

FIG. 5.1. Horizontal wind and relative humidity field on the 300 mb and 850 mb level of NCEP reanalysis data, respectively, at 1200 UTC on Mar 29 1999 (a and b) and 0000 UTC on Mar 30 1999 (c and d).

Wyoming from north to south. By 0000 UTC on 30 March 1999 (Fig. 5.1c and d), the frontal system moved eastward into the Great Basin. On the 850mb, the dry tongue as well as the anticyclone region extended into southern California, Nevada, western Utah, and Arizona. With the movement of the trough line, on the 300 mb moist air was transported from the eastern Pacific into inner continent by subtropical jet stream. The ridge just passed through northern Utah and took a position along the longitude line of 107^{o} W. Thus, the synoptic front disturbance plus the subtropical jet stream associated with maritime moist air were the main source of cirrus generation.

Checking the series of hourly satellite images from 29 to 30 March 1999, it can been seen that comma-shaped cloud bands formed over the ocean and evolved into a large axe-shape cloud band that swept over the northwest part of Northern America. Fig. 5.2 presents GOES-10 infrared channel imageries at 2100 UTC with 4-km resolution and a visible channel image at 2230 UTC with 1-km resolution. Since cirrus mammata formed beginning at 2240 UTC, these images show the cloud band just before cirrus mammatus occurrence. As indicated by the satellite imagery of Fig. 5.2a, a subtropical jet stream flew through north California, which generated a series of storms through southern Idaho and Neveda. Preceding these storm systems and along the upstream edge of the frontal cloud bands, a band of cirrus was generated. From the expanded visible channel satellite image of Fig. 5.2b, at 2230 UTC a semi-transparent cirrus cloud band was passing overhead FARS site.

According to the NCEP 850mb reanalysis at 0000 UTC on 30 March 1999, the Great Salt Lake area was locally controlled by a relatively drier area and the relative

(a)

(b)

FIG. 5.2. a) GOES-10 infrared channel image at 2100 UTC with 4-km resolution and b) visible channel image at 2230 UTC with 1-km resolution.

humidity reached to 30%-35%. However, at the 850mb, this area was located on the edge of the wet region and its maximum relative humidity exceeded 50%. Upper wet air mass \s placed on lower dry layer resulting in a relative stable condition, which is thought to be one of the environmental characteristics for the formation of mammata (Ludlam and Scorer 1953; Scorer 1958; Ludman 1980). Shown in Fig. 5.3, the height-time cross section at FARS site further confirms these features. It clearly shows that a dry layer around 400-700mb extended from 0006 UTC of March 29 to 0600 UTC of March 30 while moist air mass existed above. The cirrus clouds occurred above 370mb just above this dry layer. The upper air sounding data at 0000 UTC on 30 March 1999 (see Fig. 5.5a and b) are also helpful to understand the environmental characteristics of cirrus mammata. The interface of the dry layer and wet layer was located around 8.0 km (370 mb), just around the places where the cirrus mammata were produced. The wind velocity did not change much and kept a value of about 32.0 m/s, which indicated that there was no strong wind shear in the cloud base. Importantly, between 7.1 and 8.1 km, there is a small isothermal layer in the profile of the temperature. This observation also has been reported by the airborne measurements of anvil mammata by Windstead et al. (2001).

Early hypotheses have pointed out that the dry layer below the cloud base plays an important role for the formation of mammata (Scorer 1958, Ludman 1980). If the cloud base is brought down the air into relatively dry surroundings, the air above will be warmed at the wet adiabatic lapse rate while the air below at dry adiabatic lapse rate. It will result in local instability so that thermals penetrate into the cloud base and the cloud surface becomes wrinkled. Emanuel (1981) also remarked that the initial step resulting in

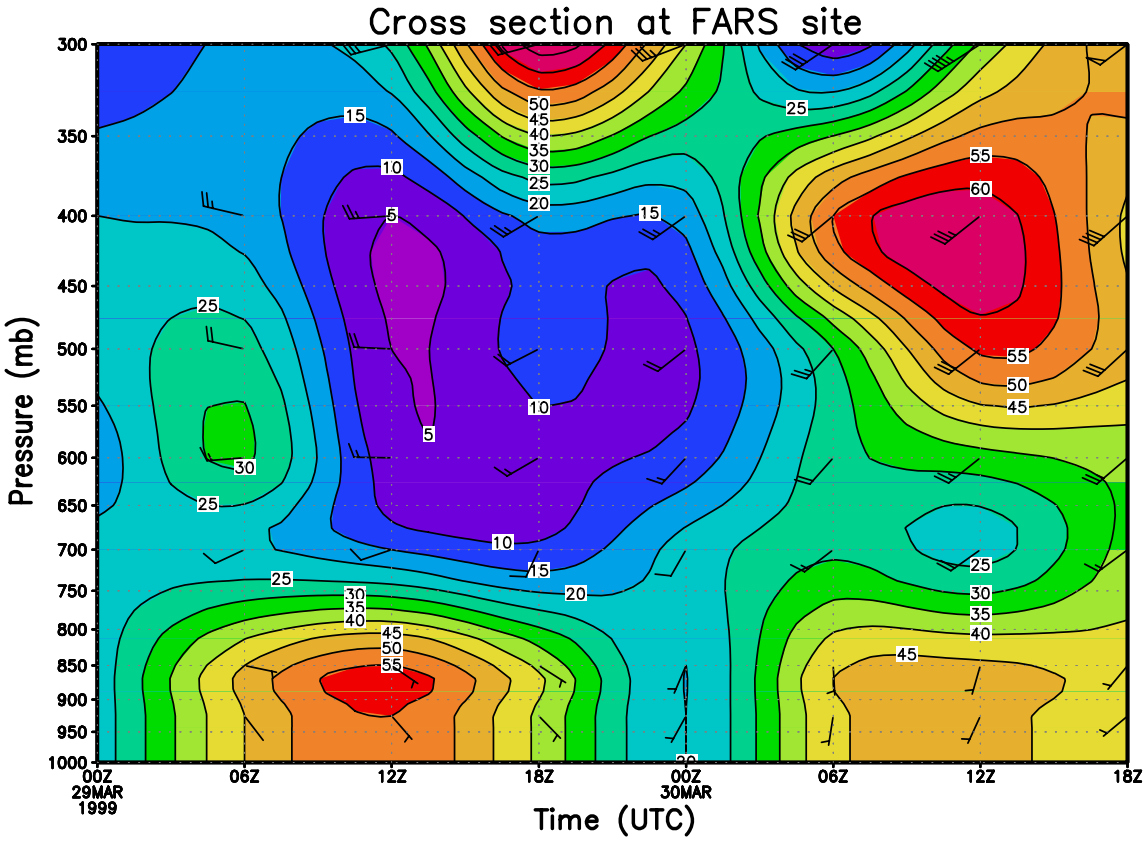

FIG. 5.3. Height-time cross sections of horizontal wind and relative humidity field at FARS site. It clearly shows that a dry layer located between 700mb and 400mb extended from 0600 UTC of March 29 to 0600 UTC of March 30 while moist air mass was in the presence above. The cirrus clouds occurring above 370mb just were located above the dry layer.

Cloud-Base Detrainment Instability (CBDI) is that cloudy air is mixed downward with unsaturated air with a larger value of distance. Some recent observations of mammata by active remote sensors also confirmed the existence of a relative dry layer below the cloud base (Martner 1995; Windstead et al. 2001).

5.2.2 Observation and analysis results

The CPL height versus time plots of relatively returned energy and linear depolarization ratio are given in Fig. 5.4, which shows the evolution of the cirrus cloud and the formation of cirrus mammata. The CPL observations began at 1803 UTC as the initial band of thin cirrus exited in the region, and just in advance of gradually deepening cirrostratus. After the initial cirrus at ~9 km departed, the next cirrus layer with cloud tops to near the 12-km tropopause gradually thickened and eventually produced optical attenuation strong enough to cause range-limiting effects at ~2230 UTC and again ~2300 UTC. By that time, the cirrus transited into altostratus because the cloud layer had thickened sufficiently. The cirrostratus-altostratus transition often occurs at the FASR site and has been discussed in detail by Sassen (2002). Beginning at 2230 UTC, the cloud base subsided down and penetrated into a relatively dry subcloud layer (see Fig. 5.4), which contained relatively weakly scattering aerosol. During 2230-2305 UTC, a series of cirrus mammatus structures were generated at the cloud base and also embedded into aerosol layer. It should be noted that the source of these aerosols can be traced to an Asian dust storm. Reliable CPL δ values showed the linear depolarization of ~0.04-0.06 (Fig. 5.4b), which are indicative of nonspherical dust particles (Mishechenko and Sassen 1998). Therefore, cirrus mammata were generated during the subsidence of the cloud

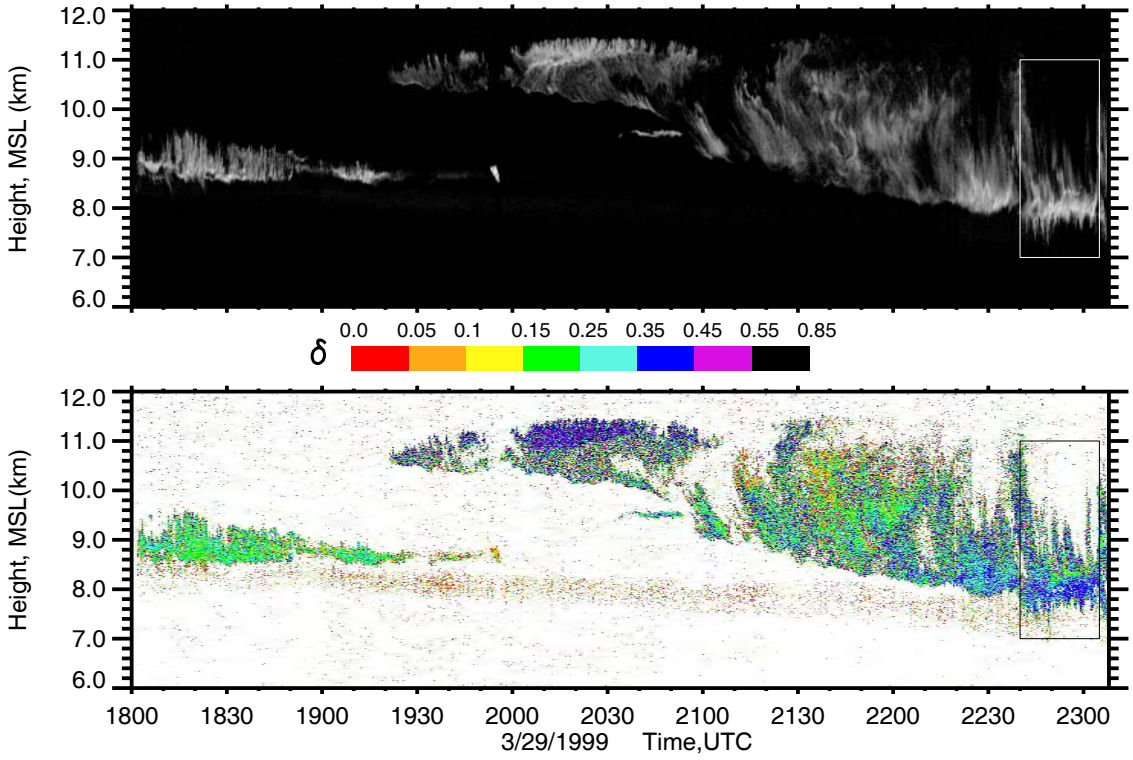

FIG. 5.4. The CPL height versus time plots of relative returned energy (top, based on logarithmic grayscale) and linear depolarization ratio (bottom, indicated by the color table). The box area shows the place where the cirrus mammata was generated and will be expanded to view in Fig. 5.5. The plots clearly show that cirrus mammatus was generated due to the subsidence of cloud base that penetrated into relative dry subcloud layer, which contained relatively weakly scattering aerosol composed by the nonspherical dust particles.

base that penetrated into a relatively dry subcloud layer, which is the initial condition for mammatus generation mechanism (Scorer 1958). Due to the local subsidence of cloud base the cloudy air descends moist adiabatically and the dry clear air below cloud dry adiabatically, producing a local instability at the cloud base. This local instable environmental condition will be helpful for the development of the small convective distribution.

The observations by the high-resolution PDL system and W-band Doppler radar are used to disclose the fine structures and dynamic characteristics of cirrus mammata. The specification and resolution of these remote sensors have been discussed in the Chapter two. As the expanded view of 7-11 km box area from 2240 to 2305 UTC indicated in Fig. 5.4, Fig. 5.5a and b, respectively, are the lidar backscattered power based on the logarithmic grayscale and linear depolarization ratio indicated by the color table. The upper air sounding profiles at 0000 UTC on 30 Mar 1999 are also shown on the left, including the profiles of the temperature, dew point, potential temperature, and horizontal wind velocity and direction. The W-band equivalent reflectivity and mean Doppler velocity are shown in Fig. 5.5c and d. It is clear that quite different images of the cloud are generated in the optical (0.532 μm) and microwave (3.2 mm) region because lidar and radar have quite different capabilities in the remote sensing of clouds (Wang and Sassen 2001). Due to its excellent temporal and spatial resolution, the PDL observation captured the fine structures of the cirrus mammatus. The lidar backscattering return power (Fig. 5.5a) clearly shows that several mammatus clouds with different vertical and horizontal scale falling down from cloud base areas. They extended 0.2-0.6

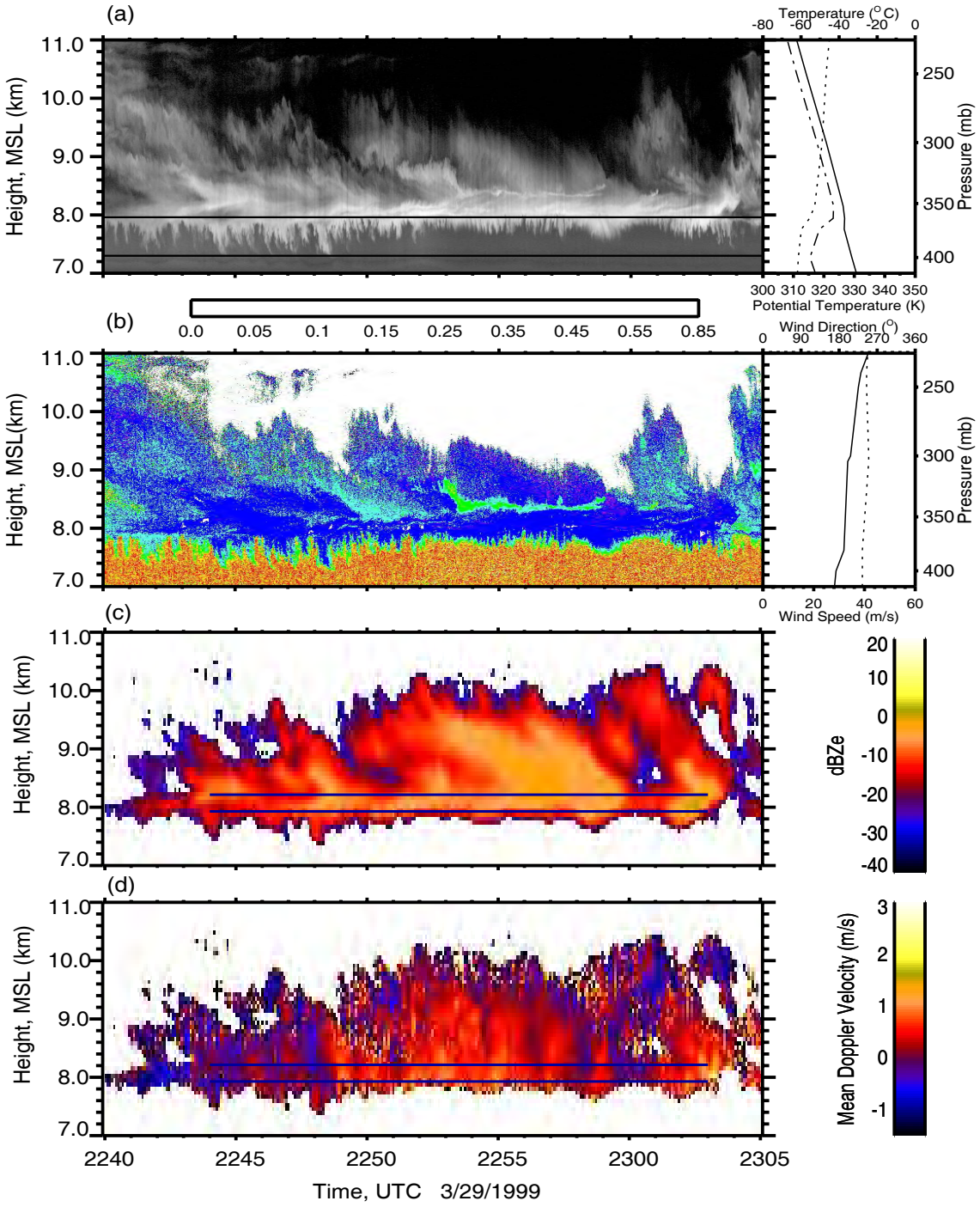

FIG. 5.5. Expanded view of cirrus mammata including: a) PDL backscattered energy (based on logarithmic grayscale); b) linear depolarization ratio; c) W-band radar reflectivity; and d) mean Doppler velocity (negative values represent updraft motions). The profiles of temperature, dew point, potential temperature, and wind velocity and direction at 0000 UTC on Mar 30 1999 are also shown. Note that the data indicated by the line will be used in the following analysis.

km vertically below the cirrus base and had a noticeably sharply outlined shape that penetrated into the aerosol layer. Different from anvil mammatus, they do not have smooth cauliflower like protuberances. Because they have a relatively low ice crystal concentrations with a small downdraft velocity that is too weak to produce the fallout front like anvil mammatus.

Wavelet methods are used to characterize the mammatus horizontal length scale. First, the "threshold" value is set to make the difference of backscattering returned power from cloud and background atmosphere (Platt et al. 1994). Then the backscattered power from the cloud will be integrated together from 7.30 to 7.96 km as indicated in Fig. 5.5a. Finally, this integrated series of cloud backscattered energy is the input of the wavelet-transform algorithms. It should be noted that using "threshold" methods to detect clouds will introduce errors, which have been discussed by authors (e.g., Wang and Sassen 2001). However, since the purpose is to derive the length scale of cirrus mammatus, but not the cloud boundaries, these errors will not effect on the results too much. The time series of integrated backscattered energy, wavelet spectral power and global power, and FFT spectral power are given in Fig. 5.6. In order to highlight the mammatus structures, statistical significance testing is performed for local wavelet spectrums by choosing white noise as background spectrum (Torrence and Compo 1998). The 95% confidence level contour is superimposed on the wavelet spectral power. From Fig. 5.6, the strong power regions with the length scale 4.0-5.0 km exist from 2240-2252 UTC and shift into 6.0-7.0 km beginning from 2253 UTC, indicating the main cirrus mammatus structures. Importantly, there still exists strong power with length scales 1.0-2.0 km, which indicates

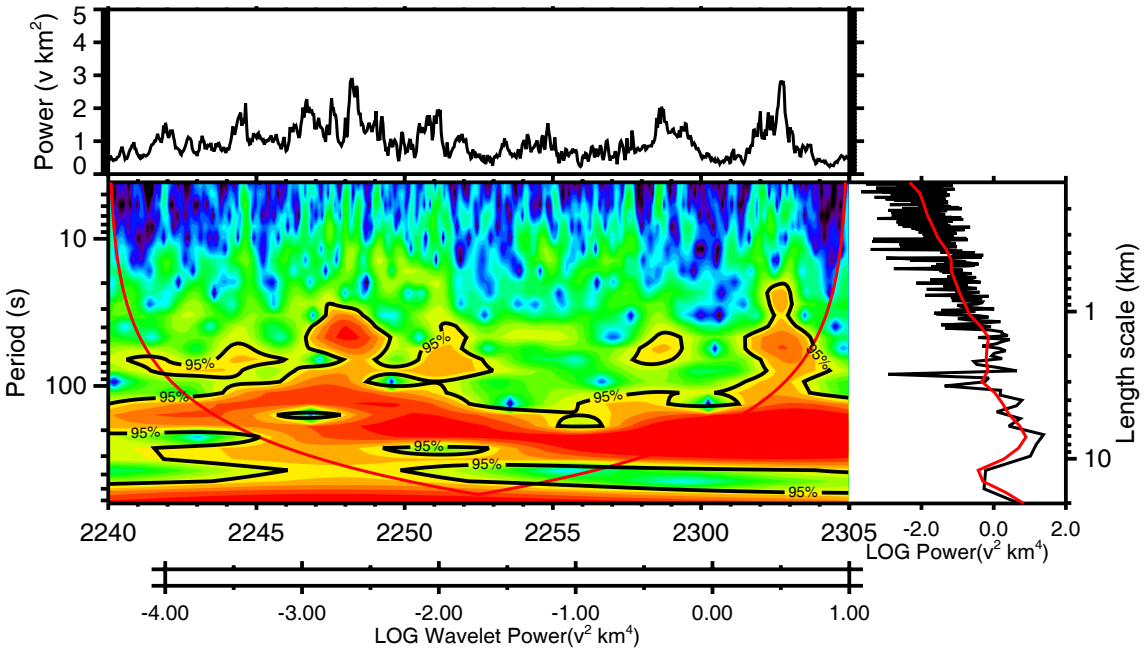

FIG. 5.6. The time series of integrated backscattered energy (top), wavelet spectral power (bottom, right), and global power and FFT spectral power (bottom, right). The 95% confidence level contour is overlapped above the wavelet spectral power.

that, within or around every main cirrus structure, much smaller cirrus mammatus structures have developed. This phenomenon also could be found by directly checking the expanded high-resolution PDL power image from 2245 to 2250 UTC shown in Fig. 5.7, though the radar reflectivity image is only capable of showing the mammatus structures with large scales. Indicated by Fig. 5.7, a series of small scale structures developed around or between the large scale fallout mammata. This implies that, the energies were cascading from large scale structures into small scale ones and various scales of turbulent eddies quickly developed. Other cirrus mammata observations by high resolution remote sensors also disclose the similar phenomenon that the various scales of turbulent eddies exist around the downward penetrating mammatus structures (Sassen 2002; Quante et al. 2002).

Checking the linear depolarization ratio (Fig. 5.5b), the δ value was 0.25-0.35 at the mammatus base and sides but 0.35-0.45 inside the mammata, which indicates that the evaporation process existed around these structures (Sassen 2000). Evaporation is the primary process involved in concept models for mammatus formation and also has been supported by many observations (Scorer 1958; Ludlam 1980; Emanuel 1981; Martiner 1995). By evaporation of the fallout ice crystal into air at same temperature, the air in the cloud is cooled to its wet-bulb temperature, which will intensify the local instability that supports to produce the convective motions propelling parcel of dry air upward into the cloud base. It should be noted that the evaporative cooling depends on the ratio of the total mass of water to the mass of dry layer (Bohren and Albrecht 1998). In other words, the smaller the relative humidity is, the greater the difference of dry- and wet-bulb

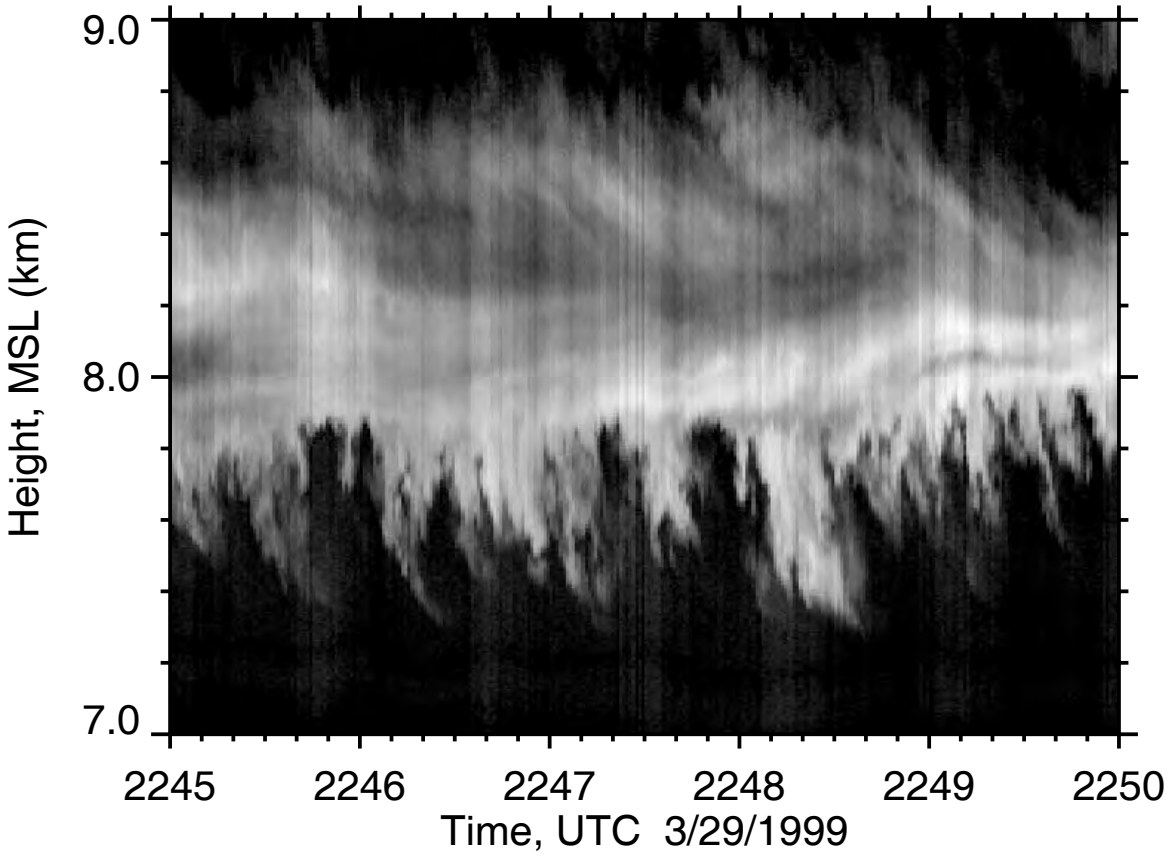

FIG. 5.7. Expanded view of the time-height display of PDL backscattered energy from 2245-2250 UTC. It clearly shows that small scale structures developed around or between the downward penetrating large scale mammatus structures.

becomes. Thus, to some extent, the existence of dry layer also intensifies the evaporative cooling resulting in deepening the local instability.

Because of its relatively low resolution (the vertical resolution 75.0 m and the temporary resolution 5 seconds), one cannot find the same fine structures of cirrus mammatus in the radar image as in the PDL observation. However, the W-band means Doppler velocity plus the equivalent radar reflectivity factors (Fig. 5.5 c and d) provide additional information to disclose the dynamic features of mammatus. Shown in the height-time display of mean Doppler velocity (Fig. 5.5d, positive values represent the downdraft motions), the altostratus clouds are dominated by strong downward motions in excess of 1.0 m/s, indicating the fallspeeds of ice-particle aggregates in the optically dense cloud. It should be highlighted that there is a series of updrafts (as high as 0.5 m/s) embedded in the cloud base. As discussed above, these updrafts are generated by the clear air convective motion due to the local instability caused by the subsidence of cloud layer and the evaporation of fallout particles. In order to characterize these small-scale motions, the time cross section of reflectivity (red line) against mean Doppler velocity (black line) at 7.9 and 8.2 km, respectively, are given in Fig. 5.8a and b. Both of them reveal that alternate up- and downdrafts exist in the cloud-base area. In addition, they tend to show a positive correlation between cloud reflectivity and downward Doppler velocities (correlation coefficients are 0.53 and 0.42 at 7.9 and 8.2 km, respectively), especially at 7.9 km. This feature was also well illustrated by previous mammatus observations (e.g. Martner 1995; Jo et al. 2003). It is not surprising that the weak reflectivity accompanies the updraft motion because the upward convection air around

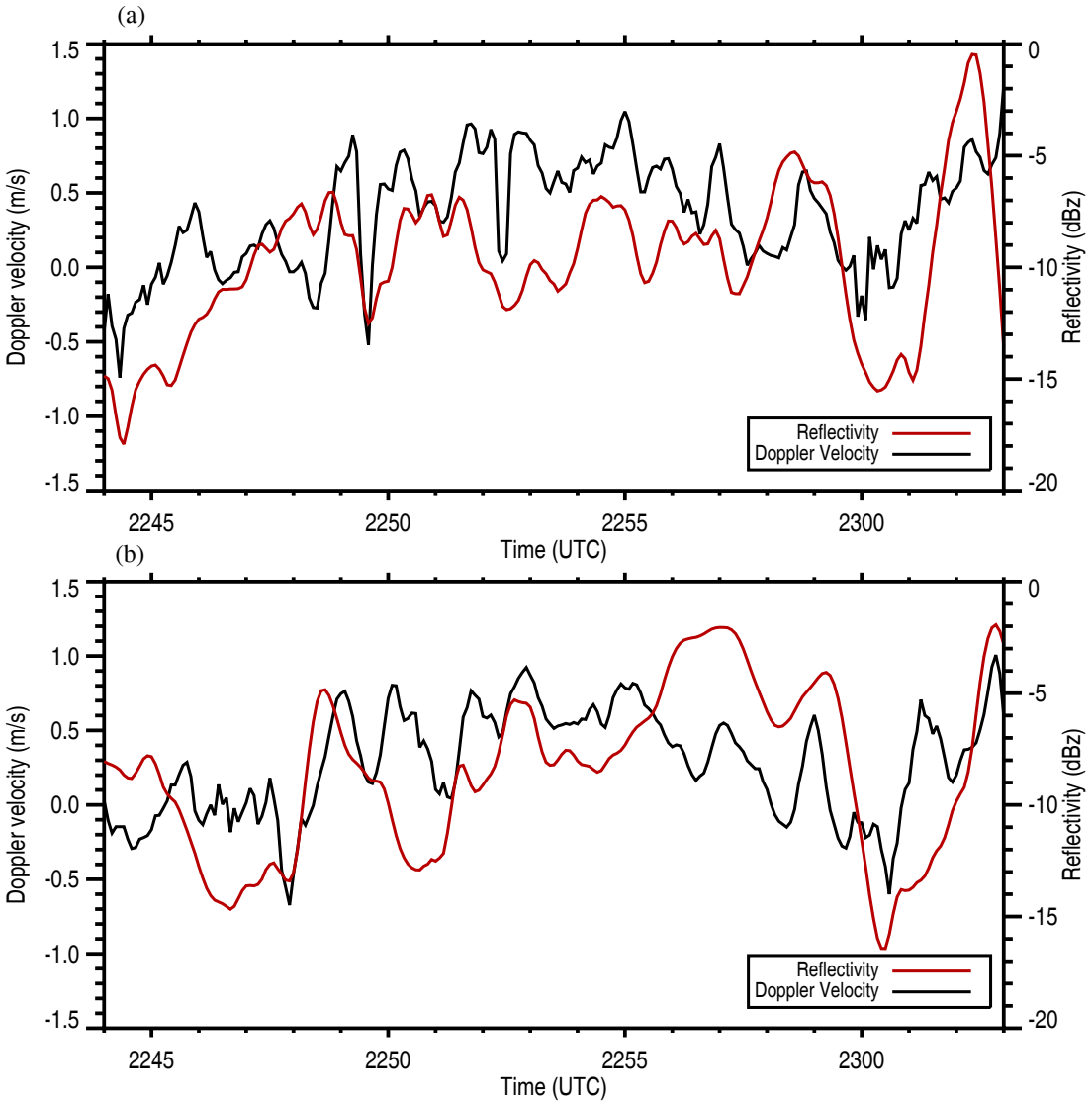

FIG. 5.8. Time cross section of reflectivity (red line) against mean Doppler velocity (black line) at a) 7.9 and b) 8.2 km, respectively. It tends to show a positive correlation between cloud reflectivity and downward Doppler velocities (correlation coefficients are 0.53 and 0.42 at 7.9 and 8.2 km, respectively), especially at 7.9 km.

fallout will penetrate into the cloud base and mix with cloud air. However, since the adjust of ice water content response to the vertical motion is much slower than the change of vertical motions, the relationship of the reflectivity and the Doppler velocity is not always apparent. Compared with Fig. 5.8b, Fig. 5.8a shows more variability of the mean Doppler velocity on 7.9 km, which suggests that small-scale updrafts and downdrafts are apparently more vigorous around the mammatus lobes than in the areas near cloud base. Given in Fig. 5.9, the energy spectrum density functions of the Doppler velocity at two altitudes further confirm it, which were obtained by performing three-point running means to the power spectra. Wind speed around the cloud base of 32 m/s is used to transform period into length scale. Although the spectrum densities of the mean Doppler velocity both display similar features for the mesoscale motion with the length scale above 10.0 km, the spectrum at 7.9 km contains much more energy at the small-scale (0.4-7.0 km) than at 8.2 km.

Importantly, the spectral slope of the mean Doppler velocity at 7.9 km is close to $-5/3$ at the range 0.4-4.0 km, which is consistent with the presence of the developed three-dimensional locally isotropic, homogeneous turbulence around the mammatus generation areas (Kolmogorov 1941). Gage (1979) and Lilly (1983) have also argued that a $-5/3$ slope law can be associated with the upscale energy transfer in stratified turbulence resulting in quasi-two-dimensional mesoscale eddies. However, because the $-5/3$ spectral occur in a locally unstable thermal stratification with relatively weak wind shear and is located in the subrange of the small length scales (0.4-4.0 km), one can identify three-dimensional turbulence generated by the positive buoyancy (Gultepe and

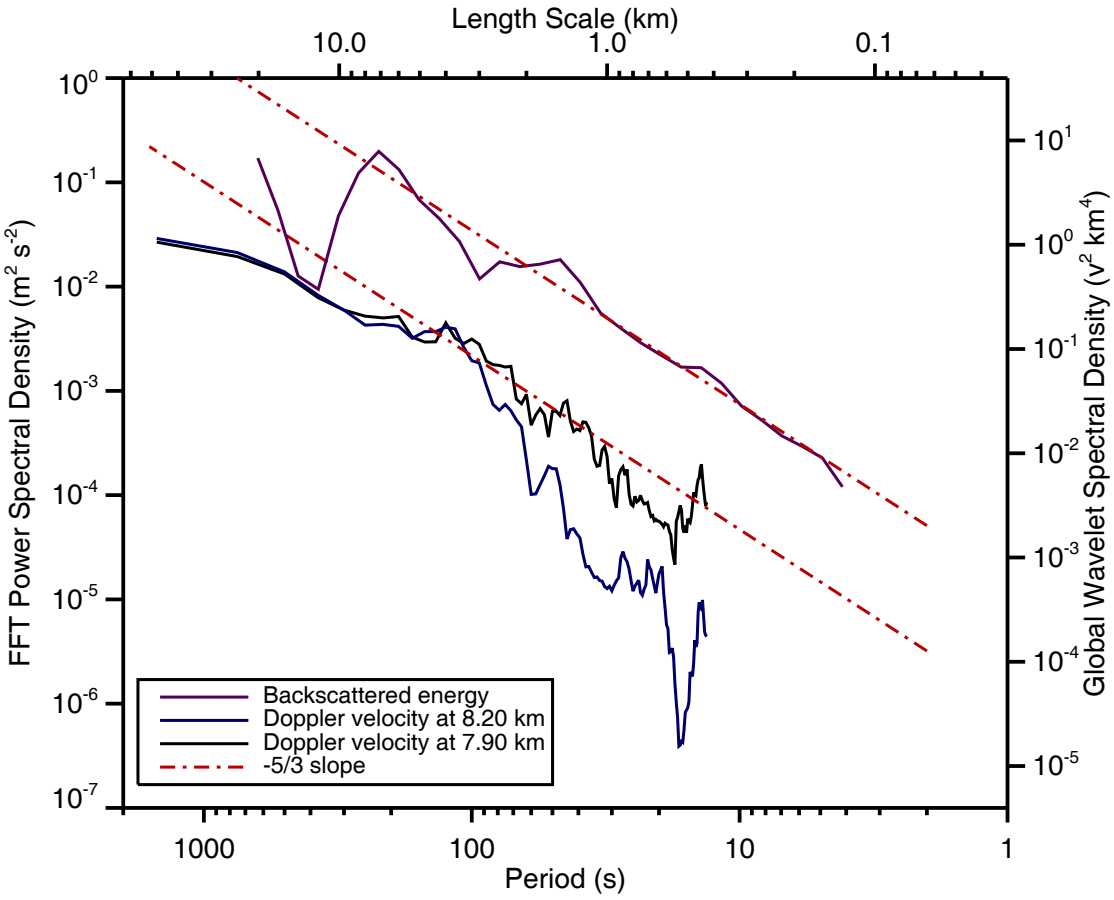

FIG. 5.9. FFT power spectral density of the mean Doppler velocity on 7.9 and 8.2 km shown in Fig. 5.8 and the mean global wavelet spectrum of the integrated backscattered energy from 7.30 to 7.96 km. The -5/3 slope line is also shown. The wind speed around the cloud base of 32.0 m/s is used to transform period into length scale. Although the spectral densities of the mean Doppler velocity both display similar features for the mesoscale motion with the length scale above 10.0 km, the spectrum at 7.9 km contains much more energy at the small scale (0.4~7.0 km) than 8.2 km. The spectral slopes of the Doppler velocity at 7.9 km and the integrated backscattered power from 7.30 to 7.96 km, respectively, are close to -5/3 at the range 0.4-4.0 km and 0.1-7.0 km, indicating the existence of the developed cascaded three-dimensional turbulence around the cirrus mammatus area.

Starr 1995; Quante and Starr 2002). The spectral slope at 8.2 km is slightly deeper than $-5/3$, indicating that the turbulence cascade was not yet fully developed.

One of the more important variables used to study turbulence and its evolution is the turbulent kinetic energy (TKE), which could be expressed symbolically as follows (Holton 1992, p.122):

$$\frac{\overline{D}(TKE)}{Dt} = MP + BPL + TR - \varepsilon \tag{5.1}$$

where $\frac{\overline{D}}{Dt} = \frac{\partial}{\partial t} + \bar{u}\frac{\partial}{\partial x} + \bar{v}\frac{\partial}{\partial y} + \bar{w}\frac{\partial}{\partial z}$ is the rate of change following the mean motion, $TKE = (\overline{u'^2} + \overline{v'^2} + \overline{w'^2})/2$ is the turbulent kinetic energy per unit mass, *MP* is the mechanical production, *PBL* is the buoyant production or loss, *TR* designates redistribution by transport and pressure forces, and ε designates frictional dissipation reflecting the dissipation of the smallest scale turbulence by molecular viscosity. Note that u', v', and w' denote the fluctuating parts of the velocity components and $\bar{u}$, $\bar{v}$, and $\bar{w}$ are the mean wind components. The buoyancy term in equation (5.1) represents a conversion of energy between the mean flow potential energy and TKE in the following form:

$$BPL = g\frac{\overline{w'\theta'}}{\bar{\theta}} \tag{5.2}$$

where θ' and $\bar{\theta}$ are the fluctuating part and the mean value of the potential temperature, respectively. With the cirrus crystals falling down from a wet environment into relative dry surroundings, it will result in local instability to produce the positive buoyancy for

the thermal air parcels. Additionally, the evaporation of ice crystals will cool the surrounding air and result in the difference of dry- and wet-bulb temperatures, which intensifies the local instability. Thus, the positive buoyancy will produce the turbulent eddies by converting mean flow potential energy into TKE. In other words, cirrus may play a role like a heat engine by crystals falling down into the dry layer and evaporation process to convert environmental mean flow potential energy into TKE and form the cirrus mammatus.

According to Kolmogorov's (1941) theory, TKE produced by the buoyancy is injected into the system to produce the large eddies. Then large eddies can feed energy to smaller eddies and these in turn feed still smaller eddies, resulting in a cascade of energy from the largest eddies to the smallest ones. Generally, a $-5/3$ slope and quasi-isotropic flow often mark the classical inertial subrange of Kolmogorov's turbulence theory, which provides the following relation:

$$E(k) = \alpha_k \varepsilon^{2/3} k^{-5/3} \qquad k > k_B, \tag{5.3}$$

where E(k) is the TKE spectral density, k_B is the buoyance wavenumber, α_k denotes Kolmogorov's universal constant and ε is the energy dissipation rate. The wavelet-analysis results (Fig. 5.6) and expanded view of the PDL backscattered energy display (Fig. 5.7) also show that small-scale structures developed between or around large-scale mammatus structures, which are consistent with the spectral features of the mean Doppler velocity.

Furthermore, due to the ability of the high-resolution PDL system to capture the cloud fine structures, to some extent, the lidar returned power may be a nice tracer for

turbulent motions (e.g., Quante et al. 2002, using radar reflectivity). Therefore, the mean wavelet global wavelet power of the integrated PDL returned energies from 7.30 to 7.96 km (Fig. 5.5c) is superimposed on the spectral density of the mean Doppler velocity. As shown in Fig. 5.9, the spectral slope of the mean global wavelet spectrum also obeys the $-5/3$ power law from the scale 0.1-7.0 km, which is the inertial subrange of Kolmogorov's turbulence. The range above 7.0 km could be thought of as the buoyancy subrange, where the positive buyancy injects the energy to maintain development of the turbulence. It is also shown that three peaks exist in the mean global wavelet spectral density. The first one ranging from 4.0-7.0 km represents the main mammatus cirrus structures. The peak located around 1.0-2.0 km indicates the small scale structures developing between or around the main mammatus cloud. The peak with the length scale 0.4 km might suggest the existence of much smaller structures.

5.2.3 Discussion of case study

First measurements of cirrus mammata using multiple remote sensors including the high resolution PDL system and W-band Doppler radar have been presented in this section. The synoptic environmental characteristics, the cirrus mammatus fine structures, and possible thermodynamic and dynamic reasons have been discussed. The NCEP reanalysis data and GOES-10 satellite images show that this cloud system was associated with a prestorm generated by a cold front from the east Pacific ocean region. Revealed by the NCEP reanalysis data and also confirmed by real-time sounding observations, the main environmental features for this process is that a dry layer was located below the cirrus cloud. Due to the local subsidence of the cloud base, the cloudy air descended

moist adiabatically and the dry clear air below cloud dry descended adiabatically, producing a local instability at the cloud base. This local instable environmental condition is necessary for the development of the small convective disturbance to generate cirrus mammata.

The measurements of the high resolution PDL system and W-band Doppler radar demonstrate their capabilities to detect cloud structures and capture the cloud scale processes. The fine structures of the cirrus mammata and significant velocity perturbations were recorded. The mammata extended 0.2-0.6 km below the usual cirrus cloud base level and had a sharply outlined shape that penetrated into the aerosol layer. It should be highlighted that they have a horizontal length scale of 4.0-7.0 km, within and around which much smaller mammatus structures with a scale of 0.7-2.5 km are also developing. The spectral power density for the mean Doppler velocity at cloud base indicates the existence of the developed cascaded three-dimensional isotropic turbulence around the cirrus mammatus area. That implies that, independent of the vertical motion or cloud structures, the energies in the cloud are cascading from large-scale into small-scale around mammatus areas. One also finds that evaporation in dry subcloud air occur in the mammatus structures, which plays an important role in mammatus formation.

Finally, the comparisons of anvil mammata and cirrus mammata from previous observations and the recent case study are presented in Table 5.1. Although anvil mammata occur at the relative low altitude compared with cirrus mammata, both of them exhibit the strong oscillation of the vertical motions. Generally, the cirrus mammata have larger length scales than anvil cirrus structures. Although all the three related processes

TABLE 5.1. Comparisons of cirrus and anvil mammatus measurements.

Case	Method	Place	Cloud type	Temperature (°C)	Altitude MSL (km)	Horizontal Scale (km)	Vertical motions ($m\ s^{-1}$)
Warner (1973)*	Stereo time-lapse photography	Alberta	Hailstorm	?	6.0-7.0	1	-3.0 to +0.5 (P)
Stith (1995)*	Aircraft	North Dakota	Hailstorm	-26°	7.0	2-3	-2.5 to +1.0 (A)
Martner (1995)*	Doppler radar	Manitoba	Convective shower	+1°to -11°	3.0-5.0	1	-3.0 to +0.5 (p)
Windstead et al. (2001)	Doppler radar	Oklahoma	Convective anvil	-15°	6.0-7.4	1-3	?
Jo and Pavlos (2003)	Doppler radar	Florida	Anvil cirrus	?	5.0-6.0	?	-4.0 to +1.0 (p)
This study	Lidar and Doppler Radar	Utah	Cirrostratus transiting into altostratus	-37°	7.4~8.0	3.0-7.0	-2.0 to +0.5 (P)

* Adapted from Martner (1995), (P) – particle motion, (A) – air motion, positive value indicates updraft motion.

including subsidence of a cloud interface layer, fallout of cloud particles, and evaporation of fallout are involved in both cirrus and anvil mammatus formation, cirrus mammata generally do not have the formation of a fallout front like anvil mammata so that they do not have a smoothed and beautiful outline. Here a unique anvil case occurring on August 26, 1998 is presented where the cirrus mammata and anvil mammata coexist together shown in Fig. 5.10. The blowup view of the anvil mammata and cirrus mammata clearly show their difference, where anvil mammtus have smooth cauliflower-like protuberances while cirrus mammata have deeply sharp outlines.

However, a single case study is not enough to fully disclose cirrus mammatus properties. Thus, the statistical properties will be presented in the following sections.

5.3. Statistical Properties of Cirrus Mammata

Unlike KH instabilities that are uncommon in cirrus clouds, cirrus mammata occur frequently in the FARS high cloud dataset. In order to characterize the thermodynamical and dynamical mechanisms of cirrus mammata, typical cases are selected whose lidar observations are simultaneous or close to the upper air sounding data, though there are enough cases of cirrus mammata in the FARS dataset. Totally, 25 cases of cirrus mammata have been chosen from FARS CPL system observations from 1992 to 2001. The information about these 25 cases including CPL observation time, upper air sounding data time, horizontal length scale, vertical maximum scale, and mammatus occurrence height, duration, distance, mean temperature and horizontal wind speed have been presented in Table 5.2. All the 25 cases were observed during 1800-0200 UTC and overlap with or 1-3 hours before the sounding observation.

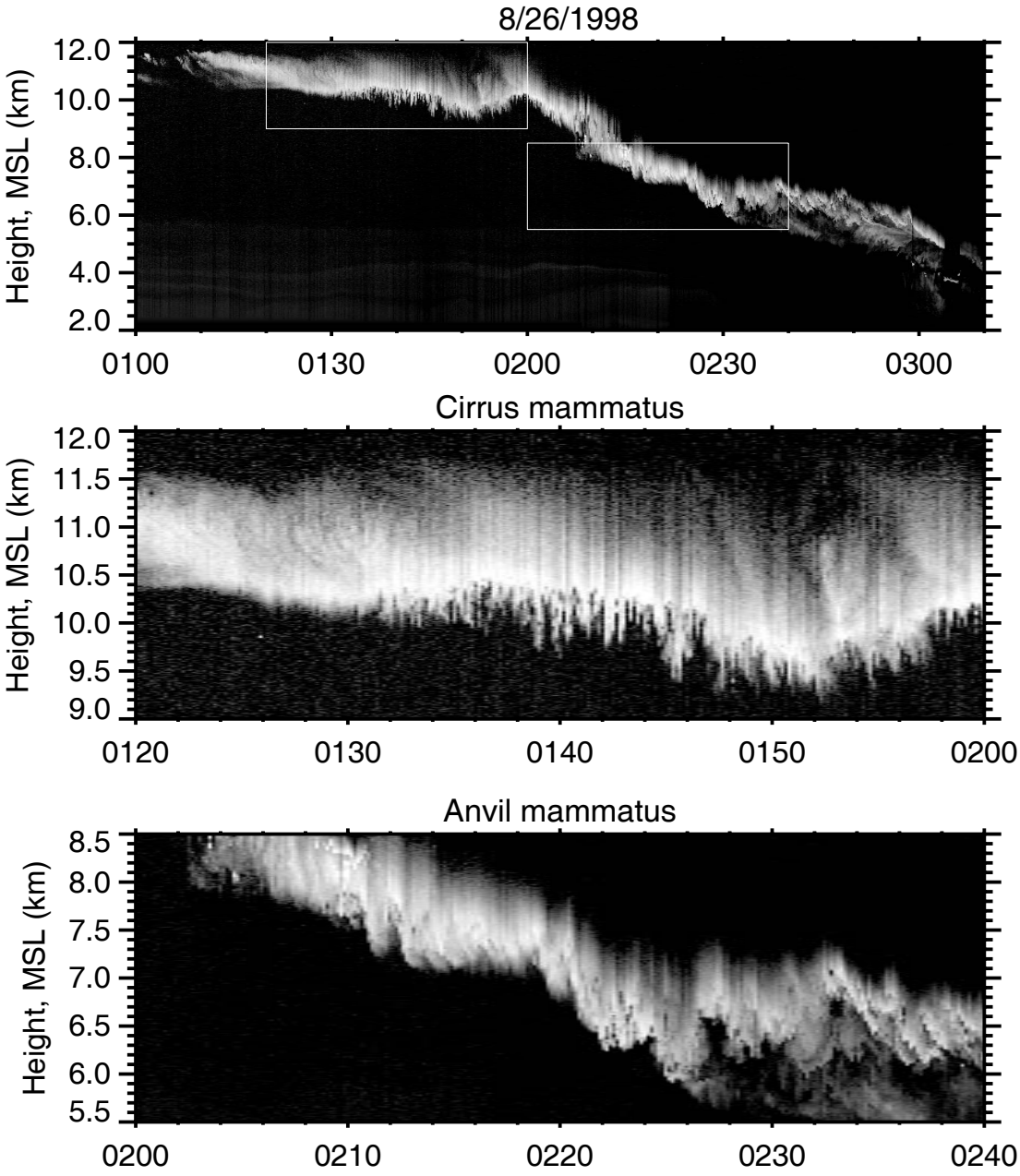

FIG. 5.10. CPL returned power display of an anvil case on August 26 1998, where the cirrus mammata and anvil mammata coexisted. The blowup view of the anvil mammatus and cirrus mammatus clearly shows that cirrus mammata have a deeply sharp outline, though anvil mammata have smooth cauliflowerlike protuberances.

TABLE 5.2. Cases of cirrus mammata found from the FARS high cloud datasets

Case #	Lidar observation	Sound file	Occurrence height (km)	Length scale (km)	Maximum vertical scale (km)	Duration (s)	Distance (km)	Mean temperature (°C)	Mean wind velocity (m/s)	Cirrus type
1	92/12/07 0047~0314	92/12/07 00Z	5.00~5.63	0.5~2.0	0.30	2700	26	-23.2	9.6	Synoptic
2	93/01/05 2016~0212	93/01/06 00Z	4.24~6.71	2.0~8.0	0.60	20310	583	-24.3	28.7	Tropical
3	93/01/12 2232~0232	93/01/13 00Z	3.90~4.73	1.0~3.0	0.50	6160	140	-15.0	22.7	Synoptic
4	93/03/12 2116~0030	93/03/13 00Z	4.89~5.34	1.0~2.0	0.30	3010	44	-20.4	14.7	Synoptic
5	93/04/21 2143~2313	93/04/22 00Z	5.24~6.50	1.0~7.0	0.90	5410	106	-19.5	19.6	Synoptic
6	93/06/10 2103~2312	93/06/11 00Z	4.08~5.82	1.0~7.0	1.10	2380	28	-8.6	11.8	Synoptic
7	93/11/29 2238~0138	93/11/30 00Z	6.73~7.94	1.0~4.0	0.45	6260	165	-29.0	26.4	Synoptic
8	93/12/14 1953~2328	93/12/15 00Z	6.75~7.78	2.0~5.0	1.00	12920	300	-33.3	23.2	Synoptic
9	93/12/26 1827~2120	93/12/27 00Z	5.18~6.44	1.0~3.0	0.60	2450	43	-19.4	17.5	Tropical
10	93/12/30 2246~2359	93/12/31 00Z	5.64~6.73	1.0~5.0	0.50	3370	57	-19.9	17.1	Synoptic
11	94/03/15 2210~2359	94/03/16 00Z	7.47~8.44	2.0~4.0	0.60	6590	126	-31.7	19.1	Tropical
12	94/12/10 2300~0245	94/12/11 00Z	5.93~8.19	2.0~8.0	0.90	10860	234	-29.1	21.5	Contrail
13	95/04/15 0034~0330	95/04/15 00Z	5.63~7.00	1.0~3.0	0.45	5650	89	-29.7	15.7	Synoptic
14	96/02/17 2039~2210	96/02/18 00Z	4.28~6.25	1.0~4.0	0.72	3270	79	-14.6	24.1	Synoptic
15	97/05/02 1854~2210	97/05/03 00Z	4.86~5.66	1.0~4.0	0.55	5140	81	-16.0	15.7	Synoptic
16	97/11/30 2047~2310	97/12/01 00Z	5.72~6.40	1.0~5.0	0.55	5210	37	-23.1	7.1	Synoptic
17	97/12/31 1726~2120	98/01/01 00Z	6.36~7.77	1.0~7.0	0.70	10470	201	-27.6	19.2	Tropical
18	98/02/19 2126~2326	98/02/20 00Z	4.30~5.38	0.7~2.0	1.00	7220	59	-21.2	8.1	Anvil
19	98/03/16 2003~2310	98/03/17 00Z	7.03~7.80	0.9~4.0	0.55	10160	122	-32.9	12.0	Anvil
20	98/10/24 2102~2336	98/10/25 00Z	4.75~5.76	2.0~7.0	0.73	3270	48	-15.2	14.8	Tropical
21	98/11/16 1925~0051	98/11/17 00Z	6.11~7.63	2.0~5.0	0.86	19100	567	-22.9	29.7	Anvil
22	98/11/26 2016~2145	98/11/27 00Z	6.86~7.86	1.0~4.0	0.90	1430	39	-27.4	27.0	Anvil
23	99/03/10 2303~0110	99/03/11 00Z	4.70~5.83	0.7~4.0	0.55	5870	75	-23.2	12.8	Anvil
24	00/11/22 1801~2132	00/11/23 00Z	4.38~5.60	0.6~3.0	0.90	12690	92	-15.2	7.2	Synoptic
25	01/11/28 1803~2010	01/11/29 00Z	3.95~4.70	2.0~7.0	0.45	6400	90	-10.9	14.0	Synoptic
	Mean value	-	6.0	2.9	0.67	-	137.2	-22.1	17.6	-

5.3.1 Typical patterns

The patterns to generate cirrus mammata can be classified into two basic categories: 1) in the downward extensions of the low end trail in the well-developed cirrus fallstreak clouds; 2) in the base of altostratus or cirrostratus-altostratus transition clouds. Fig. 5.11 presents the examples for these two kinds, the lidar returned power displays of case 5 and 13. The first type has been given fully discussed by Ludlam (1980). As shown in Fig.5.11a, cirrus mammata were generated in the well-developed cirrus fallstreak clouds, whereas the generating head and cloud fallstreaks are apparent. In the base of the trail, the cooling associated with evaporation and bringing down the wet air into a dry layer lead to the formation of cirrus mammata. Case 1, 4, 7, 13, 15, 17, 19, 21, and 23 could be classified into this category.

As far as the second pattern, the common characteristics are the existence of strong attenuation phenomena and not easy to identify the cirrus generating head and fallstreaks on the lidar backscattered power display. One can identify them as altostratus or cirrostratus-altostratus transition clouds (Sassen 2002). The case study discussed in the above section as well as case 2, 3, 5, 6, 8, 9, 10, 11, 12, 14, 16, 18, 20, 22, 24 and 25 belong to the second kind.

5.3.2 Environmental characteristics

As the discussion in the above case study, cirrus mammata are generally in the interfaces of dry and wet air layer with relatively weak wind shear. Checking the sounding data of these 25 further confirm this. Fig. 5.12 gives the relative humidity (RH) profiles of all 25 cirrus mammatus cases. The vertical and horizontal coordinates are

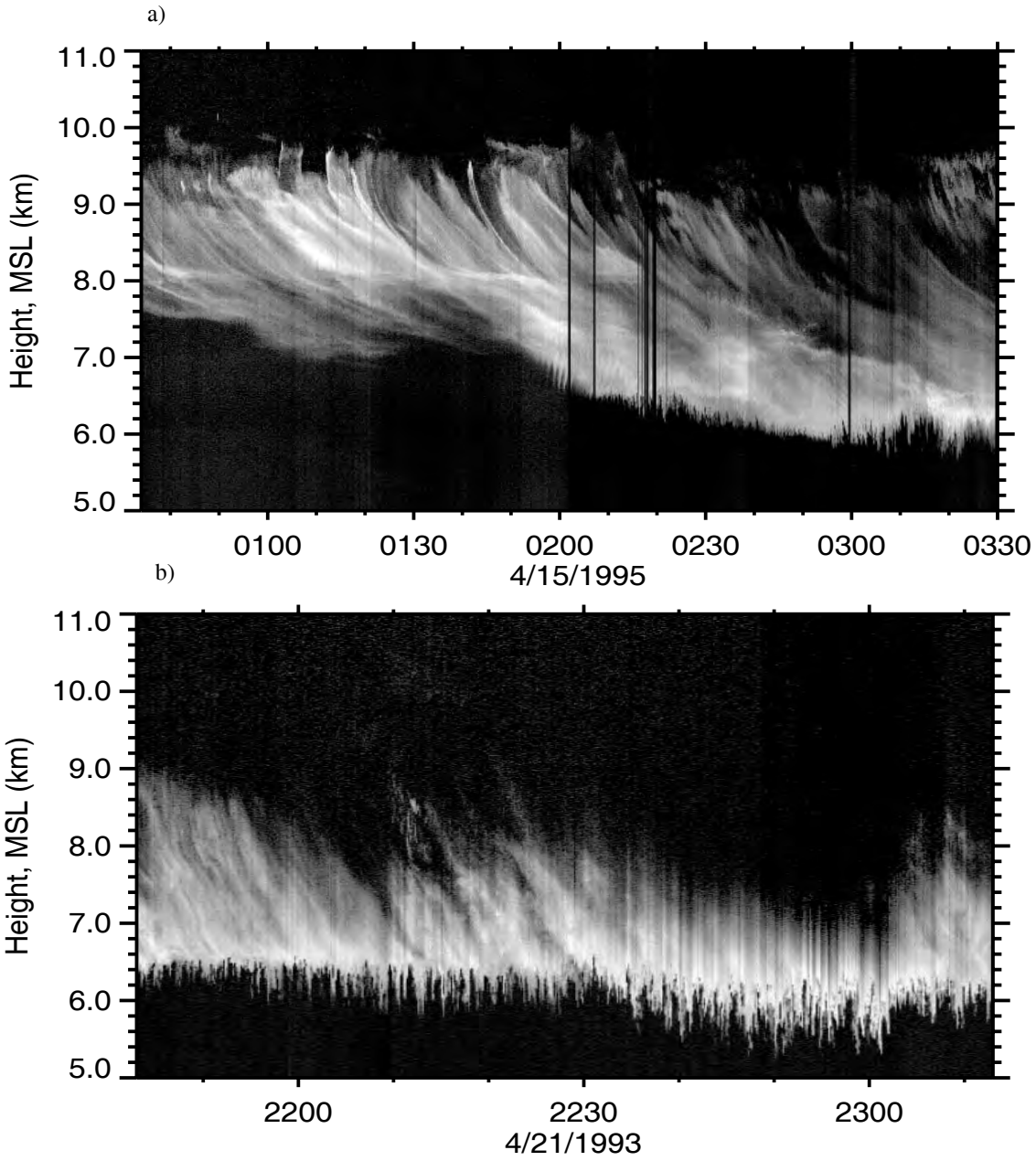

FIG. 5.11. The typical patterns to generate cirrus mammata : a) in the downward extensions of the low end of the cirrus fallstreak trail; b) in the base of altostratus or altostratus transiting from cirrostratus.

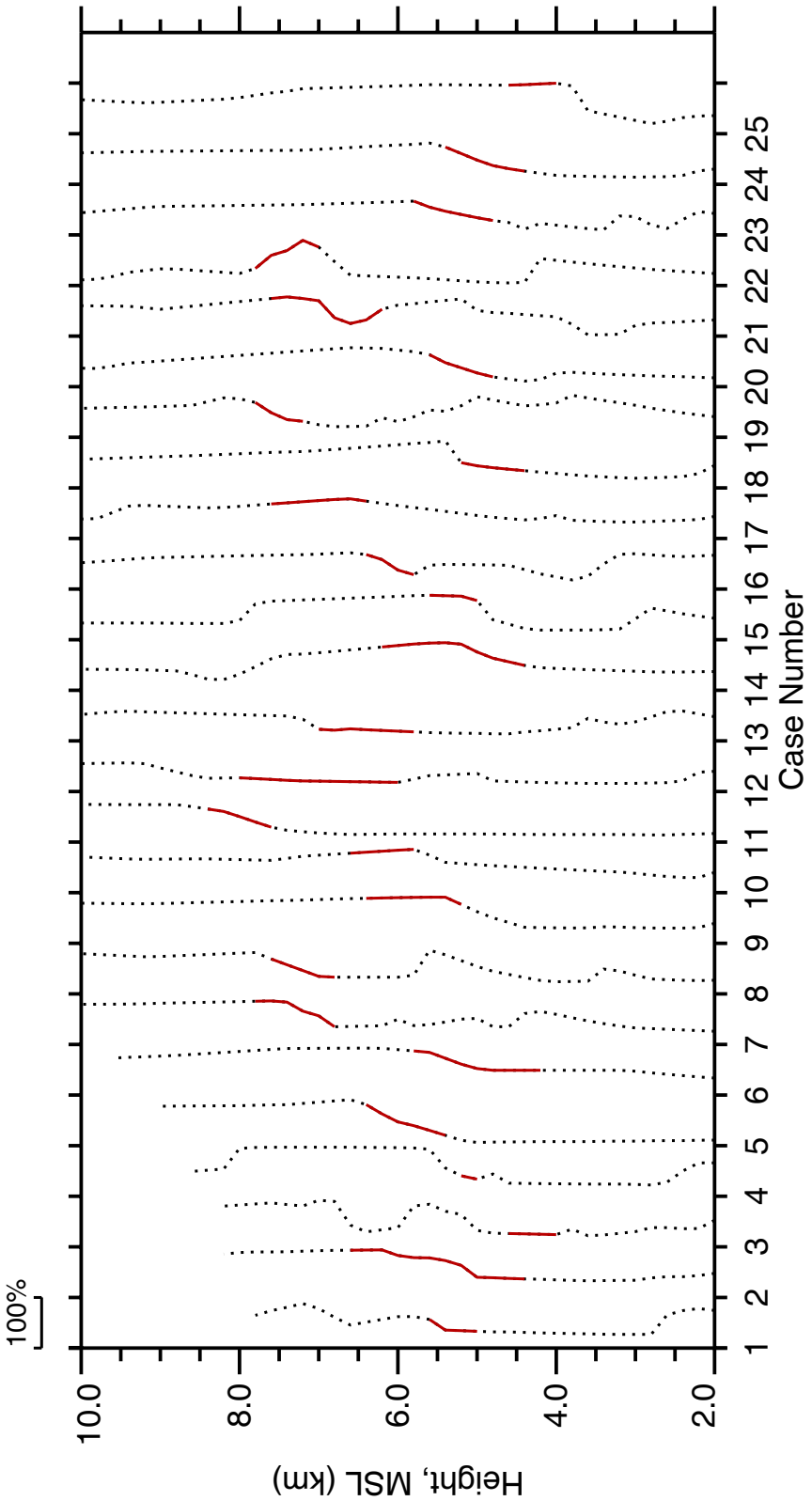

FIG. 5.12. Relative humidity (RH) profiles of all 25 cirrus mammatus cases. The vertical and horizontal coordinates are MSL height and case number, respectively. The values of RH are based on the scale indicated by the line on the top. The RH profile indicated by red color represents the position where cirrus mammatus occur. It clearly shows that most of the cirrus mammatus cases occurred around the transition place where the dry layer changed into wet layer.

MSL height and case number, respectively. The values of RH are based on the width indicated by the line shown on the top of Fig. 5.12. The part of the RH profile indicated by red color represents the position where cirrus mammata occur. It clearly shows that most of the cirrus mammatus cases occurred around the transition place where the dry layer changes into wet layer, including case 1, 2, 4, 5, 6, 7, 8, 9, 11, 13, 14, 15, 16, 17, 18, 19, 20, 21, 22, 23, and 24. Others occurred in a dry layer above which a wet layer existed (case 3 and 12) or in a wet layer below which a dry air mass is located (case 10 and 25). This is because some sounding data are two or three hours later than the occurrence of cirrus mammata and cannot disclose the local environmental features. However, the generation of cirrus mammata located between the dry and wet layer suggests that the adjustment of thermal structures and phase change from ice crystals to water vapor are mainly responsible for the formation of cirrus mammata.

In order to disclose the dynamics features, wind shear per 200 m for 25 cases is determined by:

$$Shear = \left(\left(\frac{\partial U}{\partial z} \right)^2 + \left(\frac{\partial V}{\partial z} \right)^2 \right)^{1/2} \tag{5.4}$$

where U, V are the horizontal wind speed in north-south and west-east direction, respectively. The values of wind shear are extracted from the areas where cirrus mammata occur and shown in Fig. 5.13, in which the line is the range of wind shear and the black bar indicates the mean value. Compared with maximum wind shear 0.5-6.0 m/s per 200 m for the KH cases, the maximum wind shear of cirrus mammata varies 0.5-3.0 m/s. The mean value of wind shear is less than 2.0 m/s. That implies that, different from

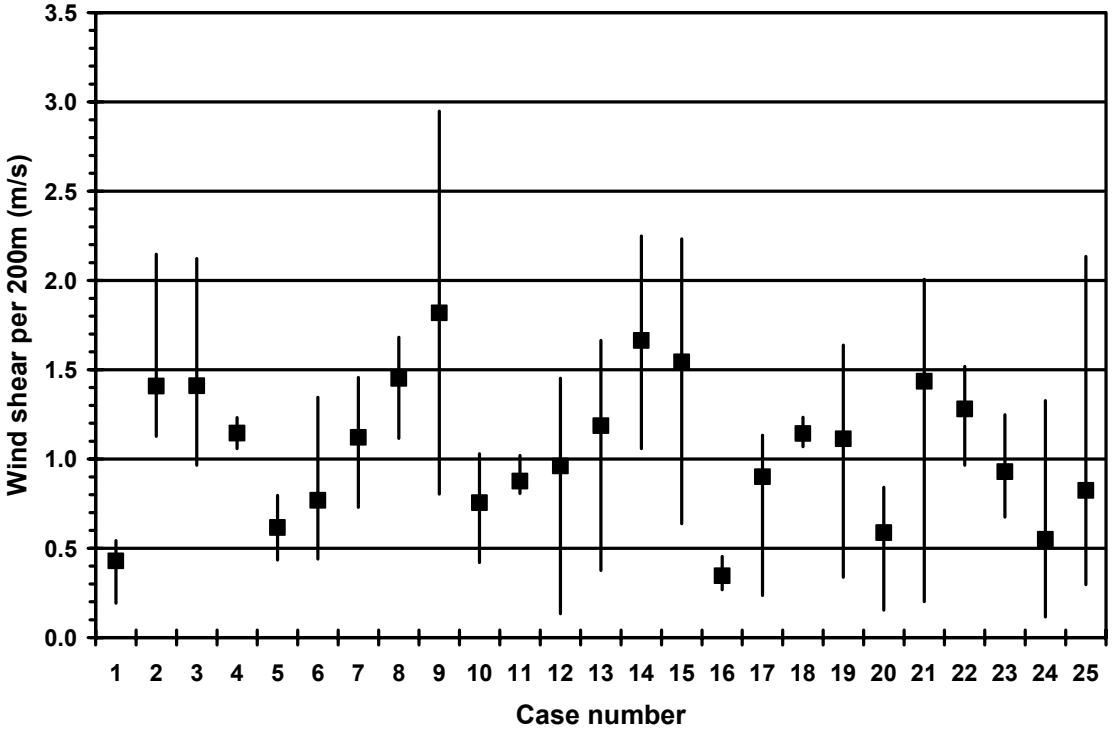

FIG. 5.13. Extracted wind shears from the areas where cirrus mammata occur. The line is the range of wind shear and the black bar indicates the mean value. Compared with maximum wind shear 0.5~6.0 m/s per 200m for the KH cases, the maximum wind shear of cirrus mammata varies 0.5~3.0 m/s and the mean value of wind shear is less than 2.0 m/s. This implies that, different from KH instabilities in cirrus, the wind shear does not play a key role for the production and development of cirrus mammata.

KH instabilities in cirrus, the wind shear does not play a key role for the production and development of cirrus mammata.

5.3.3 Vertical and horizontal length scales

The vertical and horizontal length scales of 25 cirrus mammatus cases have been given in Table 5.2. The maximum vertical extended scales for cirrus mammata have a mean value of ~0.67 km and vary from 0.3 to 1.10 km. The wavelet methods have been used to extract the length scale of cirrus mammata. The wavelet spectrum of the range-corrected lidar power is made every 37.5 m as described in Chapter 3. The wind speed from the sounding observation is interpolated on every height and then used to convert the time period into horizontal length scale. Since the cirrus mammata develop at the different length scales and do not have the regular wave pattern like KH instabilities, one just can give the length scale ranges for every cirrus mammatus case. The results show that the horizontal length scale mainly varies around 0.5-8.0 km, indicating the cirrus mammata belong to the subcloud structures.

5.4. Conclusion

Analysis of the FARS high cloud datasets to reveal the cirrus mammatus properties has been given in this chapter. First, the case study of cirrus mammata combining multiple remote sensors including high resolution PDL system and W-band Doppler radar are presented. The synoptic environmental characteristics, the cirrus mammatus fine structures, and possible thermodynamic and dynamic reasons have been discussed in the case study. Finally, 25 cirrus mammatus cases were chosen from the

FARS high cloud sets to disclose the characteristics of cirrus mammata. The typical patterns to generate cirrus mammata, environmental characteristics, and the vertical and length scale of cirrus mammata finally are proposed here.

No matter of the case study or statistical analysis of the 25 cases, all cirrus mammata occurred around the transition areas from the dry layer to wet layer with the relatively weak wind shears, which suggests that atmospheric thermal structures play a key role to generate cirrus mammata. These results are consistent with the previous theory and observation about anvil mammata (Ludlam and Scorer 1953; Scorer 1958; Ludman 1980; Emanuel 1981; Martner 1995; Windstead et al. 2001). The local instability caused by the local subsidence of the cloud base into the relatively dry surroundings and evaporative cooling process are mainly responsible for the formation and development of cirrus mammata.

The maximum vertically extended scales and horizontal length scales for cirrus mammata vary around 0.3-1.10 km and 0.5-8.0 km, respectively, indicating they are subcloud scale structures and cannot easily be captured by regular instruments. Importantly, one further finds that the small-scale structures developed between or around large-scale mammatus clouds. Moreover, the spectral slope of the lidar returned power and the mean Doppler velocity extracted from mammatus areas also indicated the presence of the developed three-dimensionally locally isotropic, homogeneous turbulence generated by the buoyancy. This implies the buoyancy injects energies into system, which then is cascading from large-scale into small-scale motion. One just guesses that, cirrus may play like a heat engine by bringing down the wet air into dry layer and

evaporation cooling to convert environmental mean flow potential energy into TKE and form the cirrus mammata.

Finally, the comparisons of anvil mammata and cirrus mammata also have been discussed. Although all of three related processes including subsidence of a cloud interface layer, fallout of cloud particles, and evaporation of fallout are involved in both cirrus and anvil mammatus formation, cirrus mammata generally do not have the formation of fallout front like anvil mammata so that they do not have the smoothed and beautiful outline. In addition, cirrus mammata also have a greater horizontal length scale than anvil counterparts that have been reported in the literature.

CHAPTER 6

CIRRUS UNCINUS CELLS

6.1 Introduction

Cirrus uncinus clouds have attracted attention of researchers for a long time due to their unique hooked shapes, which display a relatively dense generating cell "head" and "tail" of precipitation of ice crystals (colloquially "mare's tail cirrus") (Ludlam 1948, 1956, 1980; Harimaya 1968; Yagi et al. 1968; Yagi 1969; Heymsfield 1975a, b, c; Sassen et al. 1989; Sassen 2002). In general, they have been thought to be initialized by an updraft, in which the formation and growth of ice crystals occurs. As the particles grow, they fall out of the updraft, form a trail extending upshear below the head, and eventually merge into a more uniform cirrostratus layer. The early studies showed that the uncinus head generally occurs in a region containing an adiabatic lapse rate with a stable layer above and below the head (Yagi 1969; Heymsfield 1975a, b). Two mechanisms including the layer lift or wave motions in the stable layer below the head region are proposed to initialize the convective motion. The scale of updrafts has been observed up to 1 m/s in the uncinus head (Heymsfield 1975a; Sassen et al. 1989). The width of the uncinus cell head is usually on the order of 1.0 km (Heymsfield 1975b; Sassen et al. 1989; Sassen 2002).

The uncinus cell cannot only exist separately as a series of cloud bands, but also can be embedded in the extended stratiform cirrus clouds. Revealed by the high resolution remote instruments, the individual uncinus cells can be composed of group of

much smaller (~100 m) sporadic updrafts, and they also can be assembled into mesoscale uncinus complexes (MUCs) with horizontal dimension of 10-100 km that are similar in geometric appearance to the individual uncinus cells (Sassen et al. 1989; Grund and Eloranta 1990; Sassen et al. 1990; Smith et al. 1990; Starr and Wylie 1990; Gultepe et al. 1995; Sassen 2002). This indicates that small-scale convective processes are likely to be important for the persistence of cirrus clouds (Quante and Starr 2002). Using a two-dimensional (x, z) cirrus cloud model, Starr and Cox (1985a) successfully simulated these internal fine structures that developed at horizontal scales of ~1km or less, consistent with the depth of the cloud generating layer, in association with dynamical features (updrafts). Based on these results, they pointed out that the radiative heating/cooling effects associated with these internal cloud structures play an important role, which is also supported by the recent numerical simulation results (e.g., Gu and Liou 2000; Dobbie and Jonas 2001; Liu et al. 2003). Gu and Liou (2000) and Dobbie and Jonas (2001) further speculated that radiative cooling/heating driven turbulence effects the phase change of ice and the formation of ice crystal size distribution, which eventually result in the formation of these embedded cirrus generating cells. Starr and Quante (2002) also speculated that two-dimensional turbulence associated with kinetic energy cascades occurring in the upper troposphere may be involved in the persistence of these mesoscale structures.

However, to date, knowledge on cirrus generating cells is still lacking. As pointed out by Starr and Quante (2002), new and creative ideas for rigorous quantitative validation and evaluation of cirrus models using observations still are needed. Cirrus

clouds have been characterized as a highly coupled dynamic and thermodynamic system that involves in the intricate coupling of microphysics, radiation, and dynamic processes, and hence result in the coexistence of multiple scale structures (Gultepe and Starr 1995). Therefore, it is important to extract different scale processes from the observational data to study their roles and interactions in the cirrus clouds. In this chapter, a method based on discrete wavelet transform to decompose high resolution PDL observational data into different scales will be proposed. Then the mechanism of cirrus uncinus generating cells will be discussed. The purpose of this chapter is to provide some new observational facts to evaluate the cirrus model results. This chapter is organized as follows. The decomposition methods based on the discrete wavelet transform are introduced in section two. The decomposition results and analysis are presented in section three, and the chapter concludes with section four.

6.2 Decomposition Methods

In Chapter two, the basic knowledge on CWT has been discussed in detail. In order to decompose the observational data into different scale, one needs to use the wavelet spectrum to reconstruct the signal. However, the information that the CWT provides is highly redundant. This redundancy, on the other hand, requires a large amount of computation time and resources (Kumar and Foufoula-Georgiou 1994). The discrete wavelet transform (DWT), on the other hand, provides sufficient information for both analysis and synthesis of the original signal with a great reduction in the computation time. Therefore, the multi-resolution analysis based on the DWT has been successfully applied in the meteorological community (e.g., Gollmer et al. 1995; Desrochers and Yee

1999; Yano et al. 2001; Quante et al. 2002). In this section, the methods to decompose the different scale structures from high resolution PDL image will be introduced.

6.2.1. Discrete wavelet transform

The classic Fourier expansion for a finite periodic domain, say, $[0, L]$, can be generalized into a complete discrete set of functions as $\{\phi_k : k = 0, 1, ..., +\infty\}$. These functions are chosen to be orthogonal and can be normalized to yield

$$\frac{1}{L}\int_0^L \phi_k(x)\phi_l(x) = \delta_{kl}\,, \tag{6.1}$$

where δ_{kl} is Kronecker's delta function given as

$$\delta_{kl} = \begin{cases} 1 \text{ if i = j} \\ 0 \text{ otherwise.} \end{cases}$$

Therefore, any well-behaved function *f(x)* can be reconstructed as

$$f(x) = \sum_{k=0}^{\infty} \hat{f}_k \phi_k(x)\,, \tag{6.2}$$

where the coefficient $\hat{f}_k$ is defined by

$$\hat{f}_k = \int_0^L f(x)\phi_k(x)dx \tag{6.3}$$

under the condition of the orthonormality of the basic function (6.1).

Recall that the CWT was computed by changing the scale of the analysis window, shifting the window in time, multiplying the signal, and integrating over times. It could be defined as (Kumar and Foufoula–Georgiou 1994; Holschneider 2000):

$$\widehat{W}(\tau, s) = \frac{1}{(s)^{1/2}} \int_{-\infty}^{+\infty} X(t)\,\psi^*\left(\frac{t-\tau}{s}\right)dt\,, \tag{6.4}$$

where $\psi(t)$ is the element-transform wavelet function named "mother wavelet" defined by the translation and scale parameters, respectively τ and s:

$$\psi_{\tau,s}(t) = \frac{1}{(s)^{1/2}}\psi(\frac{t-\tau}{s}). \tag{6.5}$$

Analogically, in some cases, one can construct an orthonormal basis of functions in the CWT case by choosing the scales to be powers of 2 and the times to be an integer multiple of the scales (Mallat 1989). Using integer j and k to replace the translation and scale parameters, τ and s, the mother-wavelet function (6.5) will be transformed into:

$$\psi_{k,j}(t) = 2^{j/2}\psi(2^j t - k). \tag{6.6}$$

And the wavelet transformation will be given as:

$$\hat{W}(k/2^j, 1/2^j) = 2^{j/2}\int_{-\infty}^{+\infty} X(t)\psi^*(2^j t - k)dt. \tag{6.7}$$

In the case of an orthonormal wavelet, the analysis formula is called the discrete wavelet transform (DWT) given by:

$$C_{k,j} = \int_{-\infty}^{+\infty} X(t)\psi^*_{k,j}(t)dt. \tag{6.8}$$

The recovery of the signal through the synthesis formula is called the inverse discrete wavelet transform (IDWT) given by:

$$X(t) = \sum_j \sum_k C_{k,j}\psi_{k,j}. \tag{6.9}$$

There exists a variety of wavelet and scaling filters that satisfy the crucial orthonormality requirements including Haar, Daubechies, Symlets, Mayer and Coiflets wavelet functions (Daubechies 1992). Daubechies (1988, 1992) has developed the theory

for obtaining higher order mother wavelet filters with compact support and identified two sets of filter, the extremal-phase and least-asymmetric. Fig. 6.1 gives an example of Daubechies wavelet and scale function.

6.2.2. Decomposition methods

Compared to the Fourier series, the series in equation (6.8) have the following differences: 1) the series are double indexed with the indices indicating scale and location; and 2) the basic functions have the time-scale localization property in the sense as discussed in chapter three. Using an intermediate scale, equation (6.9) can be broken into two sums by choosing the appropriate wavelet function as the equation (6.6) (Kumar and Foufoula–Georgiou 1994):

$$X_s(t) = \sum_{j \geq m_0} \sum_k C_{k,j} \psi_{k,j} + \sum_{j < m_0} \sum_k C_{k,j} \psi_{k,j} \ . \tag{6.10}$$

Therefore, it is possible to partition the lidar signal into two components, one containing the small-scale structure information and the other representing the large-scale structure information. Once a partition is obtained, further analysis of each component can proceed. This method based on the DWT is called multi-resolution analysis (Mallat 1989).

Using cold midlatitude cirrus observed at the ARM CART site near Lamont, Oklahoma on 19 April 1999 as an example (Sassen et al. 1998; Khvorostyanov and Sassen 2002), Fig. 6.2 gives the scheme to show how the lidar backscattered power data are decomposed into the two parts with the different horizontal scale. First, as shown in Fig. 6.1a, the horizontal signal at every altitude is extracted from the lidar returned

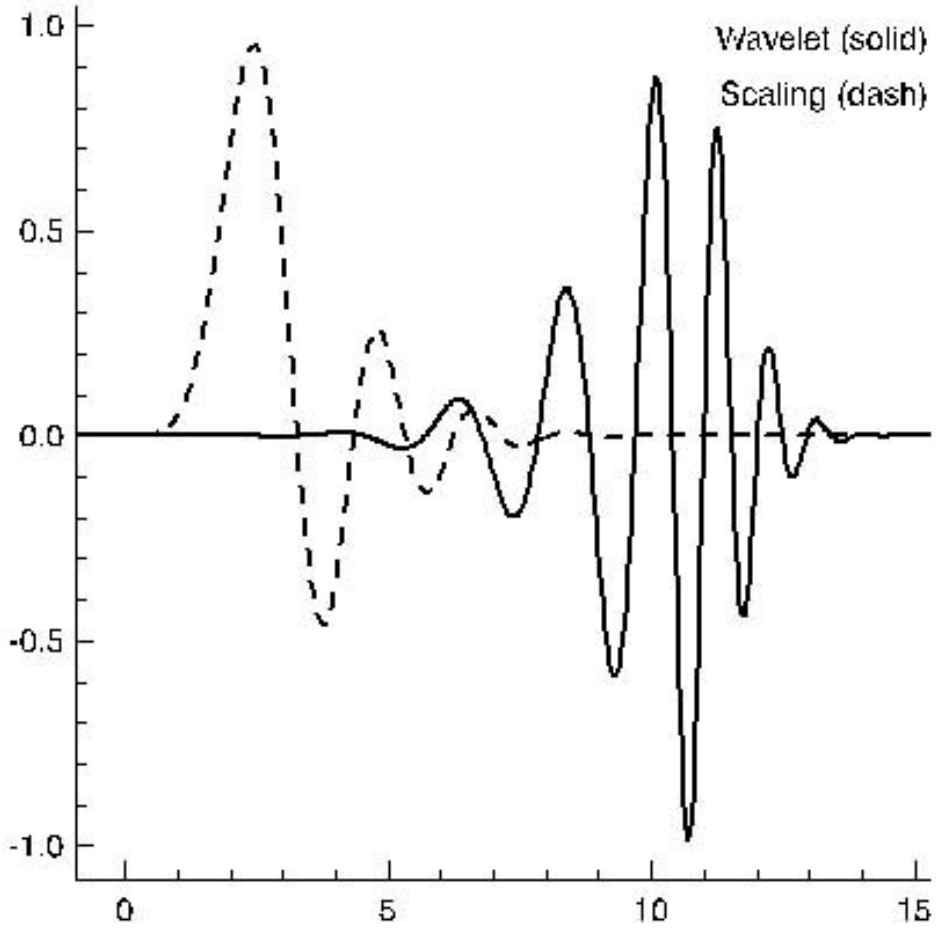

FIG. 6.1. The Daubechies wavelet and scale function with the order 11.

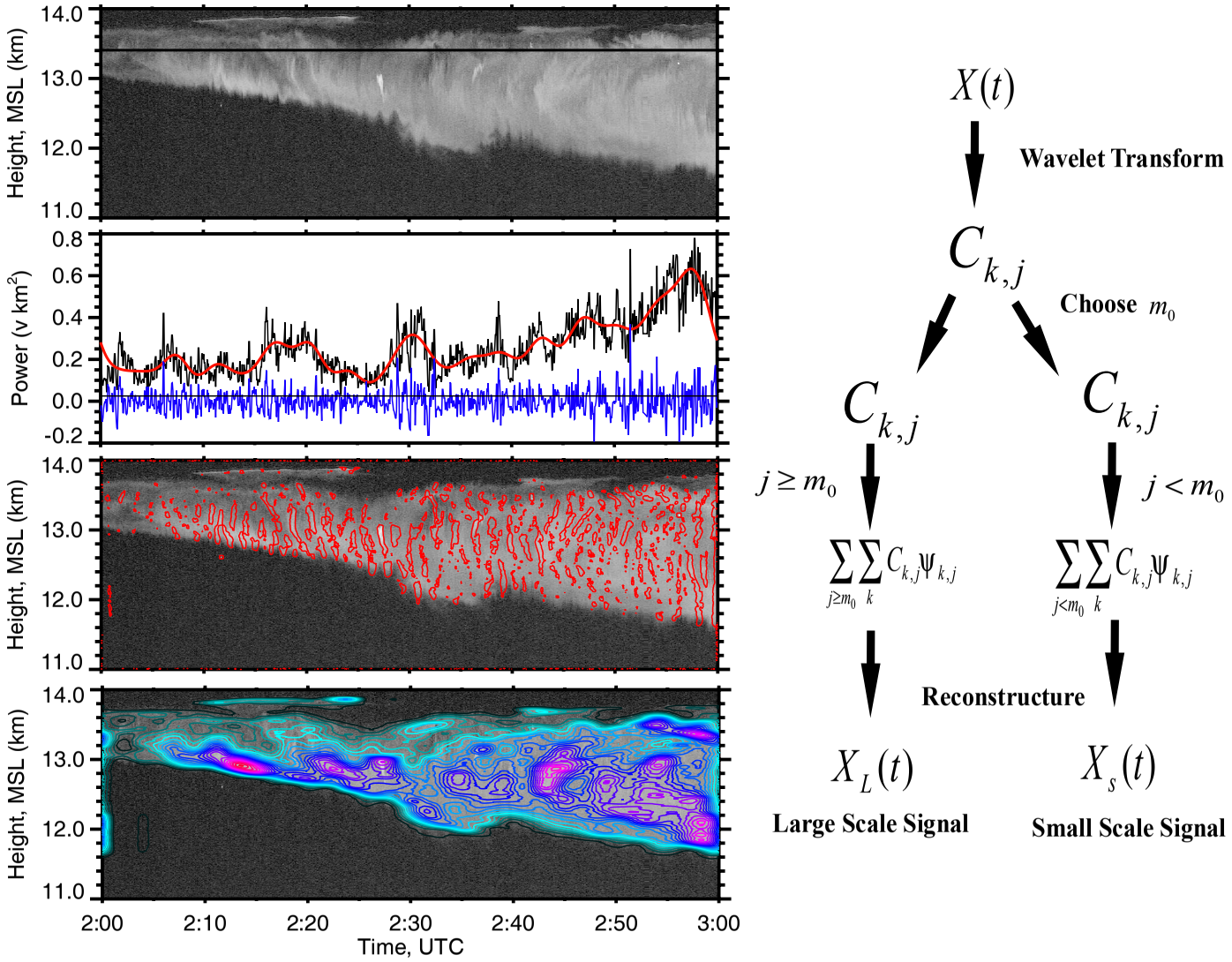

FIG. 6.2. Illustrative scheme to show how the lidar backscattered power data are decomposed into the two parts with different horizontal scales.

energy image. It should be noted that the 2-D discrete wavelet also can effectively decompose the whole image into the approximation and detail part (Mallat 1989), which is successfully applied in the meteorological research field (e.g., Desrochers and Yee 1999; Yano et al. 2001; Quante et al. 2002). However, cirrus clouds usually horizontally extend from tens to hundreds of kilometers but have vertical depth 1-3 km (Sassen and Campbell 2001; Sassen 2002). Furthermore, the remote sensing data of cirrus clouds generally have higher vertical spatial than horizontal resolution due to the large wind velocity at the height where cirrus clouds are located. This indicates that one cannot use the two-dimensional wavelet transformation to analyze the lidar power image due to the different horizontal and vertical scales. Secondly, the signal is the input into the wavelet algorithms to determine the wavelet spectrum. Thirdly, choosing the mediate scale m_0 and running the IDWT algorithms, the signal $X(t)$ is decomposed into two parts: the large-scale part $X_L(t)$ and the remained small-scale part $X_S(t)$. Fig. 6.2b shows the original signal (black line) extracted from the above lidar power image (indicated by the line), the reconstructed large scale part (red line) and small scale part (blue line). One can find that, after detrending the large scale part, the small scale part shows more variability that can be caused by the turbulent and convective motion. Finally, $X_S(t)$ and $X_L(t)$ on every height are combined to make an image again. Fig. 6.2 c and d present the contour plots for these two parts, which is obtained by performing 2-D seven-point running average. Shown in Fig. 6.2c, the part with the small horizontal scale clearly extracts the uncinus cells from the lidar original image. Also note that the three bright cloud features embedded within the cirrus correspond to the contrails produced by the citation aircraft during the field

experiment at the CART site. Importantly, the uncinus cells show the different shapes that are caused by the positive and negative shear conditions (Heymsfield 1975b), which indicates that local turbulent and convective motions play an important role for their initial development. On the other hand, the large scale part in Fig. 6.2d shows the mesoscale structures in the bottom of cirrus clouds. Therefore, the decomposition methods can effectively separate different scale structures of cirrus cloud systems and will be used in the following case study.

6.3 Case study

6.3.1 Weather system and environmental conditions

On 19 November, 1999, a frontal system swept over the west coast of North America from the northeast Pacific. A series of cirrus cloud band were generated ahead of the warm front system due to the baroclinic front uplift (Wylie 2002). The infrared satellite imageries with 4 km resolution from 1200 UTC on November 19 to 0000 UTC on November 20 are provided in Fig. 6.3. At 1200 UTC, the cold front cloud bands were moving from the northeast Pacific into northern California, Oregon, and Washington. Ahead of the cold front, an active warm or occluded front was approaching Utah and Nevada, followed by a sequence of clouds including cirrus, cirrostratus, altostratus, and nimbostratus. Among the FARS high cloud datasets, there are many fine cirrus clouds observed ahead of and above warm fronts that initially formed independent of the frontal middle cloud shield, though later it may trail downward to join the altocumulus and altostratus cloud shields (Sassen and Campbell 2001; Sassen 2002). At 2000 UTC, with

a

b

c

d

FIG. 6.3. GOES-10 infrared channel images at a) 1200, b) 1600, c) 2000 on Nov 19 1999 and d) 0000 UTC on Nov 20 1999.

the frontal system moving east, a thick cirrus layer was passing overhead of the Great Salt Lake area. By 0000 UTC on November 20, the storm associated with the cold-front system finally reached Utah.

The NCEP reanalysis data are used to further characterize the environmental condition for this cirrus case. The detail information about the NCEP reanalysis data can be referred to Kalnay et al. (1996) and Kistler et al. (2001). The height-time cross section of the horizontal wind speed and temperature at the FARS site (40º 46' 48" N, 111º 57' 36" W) is given in Fig. 6.4. The color contours denote the horizontal wind velocity larger than 20.0 m/s with an interval of 5.0 m/s. The box area indicates the cirrus cloud region detected by the FARS CPL system. Apparently, the cirrus clouds are located just below the level of the relatively weak subtropical jet stream core with a maximum wind speed 35.0 m/s. Therefore, there must be stronger wind shear in the lower part of cirrus layer than in the upper part, which indicates that variant local conditions possibly exist in the cloud layer. The sounding data at 0000 UTC on 20 November 1999 (Fig. 6.6) further reveal this, although the data are collected three hours later than the lidar observation. The wind speed increased from 27.0 m/s at 10.6 km to 34.0 m/s at 12.6 km and then kept the same value until 13.2 km. The horizontal wind direction was around 245°-250° and did not change much from cloud base to cloud top. From the thermodynamic view, the cirrus layer was located in the stable layer of the upper troposphere (10.0-13.2 km) and the transition area from the troposphere to stratosphere (13.2-13.6 km). Disclosed by the sounding data (Fig. 6.6), the tropopause was at 13.2 km height and the lowest temperature reached -74.4 °C. Therefore, this cirrus case can be classified into the type of

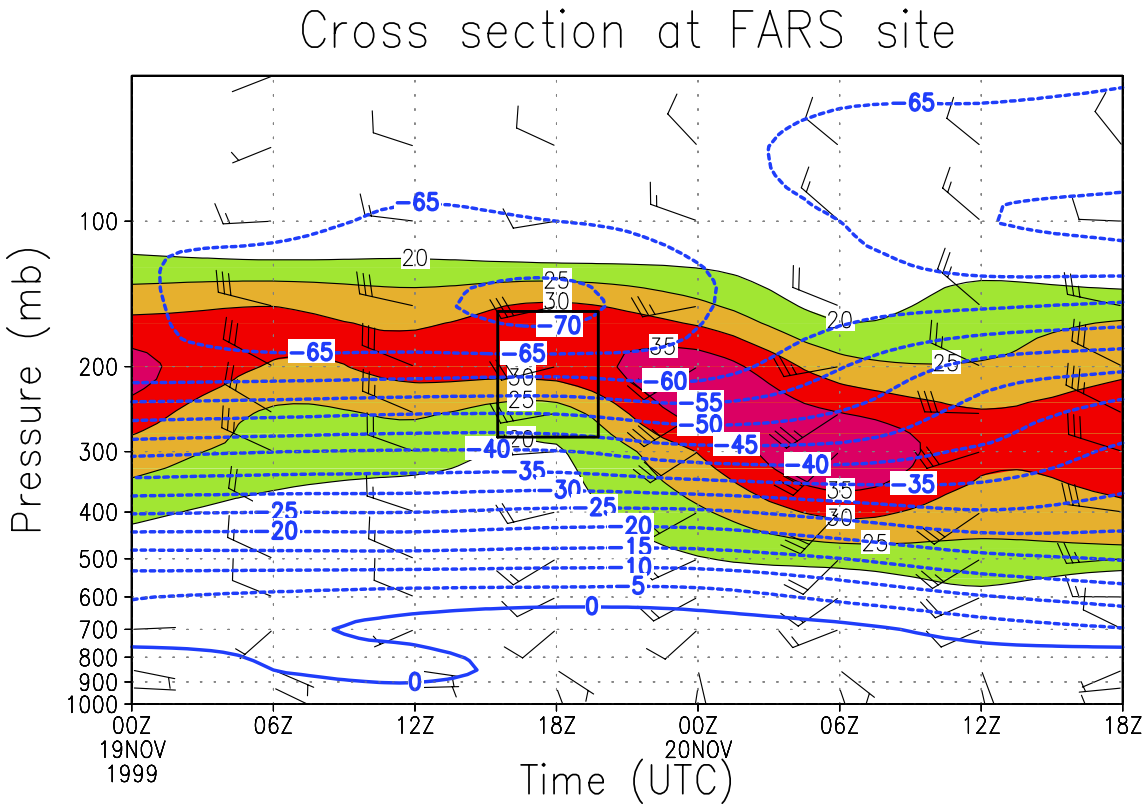

FIG. 6.4. Height-time cross sections of horizontal wind and temperature field at the FARS site from 0000 UTC 19 November to 1800 UTC 20 November 1999. The color contour indicates the horizontal wind velocity above 20.0 m/s with the interval 5.0 m/s . The cirrus area observed by the FARS lidar is indicated by the box.

high and cold cirrus in a stable layer that is associated with an elevated tropopause and extending into the lower stratosphere, which has been paid more attention recently because the troposphere/stratosphere exchange may contribute to the formation and persistence of such cirrus clouds (e.g., Sassen et al. 1998; Liu et al. 2003).

6.3.2 Lidar observations

The whole cloud structures and properties can be partially understood by the CPL lidar data, though its relatively low resolution (10 Hz) is not enough to capture the smallest structures in cirrus clouds. The detailed specification and description about the CPL system was introduced in Chapter two. Beginning from 1724 to 2115 UTC on 19 November 2003, the backscattered energy based on logarithmic grayscale and the linear depolarization ratio (LDR) indicated by the color table are provided in Fig. 6.5. The box indicates the region observed by the PDL system that will be shown in Fig. 6.6. Checking the lidar power image, a cirrostratus layer is located around 13.5-10.0 km, which just is the tropopause region. It can be separated into two different layers. Between 12.0 and 13.2 km, ice crystals formed in the lowermost stratosphere, fell out through the tropopause, and finally were evaporated at ~12.0 km. Another cirrus layer was apparently induced below the upper cirrus layer (especially 1930-2010 UTC), in which some uncinus cells were embedded. Such structure is often revealed in the modern active remote sensing observations of cirrus (e.g., Sassen et al. 1995) and has been explained by Starr and Cox (1985a) using model simulations. They hypothesized that new convective cloud-generating layers might arise at some distance below an initial cloud-generating layer through the cumulative effects of moistening associated with evaporation of crystals

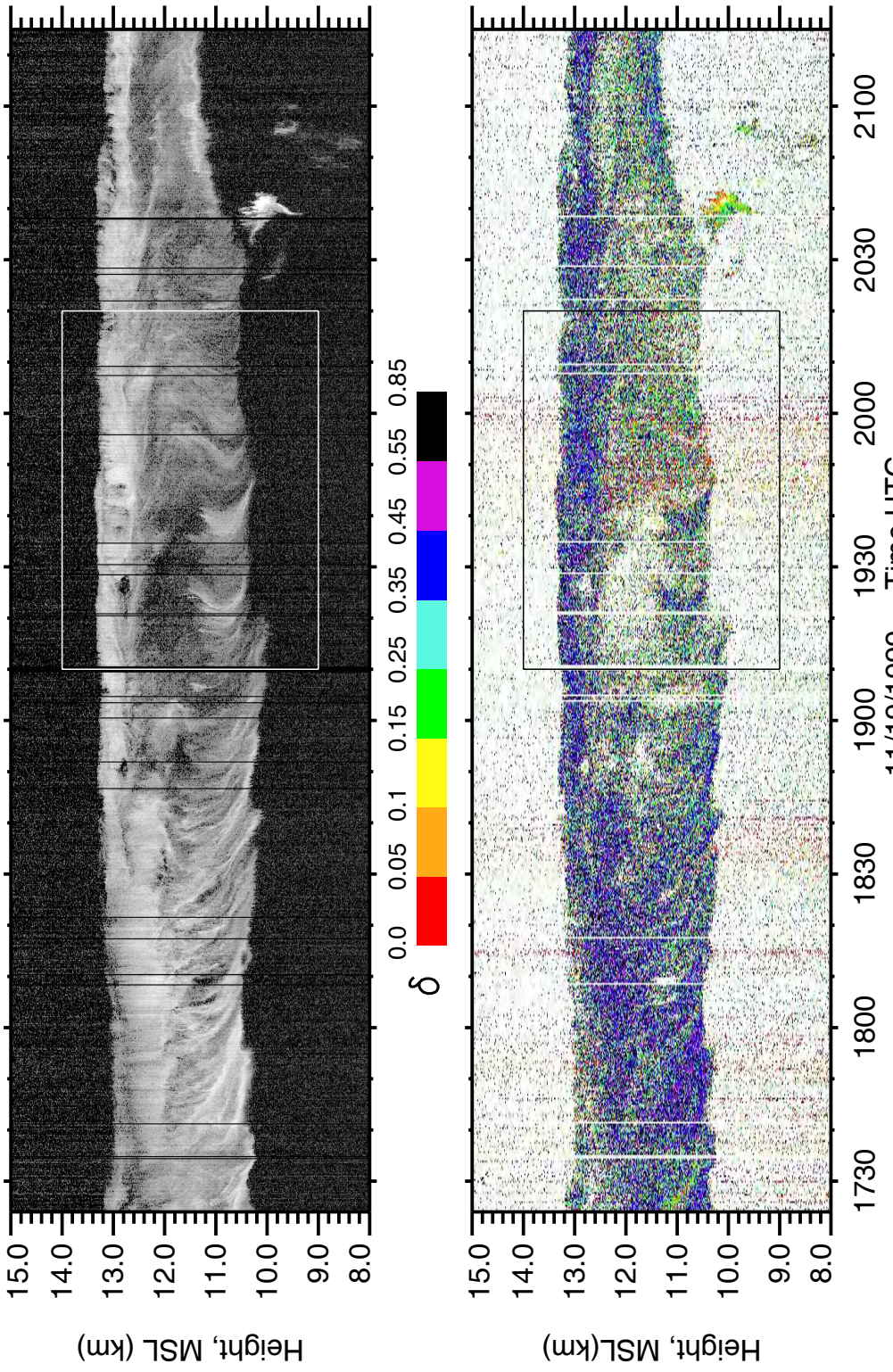

FIG. 6.5. The backscattered energy based on logarithmic grayscale and the linear depolarization ratio (LDR) indicated by the color table by the CPL system. The box indicates the region observed by the PDL system that will be shown in the Fig. 6.6.

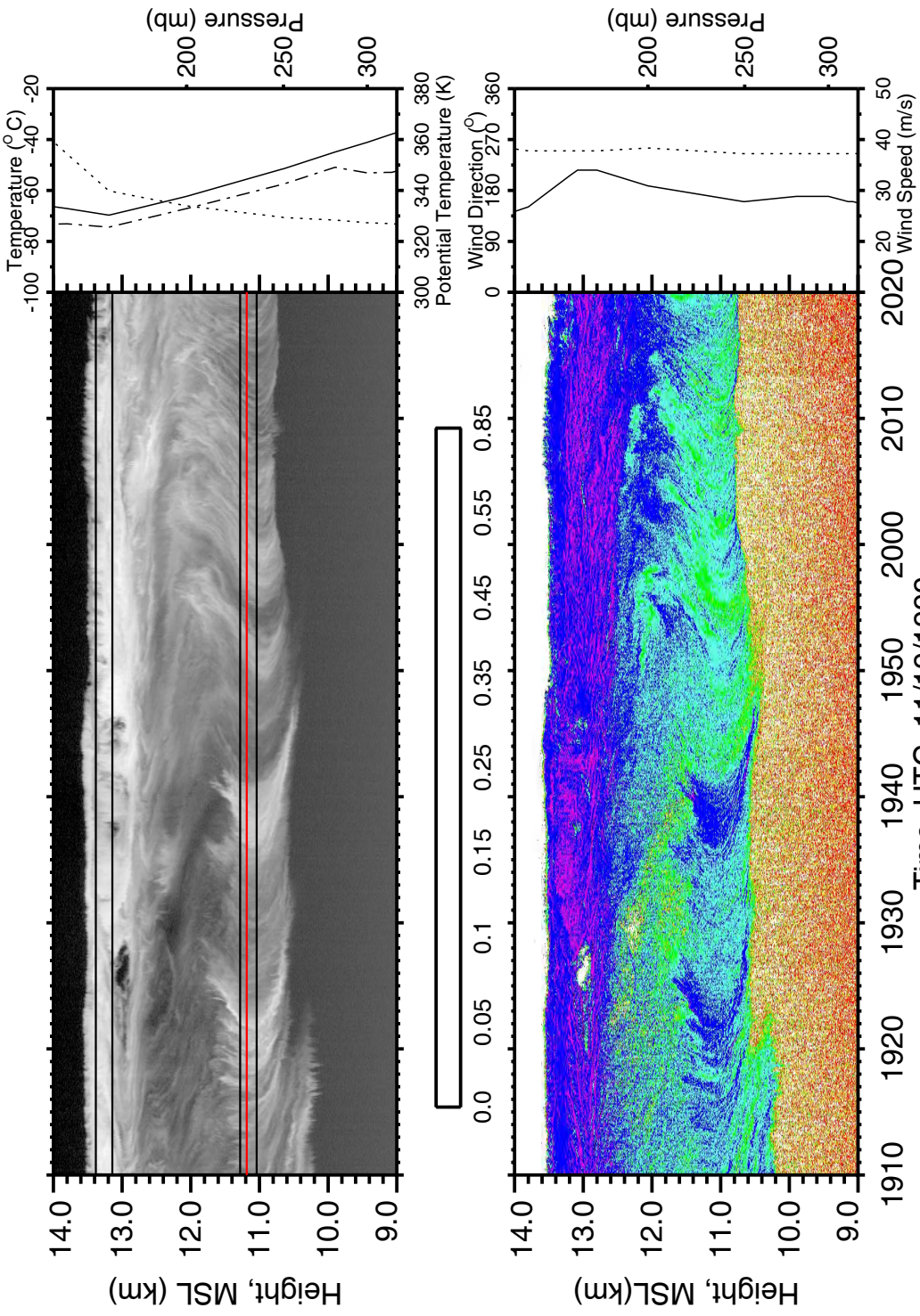

FIG. 6.6. The high-resolution PDL measurements including the backscattered power and the LDR from 1910 to 2020 UTC between 9.0 and 14.0 km. The signal indicated by the red line will be input into the CWT algorithms. For the signals between the two blacklines, their global wavelet spectra will be shown in Fig.6.8.

falling from the overlaying layer together with the tendency toward unstable thermal stratification arising from the vertical pattern of sublimation cooling. Gu and Liou (2003) showed that turbulent energy appeared to play an important role in this process evident from the incorporation of second-order closure in their models that reduced low-level stability. The LDR data are a little noisy due to the low resolution. However, one still can find that the LDR value 0.45-0.55 is dominant in the top layer while the LDR is mainly 0.15-0.45 in the lower layer.

Given in Fig. 6.6, the high-resolution PDL measurements including the backscattered power and the LDR from 1910 to 2020 UTC between 9.0 and 14.0 km are used to capture the fine structures that occurred within the cirrus. In addition to the two layer cirrus structures clearly shown in the power image (Fig. 6.6a), a series of mesoscale uncinus complexes (MUCs) developed in the lower cirrus layer. MUCs were first defined by Sassen et al. (1989) and also observed in many other studies (e.g., Grund and Eloranta 1990; Sassen et al. 1990; Smith et al. 1990; Starr and Wylie 1990; Gultepe et al. 1995; Sassen 2002), which are referred to the characteristic mesoscale structures of cirrus cloud system with dimensions range from ~15km, in the case of narrow cirrus clouds bands, up to ~100 km in deep cirrostratus, composed of individual uncinus cells. Small cell structures are also embedded in the top layer. However, they do not show the typical uncinus structures due to the relative weak wind shear at this altitude.

The lidar LDR value display reveals the information of the ice crystal shape and orientation in cirrus clouds (Sassen 2000; Sassen and Benson 2001). The upper cloud layer in contact with tropopause is dominant with the high 0.45-0.50 value, whereas the

LDR below ranges 0.15-0.40. The presence of the relatively high LDR value in the upper region of cirrus clouds in contact with tropopause folds also have been found by Sassen et al. (1998), which may be caused by the effects of ice particles nucleation and growth of homogeneously frozen sulfuric acid droplets of stratospheric/volcanic origin. At the 10.0-12.0 km regions where the MUCs occurred (1910-1950 UTC), the high 0.45-0.50 LDR values are scattered into the dominant low value 0.15-0.40. This is because that the convective activities within the cirrus clouds cause the change of the falling ice crystal orientation, resulting in the high LDR value.

6.3.3 Wavelet analysis results

The continuous and discrete wavelet transform methods are used to characterize the length scale of the cirrus uncinus cells. The horizontal lidar backscattered power signals at the height 11.185 km (indicated by the red line in Fig. 6.6a) are extracted and put into the CWT algorithms. The CWT methods have been given a detailed discussion in Chapter two. The time series of horizontal backscattered energy on 11.185 km, wavelet spectral power and global power, 95% confidence level contour, and FFT spectral power are given in Fig. 6.7. Since the horizontal wind velocity did not change much (27.8-33.0 m/s) and the wind direction almost kept the same value (~250°) in the cloud layer, a mean horizontal wind velocity of 31.0 m/s is used to transfer the time period into the spatial length scale. Note that the red line in the wavelet power spectrum display represents the areas "cone-of-influence", which is subject to padding of the time-series and edge effects (Lau and Weng 1995; Torrence and Compo 1998). In order to simplify the question and highlight the structures, statistical significance testing has been carried

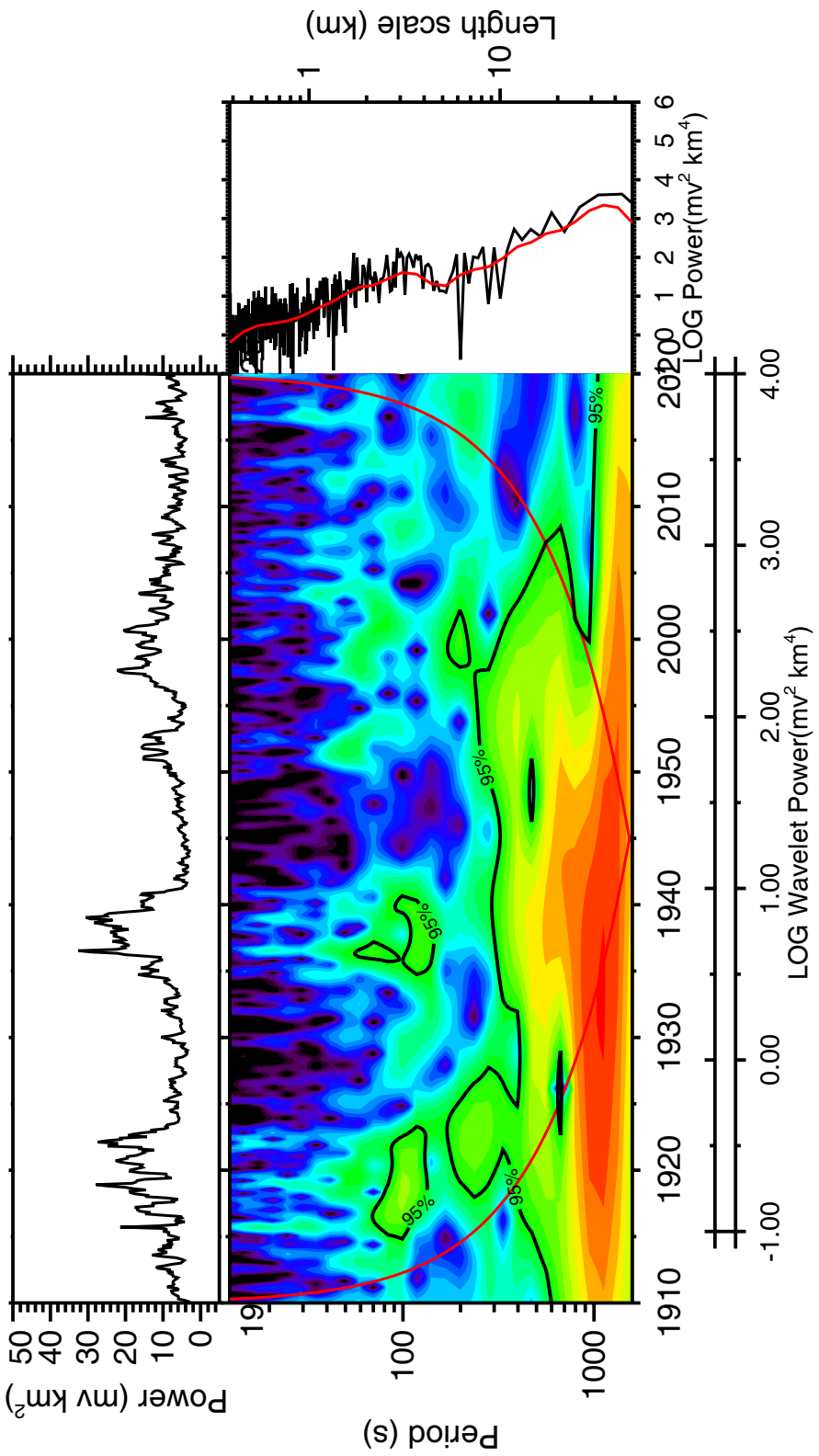

FIG. 6.7. Time series of horizontal backscattered energy (top), wavelet spectral power (bottom, right), and global power and FFT spectral power (bottom, right). The 95% confidence level contour is superimposed on the wavelet spectral power.

out for local wavelet spectra by choosing white noise as the background spectrum (Torrence and Compo 1998). The 95% confidence level contour is superimposed on the wavelet spectral power. Checking Fig. 6.7 first, the strong wavelet powers with a length scale of 30.0-40.0km occupy the all the time domain, indicating that the series of MUCs probably caused by the gravity wave developed in the lower cirrus layer. Notice that the local wavelet powers with the length scale 1.0-4.0 km are also embedded into every single MUC, which agrees with observational facts by others that the width of the uncinus cell head is on the order of 1.0 km (Heymsfield 1975b; Sassen et al. 1989; Sassen 2002). Especially, in 1915-1925 UTC and 1935-1945 UTC, compared with the mean global wavelet power as the background, the local wavelet powers fall into the 95% confidence interval level. These structures may be caused by the cloud scale convection or turbulence. The wavelet results further confirm that the different scale structures caused by the different dynamic mechanisms can coexist in the cirrus, especially for the typical MUC cases. Therefore, it is necessary to separate these two structures from cirrus clouds and then consider their interactions for the development of the cirrus clouds.

The dynamical structures of cirrus clouds can be further quantified using the spectral analysis of the horizontal lidar returned power (e.g., Quante et al. 2002 using radar reflectivity), although the traditional methods extract the dynamic characteristics by calculating the spectral of the velocity components collected by the air measurements (Quante and Starr 2003). The relationship between spectral energy and scale is analyzed in terms of spectral slope, corresponding to the simple power law. In practice, significant variations about a line of constant spectral slope may be found. Since the global wavelet

power can be thought as the mean Fourier spectrum (Torrence and Compo 1998), the global wavelet spectra of the lidar power at every height from the top cloud layer (11.04-11.28 km) and lower layer (13.14-13.38 km) are combined together and shown in the Fig. 6.8. The -3 and -5/3 slopes are also superimposed on the global wavelet spectra. Like the above, the mean horizontal wind velocity 31.0 m/s is used to transform the time period into the spatial length scale. Clearly, the spectrum of the large-scale structures (larger than 6.0 km) and small-scale ones (less than 3.0 km) show their own different behaviors. Specifically, the spectra of the small-scale structures caused by the convective and turbulent activities were characterized by a $k^{-5/3}$ power law dependence over the resolved spectral range (0.3 to 3.0-4.0 km), whereas a steeper power spectral slope k^{-3} can be found over the large-scale range (4.0 to 10.0-20.0 km). A -5/3 slope would be consistent with the presence of three-dimensional isotropic turbulence, as in the inertial subrange. However, in the fully stratified and stable flow, a -5/3 power can be associated with the upscale energy transfer in stratified turbulence resulting in two-dimensional horizontal mesoscale eddies (Gage 1979; Lilly 1983). Given the stable thermal stratification near the tropopause, the -5/3 spectral dependence can be associated with intermediate quasi-two-dimensional turbulence (Starr and Gultepe 1995). Therefore, the upscale energy transport originating from the small scale or three-dimensional turbulence by the quasi-two-dimensional turbulence may be responsible for the existence of these MUCs.

The different behaviors of the spectrum slope over the large-scale structures and small-scale ones allow for using the DWT methods to separate these two different structures from the whole cloud systems. Indicated in Fig.6.8, there is a “gap” between

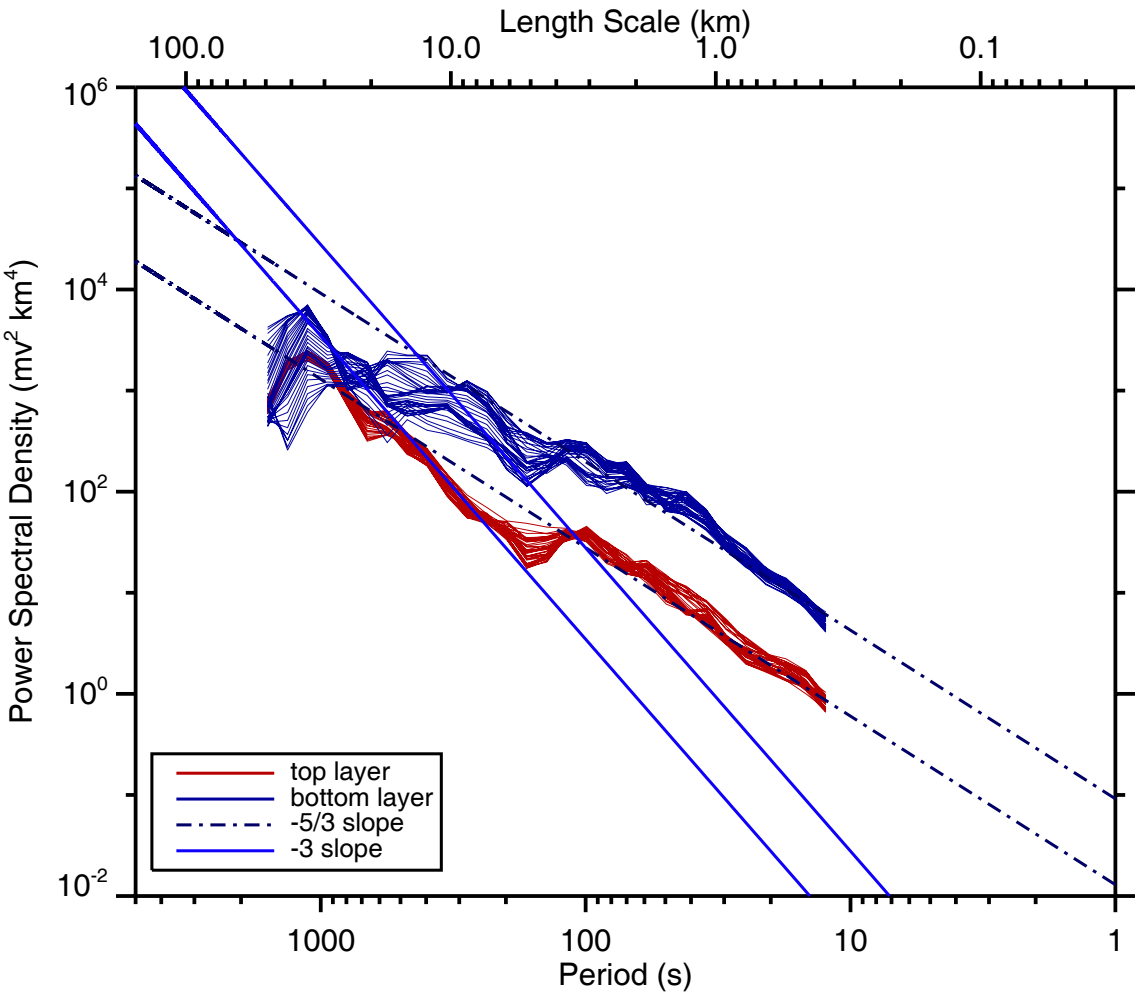

FIG. 6.8. The global wavelet spectra of the signals from the cloud top layer and bottom layer.

100.0-200.0 seconds in time periods or 4.0-6.0 km in length scale. Since the discrete wavelet coefficients change as the logarithmic scale based on two, the closest length scale 4.4 km (140.6 seconds) at the sixth level coefficient is chosen as the intermediate length scale to separate two different structures. Just as discussed in section 6.2, one can make two filters using the discrete wavelet coefficients. One just keeps the coefficients larger than the intermediate length scale while the other just keeps the coefficients at the small scales. Then, the inverse DWT is operated to reconstruct these two different images. The reconstructed images by the DWT filter have been presented in Fig.6.9. Fig. 6.9a shows the lidar backscattered power extracted at the height 11.185 km (has been used in CWT analysis shown in Fig. 6.7), the decomposed large scale party (indicated by red line) and small scale party (indicated by blue line). Then, the decomposed signals at every height are combined together to make a new contour image, respectively, shown in Fig. 6.9b and c. It should be noted that only the positive contour at the level indicated by the dot line in Fig. 6.9a are shown because the negative part just represents the signal variability and cannot reflect the real cirrus structures.

Fig. 6.9b represents the structures larger than 4.4 km, which can be classified into the mesoscale range. Importantly, the top and bottom cirrus layers show the different structures because of their own environmental characteristics. Since there is no strong wind shear at 12.6-13.2 km, the top layer shows the stratiform structures though there are still some cells embedded in. However, the apparent cell structures can be found in the bottom layers, including the MUCs (the length scale 30.0-40.0 km) at 1910-1945 UTC and five cell structures (the length scale 7.0-8.0 km) caused by the cumulative effects of

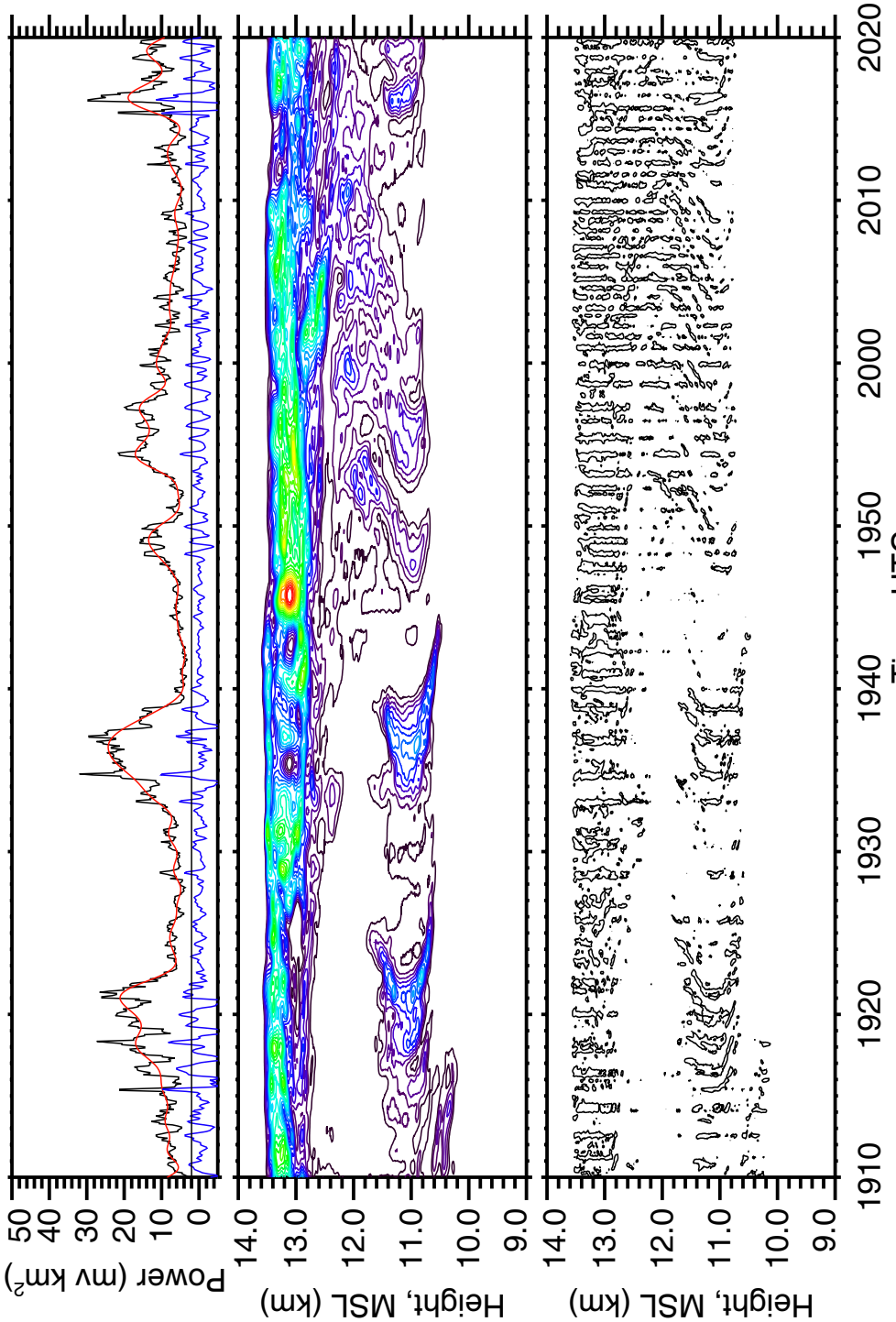

FIG. 6.9. The images reconstructed by performing the DWT-based decomposition method including the large scale part (middle) and small scale part (bottom). The top plots shows the lidar backscattered power extracted at the height 11.185 km (used for CWT analysis in Fig. 6.7), the decomposed large scale party (indicated by red line) and small scale party (indicated by blue line). Note that the contour at the value 2.0 mv km^2 is shown in the middle plot, which are indicated by the black straight line.

moistening associated with evaporation of crystals falling from the top layer (Starr and Cox 1985a). In their numerical simulations, Lin et al. (1998) showed that the amplitude of the mesoscale wave is the key parameter in determining the ice-crystals concentration number during the development and formation of the cirrus clouds. There are still many observational facts that the gravity waves occurring near the tropopause play an important role in the dynamical process in cirrus (e.g., Sassen et al. 1989; Starr et al. 1992; Gultepe and Starr 1995; Demoz et al. 1998). Therefore, these structures with the length scale tens kilometers occurring in the stable environment can be caused by the gravity waves. Fig. 6.9c shows the contour with the value 2.0 mv km^2 of the scale less than 4.4 km, which can be thought as the cloud scale structures caused by the convective and turbulent activities (Gu and Liao 2003). These cloud-scale structures both are embedded in the top and bottom layers except that the ones in the bottom layers represent arc shapes due to the strong with shear from 10.4-12.2 km. Especially from 1910 to 1945 UTC in the bottom layer, these cloud-scale structures combine together in every mesoscale structure, which are named Meoscale Uncinus Complexes proposed by Sassen et al. (1989).

6.3.4 Discussion and Conclusion

A case study of typical uncinus cirrus has been presented in this chapter. Disclosed by the satellite imageries, the weather system associated with this uncinus case can be characterized to a warm front process. The uncinus clouds captured by the FARS active remote sensors were just located in the edge of the warm front. The NCEP reanalysis and radiosonde data are used to reveal the environmental condition of this case.

The cirrus clouds were located just below the level of the relatively weak subtropical jet stream core with a maximum wind speed 35.0 m/s. Therefore, a stronger wind shear existed in the lower part of cirrus layer than in the upper part, which indicates the different environmental condition in this case. From the thermodynamic view, the cirrus layer was located in the stable layer of the upper troposphere (10.0-13.2 km) and transition areas from the troposphere to stratosphere (13.2-13.6 km). Therefore, this cirrus case can be classified into the type of high and cold cirrus in a stable layer that is associated with elevated tropaopause and typically extends into the lowermost stratosphere (Sassen et al. 1998; Liu et al. 2003). In addition, disclosed by the LDR values, the homogeneously frozen sulfuric acid droplets of stratospheric/volcanic origin can probably effect on cirrus ice particles nucleation and growth.

Disclosed by the CPL lidar data, the whole cloud structures can be characterized as two-layer cirrus occurring in the distinct dynamic environment, which can be caused by the cumulative effects of moistening associated with evaporation of crystals falling from the overlaying layer together with the tendency toward unstable thermal stratification arising from the vertical pattern of sublimation cooling (Starr and Cox 1985a). The top layers looked more uniform, though the small-scale cells are still can be found. Importantly, a series of mesoscale uncinus complexes (MUCs) developed in the lower cirrus layer, which is the characteristic mesoscale structure with 10-100 km scale of with the similar uncinus shape but composed by ~1km individual uncinus cells (Sassen et al. 1989). The continuous wavelet-transform methods are used to characterize the length scale of these MUC structures. According to the local wavelet powers, the

individual uncinus cells embedded in every single MUC have the length scale 1.0-4.0 km, which is consistent with the previous observational facts by others that the width of the uncinus cell head is on the order of 1.0 km (Heymsfield 1975b; Sassen et al. 1989; Sassen 2002). The MUC structures are on the scale of 30.0-40.0 km probably caused by the gravity waves. Checking the global wavelet power of the horizontal lidar returned power, one finds that the large-scale structures (larger than 6.0 km) and small-scale ones (less than 3.0 km) show different behaviors. Specifically, the spectra of the small-scale structures caused by the convective and turbulent activities were characterized by a $k^{-5/3}$ power law dependence over the resolved spectral range (0.3 to 3.0-4.0 km), whereas a steeper power spectral slope k^{-3} can be found over the large-scale range (4.0 to 10.0-20.0 km). One can speculate that these cloud-scale structures can be associated with two-dimensional horizontal mesoscale eddies, which may be responsible for the existence of these MUC structures by the upscale energy transport originating from the small-scale or three-dimensional turbulence. Therefore, it is suggested that future model simulations should consider the mechanism of the two-dimensional eddies.

The scale decomposition methods based on the DWT are successfully developed, which have ability to decompose the high resolution PDL backscattered power image into two parts including the mesoscale and cloud scale structures respectively. Compared with other methods, the wavelet spectra have the time-scale localization property in the sense. Therefore, the reconstructed signal using the wavelet spectra can effectively highlight the cirrus structures, which often coexist with the different length scale in the one system. By choosing the intermediate length scale, the lidar backscattered power image is separated

into two parts: the mesoscale part and cloud-scale part. In the image containing the mesoscale structures, the top layer shows the stratiform structures whereas the apparent gravity cell structures can be found in the bottom layers. In the images just including the cloud-scale information, the cloud-scale structures caused by the convective and turbulent activities both are embedded in the top and bottom layer except that the ones in the bottom layers represent arc shapes due to the strong wind shear from 10.4-12.2 km. Thus, this method can be applied into the lidar image processing in the cirrus structure study.

CHAPTER 7

CLIMATOLOGY OF CIRRUS HORIZONTAL INHOMOGENEOUS STRUCTUAL PROPERTIES

7.1 Introduction

The cloud inhomogeneous properties are generally categorized into vertical inhomogeneities and horizontal inhomogeneities. The former can be quantitatively described by the parameters with respect to cloud overlap (e.g., Tian and Curry 1989; Mace and Benson 2001), while the latter is characterized by the cloud fraction (e.g., Teixeira 2001; Astin and Di Girolamo 2003) and the subgrid horizontal variability of cloud properties (e.g., Gollmer et al. 1995). The horizontal inhomogeneous structural properties discussed here are limited to the subgrid horizontal variability of clouds. From the physical view, the cloud inhomegeneous properties can be represented by the microphysical properties such as IWC/LWC or IWP/LWP (e.g, Gollmer et al. 1995; Marshak et al. 1997) or radiative properties, e.g. optical depth (e.g, Pincus et al. 1999; Carlin et al. 2002). In the statistical sense, the exact description of the variability for a physical quantities depends on not only the one-point statistics (the mean and variance of the quantity's distribution) but also the two-point statistics (how it varies with a change in spatial scale) (Cahalan 1994a ; Gollmer et al. 1995). To address the first kind of question there are many efforts for parameterization of optical depth variability based on cloud

type (Pincus et al. 1999), cloud fraction (Barker et al. 1996), mean optical thickness (Oreopoulos and Davies 1998b), ice water path and optical depth (Carlin et al. 2002), and cloud layer thickness and layer mean temperature (Mace 2002). Recent efforts to the study of the second kind of question have become the popular topic in the cloud research community since Lovejoy (1982) firstly connected the cloud filed with the fractal concept (e.g., Cahalan and Joseph 1989; Cahalan 1994a; Gollmer et al. 1995). However, these studies were just based on a limited dataset and not enough to provide the basic observational facts.

As discussed in the Chapter one, the horizontal inhomogeneous properties of clouds play a key factor for the radaitive calculation both in the climate model (Cahalan 1994; Liou and Rao 1996; Gu and Liou 2001; Fu et al. 2000; Pomroy et al. 2000; Carlin et al. 2002) and remote sensing cloud properties (Marshak et al. 1995; Loeb and Davies, 1996; Oreopoulos and Davies 1998a, b; Loeb and Coakley 1998; Chambers et al. 2001; Várnai and Marshak 2001; Iwabuchi and Hayasaka 2002; Várnai and Marshak 2002). As one of the major unsolved cloud types in climate system, cirrus clouds have the complicated structures, irregular geometric shapes, and various spatial patterns (Lynch 2002; Sassen 2002). Thus, their horizontal inhomogeneous properties should be deeply understood in order to improve the cloud parameterization in climate models and the space-based retrieval algorithms. Lidar, one of the modern effective remote sensors, is ideally suited to research cirrus inhomogeneous properties because of the great sensitivity of light scattering to the presence of ice crystals, thereby having the ability to capture the fine structures of cirrus clouds (Sassen 1991; Platt 1994; Sassen and Mace 2002).

Furthermore, at the FARS in the University of Utah, Sassen with his colleagues have collected fourteen year high cloud data beginning from 1987 using lidar and other groundbased instruments (Sassen et al. 2001). Because of their longtime duration and high resolution, it is possible to derive the climatology characteristics of the midlatitude cirrus horizontal inhomogeneous properties from the lidar backscattered power data, the proxies of the real cirrus clouds.

Using the uniquely extended FARS high cloud dataset, Sassen and Campbell (2001) examined the macrophysical properties of high clouds by developing a climatology of cirrus cloud heights and temperatures and characterized the synoptic weather patterns responsible for the cirrus; Sassen and Benson (2001) analyzed the linear depolarization ratios (LDR) in term of cirrus cloud microphysical content and revealed fundamental distinctions in cirrus cloud particle properties that vary with temperature and probably geographical location; Sassen and Comstock (2001) used the combined lidar and infrared radiometer (LIRAD) method to derive the radiative properties of cirrus clouds including the visible optical depths and infrared layer emittance; and Sassen et al. (2003) characterized the occurrence of optical displays including halo, arc, and corona according to their appearance, longevity, and the meteorological source of cirrus. As an additional part of this series of research using the extended time observations of cirrus clouds from the FARS, the climatology of the cirrus horizontal inhomogeneous properties will be developed by analyzing the lidar backscattered power data, the proxy of the true clouds. The final purpose of this part is to answer the following questions: Are cirrus clouds homogeneous? If not, do they distribute with the spatial length scale feature or

not? What suggestions can one provide to model researches about cloud inhomogeneities?

This chapter is organized as follows. First, cloud inhomogeneous properties with periodic features have been examined based on the wavelet transform results. The methods are introduced in section two. The classification of the FARS data will be discussed in section three, the statistical results are presented in section four. Secondly, the properties of cirrus clouds containing aperiodic structures are discussed on section five. This chapter concludes with section six

7.2 Methods

The procedures to derive the cirrus inhomogeneous properties from the horizontal lidar backscattered power are shown in the illustrative flow chart of Fig.7.1. Five steps are mainly involved in the algorithms including: 1) preliminary data processing; 2) cloud boundary detection; 3) wavelet transform; 4) confidence testing, and 5) combination of the data. In addition, the mean horizontal wind velocity from cloud base to cloud top measured by the radiosonde is used to transfer the time period into the length scale. In the following, the cirrus case observed by the FARS CPL system on 17 October 1992 is chosen as an example to show the data analysis methods step by step. Fig.7.2 gives a time-height display of the original data including the lidar backscatterings (based on logarithmic grayscale) and the linear depolarization ratio (indicated by the color bar) with the 7.5 m sample rate and the 12 second horizontal resolution. The radiosonde data at 0000 UTC on 17 October 1992 also are given on the right. Clearly, particularly on the right, the series of the MUC structures probably caused by the gravity waves in the upper

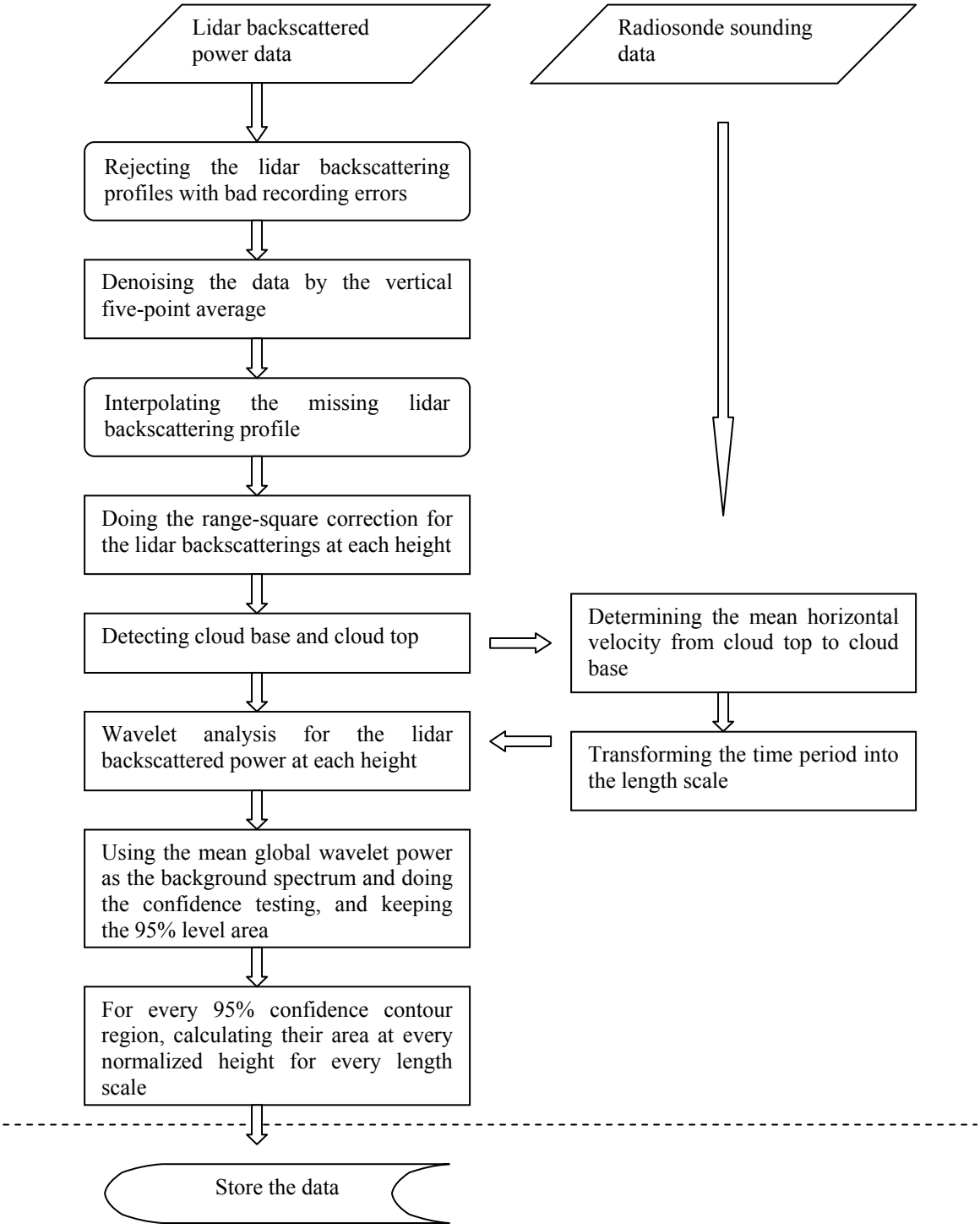

FIG.7.1. Flow chart to illustrate how the lidar backscattered power is processed to derive the inhomogeneous properties of cirrus clouds.

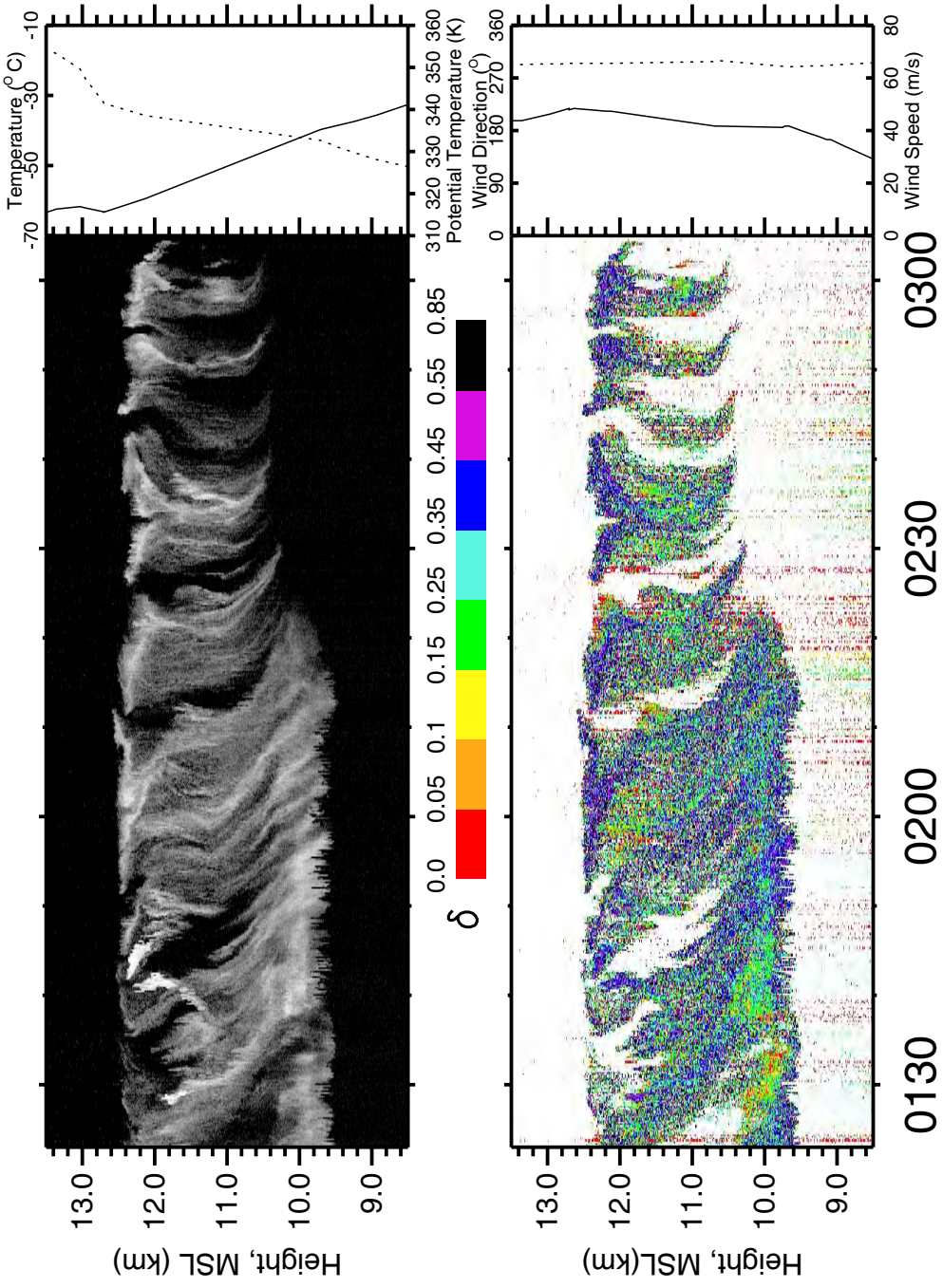

FIG. 7.2. Backscattered energy based on logarithmic grayscale and the linear depolarization ratio (LDR) indicated by the color table observed on Oct 17 1992 by the FARS CPL system. The radiosonde data are given on the right including the temperature, potential temperature, and wind velocity and direction profile.

troposphere are presented (Sassen et al. 1989; Sassen 2002), with each cloud-top generating region producing a sheared mesoscale fallstreak. From 0140 to 0210 UTC, the cirrus cloud mammata-like structures can be found at the cloud base. Also note that three embedded aircraft contrails at an altitude of ~12.0 km are revealed by the strongly scattering streaks near the beginning of the period. As the typical cirrus case, the tendency of the linear depolarization has larger values near the cloud top (ice-crystal growth) and decreasing values below (at the warmer temperatures) (Sassen 2000).

7.2.1 Data preliminary processing and cloud boundary detection

Since the procedures of data preliminary processing have been fully discussed in Chapter three, here just a brief description is given. First, after rejecting the profiles with recording errors, the lidar backscattered power profiles are saved at each time moment. Then, the white noise is smoothed by performing the five-point average in the altitude direction. Third, the linear interpolation method is used to fill the missing profile from the neighboring points at the same height. Finally, the data at each height are transformed into the range square corrected backscattered power and then put into the wavelet transform algorithms. In addition, in order to calculate the average horizontal wind velocity from cloud base to top, the cloud boundary values are needed. Fortunately, the universal cloud detection algorithms have been successfully developed to detect cloud base and top from the lidar backscattering and radar reflectivity profile in the FARS (Wang and Sassen 2001).

Figure 7.3 shows the lidar backscattered power image (based on the logarithmic grayscale) after the preliminary processing and the cloud base and top retrieved by the

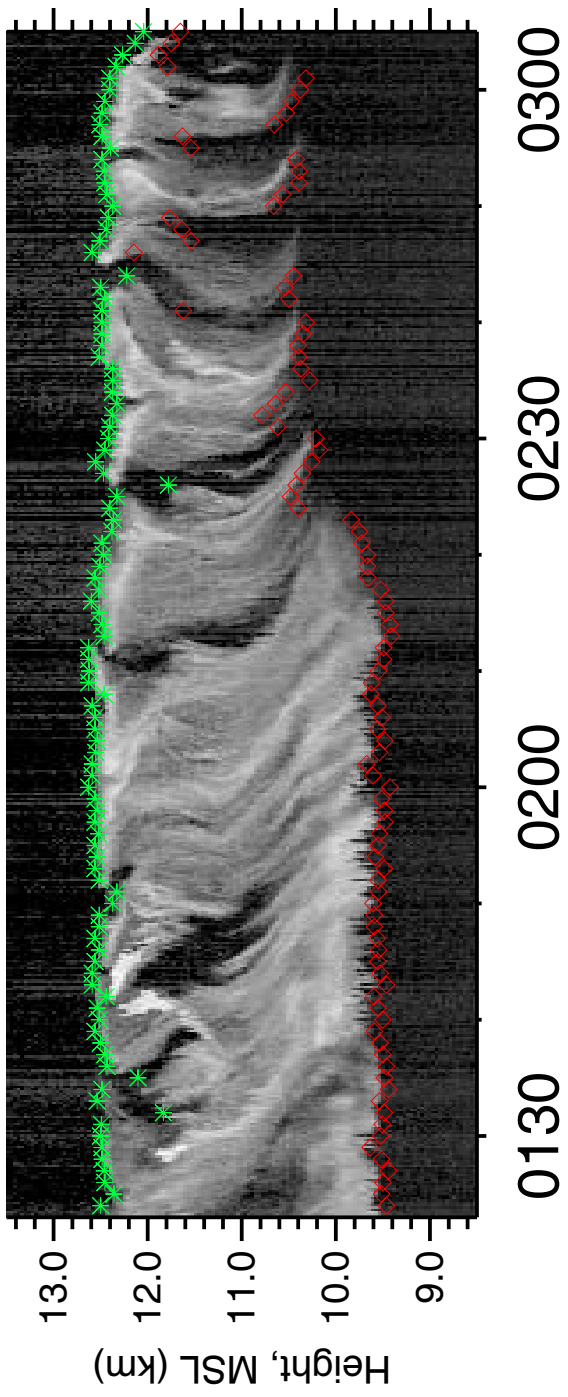

FIG. 7.3. Lidar backscattered power image (based on the logarithmic grayscale) after the preliminary processing and the cloud base (red) and top (green) retrieved by the FARS universal cloud detection algorithms.

FARS universal cloud detection algorithms. The image looks much smoother than the original one due to the five-point average in the altitude direction (the vertical resolution is decreased to 37.5 m). The cloud-detection algorithms successfully retrieve the cloud boundary. Specifically, the cloud-base heights vary from 9.4 to 12.1 km with the mean value 10.0 km while the cloud top ranging 11.8-12.6 km has the mean value 12.5 km.

7.2.2 Wavelet transform and confidence testing

After the preliminary data processing, the range-corrected backscattered power data at each height are input into the CWT algorithms to calculate the wavelet spectrum. The detailed description of the wavelet transform can be referred to Chapter three. The Morlet wavelet function with the wavenumber w_0=6 is chosen as the "mother" wavelet function. By decomposing the lidar backscattering by the wavelet transform, one can construct a picture of the energy as a function of time, wavelet scale (or frequency), and corresponding height. The next step is to pick up the wavelet energy peaks that are more "significant" to reflect the cirrus structural information than others. To determine significant levels for either Fourier or wavelet spectra, the first step is to choose an appropriate background spectrum. By assuming that different realizations of the geophysical process will be randomly distributed above this mean or expected background, then one can compare the actual spectrum against this random distribution (Chatfield 1996). The null hypothesis is defined for the confidence testing of the wavelet power as follows: It is assumed that time series have a mean background power spectrum; if a peak in the wavelet power spectrum is significantly above this background spectrum, then it can be assumed to be a true feature with a certain percent confidence. Since it is

reasonable to assume that the wavelet coefficients are normally distributed above the background spectrum (Torrence and Compo 1998), the wavelet spectrum will be chi-square distributed with two degree of the freedom (Wilks 1995). Therefore, one can simplify the significance testing by using the chi-square distribution to determine the certain confidence level. Torrence and Compo (1998) gave a full discussion of the significance testing for the wavelet spectrum based on the above ideas.

The remaining question here is to choose the appropriate background spectrum that can be used for the significance testing. It has been found that, for many geophysical time series, their spectra have the features of "red noise", which has increasing power with decreasing frequency resulting in a negative slope of the power spectrum (Gilman et al. 1963). This type of noise can be explained in term of the slow-response components in the geophysical process providing a memory that effectively integrates the forcing of such fast-reponse and white noise-like components such as turbulence, which produces a temporal persistence that leads to great noise energy at lower frequencies. Percival (1995) showed that the global wavelet spectrum provides an unbiased and consistent estimation of the true power spectrum of a time series. Thus, it has been suggested that the global wavelet spectrum could provide a useful measure of the background spectrum, against which peaks in the local wavelet spectra could be tested (Torrence and Compo 1998). In addition, the time-averaged global wavelet spectrum also has the characteristics of "red noise" and thus can be treated as an appropriate background noise spectrum. In the methods applied here, all the global wavelet spectrum of the cloud backscattered returns are averaged as the background noise spectrum.

Figure 7.4 gives the time-averaged global wavelet spectrum power for the horizontal lidar backscatterings at each height from 9.0 to 13.0 km for the case of October 17 1992, which shows different characteristics with height. The global wavelet spectra between 9.53-12.57 km have a negative slope of the power spectrum ("red noise" features) because they reflect the cloud dynamical processes. Compared with them, the spectra above the cloud top (12.57-13.00 km) and below the cloud base (9.00-9.53 km) have the relatively flat slope due to the existence of "white noise" in the air molecule backscattering. Shown in Fig.7.4 by the red line, the mean global wavelet spectrum calculated from the cloud signal spectra is used as the background spectrum for the significance testing while the blue line is the 95% confidence level for the background spectrum according to the chi-square distribution with two degrees of the freedom. In other words, if the local wavelet power is stronger than the 95% confidence level indicated by the blue line, it is significantly above the background with a true feature with 95% confidence.

Figure 7.5 gives an example of the confidence testing results for the local wavelet power for the horizontal lidar backscattering power at 12.19 km. The mean horizontal wind velocity of 43.8 m/s from the mean cloud top to cloud base is used to transfer the time period into the length scale. The 95% confidence contours with the horizontal scale 30-50 km identify the mesoscale uncinus structures while ones with the scale 7-10 km indicate the internal cloud-scale structures, for example, the contrail streak at 0135-0150 UTC. The turbulent and convective activities at the cloud top are presented by the 95% contour area with 1-3 km length scale. Thus, the wavelet transform with the confidence

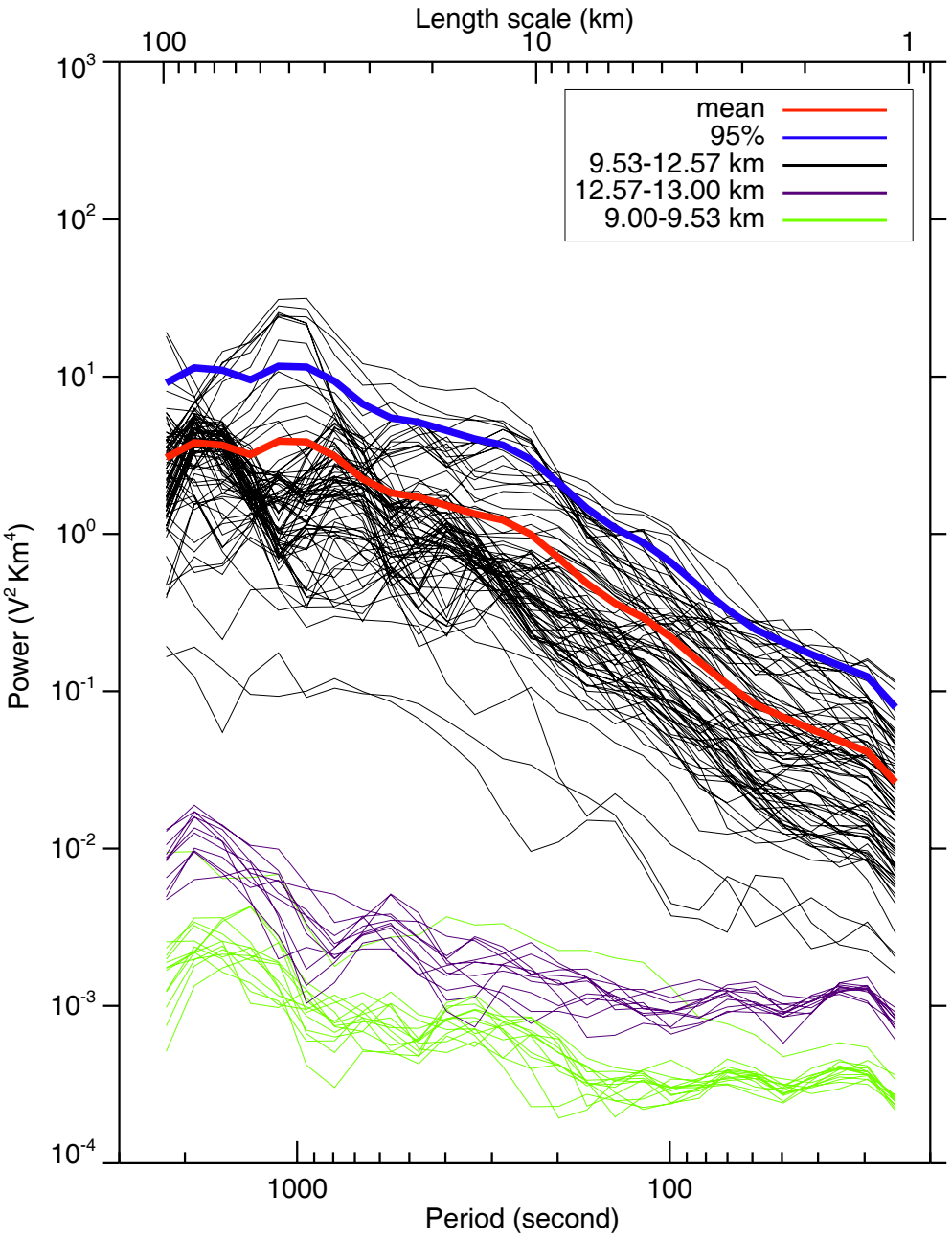

FIG. 7.4. The time-averaged global wavelet spectrum power for the horizontal lidar backscatterings at each height from 9.0 to 13.0 km for the case of Oct 17 1992. The mean global wavelet spectrum (red line) calculated from the cloud signal spectral is used as the background spectrum for the significance testing while the blue line is the 95% confidence level for the background spectrum according to the chi-square distribution with two degree of the freedom.

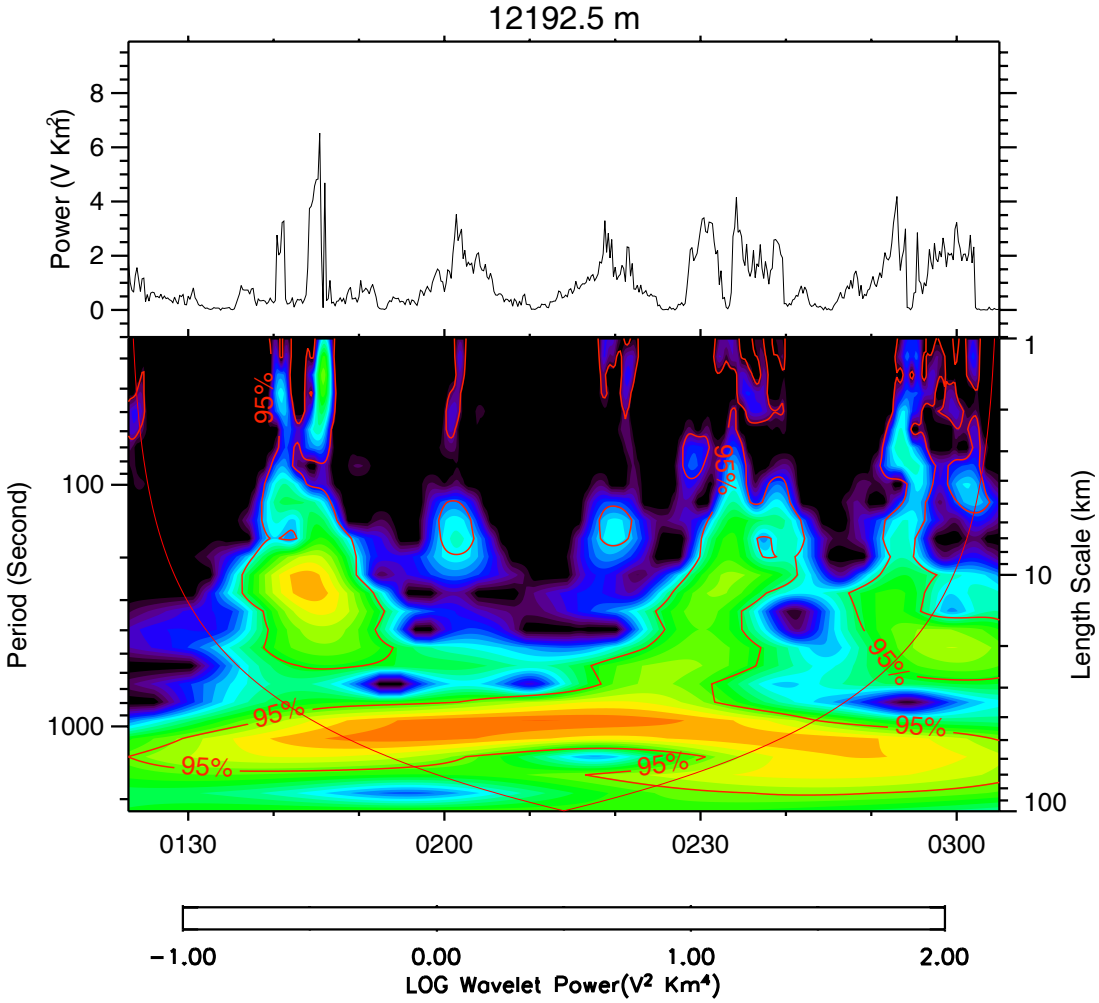

FIG. 7.5. Confidence testing results for the local wavelet spectrum (bottom) of the horizontal lidar range-square corrected backscatterings at 12.19 km (top). The region of the "cone of influence" is indicated by the red line.

testing can successfully and efficiently characterize the cloud structural variability by analyzing the lidar backscattering power.

7.2.3 Combination of the data

The wavelet spectrum with the 95% confidence contour is a function of time, length scale, and height. Whereas it can grasp the detailed information of the cirrus cloud structures, it is too redundant to display the "whole pictures" of cirrus inhomogeneous property distribution. Therefore, the wavelet transform results are simplified by calculating the percentage of how many points at every length scale fall in the 95% confidence level area in total "cone of influence" samples. Note that some wavelet power peaks are not counted because they completely fall out of the "cone of influence" so that they do not really reflect the real time series structure, though they are still above the 95% confidence level compared with the background spectrum. In other words, just the samples that fall in both the 95% confidence level and the area of "cone of influence" are surveyed.

Indicated by the color bar, the percentage distribution of the 95% confidence area as a function of the cloud height and the length scale is given in Fig.7.6. The top plot in Fig.7.6 shows the percentage of effective "cone of edge" points against the total samples at each length scale. The bottom shows that, in the total effective samples, how many samples in percentage are falling in 95% confidence level. The mesoscale structures with a length scale of 30-50 km, making up 70-100% of the "cone of edge" samples, are dominant near the cloud top. At the cloud base, the existence of the local maximum area with the length scale less than 5 km indicates the cirrus mammattus structures from 0140-

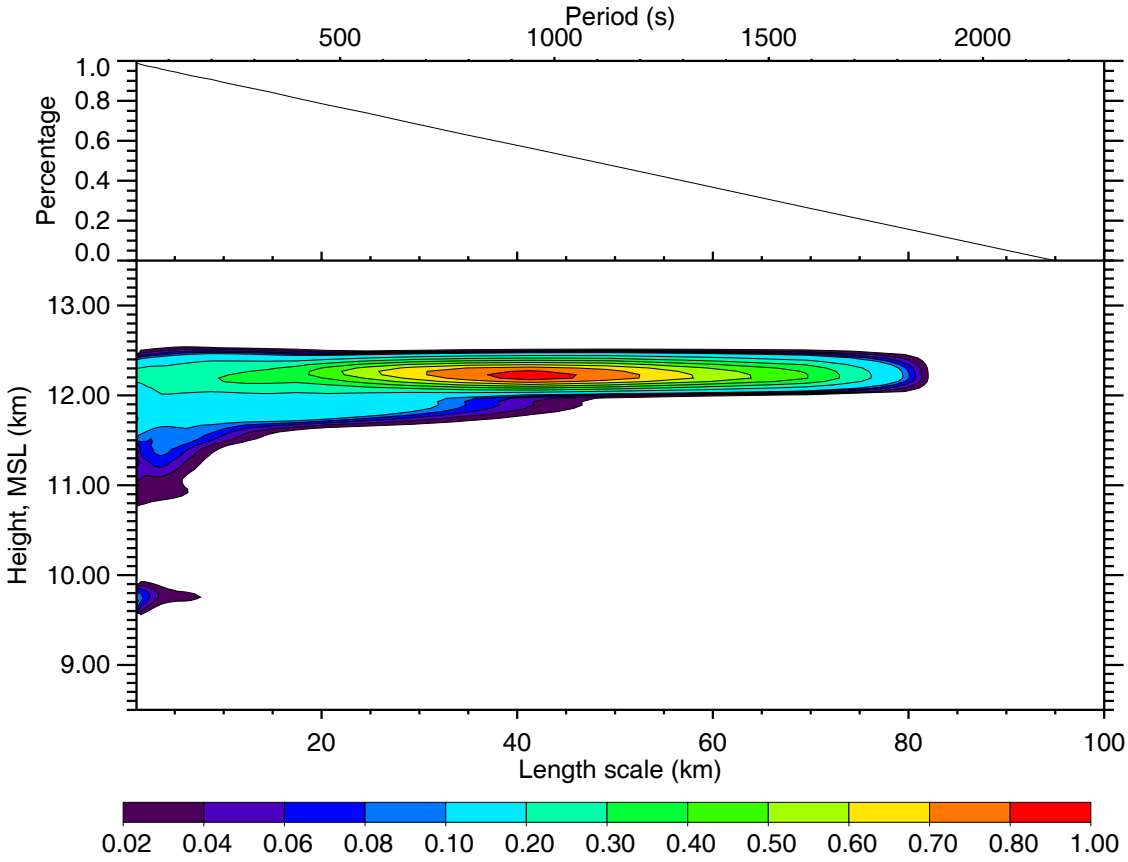

FIG. 7.6. The percentage of "cone of effective" points against the total samples at each length scale (top) and the percentage ratio of the 95% confidence area in the "cone of effective" points as a function of the length scale and cloud height (bottom).

0210 UTC. The cloud top has relatively stronger structural characteristics than the cloud base. This is because the cirrus ice crystals formed and grew in the cloud top and then fell in the warmer environments, resulting in stronger backscattered power at the cloud top.

7.2.4 Results of the other two cases

Here other two cases on October 6 1992 and March 29 2000 will be shown, to demonstrate the ability of the methods to identify cirrus structural characteristics. Given in Fig. 7.7, the first case observed on October 6 1992 can be classified into cirrostratus altocumulus-genitus (Sassen 2002), in which the small, strongly scattering, and nearly nondepolarizing cloud cells intermittently located on the top of the ice fallstreaks represent individual supercooled altocumulus cells. The ice virga produced by the altocumulus cells formed the series of ice fall streak cells that continued to resemble together and were ready to transit into cirrostratus. The mean wind velocity at the cloud area was 13.8 m/s and the wind direction kept around 270°. The percentage distribution of the 95% confidence area with the height and length scale is shown at the bottom of Fig. 7.7. The maximum areas making up 60-70% of the observational domain with the length scale 5.0-9.0 km located ~6.5 km represent the ice-fallstreak cells produced by the altocumulus cell. Note that at the cloud base of the height ~6.2 km, these structures also are apparent as the ice fell into the relatively drier and warmer environment and began to evaporate. The small-scale structures with length scale less than 1 km have more percentage in the mid-cloud than the cloud and top because the ice crystals grow quickly in the mid cloud resulting in the strong backscatterings.

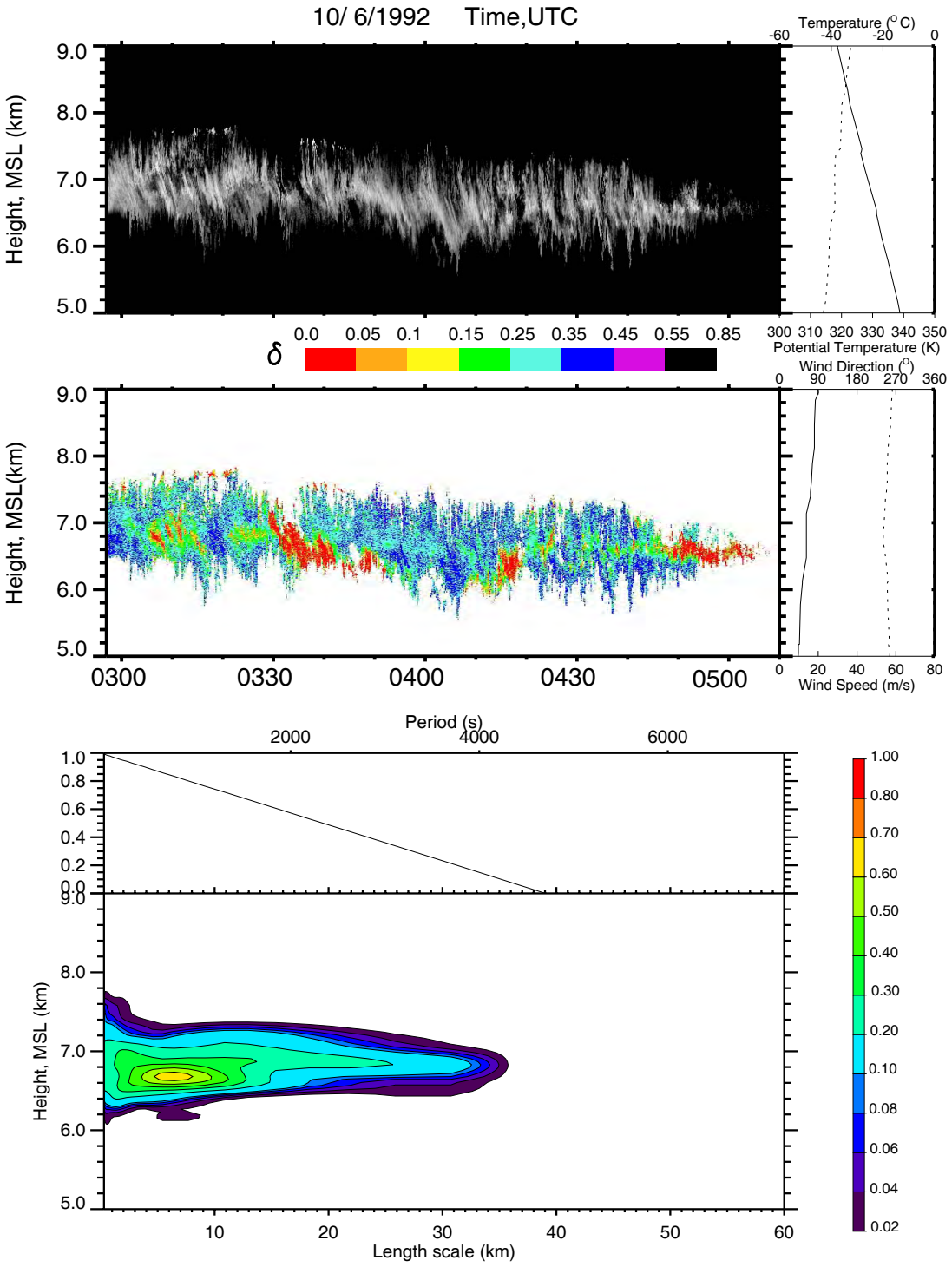

FIG. 7.7. The backscattered energy based on logarithmic grayscale (top) and the linear depolarization ratio indicated by the color table (middle) observed on Oct 6 1992 by the FARS CPL system. The radiosonde data at 0000 UTC on Oct 7 1992 also are given on the right. The percentage of points falling in "cone of effective" against total samples and the percentage distribution of the 95% confidence area as a function of the length scale and cloud height (bottom).

Shown in Fig. 7.8, the second case is typical for broken fibratus observed by the CPL system on March 29 2000. The linear depolarization has the value 0.15-0.25 from the cloud top to cloud base possibly because the falling ice crystals kept the similar orientation in the relatively weak shear environment (Sassen 2000). The lidar backscattered power image shows the cloud cellular patches at 7.0-8.0 km, which were generated by the regional upstream orographic waves according to the FARS observational notes (Sassen 2002). The percentage distribution of the 95% confidence area of the wavelet spectrum has a comparatively small value due to the short duration of cloud against the observation domain. The length scale 4.0-10.0 km is dominant in the upper cloud top region (7.5-8.0 km) whereas the structures with the smaller scale less than 2.0 km are noticeable at the cloud bottom area (7.4-7.0 km). This is because the cellular patches fell down to evaporate and then broke into the sharp streaks with much smaller length scale in the lower cloud region. Notice that the cloud base has wave-like form that can be signified by the area with the length scale 10.0-30.0 km. The area with the length scale larger than 30.0 km is unreliable due to the edge effects at the large-scale.

One can draw the following conclusions based on the above case studies. First, the methods have the ability to disclose cirrus structural distribution based on lidar backscatterings data and radiosonde data; therefore, it is possible to develop the climatology of the cirrus inhomogeneous properties with periodic features by analyzing a larger amount of data. Furthermore, these characteristics vary greatly with the cirrus generation mechanism and cloud vertical position that imply the importance of deriving the statistical cirrus inhomogeneous properties.

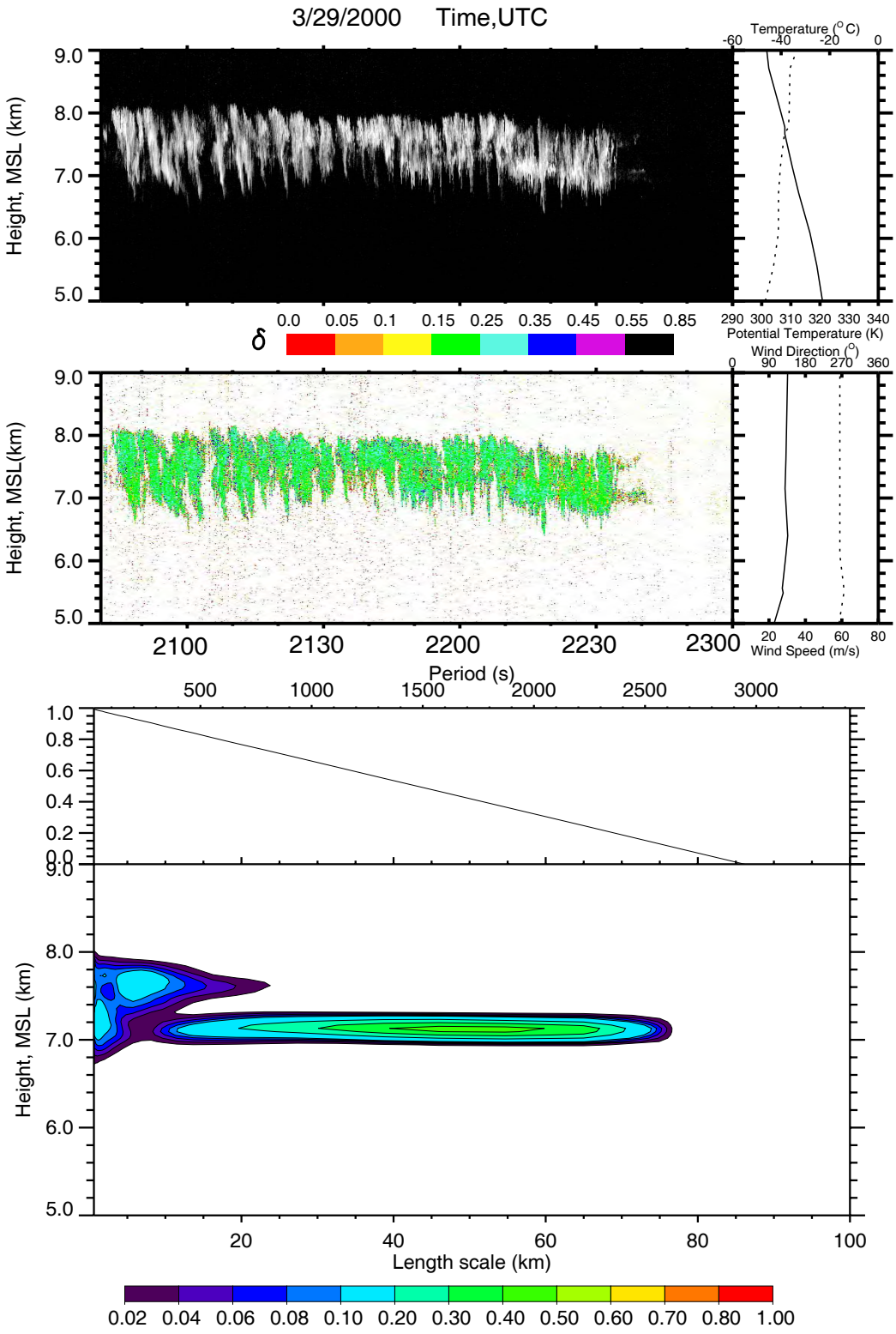

FIG. 7.8. Same as Fig. 7.7 but on Mar 29 2000.

7.3 Quality Classification of the FARS CPL High Cloud Dataset

In Chapter two, the basic review for the FARS 2,208 hour CPL high cloud data from 1992-2001 was given including the yearly, monthly and hourly breakdown and the classification based on cirrus generating mechanism. Since the algorithms are based on the continuous wavelet transform, the horizontal backscattering signal cannot be discrete in the observational duration. According to the data quality and algorithms requirements, the data are categorized into five different types as shown in Table 7.1. Type one contains all the data with the best quality though they miss backscattering profiles at some moment but does not affect on deriving cirrus inhomogeneous properties correctly. Sometimes the lidar is subject to significant attenuation in moderately thick cirrus though they are fortunately relatively uncommon in cirrus (Sassen and Mace 2002). This kind of data just can characterize the structures occurring at the cloud base area, but do not have the ability to disclose the inhomogeneous properties at the cloud top, which are put into category two. Additionally, a fraction of cirrus occurs in conjunction with liquid-phase clouds at lower level, which can completely extinguish the signal from a ground-based lidar. These data are classified into three types and cannot be used in this analysis. Category four includes all the data that are too noisy to be analyzed due to all kinds of reasons, for example, those with too short observational duration or bad quality. In addition to concentrate on the high cloud, some FARS data collected for the Asian dust and aerosol research are not involved in high clouds (Sassen et al. 2001), which are categorized into type five.

TABLE 7.1 Data classification based on the quality and algorithms requirements

Type number	Description
1	Best data quality
2	Some attenuation at cloud top but still can be used
3	Strong attenuation by lower clouds
4	Noisy data
5	Asian dust or aerosol data

The breakdown of the FARS CPL lidar data from 1992-2002 is given in Fig.7.9 based on the data quality. Since the FARS instrument were involved in the Vertical Transport and Mixing (VTMX) campaign that took place in the Salt Lake Valley in October 2000 (Doran et al. 2002), there are more observational data for boundary aerosols (type five) in 2000 than other years. The FARS observations ended in April, 2002. In total, there are 1382 hour data including 533 cases (Type one), 62.6% of total observations, which can be used for the wavelet analysis. The moderately thick cirrus cases that attenuate the laser beam occupy 8.9% (194.6 hours) of the total observations, which will be used to retrieve the structural information at the cloud base in future research. The remaining 29.2% (645.9 hours) of the observations are classified into type three, four or five due to all kinds of noisy problems, which will not be used in the analysis. Since the CPL lidar system is typically operated with 10 or 12 seconds time resolution with the typical three hour observational duration (Sassen et al. 2001), it is possible to derive the climatology of cirrus length scale distribution.

7.4 Analysis Results and Discussion

7.4.1 Detectable length scale range

For every case that belongs to type one, the cloud boundary value is present, the wind profile is extracted from the radiosonde data that is closest to the lidar observations, and the lidar backscatterings are put in at every layer into the algorithms based on wavelet analysis discussed in section two. For all 533 cases, each one outputs the length scale distribution with the height. Since each case has its own observation duration, it will affect the ability to detect the large-scale structures due to the edge effects of wavelet

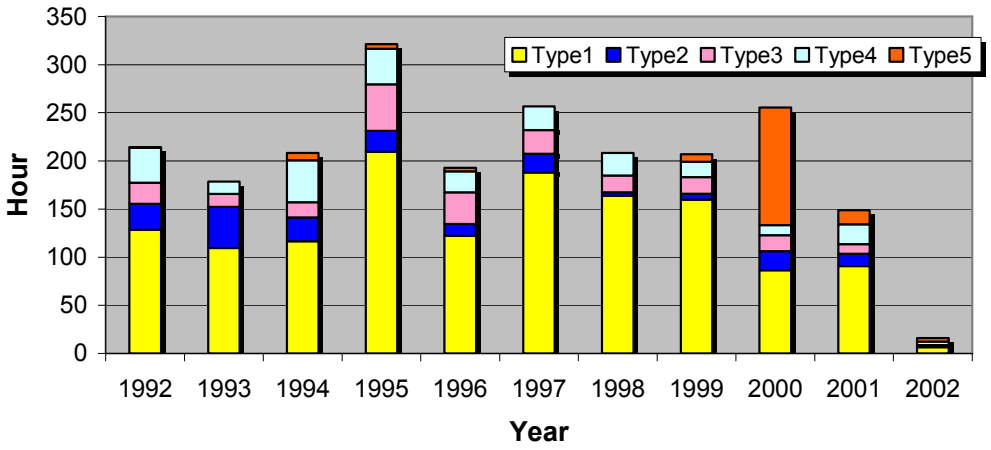

FIG.7.9. Breakdown of the FARS CPL lidar data from 1992-2000 based on the quality.

transform (Lau and Weng 1995; Torrence and Compo 1998). In addition, the transformation of length scale from the time to the space is also dependent on the mean horizontal wind velocity calculated from cloud base to cloud top. Therefore, it is necessary to first examine the effective length scale range that can be detected based on the FARS data and the analysis methods.

First, the statistics of cloud-boundary values and the mean horizontal wind velocity used for transform of time period are inspected. The mean cloud base and top derived from the universal cloud boundary algorithms (Wang and Sassen 2001) against the corresponding mean horizontal wind velocity within clouds is given in Fig. 7.10. The cloud top (blue symbol) varies from 6.0-14.0 km while the cloud base (red symbol) falls in the range 4.0-13.0 km. Most values of the mean horizontal wind velocity are located around 10.0-30.0 m/s. These results are consistent with Sassen and Campbell's (2002) results, in which they inspected the cirrus macroproperties and synoptic conditions using the FARS data during 1987-1999.

In addition to the mean horizontal wind speed, there are still two factors that limit the detection ability of the length scale: observational duration and temporal sample resolution. The temporal sample resolution for the FARS lidar observation is usually 10 or 12 seconds, while the observational duration ranges from 1-5 hours with the typical value of 3 hours (Sassen et al. 2001). In other words, the longer the observational duration, the more one can see the large scale structures. Thus, one needs to inspect the distribution of the sample horizontal points with the spatial length scale, by which one can check how many horizontal samples at each length scale for every case are falling in

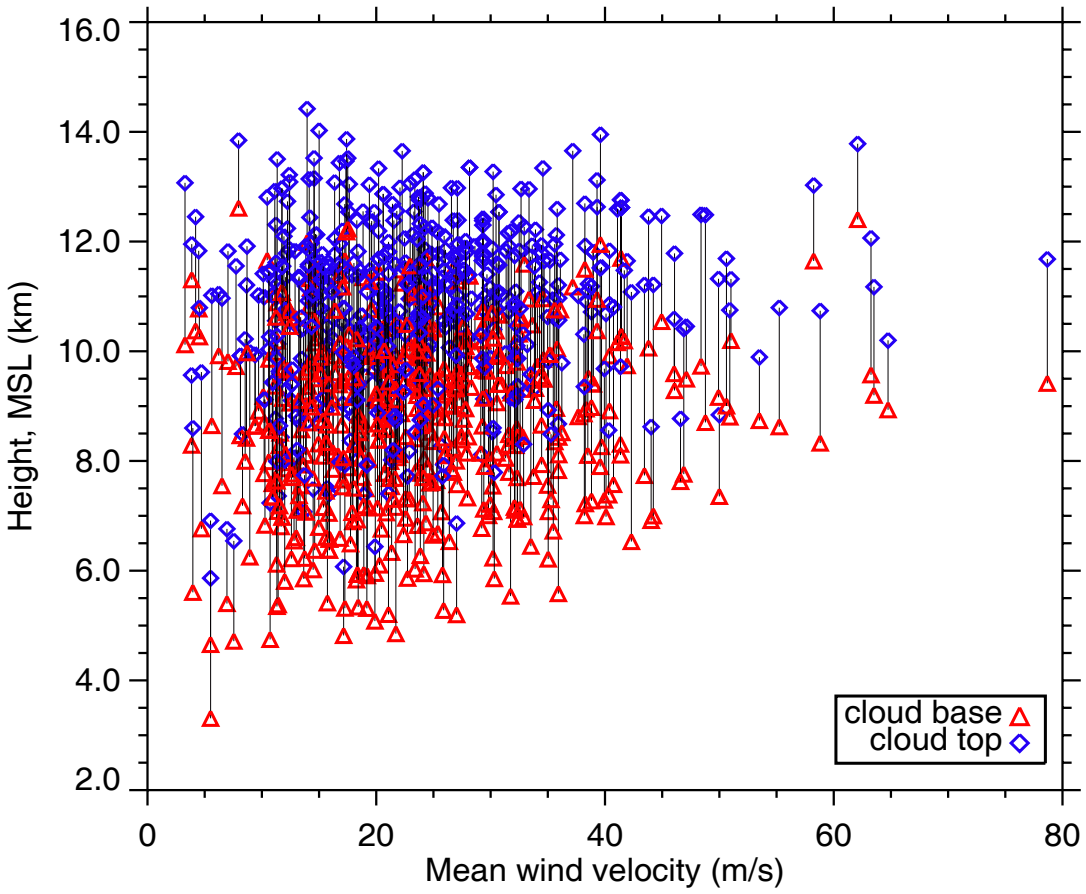

FIG.7.10. Mean cloud base and top derived from the universal cloud boundary algorithms against the corresponding mean horizontal wind velocity within clouds for all the cases used in this study.

the “cone of effects” (see Fig.7.5) that can effectively reflect the horizontal structural information. The number of effective sample points against the length scale for each case is presented in Fig.7.11. For every case, the effective sample points decrease with the length scale because the edge effects become important at the larger scale. Totally, the detection length scale varies from 0.07-1000.0 km but most of them are located in 0.5-100.0 km. In other words, the detectable length scale range in this research is limited at 0.5-100.0 km.

According to the physical mechanisms and theoretical consideration, the atmospheric motions can be classified into the following different scale: a) synoptic scale – for motions that are quai-geostrophic and hydrostatic; b) mesoscale – for motions which are nonquasi-geostrophic and hydrostatic; and c) microscale – for motions which are non-geostrophic, nonhydrostatic and turbulent (Thunis and Bornstein 1996). However, how to exactly distinguish these motions based on the spatial length scale does not form uniform definition (e.g., Orlanski 1975; Fujita 1981; Pielke 1984; Stull 1988). Specifically in this research, one categorize the cirrus structures into: a) synoptic scale: L >1000 km, b) transition scale from synoptic scale to mesoscale motion: 200km < L < 1000 km; c) mesoscale: 0.5 km < L < 200 km, and d) microscale: L<0.5 km, where L represents the horizontal scale of the cirrus structures. Based on this classification scheme, the FARS data have good ability to detect the mesoscale structures occurring within cirrus. In other words, the data can characterize the length scale distribution of cirrus internal structures revealed by the previous observations, which range from meters to hundreds of kilometers within cirrus clouds, such as turbulence, Kelvin-Helmholtz

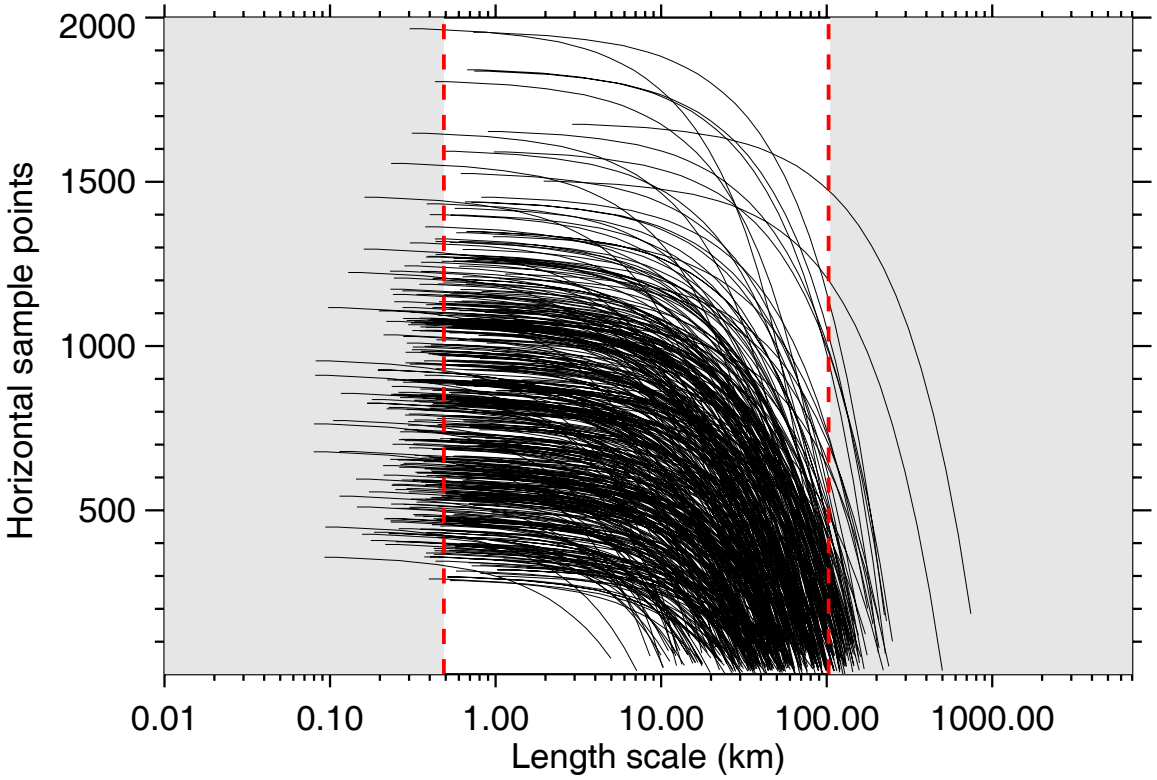

FIG.7.11. Effective sample points in the observational duration in each case that fall in the "cone of effects". The length scale varies from 0.07-1000.0 km but most of them fall in the range 0.5-100.0 km. It reveal that the detectable length scale based on the FARS dataset is 0.5-100.0 km, indicated by the red dash line.

(KH) instabilities, small scale cellular structures, convective cells, gravity waves, and Mesoscale Unicinus Complexes (MUC), and mammata (Heymsfield 1975; Auria and Campistron 1987; Sassen et al. 1989; Starr and Wylie 1990; Sassen et al. 1990; Grund and Eloranta 1990; Smith et al. 1990; Gultepe and Starr 1995; Gultepe et al. 1995; Sassen 1995; Sassen et al. 1995; Smith and Jonas 1996; Demoz et al. 1998; Sassen et al. 1998; Quante et al. 2002; Quante and Starr 2002; Sassen 2002; Sassen et al. 2002; Starr and Quante 2002; see Table 1.1).

7.4.2 Final results

Considering the large variability of real cloud boundary of the cirrus clouds occurring at the FARS site (Sassen and Campbell 2001), it is convenient to normalize the cloud altitude as the following definition:

$$H_{Normal} = \frac{h - base}{top - base} \times 100\% \tag{7.1}$$

where h is the actual altitude of each horizontal lidar backscatterings, *top* and *base* are the cloud base and top altitudes defined as the minimum/maximum altitude where the 95% confidence samples exceed 2% of the total observational samples. Then the results of each case are normalized on a regular grid at every preset length scale bin and normalized cloud height. Thus, one can combine all the data into one plot to show the statistical distribution of the cirrus inhomogeneous properties with the periodic features. Finally, shown in Fig. 7.12, the percentage ratio of the 95% confidence samples against the total samples is determined at each grid (every length scale and normalized height). In order to highlight the vertical distribution characteristics of cirrus structures, given on the right of

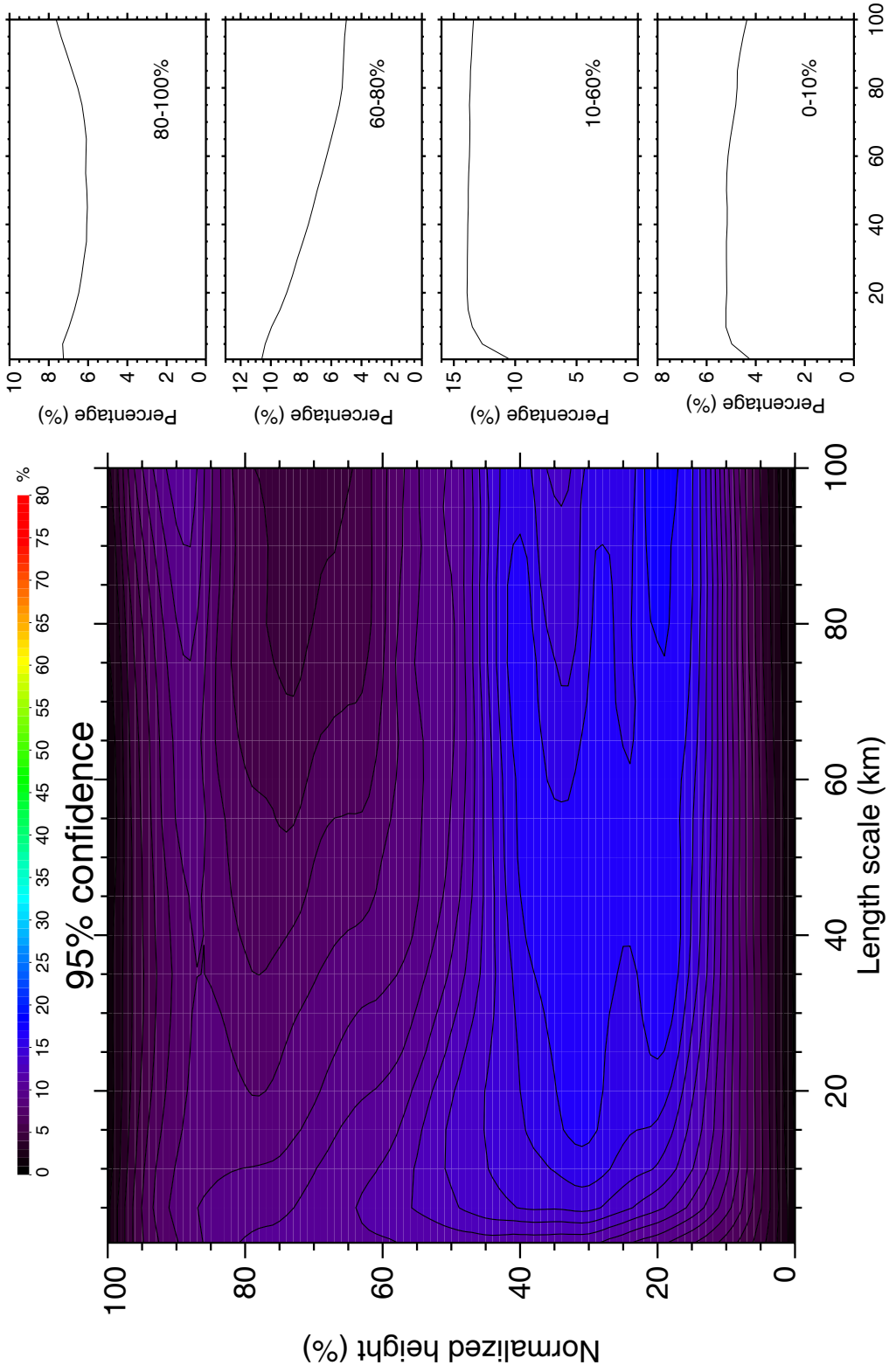

FIG. 7.12. Percentage ratio of the 95% confidence samples in the total samples varying with the normalized cloud height and length scale. From top to bottom on the left, respectively, the percentage ratios with the length scale are shown at the cloud top (80-100%), upper mid-cloud (60-80%), lower mid-cloud (10-60%), and cloud base (0-10%).

Fig. 7.12, the average percentage value is derived at different cloud regions based on the normalized cloud height H_n: 1) cloud top where $H_n > 80\%$; 2) upper mid-cloud where $60\% < H_n \leq 80\%$; 3) lower mid-cloud region where $10\% < H_n \leq 60\%$, and 4) cloud base where $H_n \leq 10\%$.

Fig. 7.12 shows that the mesoscale structures at the range 20-100 km are dominant in the lower mid cloud while the structures with the length scale smaller than 10 km concentrate in the upper mid-cloud. Possible mechanisms generating cirrus mesoscale structures can be classified into the following types: 1) gravity waves forced by wind shear, synoptic-scale weather disturbances, thunderstorm convections, and orographic effects (e.g., Sassen et al. 1989; Starr et al. 1992; Smith and Jonas 1996; Demoz et al. 1998; Sassen 2002); 2) energy transfer from either synoptic scale or small scale motions, for example MUCs (Smith et al. 1990; Quante and Starr 2002; Starr and Quante 2002); 3) instabilities occurring on the mesoscale, such as baroclinic, barotropic, and convective instability (e.g., Gultepe and Starr 1995); and 4) interaction of cloud microphysics and dynamics, for example, cirrus fallstreaks (e.g., Sassen et al. 1998). It should be noted that these mechanisms often interact and coexist in the same cirrus cloud system so that it is not easy to distinguish them. The possible reason why these mesoscale structures are located in the mid-cloud area is most of midlatitude clouds cirrus are generated by the top-down mechanism - cirrus clouds typically form from the cloud top (where the particle generation occurs) and grow with the particle sedimentation process, resulting in more mesoscale structures generated in the mid-cloud region when interacting with the evaporation processes (Starr and Cox 1985a; Sassen 2002). Since the

cloud base and top vary extremely in the FARS observations, it does not show the apparent characteristics in the cloud base and top region.

In order to exactly derive the vertical distribution of cirrus horizontal structures, especially in the cloud top and base region, it simplifies the question to pick up the cases with relatively small variability of cloud boundaries. Totally, 309 cases with the even cloud boundaries (60% of the whole dataset) are found. Same as Fig. 7.12, the percentage ratio of 95% confidence samples in total samples is shown as a function of length scale and normalized height in Fig. 7.13. Besides the mesoscale structures occurring in the mid-cloud region shown in Fig. 7.12, the distinct features exist in the cloud top and base region from Fig. 7.13. At the cloud top, the percentage of 95% confidence samples have high values at the length scale less than 10 km, indicating the cirrus generating cells occurring the cloud top area (Ludlam 1948, 1956, 1980; Harimaya 1968; Yagi et al. 1968; Yagi 1969; Heymsfield 1975a, b, c; Sassen et al. 1989; Sassen 2002). The peak with length scale ~5 km at the cloud base can be thought as the cirrus mammatus structures (Scorer 1953, 1973, 1997; Sassen 2002; Jo et al 2003), which have been fully studied in Chapter five. Importantly, the results disclose that cirrus clouds do not homogeneously distribute with internal vertical position.

The cloud field distributes in the space in three ways: 1) homogeneously; 2) inhomogeneously with periodic features; and 3) inhomogeneously without periodic features. In common sense, most of clouds inhomogeneously distribute in the space. If averaging Fig. 7.12 or Fig. 7.13 from cloud base to cloud top, ~10% of the total samples have apparent periodic features and fall in 95% confidence level. It implies that the cirrus

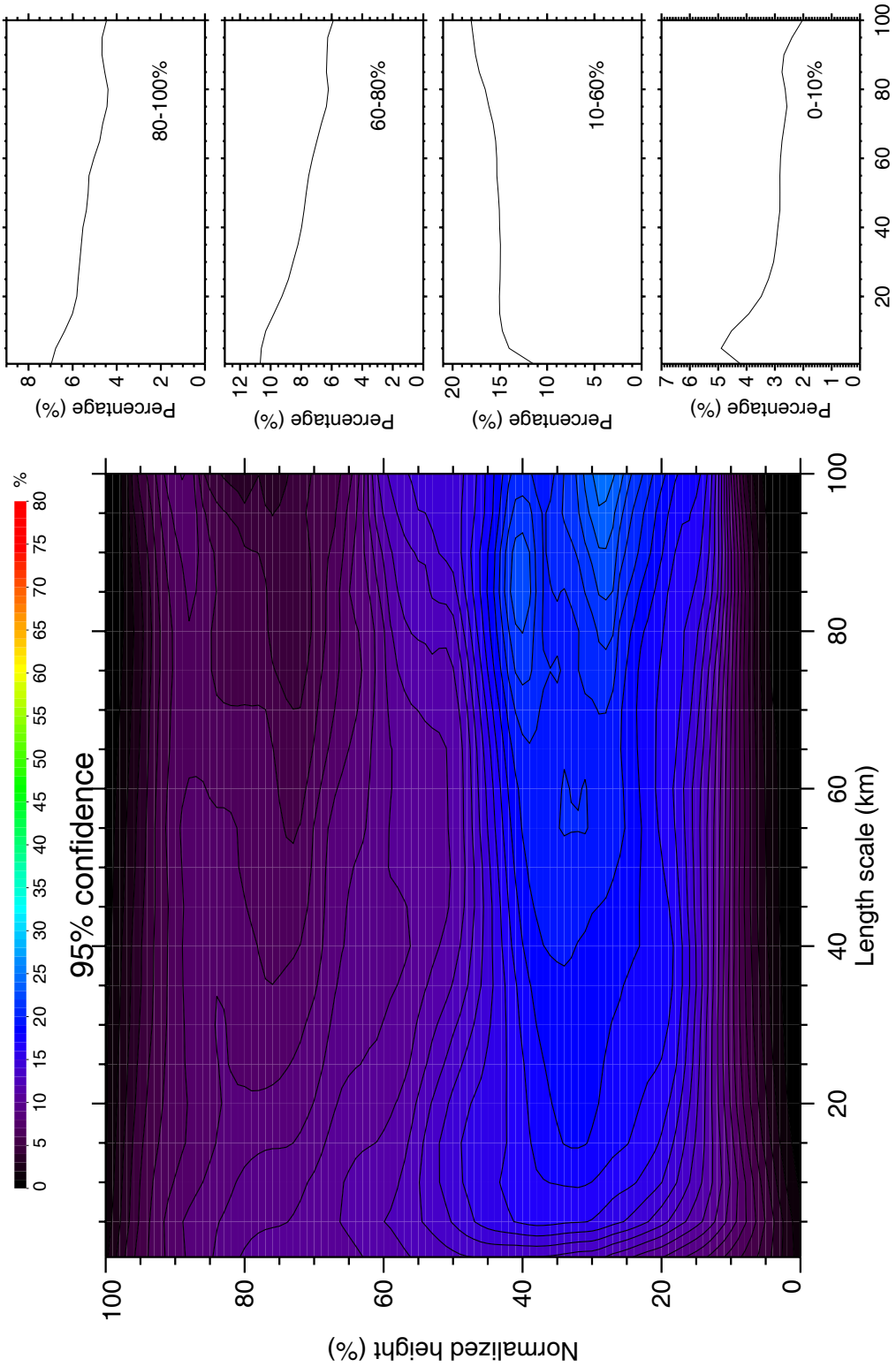

FIG. 7.13. The same as Fig. 7.12, but from the cases with even cloud top and base.

cloud inhomogeneous properties are dominant with aperiodic structures. In the next section, the analysis will be extended to the cirrus inhomogeneous properties without periodic features.

7.4.3 Sensitive test

Just like any confidence test, the 95% confidence level implies that for a random time series, 5% of the points will be above that threshold just by chance. By assuming the mean global wavelet spectrum as the background, our methods only pick up the sharp peaks and ignore the broad ones from the wavelet energy spectrum. In other words, our analysis only surveys the cirrus structures with the strong periodic features. Therefore, it is interesting to see how the final results change if we lower the confidence level. Fig. 7.14, Fig. 7.15, Fig. 7.16, and Fig. 7.17 present the vertical distribution of cirrus periodic structures when 90%, 80%, 70%, and 50% confidence level is chosen.

In the statistical sense, lowering confidence level is equivalent to expand interval level of energy peak. Thus, it is reasonable that the percentage values get larger when the confidence level is decreased, just as shown in Fig. 7.13-7.17. Comparing these four plots, all reveal a maximum region of mesoscale structures with a length scale of 40-100.0 km located in the lower mid-cloud region. It indicates that the mesoscale structures are dominant in the periodic structures thus are not sensitive to the values of confidence level.

However, the plots with 80% and 90% confidence levels chosen (Fig. 7.14 and Fig. 7.15) still show the maximum peak with the length scale less than 10 km while they disappear on the 70% and 50% confidence levels plots (Fig. 7.16 and Fig. 7.17). In other words, the small scale structures occurring at the cloud base and top region are sensitive

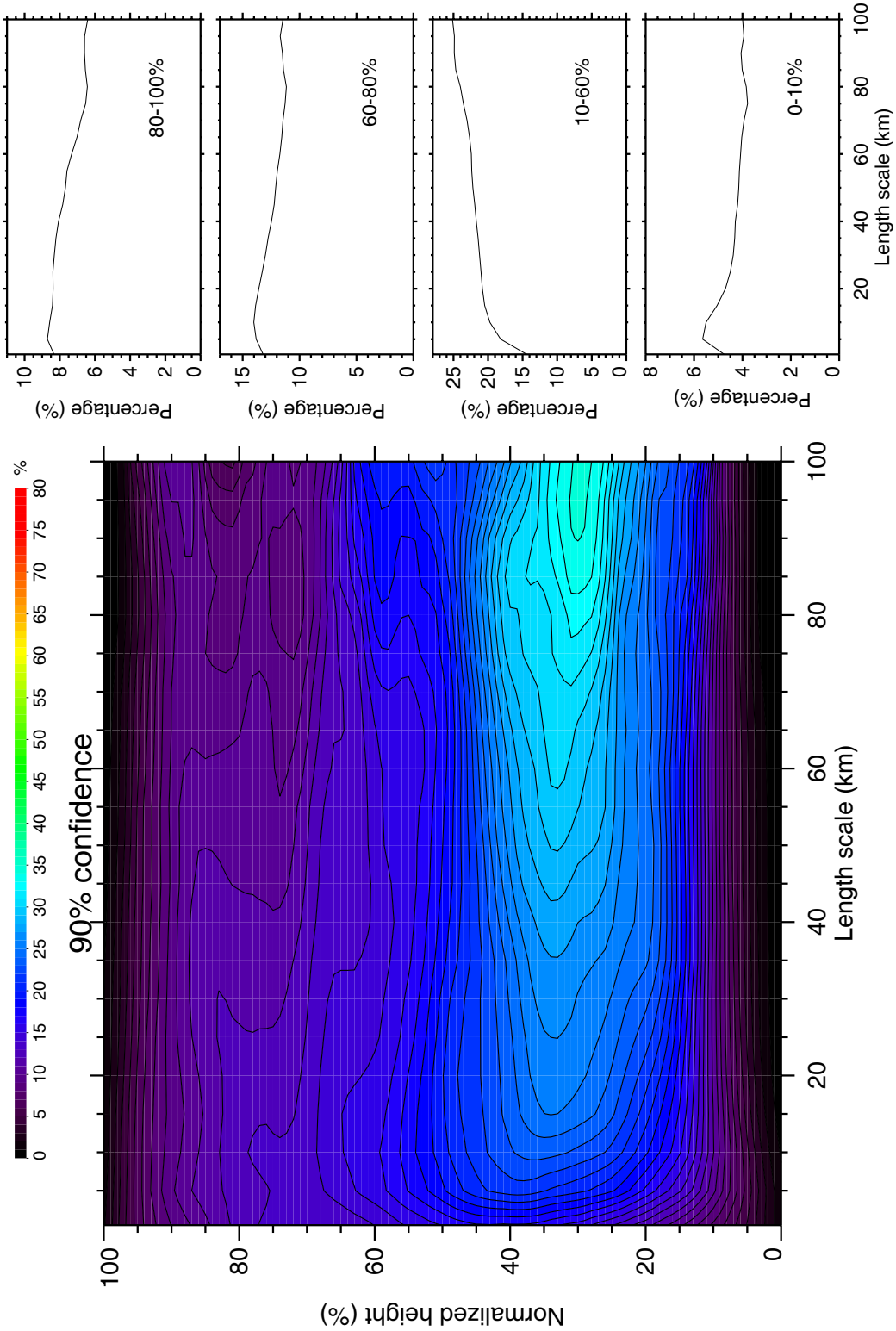

FIG. 7.14. Same as Fig. 7.13, but chose the 90% confidence level.

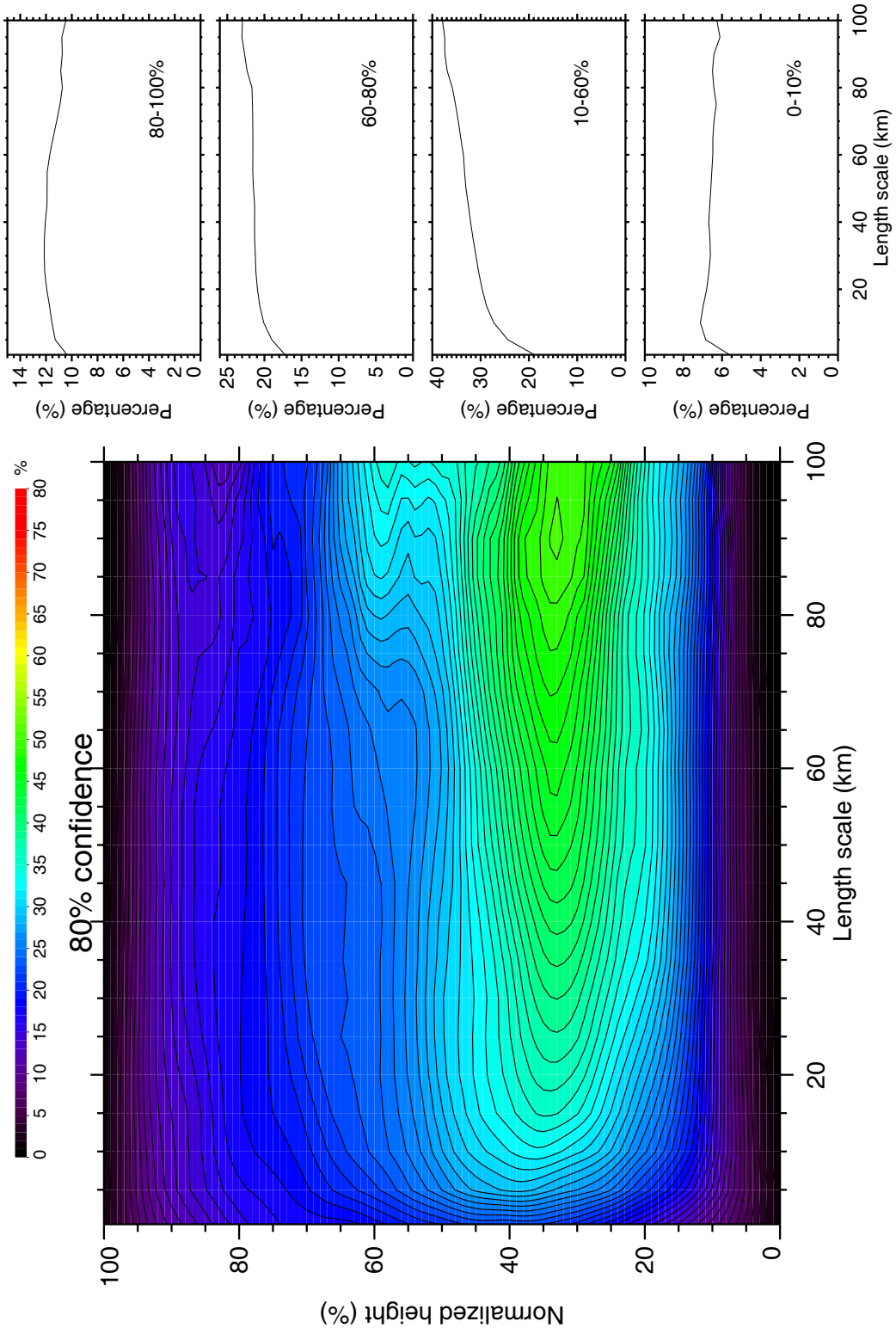

FIG. 7.15. Same as Fig. 7.13, but chose the 80% confidence level.

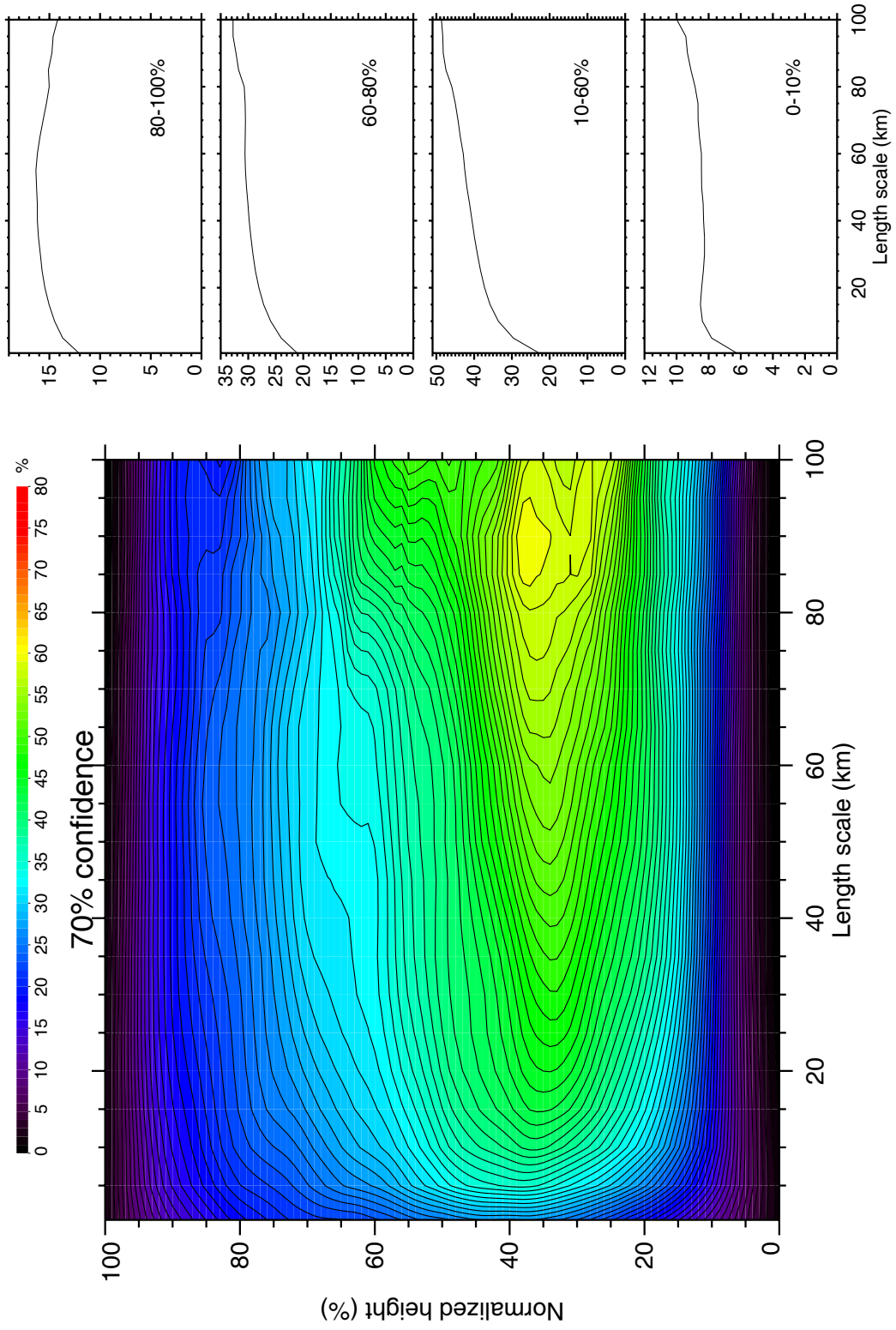

FIG. 7.16. Same as Fig. 7.13, but chose the 70% confidence level.

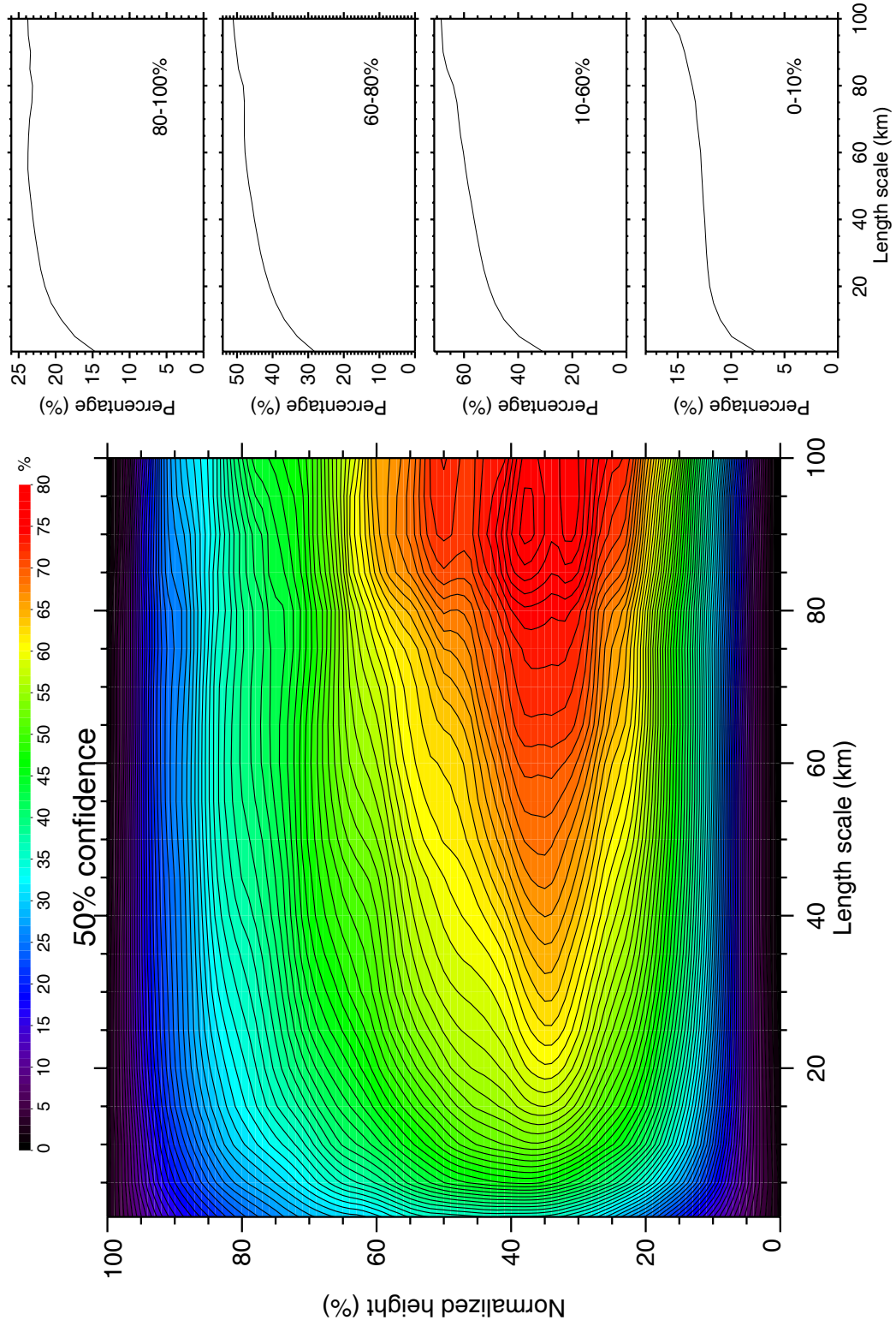

FIG. 7.17. Same as Fig. 7.13, but chose the 50% confidence level.

to confidence level threshold. It indicates that, different from mesoscale structures, these periodic structures occur intermittently in patches within cirrus clouds. Choosing the lower confidence level will smooth them out with the cirrus structures that do not have strong periodic features.

7.4.4 Temporal variability

The temporal variability of cirrus horizontal length scale generally includes the diurnal and seasonal variability. Since the FARS CPL observations were mainly operated in the daytime (see Fig. 2.3), one cannot derive the diurnal cycle of cirrus length scale change. However, there are enough samples at each month to survey the seasonal change of the cirrus horizontal length scale. First, the data are broken down based on month. The distribution of the total samples and the samples that fall in the 95% confidence area with the month is given in Fig.7.18a. One can find the samples are nearly uniformly distributed with the month. For each month at each length scale, the variability of the total samples (solid line) and the samples that fall in the 95% confidence area (dash line) are presented in Fig.7.18b, which has the similar characteristics as Fig.7.11. Finally, we calculate the percentage ratio of the 95% confidence area points against total samples at each length scale shown in Fig.7.18c, which represents the frequency of horizontal length scale of cirrus structures observed at the FARS site varying with the season. Considering the uniform distribution of samples, we limit the final results at the range 0.5-100.0 km. In other words, the results out of this range can not be fully trusted because of too few samples.

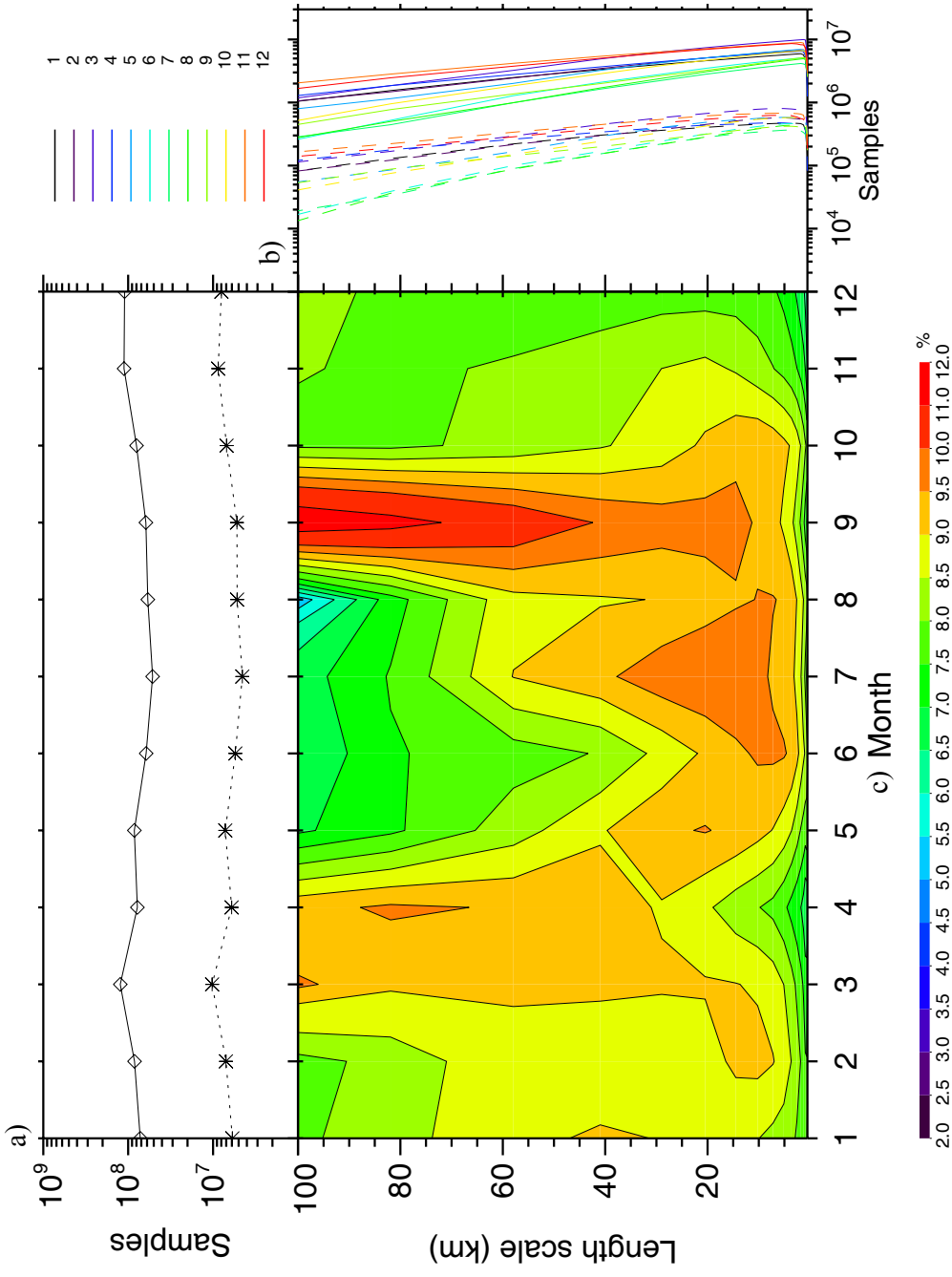

FIG.7.18. a) Monthly distribution of the total samples (solid line) and the 95% confidence samples (dot line); b) the total samples (solid line) and the samples that fall in the 95% confidence area (dash line) with the length scale; and c) the percentage ratio of the 95% confidence area points against total samples at each length scale varying with month.

The mesoscale structures ranging 5-100 km are extremely vigorous during the summer season, especially from June to August at the length scale 5-20 km and in September at the length scale 50-100 km. During the summer season, the main source of cirrus at FARS is the residual effects of monsoonal cumulonimbus clouds—anvils derived from both local (orographic) and more distant sources in the Southwest (Comstock 2000; Sassen and Campbell 2002; also see Fig.7.19), which form under the strong updrafts of cumulonimbus clouds and tend to spread away from convective centers by vertical wind shear located near the cloud top (Lilly 1998). It has been believed that the convection caused by the local or regional thunderstorm could be one of important sources to excite the gravity wave propagating both in vertical and horizontal direction (e.g., Lane et al. 2001; Horinouchi et al. 2002). Therefore, these energic cirrus mesoscale structures may be caused by the convection-generated gravity wave. In contrast, during the winter and transitional periods, the local cirrus are primarily the result of clouds advected by midlatitude jet streams propagating eastward from synoptic-cloud-generating regions over the Pacific Ocean, though the local orographic generation of cirrus wave clouds is not uncommon because of the mountainous terrain (Sassen and Campbell 2002). Thus, as indicated in Fig.7.18c, the structures with the length around 100 km mainly concentrate in March, April and September. These cirrus structures may be produced due to energy transfer from the synoptic scale to mesoscale. In summary, the temporal variability of cirrus horizontal length scale is significantly dependent on the synoptic patter and local geographic condition.

7.5 Analysis of Aperiodic Inhomogeneous Properties

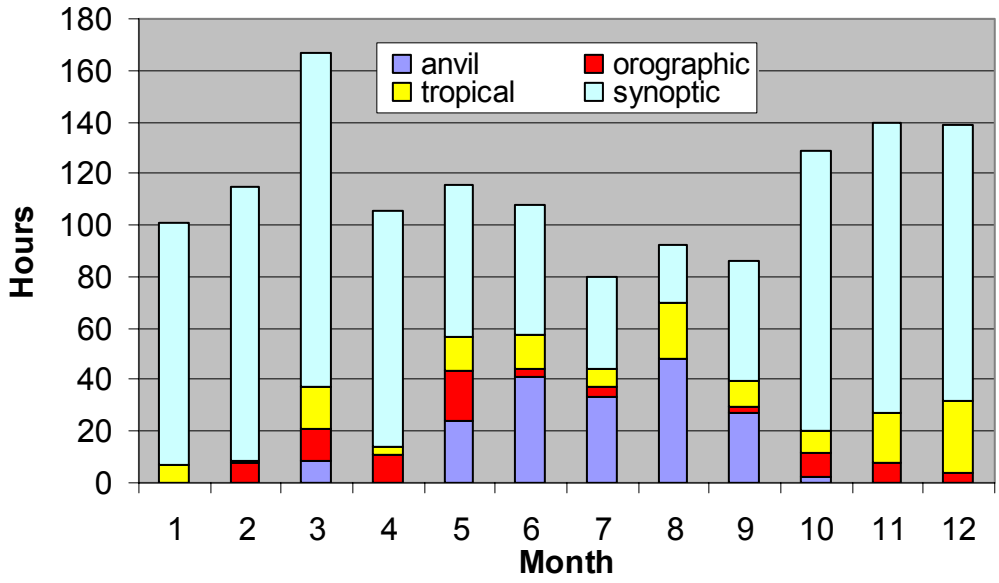

FIG.7.19. Monthly breakdown of the four types of cirrus based on the cirrus generation mechanisms.

The above results show that ~10% of the total samples fall in the 95% confidence level by analyzing the wavelet spectrum of lidar backscatterings, which indicates that most of clouds distribute in the sky without apparent periodic features. The purpose of this study is trying to provide some observational facts for cirrus cloud inhomogeneous properties that can be used in the model research. In the following, the analysis is extended to the cirrus structures without periodic features.

Since cloud optical thickness is used as the radiation transfer calculations in the current GCMs, our purpose is hope to analyze the physical quantities related to cloud optical thickness. The integrated lidar backscattered power from the cloud base to cloud top can be thought as the equivalent of cloud optical thickness, though the exact retrieval of cloud optical thickness from the lidar backscattered power requires the relationship of extinction coefficient and backscattering coefficient (Comstock 2000). Therefore, the integrated lidar backscattered energy can be derived for each case. Since the standard deviation can measure the spread of the samples compared to the mean, its value can be used to measure the variability of cloud field. Fig. 7.20 gives the scatter plot of the mean and the standard deviation of integrated cloud signals for all the cases. It shows the positive relationship of the mean and standard deviations of integrated cloud signals. In other words, larger mean value of cloud optical thickness implies the greater variance of the cloud field. This relationship suggests that one can parameterize the cloud variability by the mean cloud optical thickness or cloud thickness (e.g., Oreopoulos and Davies 1998b; Mace 2002).

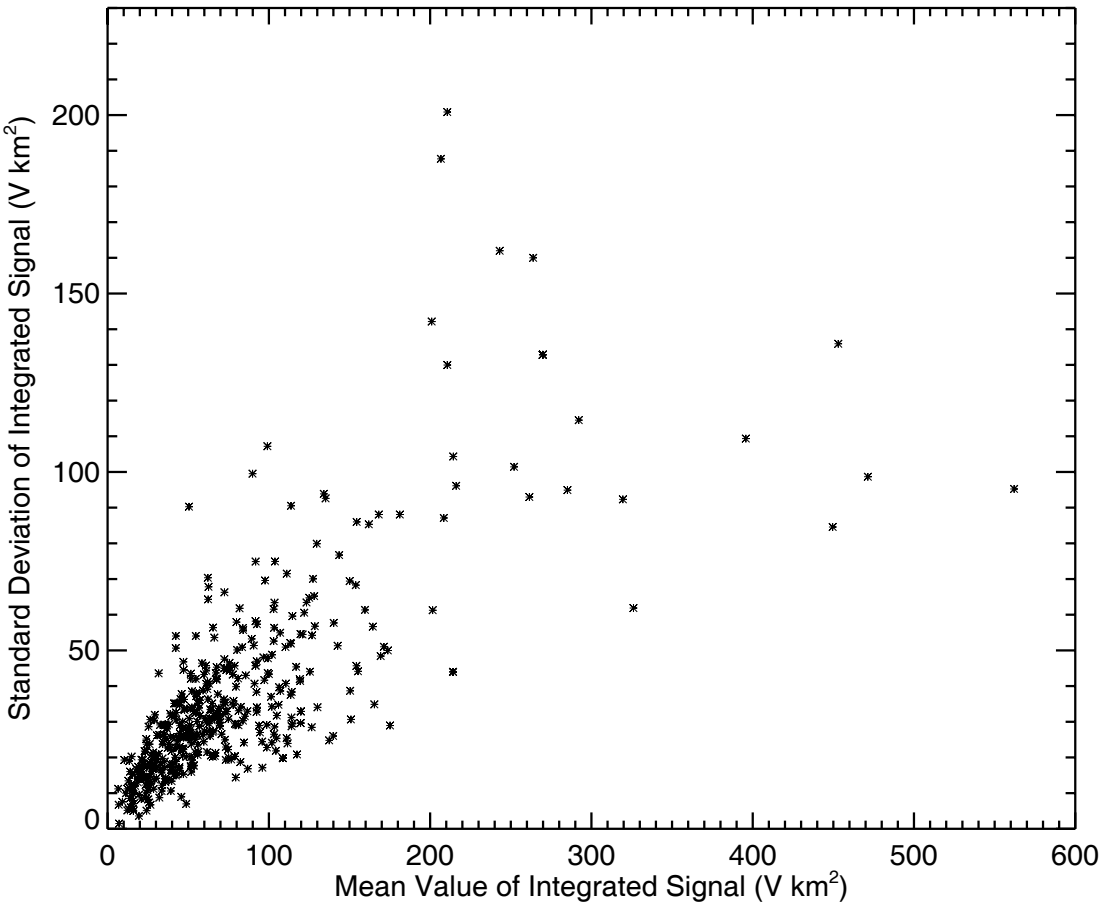

Fig. 7.20. Scatter plot of the mean and the standard deviation of integrated cloud signals for all the cases.

Starting from the radiation calculations in the models, the radiative effects of cloud horizontal inhomogeneity may be divided into two parts: 1) the heterogeneity effect due to optical property variability, and 2) the horizontal transport effect of photon moving between neighboring columns (see Fig. 1.2; Várnai and Devies 1999; Carlin et al. 2002). To address first effect, one only needs the distribution of cloud optical thickness. However, if considering the horizontal transport effect of photon moving between neighboring columns, we also want to know how the neighboring columns are related to each other once column size is chosen. Therefore, we use the different box size (1-50 km) to average the integrated cloud backscattered power time series and then determine the lag1 autocorrelation at each box size. The frequency distribution of lag1 autocorrelations varying with the grid size is shown in Fig. 7.21. The black line indicates the mean value of lag1 autocorrelations that shows a rapid decorrelation as the size scale increases. According to the autocorrelation frequency distribution, the neighboring columns are strongly positively correlated when the grid size is 1-10 km. It suggests that, when the grid size 1-10 km is chosen, the columns with the close value of optical thickness should be put together. From 35-50 km, most of autocorrelations are close to zero, indicating they are randomly related to each other. However, how to apply these results into the model research still remains a question. We will continue to make our effects on it in the future study.

7.6 Conclusion

In this chapter, the climatology characterizing the cirrus horizontal structural properties is developed by analyzing the wavelet transform results of the FARS 10-year

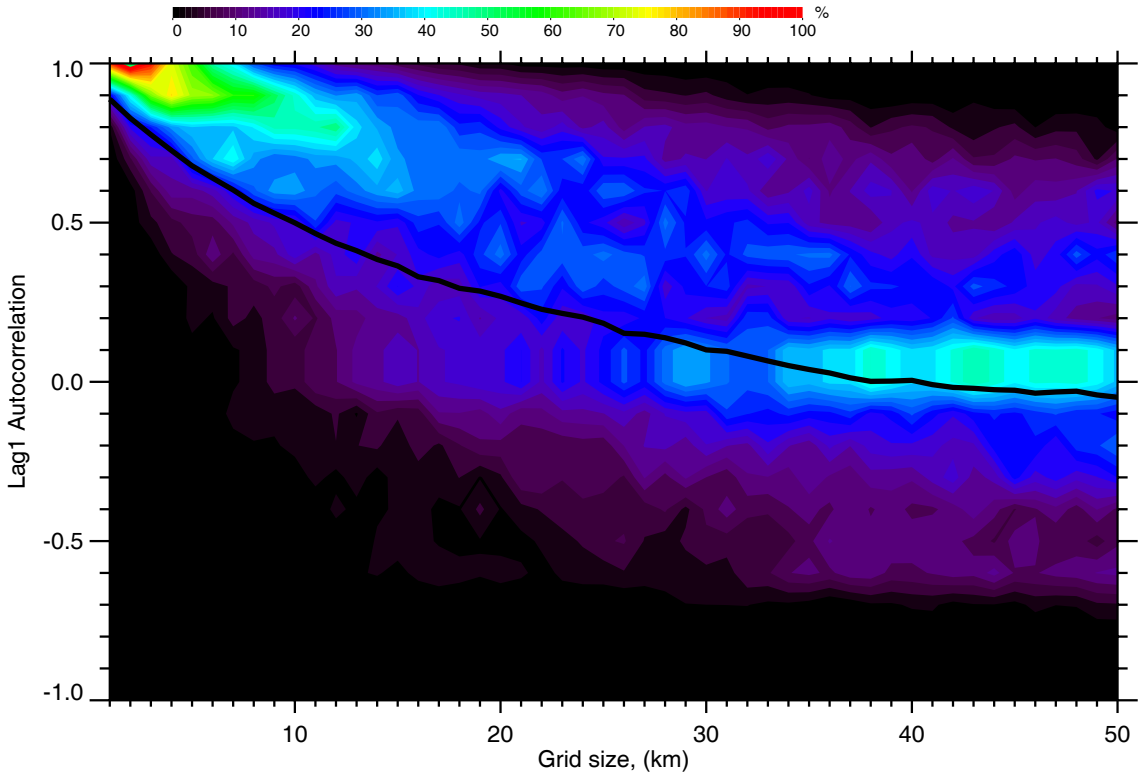

FIG. 7.21. Frequency distribution of lag1 autocorrelations varying with the different average grid size. The black line indicates the mean value.

lidar backscattering data. First, using the lidar backscatterings as the proxy of real clouds, the methods based on the wavelet transform are developed to derive the cirrus horizontal structural information. Three case studies indicate that this method has the ability to disclose cirrus structures with periodic feature from lidar backscatterings. Using this method, the 10-year lidar backscattering data including 1382 hour data and 533 cases are analyzed. Their vertical distribution and temporal distribution is discussed. In the final, the analysis is extended to aperiodic cirrus structures. The following conclusion can be drawn from the results.

Our results disclose that ~10% of the total samples have apparent periodic features and fall in 95% confidence level. It implies that the cirrus cloud inhomogeneous properties are dominant with aperiodic structures.

For the periodic cirrus structures, the mesoscale structures at the range 40-100 km are mainly located in the lower mid-cloud while the structures with the length scale smaller than 10 km concentrate in the upper mid-cloud. At the cloud top, the percentage of 95% confidence samples have high values at the length scale range 0.2-2 km, indicating the cirrus connective generating cells occurring the cloud top. The peak with length scale 5-8 km at the cloud base can be thought as the cirrus mammatus structures frequently generated at the cloud base. The mesoscale structures ranging 5-100 km are active during the summer season, especially from June to August at the length scale 5-20 km and in September at the length scale 50-100 km. One can speculate that possible mechanisms generating cirrus mesoscale structures can be from gravity waves (forced by wind shear, synoptic-scale weather disturbances, thunderstorm convection, and

orographic effects), scale interaction (energy transfer from either synoptic scale or small scale motions), mesoscale instabilities (e.g., baroclinic, barotropic, and convective instabilities), and interaction of cloud microphysics and dynamics (e.g., fallstreak). Thus, it is suggested that the mesoscale cloud model should continue to be developed to deeply understand these mesoscale structures.

The effects are made to extend the analysis on aperiodic cloud structures. It shows the positive relationship of the mean and standard deviations of integrated cloud signals. This relationship suggests that one can parameterize the cloud variability by the mean cloud optical thickness or cloud thickness. We use the different box size (1-50 km) to average the integrated cloud backscattered power time series and then determine the lag1 autocorrelation at each box size. It shows a rapid decorrelation as the size scale increases. According to the autocorrelation frequency distribution, the neighboring columns are strongly positively correlated when the grid size is 1-10 km. It suggests that, when the grid size 1-10 km is chosen, the columns with the close value of optical thickness should be put together. From 35-50 km, most of autocorrelations are close to zero, indicating they are randomly related to each other. However, how to apply these results into the model research still remains a question. We will continue to make our effects on it in the future study.

It has to be admitted that only in situ measurements are not enough to characterize "whole picture" of the midlatitude cirrus horizontal structures. The lidar backscattering data unavoidably bring some uncertainness to capture the real cloud structures. However,

this is first efforts to derive the cirrus horizontal structural climatology using the long-term high-resolution data, which will be helpful for us to deeply understand cirrus.

CHAPTER 8

SUMMARY AND RECOMMENDATIONS FOR FUTURE WORK

8.1 Summary

Since the knowledge on cirrus inhomogeneous structural properties is important not only in radiation calculation but also in deeply understanding dynamics mechanisms including the formation, development, and dissipation of cirrus clouds, in this research, the midlatitude cirrus structures have been given fully studied by the FARS long-term and high-resolution ground-based remote sensor data. To summarize this research, three goals have been reached: 1) successfully developing the means by analyzing the lidar data using wavelet transform to obtain information on the structures of cirrus clouds; 2) further improving the understanding of cirrus typical structures including KH waves, mammata, and uncinus cells by case studies and statistical survey; and 3) first advancing the climatology of midlatitude cirrus horizontal structures by analyzing the FARS 10-year high cloud dataset.

Using the lidar backscattered power as the proxy of real clouds, a method based on wavelet transform is developed to detect the cirrus structures from the FARS 10-year high cloud datasets. By decomposing a signal using a particular wavelet function, wavelet transform method can construct a picture of the energy within the signal as a function of both spatial dimension (or time) and wavelet scale (or frequency). Thus, these methods are effective to identify the scale-dependent dynamical processes and explore their characteristic structures and behaviors within cirrus, a highly coupled microphysical-

radiative-dynamical system. The method based on the continuous wavelet transform can effectively characterize the length scale of different processes that coexist in the same cloud system, for example KH waves (Chapter four) and cirrus mammata (Chapter five). Using the discrete wavelet transform, the lidar power image can be decomposed into two parts: one containing the cloud scale structures and the other representing the mesoscale processes, which have successfully highlighted the structures of the cirrus uncinus cells and mesoscale uncinus complex in Chapter six. In Chapter seven, we further make use of the wavelet transform results to develop the climatology of cirrus horizontal structures by analyzing the long-term lidar backscattering data. Importantly, our methods extend the application field of lidar data, which not only can be used for cloud macrophysical (e.g., Sassen and Campbell 2001), microphysical (e.g., Sassen and Benson 2001), and radiative property studies (e.g., Sassen and Comstock 2001) but also can derive the cirrus structural information to understand their dynamical behavior.

In Chapter four, the features of Kelvin – Helmholtz (KH) instabilities associated with the cirrus clouds occurring in the upper troposphere are examined by the analysis of nineteen cases from the FARS datasets. The results disclose that the KH instabilities in cirrus clouds frequently occur in three places: a) the leading edge of cirrus cloud top; b) the back of the trail of down-draft crystal fallstreak; and c) the cirrus cloud bottom area. Generally, we found that, the values of the bulk Richardson number (Ri) is less than 1.0 that could be treated as the critic value for the onset of the KH instabilities, which is larger than the critical value of 0.25 from theoretical calculations. Compared with the previous observations, our results showed that the KH instabilities associated with cirrus

clouds generally have the wavelength between 1 and 10 km, of which 37% (10/27) are less than 5 km and 63% (17/27) range 5~10 km. Importantly, combined with the previous observations, the trend of KH instability wavelength increases with the height. The ratios of the wave height to wavelength vary from 0.04 to 0.45 and have the mean value 0.16, indicating the billow shape can be used to infer the local Ri.

In Chapter five, the properties of cirrus mammata are investigated by the case study and statistical analysis by combining multiple remote sensors. Although the common knowledge usually associates mammata with cumulus anvils that have smooth and beautiful outline, cirrus mammata are also prevalent in the atmosphere. We found that cirrus mammata generally happen around the transition areas from the dry layer to wet layer with relatively weak wind shears, which suggests that atmospheric thermal structures play a key factor to generate cirrus mammata. The local instability caused by the subsidence of cloud base into the relative dry surroundings and evaporative cooling process is mainly responsible for the formation and development of cirrus mammata. The maximum vertical extended scales and horizontal length scales for cirrus mammata vary around 0.3~1.10 km and 0.5~8.0 km, respectively. Importantly, we further find that the small scale structures developed among or around large scale mammatus clouds. Moreover, the spectral slope of the lidar backscattered power and the mean Doppler velocity extracted from mammatus areas also indicated the presence of the developed three-dimensional locally isotropic, homogeneous turbulence generated by the buoyancy.

In Chapter six, a case study of typical mesoscale uncinus complex has been studied by the scale decomposition methods based on the discrete wavelet transform.

Disclosed by the CPL lidar data, the whole cloud structures can be characterized as two-layer cirrus occurring in the distinct dynamic environment, which can be caused by the cumulative effects of moistening associated with evaporation of crystals falling from the overlaying layer together with the tendency toward unstable thermal stratification arising from the vertical pattern of sublimation cooling (Starr and Cox 1985a). According to the local wavelet powers, the single uncinus cells embedded in every single MUC have the length scale 1.0~4.0 km while the MUC structures are on the scale of 30.0~40.0 km probably caused by the gravity waves. Checking the global wavelet power of the horizontal lidar returned power, we find that the large scale structures (larger than 6.0 km) and small scale ones (less than 3.0 km) show different behaviors. Specifically, the spectra of the small scale structures caused by the convective and turbulent activities were characterized by a $k^{-5/3}$ power law dependence over the resolved spectral range (0.3 to 3.0-4.0 km), whereas a steeper power spectral slope k^{-3} can be found over the large scale range (4.0 to 10.0-20.0 km). We speculate that these cloud scale structures can be associated with two-dimensional horizontal mesoscale eddies, which may be responsible for the existence of these MUC structures by the upscale energy transport originating from the small scale or three-dimensional turbulence.

Using the lidar backscatterings as the proxy of real clouds, the climatology characterizing the cirrus horizontal structural properties is first developed by analyzing wavelet transform results of the FARS 10-year lidar backscattering data including 1382-hour observations (10 or 12 second resolution) and 533 cases. Our results disclose that ~10% of the total samples have apparent periodic features and fall in 95% confidence

level. It implies that the cirrus cloud inhomogeneous properties are dominant with aperiodic structures.

For the periodic cirrus structures, the mesoscale structures at the range 40-100 km are mainly located in the lower mid-cloud while the structures with the length scale smaller than 10 km concentrate in the upper mid-cloud. At the cloud top, the percentage of 95% confidence samples have high values at the length scale range 0.2-2 km, indicating the cirrus connective generating cells occurring the cloud top. The peak with length scale 5-8 km at the cloud base can be thought as the cirrus mammatus structures frequently generated at the cloud base.

The effects are made to extend the analysis on aperiodic cloud structures. It shows the positive relationship of the mean and standard deviations of integrated cloud signals. This relationship suggests that one can parameterize the cloud variability by the mean cloud optical thickness or cloud thickness. We use the different box size (1-50 km) to average the integrated cloud backscattered power time series and then determine the lag1 autocorrelation at each box size. It shows a rapid decorrelation as the size scale increases. According to the autocorrelation frequency distribution, the neighboring columns are strongly positively correlated when the grid size is 1-10 km. From 35-50 km, most of autocorrelations are close to zero, indicating they are randomly related to each other.

We admit that only in situ measurements are not enough to characterize “whole picture” of the midlatitude cirrus horizontal structures. The lidar backscattering unavoidably brings some uncertainness to capture the real cloud structures. However, this

is first efforts made to study the cirrus structures using the long-term high-resolution data, which will be helpful for us to deeply understand cirrus.

8.2 Recommendations for Future Work

Although the first efforts have been made to study the cirrus structures using the long-term high-resolution data, the analysis of available cirrus cloud observations to study cirrus dynamics and statistical properties is still a challenge work. New and creative ideas on how to use the current observations to provide models with the useful information still are needed. Thus, the following suggestions for future work have been given based on this research.

First, evaluation of the statistics of the cloud vertical structures can be another issue on how to use the FARS long-term high cloud dataset. For instance, the models predict that, also revealed by modern active remote sensing observations (e.g, Sassen et al. 1995), the new convective cloud generating layers may arise at some distance below an initial cloud-generating layer through the cumulative effects of moistening associated with evaporation of crystals falling from the overlaying layer together with the tendency toward unstable thermal stratification arising from the vertical pattern of sublimation cooling (Starr and Cox 1985a; Starr and Quante 2002). As another example, it is frequently observed that the subcloud altocumulus formation is associated with upper embedded cirrus clouds (Sassen et al. 1989, 1995), which can be explained by the evaporation of cirrus precipitation shaft penetrating in dry air resulting in super liquid water formation in ice saturation condition (Sassen 2002). Furthermore, parameterization

of cloud overlap is another unsolved problem in current climate model, which is generally believed to be associated with the cloud spatial scale, cloud type, and synoptic situation (Tian and Curry 1989; Mace and Benson 2001). It is possible to derive the cirrus overlap statistics under the condition without lower water cloud from the lidar measurements. Therefore, the FARS long-tem and high-resolution high cloud dataset provides a good opportunity to revisit these issues.

Secondly, the wavelet transform methods can be extended to retrieve the cloud boundary value by analyzing the vertical lidar backscattering profile. Recently, we have noticed that several studies have utilized Harr wavelet covariance transform to provide automated detection of the boundary layer top from lidar backscattering profiles (e.g., Brooks 2003). At the transition position from cloud to free atmosphere, the lidar backscattering profile also has the feature of sharp increment/decrement, which also can be used to detect cloud boundary by the wavelet transform of lidar profile. Importantly, we believe that the wavelet-based algorithms can provide more exact, effective, objective, high-resolution cloud boundary value compared with other algorithms.

Thirdly, our results disclosed that the cirrus cloud inhomogeneous properties are dominant with aperiodic structures. However, how to represent aperiodic cloud structures in the models still remains a question. We will continue to make our effects on it in the future study.

REFERENCE

Acheson, D.J., 1974: On over-reflection. *J. Fluid Mech.,* **77**, 433-472.

_____, 1990: *Elementary Fluid Dynamics.* Clarendon, 397 pp.

Ackerman T., S. Ackerman, S. Cox, A. D. Genio, G. Mace, P. Minnis, D. O. C. Starr, and B. Wielicki, 2001: CRYSTAL research plan, 57 pp.

Astin, I., and L. Di Girolamo, 2003: Minimizing systematic errors in cloud fraction estimates from spaceborne cloud radars. *J. Ocean. Atmos. Tech*., **20**, 707-716.

Atlas, D., J. I. Metcalf, J. H. Richter, and E. E. Gossard, 1970: The birth of "cat" and Microscale turbulence, *J. Atmos. Sci.,* **27,** 903-913

Auria, R., and B. Campistron, 1987: Origin of precipitation and dynamic organization in wavelike precipitation bands. *J. Atmos. Sci.*, **44,** 3329-3340.

Axford, D. N., 1973: On an observation of turbulence waves on the tropaopause surface. *Quart. J. Roy. Meteorol. Soc.,* **99,** 438-449.

Baker, M. B., 1997: Cloud microphysics and climate. *Science*, **276,** 1072-1078.

Balachandran, N. K., 1980: Gravity waves from thunderstorms. *Mon. Wea. Rev.*, **108,** 804-816.

Barker, H. W., 1996a: A parameterization for computing grid-averaged solar fluxes for inhomogeneous marine boundary layer clouds. Part I: Methodology and homogeneous biases. *J. Atmos. Sci.*, **53**, 2289-2303.

_____, 1996b: Estimating cloud field albedo using one-dimensional series of optical depth. *J. Atmos. Sci.,* **53**, 2826–2837.

_____, and J. A. Davies, 1992: Cumulus cloud radiative properties and the characteristics of satellite radiance wavenumber spectra. *Remote Sens. Environ.,* **42**, 51–64.

_____, B. A. Wiellicki, and L. Parker, 1996: A Parameterization for Computing Grid-Averaged Solar Fluxes for Inhomogeneous Marine Boundary Layer Clouds. Part II: Validation Using Satellite Data**.** *J. Atmos. Sci.,* **53**, 2304–2316.

_____, J. J. Morcrette, and G. D. Alexander, 1998: Broadband solar fluxes and heating rates

for atmospheres with 3D broken clouds. *Quart. J. Roy. Meteor. Soc.,* **124,** 1245–1271.

Barnett, M. J., 2000: Remote sensing of midlatitude cirrus radiative properties: A seven year climatology. Ph.D. Dissertation, University of Utah, 226 pp.

Bäuml, G., A. Chlond, and E. Roeckner, 1999: Accounting for subgrid-scale variability in solar radiative transfer calculations. *Scientific Group Meeting of Climate modeling Group*, Salzau, Germany, Max Planck Institute.

Beer, T., 1974: *Atmospheric Waves*. Wiley and Sons, 397 pp.

Benson, S., 1999: Lidar depolarization study to infer cirrus cloud microphysics. M.S. thesis, Department of Meteorology, University of Utah, 136 pp.

Blumen, W., R. M. Banta, S. P. Burns, D. C. Fritts, R. K. Newsom , G. S. Poulos, J. Sun, 2001: Turbulence statistics of a Kelvin-Helmholtz billow event observed in the nighttime boundary layer during the CASES-99 field program. *Dyn. Atmos. Oceans,* **34,** 189-204.

Bohren, C.F., and B.A. Albrecht, 1998: *Atmospheric Thermodynamics*. Oxford University Press, 402 pp.

Borrmann, S., S. Solomon, J.E. Dye, and B. Luo, 1996: The potential of cirrus clouds for heterogeneous chlorine activation. *Geophys. Res. Lett.*, **23,** 2133-2136.

Brooks, I. M. 2003: Finding Boundary Layer Top: Application of a Wavelet Covariance Transform to Lidar Backscatter Profiles. *J. Atmos. Oceanic Techno.,* **20**, 1092–1105.

Browning, K.A., 1971: Structure of the atmosphere in vicinity of large-amplitude Kelvin-Helmholtz billows, *Quart. J. Roy. Meteorol. Soc.,* **97**, 283-299.

——, and C. D. Watkins, 1970: Observations of clear air turbulence by high power radar, *Nature*, **227**, 260-263.

——, G. W. Bryant, J. R. Starr, and D. N. Axford, 1973: Air motion within Kelvin-Helholtz billows determined from simultaneous Doppler Radar and aircraft measurements. *Quart. J. Roy. Meteorol. Soc.,* **99**, 608-618.

——, P. K. James, D. M. Parkes, C. Rowley, and A. J. Whyman, 1978: Observation of strong wind shear using pulse compression radar. *Nature*, **271**, 529-531.

____, A., A. Betts, P. R. Jonas, R. Kershaw, M. Manton, P. J. Mason, M. Miller, M. W.

Moncrieff, H. Sundqvist, W. K. Tao, M. Tiedtke, P. V. Hobbs, J. Michell, E. Raschke, R. E. Stewart, and J. Simpson, 1993: The GEWEX Cloud System Study (GCSS). *Bull. Amer. Meteor. Soc.*, **74,** 387-400.

Byrne, R. N., R. C. J. Somerville, and B. Subasilar, 1996: Broken-cloud enhancement of solar radiation absorption. *J. Atmos. Sci.*, **53,** 878-886.

Bühler, O., and M. E. McIntyre, 1999a: On shear-generated gravity waves that reach the mesosphere. Part II: Wave propagation. *J. Atmos. Sci.,* **56,** 3764–3773.

Busack, B., and B. Brummer, 1988: A case study of Kelvin-Helmholtz waves within an off-shore stable boundary layer: Observation and linear theory. *Bound.-Layer Meteor.*, **44**, 105-135.

Cahalan, R. F., 1994: Bounded cascade clouds: albedo and effective thickness. *Nonlinear Proc. Geophys.*, **1,** 156-167.

Cahalan, R. F., and J. H. Joseph, 1989: Fractal statistics of cloud fields. *Mon. Wea. Rev.* **117**, 261–272.

____, W. Ridgway, and W. J. Wiscombe, 1994: Independent pixel and Monto Carlo estimates of stratocumulus albedo. *J. Atmos. Sci.*, **51,** 3736-3790.

____, ____, ____, and T. L. Bell, 1994: The albedo of fractal stratocumulus clouds. *J. Atmos. Sci.*, **51,** 2434-2455.

Cairns, B., A. A. Lacis, and B. E. Carlson, 2000: Absorption within inhomogeneous clouds and its parameterization in general circulation models. *J. Atmos. Sci*., **57**, 700-714.

Campbell, J. R., 1997: A mid-latitude cirrus climatology from the ten-year Facility for Atmosphere Remote Sensing high cloud dataset. M.S. thesis, Department of Meteorology, University of Utah, 112 pp.

Carlin, B., Q. Fu, U. Lohmann, G. G. Mace, K. Sassen, and J. M. Comstock, 2002: High-Cloud Horizontal Inhomogeneity and Solar Albedo Bias. *J. Climate,* **15**, 2321–2339.

Chambers, L. H., B. A. Wielichi, and N. G. Loeb, 2001: Shortwave flux from satellite-measured radiance: A theoretical study over marine boundary layer clouds. *J. Appl. Meteoro.,* **40,** 2144-2161**.**

Chapman, D., and K. A. Browning, 1997: Radar observations of wind-shear splitting within evolving atmospheric Kelvin-Helmholtz billows. *Quart. J. Roy. Meteorol. Soc.,* **123,** 1433-1439.

——, ——, 1999: Release of potential shearing instability in warm frontal zones. *Quart J. Roy. Meteorol. Soc.,* **125,** 2265-2289.

Chatfield, C., 1996: *The Analysis of Time Series: An Introduction*. 5th ed. Chapman & Hall, 283 pp.

Chilson, P. B., A. Muschinski, and G. Schmidt, 1997: First Observations of Kelvin–Helmholtz billows in an upper level jet stream using VHF frequency domain interferometry. *Radio Sci.,* **32,** 1149–1160.

Chimonas, G., J.R. Grant, 1984a: Shear excitation of gravity waves. Part I: Modes of a two-scale atmosphere. *J. Atmos. Sci.*, **41**, 2269–2277.

——, ——, 1984b: Shear excitation of gravity waves. Part II: Upscale scattering from Kelvin-Helmholtz waves. *J. Atmos. Sci.*, **41**, 2278–2288.

Chou, M. D., M. J. Suarez, C. H. Ho, M. M.-H. Yan, and K.-T. Lee, 1998: Parameterizations for cloud overlapping and shortwave single-scattering properties for use in general circulation and cloud ensemble models. *J. Climate.*, **11,** 202–214.

Chui, C. K., 1992: *An Introduction to Wavelets.* Vol. 1, *Wavelet Analysis and its Applications,* Academic Press, 266 pp.

Clarke, R. H., 1962: Pressure oscillations and fallout downdraughts. *Quart. J. Roy. Meteor. Soc.*, 88, 459-469.

Comstock, J. M., 2000: Remote sensing of midlatitude cirrus radiative properties: A seven-year climatology. Ph.D. dissertation, University of Utah, 220 pp.

Cox, S. K., D. S. McDougal, D. A. Randall, and R. A. Schiffer, 1987: FIRE - First ISCCP Regional Experiment. *Bull. Amer. Meteor. Soc.*, **68,** 114–118.

Daubechies, I., 1988: Orthonormal bases of compactly supported wavelets. *Comm. Pure & Appl. Math.*, **41**, 909–996.

_____, 1990: The wavelets transform, time-frequency localization and signal analysis. *IEEE Trans. Inform. Theory,* **36**, 961-1005.

_____, 1992: *Ten lectures on wavelets*, SIAM, 357 pp.

Demoz, B. B., D.O'C. Starr, K.R. Chan, and S.W. Bowen, 1998: Wavelet analysis of dynamical processes in cirrus clouds. *Geophys. Res. Lett.*, **25,** 1347-1350.

Desrochers, P. R., and S. Y. K. Yee, 1999: Wavelet applications for mesocyclone identification in Doppler radar observations. *J. Appl. Meteor.*, **38**, 965-980

Dobbie, S., and P. Jonas, 2001: Radiative influences on the structure and lifetime of cirrus clouds. *Quart. J. Roy. Meteor. Soc.*, **127,** 2663-2682.

Doran, J. C., Fast, J. D., Horel, J. 2002: The VTMX 2000 Campaign. *Bull. Amer. Meteor. Soc.*, **83**, 537–551.

Dowling, D. R., and L. F. Radke, 1990: A summary of the physical properties of cirrus clouds. *J. Appl. Meteor.*, **29,** 970–978.

Drazin, D.G., and L.N. Howard, 1966: Hydrodynamic stability of parallel flow of inviscid fluid. *Advances in applied mechanics*, Vol 9, Academic Press, 1-89

Einaudi, F., and A.J. Bedard Jr., J.J. Finnigan, 1989: A climatology of gravity waves and other coherent disturbances at the boulder atmospheric observatory during March–April 1984. *J. Atmos. Sci.*, **46**, 303–329.

Emanuel, K. A., 1981: A similarity theory for unsaturated downdrafts within clouds. *J. Atmos. Sci.*, **38**, 1541-1557.

Erickson, C.O., and L. E. Whitney, Jr, 1973: Picture of the month-Gravity waves following severe thunderstorms. *Mon. Wea. Rev.*, **101**, 708-711.

Evans, F. K., 1993: Two-dimensional radiative transfer in cloudy atmospheres: The spherical harmonic spatial grid method. *J. Atmos. Sci.,* **50**, 3111–3124.

_____, and S. A. McFarlane, 2001: The importance of three-dimensional solar radiative transfer in small cumulus cloud fields derived from the Nauru MMCR and MWR, *Proceedings of the Eleventh ARM Science Team Meeting***,** Atlanta, Georgia, U.S. Department of Energy.

Farge, M., 1992: Wavelet transforms and their applications to turbulence. *Ann. Rev. Fluid Mech.*, **24,** 395-457.

Fournier, A., 2000: Introduction to orthonormal wavelet analysis with shift invariance: application to observed atmospheric blocking spatial structure. *J. Atmos. Sci.*, **57**, 3856-3880.

Fritts, D. C., 1982: Shear excitation of atmospheric gravity waves. *J. Atmos. Sci.,* **39**, 1936–1952.

——, 1984: Shear excitation of atmospheric gravity waves. Part II: Nonlinear radiation from a free shear layer. *J. Atmos. Sci.,* **41,** 524–537.

——, P. K. Rastigi: Convective and dynamical instability due to gravity wave motions in the lower and middle atmosphere: Theory and observations. *Radio Sci.,* **20**, 1247-1277**.**

——, T.L. Palmer, Ø. Andreassen, and I. Lie, 1996: Evolution and breakdown of Kelvin–Helmholtz billows in stratified compressible flows. Part I: Comparison of two- and three dimensional flows, *J. Atmos. Sci.,* **53,** 3173-3189.

Fu, Q., B. Carlin, and G. Mace, 2000: Cirrus horizontal inhomogeneity and OLR bias. *Geophys. Res. Lett.*, **27,** 3341-3344.

____, M. C. Cribb, H. W. Barker, S. K. Krueger, and A. Grossman, 2000: Cloud Geometry Effects on Atmospheric Solar Absorption**.** *J. Atmos. Sci.,* **57**, 1156–1168.

Fujita, T. T., 1981: Tornadoes and downbursts in the context of generalized planetary scales. *J. Atmos. Sci.*, **38**, 1512-1534.

Gabor, D., 1946: Theory of Communication, *J. IEE (London)*, **93(III)**, 429-457.

Gage, K. S., 1979: Evidence of for a $k^{-5/3}$ power law inertial range in mesoscale two dimensional turbulence. *J. Atmos. Sci.*, **36**, 1950-1954.

____, 1990: Radar observation of free atmosphere: Structure and dynamics. *Radar in meteorology*. D. Atlas ed., Am. Meteorol. Soc. Boston. 534-565.

Gedzelman, S. D., 1983: Short-period atmosphere gravity waves: a study of their statistical properties and source mechanism. *Mon. Wea. Rev.*, **111**, 1293-1299.

Glickman, T. S., 2000: *Glossary of Meteorology.* 2nd ed. American Meteorological Society, 855 pp.

Gilman, D. L., F.J. Fuglister, and J.M. Mitchel, Jr., 1963: On the power spectrum of "red noise". *J. Atmos. Sci.*, **20,** 182-184.

Glover, K. M., Boucher, R. J., H. Ottersten, and K. R. Harday, 1969: Simultaneous Radar, aircraft and meteorological investigation of clear air turbulence. *J. Appl. Meteor.,* **8**, 634-640.

Gollmer, S. M., Harshvardhan, R. F. Cahalan, and J B. Snider, 1995: Windowed and wavelet analysis of marine stratocumulus cloud inhomogeneity. *J. Atmos. Sci.*, **52**, 3013-3030.

Gossard, E. E., and W.H. Hooke, 1975: *Waves in the Atmosphere: Atmospheric Infrasound and Gravity Waves – their Generation and Propagation* . Elsevier, 456 pp.

——, 1990: Radar research on the Atmospheric boundary layer. *Radar in meteorology*. D. Atlas ed., Am. Meteorol. Soc. Boston. 477-527.

Grimshaw, R., 1976: Nonlinear aspects of an internal gravity wave coexisting with an unstable mode associated with Helmholtz velocity profile, *J.Fluid Mech.*, **76**, 65-83.

Grund, C. J., and E.W. Eloranta, 1990: The 27–28 October 1986 FIRE IFO cirrus case study: Cloud optical properties determined by High Spectral Resolution Lidar. *Mon. Wea. Rev.*, **118,** 2344-2355.

Gu, Y., and K.N. Liou, 2000: Interactions of radiation, microphysics, and turbulence in the evolution of cirrus clouds. *J. Atmos. Sci.*, **57,** 2463-2479.

____, and ____, 2001: Radiaion parameterization for three-dimensional inhomogenenous cirrus clouds: Application to climate models. *J. Climate*, **14,** 2443-2457.

Gultepe, I., and D.O'C. Starr, 1995: Dynamical structure and turbulence in cirrus clouds: Aircraft observations during FIRE. *J. Atmos. Sci.*, **52,** 4159-4182.

Hallett, J., W.P.Arnott, M.P.Bailey, and J.T. Hallett, 2002: Ice crystal in Cirrus. *Cirrus*, D.K. Lynch, K. Sassen, D.O'C. Starr, and G. Stephens, Eds., Oxford University Press, 41-77.

Harimaya, T., 1968: On the shape of cirrus uncinus clouds: a numerical computations – Studies of cirrus clouds: Part III. *J. Meteor. Soc. Japan*, **46**, 272-279.

Harshvardan, and D. A. Randall, 1985: Comments on "The parameterization of radiation for numerical weather prediction and climate models.". *Mon. Wea. Rev.,* **113**, 1832–1833.

Hartmann, D.L., J.R. Holton, and Q. Fu, 2001: The heat balance of the tropical tropopause, cirrus and stratospheric dehydration. *Geophys. Res. Lett.,* **28**, 1969-1972.

Helmholtz, H., 1868: On discontinuous movement of fluid (translated from German by F. Gurthrie.) *Philos. Mag.*, **36**, 337-346.

Heymsfield, A. J., 1975a: Cirrus uncinus generating cells and the evolution of cirriform clouds. Part I: Aircraft observation of the growth the ice phase. *J. Atmos. Sci.*, **32,** 799-808.

_____, 1975b: Cirrus uncinus generating cells and the evolution of cirriform clouds. Part II: The structure and circulations of the cirrus uncinus generating head. *J. Atmos. Sci.*, **32,** 809-819.

_____, 1975c: Cirrus uncinus generating cells and the evolution of cirriform clouds. Part III: Numerical computations of the growth of ice phase. *J. Atmos. Sci.*, **32,** 809-819.

_____, K. M. Miller, and J. D. Spinhirne, 1990: The 27–28 October 1986 FIRE IFO cirrus case study: Cloud microstructure. *Mon. Wea. Rev.*, **118,** 2313–2328.

Hicks, J. J., 1969: Radar observation of a gravitaional waves in clear air near the tropopause associated with CAT. *J. Appl. Meteor.,* **8**, 627-633.

_____, and J. K. Angell, 1968: Radar Observation of breaking gravitational waves in the visually clear atmosphere, *J. Appl. Meteor.,* **7**, 114-121.

Hildebrand, F. B., 1956: Introduction to numerical analysis**.** McGraw-Hill, 511 pp.

Hlad, C. J., 1944: Stability-tendency and mammatocumulus clouds. *Bull . Amer. Meteor. Soc.*, **25**, 327-331.

Holschneider, M., 2000: Introduction to continuous wavelet analysis. *Wavelets in the geosciences*, R. Klees and R. Haahmans, Eds., Springer-Verlag, 1-71.

Holton, J. R., 1992: *An Introduction to Dynamic Meteorology, Third Edition.* Academic Press, pp. 511.

Horinouchi, T., T. Nakamura, and J.-i. Kosaka, 2002: Convectively generated mesoscale gravity waves simulated throughout the middle atmosphere. *Geophys. Res. Lett.*, **29**, 2007-2011.

Houze, R. A., Jr., 1993: *Cloud Dynamics.* Academic, 573 pp.

Howard, L. N., 1961: Note on a paper of John Miles. *J. Fluid Mech.*, **10,** 509-512.

IPCC, 1996: *The Science of Climate Change, in Climate Change 1995*. Cambridge University Press.

Iwabuchi, H., and T. Hayasaka, 2002: Effects of cloud horizontal inhomogeneity on the optical thickness retrieved from moderate-resolution Satellite data. *J. Atmos. Sci.,*

59, 2227-2442**.**

James, P.K., and K.A. Browning, 1981: An observational study of primary and secondary billows in the free atmosphere, *Quart. J. Roy. Meteorol. Soc.,* **107**, 351-365.

Jensen, E.J., O.B. Toon, L. Pfister, and H. Selkirk, 1996: Dehydration of the upper troposphere and lower stratosphere by subvisible cirrus clouds near the tropical tropopause. *Geophys. Res. Lett.,* **23**, 825-828.

_____, L. Pfister, A.S. Ackerman, A. Tabazadeh, and O.B. Toon, 2001: A conceptual model of the dehydration of air due to freeze-drying by optically thin, laminar cirrus rising slowly across the tropical tropopause. *J. Geophys. Res.*, **106**, 17237-17252.

Jo, I., B. A. Albrecht, and P. Kollias, 2003: 94-GHz Doppler radar observation of mammatus in tropical anvils during CRYSTAL-FACE. *31st International Conference on Radar Meteorology,* Seattle, WA, Amer. Meteor. Soc..

Jones, R. H., 1975: Estimating the variance of time averages. *J. Appl. Meteor.*, **14,** 159-163.

Jones, W. L., 1968: Reflection and stability of waves in stably stratified fluid with shear flow: A numerical study. *J. Fluid Mech.,* **34**, 609-624.

Kalnay, E., and Co-Authors, 1996: The NCEP/NCAR 40-year reanalysis project. *Bull. Amer. Meteor. Soc.*, **77**, 437-472.

Kelvin, W. 1871: The influence of wind on waves in water supposed frictionless. *Philos. Mag.*, **42**, 368-374.

Khvorostyanov, V. I., and Sassen, K., 1998a: Cirrus cloud simulation using explicit microphysics and radiation. Part I: Model description. *J. Atmos. Sci.*, **55**, 1808-1821.

_____, and _____, 1998b: Cirrus cloud simulation using explicit microphysics and radiation. Part II: Microphysics, vapor and ice mass budget, and optical and radiative properties. *J. Atmos. Sci.*, **55**, 1822-1845.

_____, and _____, 2002: Microphysical processes in cirrus and their impact on radiation: A Mesoscale modeling perspective. *Cirrus*, D.K. Lynch, K. Sassen, D.O'C. Starr, and G. Stephens, Eds., Oxford University Press, 397-432.

Kistler, R., and Co-Authors, 2001: The NCEP-NCAR 50-year reanalysis: monthly means CD-ROM and documentation. *Bull. Amer. Meteor. Soc.,* **82**, 247-268.

Klett, J. D., 1981: Stable analytical inversion solution for processing lidar returns. *Appl. Opt.,*, **20,** 211-220.

Kley, D., P.J. Crutzen, H.G.J. Smit, H. Voemel, S.J. Oltmans, H. Grassl, and V. Ramanathan, 1996: Observations of near-zero ozone concentrations over the convective pacific: Effects on air chemistry. *Science*, **274,** 230-233.

Klostermeyer, J., and R. Rüster, 1980: Radar observation and model computation of jet stream generated Kelvin-Helmholtz instability. *J. Geophys. Res.,* **85**, 2841-2846.

Kolmogorov, A. N., 1941: The local structure of turbulence in incompressible viscous fluid for very large Reynolds numbers. *Dokl. Akad. Nauk. SSSR*, **30**, 301-305.

Kondratyev, K. Y. 1999: *Climatic Effect of Aerosols and Clouds*. Spinger, 264 pp.

Kumar, P., and E. Foufoula-Georgiou, 1994: Wavelet analysis in geophysics: An introduction. *Wavelet in geophysics,* P. Kumar and E. Foufoula-Georgiou, Eds., Academic, 1-42.

Lalas, D.P., and F. Einaudi, 1976: On the characteristics of gravity waves generated by atmospheric shear layers. *J. Atmos. Sci.,* **33**, 1248–1259.

Lane, D. M., cited 2002: HyperStat Online Textbook. [Available online at http://davidmlane.com/hyperstat/]

Lane, T. P., M. J. Reeder, and T. L. Clark, 2001: Numerical Modeling of Gravity Wave Generation by Deep Tropical Convection. J. Atmos. Sci., **58**, 1249-1274

Lau, K.-M., and H. Weng, 1995: Climate signal detection using wavelet transform: How to make a time series sing. *Bull. Amer. Meteor. Soc.*, **76,** 2391 - 2402.

Lewalle, J., cited 1995: Tutorial on Continuous Wavelet Analysis of Experimental Data. [Available online at http://www.ecs.syr.edu/faculty/lewalle/tutor/tutor.html]

Lhermitte, R., 2002: *Centimeter and Millimeter Wavelength Radars in Meteorology*. 550pp.

Lilly, D. K., 1983: Stratified turbulence and the mesoscale variability of the atmosphere. *J. Atmos. Sci.,* **40,** 749-761.

____, 1988: Cirrus outflow dynamics. *J. Atmos. Sci.,* **45,** 1594-1605.

Lin, H., K. J. Noone, J. Ström, and A. J. Heymsfield, 1998: Dynamical influences on cirrus cloud formation process. *J. Atmos. Sci.*, **55**, 1940-1949.

Lindzen, R. S., 1974: Stability of a Helmholtz velocity profile in a continuously stratified, infinite Boussineq fluid – Application to clear air turbulence, *J. Atmos. Sci.,***31,** 1507-1514

——, 1981: Turbulence and stress owing to gravity wave and tidal breakdown, *J. Geophys. Res.*, **86**, 9707-9714.

Liou, K.-N., 1986: Influences of cirrus cloud on weather and climate processing: A global perspective. *Mon. Wea. Rev.*, **116,** 1167-1199.

_____, 1992: *Radiation and Cloud Processes in the Atmosphere.* Oxford University Press, 487 pp.

____, 2001: *An Introduction to Atmospheric Radiation.* 2nd edition, Academic Press, 583 pp.

____, and N. Rao, 1996: Radiative transfer in cirrus clouds. 4: On cloud geometry, inhomogeneity and absorption. *J. Atmos. Sci.*, **53,** 3046–3065.

Liu, H.-C., P. K. Wang, and R. E. Schlesinger, 2003: A numerical study of cirrus clouds. Part II: Effects of ambient temperature, stability, radiation, ice microphysics, and microdynamics on cirrus evolution. *J. Atmos. Sci.*, **60**, 1097-1119.

Liu, P. C., 2000: Wavelet transform and new perspective on coastal and ocean engineering data analysis. In Advanced in Coastal and Ocean Engineering, P.L-F. Liu, Ed., World Scientific, 57-101.

____, and G. S. Miller, 1996: Wavelet transforms and ocean current data analysis. *J. Atmos. Oceanic Technol.*, **13,** 1090–1100.

Livezey, R. E., and W.Y. Chen, 1983: Statistical Field Significance and its Determination by Monte Carlo Techniques. *Mon. Wea. Rev.*, **111,** 46-59.

Loeb, N., and R. Davies, 1996: Observational evidence of plane parallel model biases: Apparent dependence of cloud optical depth on solar zenith angle. *J. Geophys. Res.,* **101,** 1621–1634

____, and J. Coakley, 1998: Inference of marine stratus cloud optical depths from satellite measurements: Does 1D theory apply? *J. Climate.,* **11**, 215–233.

Los, A., and P. G. Duynkerke, 2001: Parametrization of solar radiation in inhomogeneous

stratocumulus: Albedo bias. *Quart. J. Roy. Meteorol. Soc.,* **127,** 1593-1614**.**

Lovejoy, S., 1982: Area-perimeter relation for rain and cloud areas, *Science*. **216,** 185-187.

Lynch, D. K., 2002: Cirrus: History and Definition. *Cirrus*, D. K. Lynch, K. Sassen, D. O'C. Starr, and G. Stephens, Eds., Oxford University Press, 3-10.

_____, and K. Sassen, 2002: Subvisual Cirrus. *Cirrus*, D. K. Lynch, K. Sassen, D. O'C. Starr, and G. Stephens, Eds., Oxford University Press, 256-264.

_____, K. Sassen, A.D. Genio, A. J. Heymsfield, P. R. Minnis, C. M. R. Platt, M. Quante, U. Schumann, and H. Sundqvist, 2002: Cirrus: The future. D. K. Lynch, K. Sassen, D. O'C. Starr, and G. Stephens, Eds., Oxford University, 449-455.

Ludlam, F. H., 1948: The forms of ice clouds. *Quart. J. Roy. Meteorol. Soc.,* **74,** 39-65.

——, 1956: The forms of ice clouds, II. *Quart. J. Roy. Meteorol. Soc.,* **82,** 257-265.

——, 1967: Characteristics of billow clouds and their relation to clear air turbulence. *Quart. J. Roy. Meteorol. Soc.,* **93,** 419-415.

——, 1980: *Clouds and Storms: The Behavior and Effect of Water in the Atmosphere.* The Pennsylvania State University Press, 404 pp.

_____, and R. S. Scorer, 1953: Convection in the atmosphere. *Quart. J. Roy. Meteor. Sco.,* **79**, 317-341.

Mace, G. G., C. Jakob, and K. P. Moran, 1998: Validation of hydrometeor occurrence predicted by the ECMWF model using millimeter wave radar data. *Geophys. Res. Lett.*, **25,** 1645-1648.

_____, E.E. Clothiaux, and T. P. Ackerman, 2001: The composite characteristics of cirrus clouds: Bulk properties revealed by one year of continuous cloud radar data. *J. Climate*, **14,** 2185–2203.

_____, and S. Benson, 2002: Cloud-layer overlap characteristics derived from long-term cloud radar data**.** *J. Climate*. **15**, 2505–2515.

_____, 2002: Parameterizing the moments of cirrus cloud property distributions in terms of cloud layer thickness and layer mean temperature using cloud microphysical properties derived from ARM data. *11th Conference on Atmospheric Radiation and the 11th Conference on Cloud Physics Meeting*. Orgden, Utah, Amer. Meteor. Soc.

Mak, M., 1995: Orthogonal wavelet analysis: Interannual variability in the sea surface temperature. *Bull. Amer. Meteor. Soc.,* **76,** 2179–2186.

Mallat, S. G., 1989: A Theory for Multiresolution Signal Decomposition: The Wavelet Representation. *IEEE Trans. Pattern Analysis Machine Intel.*, **11**, 674-693.

Marshak, A., A. Davis, W. Wiscombe, and G. Titov, 1995: The verisimilitude of the independent pixel approximation used in-cloud remote-sensing. *Remote Sens. Environ.* **52**, (1), 71–78.

_____, _____, _____, and R. Cahalan, 1995: Radiative smoothing in fractal clouds. *J. Geophys. Res.,* **100,** 26,247-26,261**.**

_____, _____, _____, R. Cahalan, 1997: Scale invariance in liquid water distributions in marine stratocumulus. Part II: Multifractal properties and intermittency issues. *J. Atmos. Sci.* **54**, 1423–1444.

_____, _____, _____, W. Ridgway, and R. Cahalan, 1998: Biases in shortwave column absorption in the presence of fractal clouds. *J. Climate*, **11**, 431-446, 1998.

Martner, B. E., 1995: Doppler radar observations of mammatus. *Mon. Wea. Rev.*, **123**, 3115-3121.

McFarquhar, G. M., A. J. Heymsfield, J. Spinhirne, and B. Hart, 2000: Thin and subvisual tropopause tropical cirrus: Observations and radiative impacts. *J. Atmos. Sci.,* **57,** 1841-1853.

Measures, R. M., 1984: *Laser remote sensing: fundamentals and applications.* Wiley, 510 pp.

Merrill, J. T., 1977: Observational and theoretical study of shear instability in the airflow near the ground. *J. Atmos. Sci.,* **34**, 911-921.

Meyers, S. D., B.G. Kelly, and J.J. O'Brien, 1993: An introduction to wavelet analysis in oceanography and meteorology: With application to the dispersion of Yanai waves. *Mon. Wea. Rev.*, **121,** 2858-2866.

Miles, J. W., 1961: On the stability of heterogeneous shear flows. *J. Fluid Mech.*, **10,** 496-508.

——, and L. N. Howard, 1964: Note on heterogeneous flow. *J. Fluid Mech.*, **20,** 331-336.

Morcrette, J.-J., and C. Jakob, 2000: The response of the ECMWF model to changes in the cloud overlap assumption. *Mon. Wea. Rev.*, **128,** 1707-1732.

Newsom, R. K., W. A. Brewer, R. M. Hardesty, and V. Wulfmeyer, 2001. Development and meteorological applications of the NOAA/NCAR high-power 2mm Doppler lidar. *Optical Remote Sensing of the Atmosphere,* OSA Technical Digest (Optical Society of America, Washington DC), pp. 102-104.

Nielsen, J. W., 1992: In Situ Observations of Kelvin-Helmholtz Waves along a Frontal Inversion. *J. Atmos. Sci.,* **49**, 369–386.

Orden, R. T., 1997: *Essential Wavelets for Statistical Applications and Data Analysis*. Birkhäuser, 206 pp.

Oreopoulos, L., and R. Davies, 1998a: Plane parallel albedo bias from satellite observations. Part I Dependence on resolution and other factors. *J. Climate ,* **11**, 919-932.

_____, and _____, 1998b: Plane parallel albedo bias from satellite observations. Part II : Parameterization for bias removal. *J. Climate,* **11**, 933-944.

Orlanski, I., 1975: A rational subdivision of scales for atmospheric processes. *Bull. Amer. Meteor. Soc.*, **56**, 527-530.

Ou, S. C., and K.N. Liou, 1995: Ice crystal and climatic temperature feedback. *Atmos. Res.*, **35,** 127-138.

Palmer, T. L., D. C. Fritts, and Ø. Andreassen, 1996: Evolution and breakdown of Kelvin–Helmholtz billows in stratified compressible flows. Part II: Instability structure, evolution, and energetics. *J. Atmos. Sci.,* **53**, 3192–3212

Pavelin, E., and J. A. Whiteway, 2002: Gravity wave interactions around the jet stream. *Geophys. Res. Lett.,* **29,** 2024-2028.

Percival D.B., 1995: On estimation of the wavelet variance. *Biometrika*, **82**, 619-31.

Pielke, R., 1984: *Mesoscale Meteorological Modeling.* Academic Press, 468 pp.

Pincus, R., S. A. McFarlane, and S.A. Klein, 1999: Albedo bias and the horizontal variability of clouds in subtropical marine boundary layers: Observation from ships and satellite. *J. Geophys. Res.,* **104,** 6183-6191**.**

Platt, C. M., S. A. Young, A. I. Carswell, S. R. Pal, M. P. McCormick, D. M. Winker, M. DelGuasta, L. Stefanutti, W. L. Eberhard, M. Hardesty, P. H. Flamant, R. Valentin,

B. Forgan, G. G. Gimmestad, H. Jäger, S. S. Khmelevtsov, I. Kolev, B. Kaprieolev, D. Lu, K. Sassen, V. S. Shamanaev, O. Uchino, Y. Mizuno, U. Wandinger, C. Weitkamp, A. Ansmann, and C. Wooldridge, 1994: The experimental cloud lidar pilot study (ECLIPS) for cloud-radiation research. *Bull. Amer. Meteor. Soc.*, **75,** 1635-1654.

Pomroy, H. R., and A. J. Illingworth, 2000: Ice cloud inhomogeneity: Quantifying bias in emissivity from radar observations. *Geophys. Res. Lett.*, **27,** 2101-2104.

Polikar, R. cited 1994: Engineer's Guide to Wavelet Analysis. [Available online at http://engineering.rowan.edu/~polikar/WAVELETS/WTtutorial.html]

Potter, B. E., and J. R. Holton, 1995: The role of monsoon convection in the dehydration of the lower tropical stratosphere. *J. Atmos. Sci.,* **52,** 1034-1050.

Quante, M., and D. O'C. Starr, 2002: Dynamical process in cirrus clouds: A Review of observational results. *Cirrus*, D. K. Lynch, K. Sassen, D. O'C. Starr, and G. Stephens, Eds., Oxford University Press, 346-374.

_____, P. R. A. Brown, R. Baumann, B. Guillemet, and P. Hignett, 1996: Three-aircraft intercomparison of dynamical and thermodynamical measurements during the pre-EUCREX Campaign. *Contr. Atmos. Phy.*, **69,** 129-146.

_____, G. Teschke, M. Zhariy, P. Maaß, and K. Sassen, 2002: Extraction and analysis of structural features in cloud radar and lidar data using wavelet based methods. *Proceedings of the Second European Conference on Radar Meteorology.* Delft, Netherlands, European Meteorological Society, 95-103.

Raschke, E., 1988: The international satellite cloud climatology project, ISCCP, and its European regional experiment ICE (International Cirrus Experiment). *Atmos. Res.*, **21,** 191-201.

Ramanathan, V., R.D. Cess, E.F. Harrison, P. Minnis, B.R. Barkstrom, E. Ahmad, and D Hartmann, 1989: Cloud-radiative forcing and climate: Results from the Earth Radiation Budget Experiment. *Science*, **243,** 57-63.

Reed, R. J., and K. R. Hardy, 1972: A case study of persistent, intense, clear air turbulence in an upper level frontal zone. *J. Appl. Meteor.,* **11,** 541-549.

Reiss, N.M., and T. J. Corona, 1977: An Investigation Kelvin-Helmholtz billow cloud. *Bull . Amer. Met. Soc.*, **58,** 159-162.

Rosenfield, J. E., D. B. Considine, M. R. Schoeberl, and E. V. Browell, 1998: The impact of subvisible cirrus clouds near the tropical tropopause on stratospheric water vapor. *Geophys. Res. Lett.*, **25** , 1883-1886.

Rossow, W. B., and R. A. Schiffer, 1991: ISCCP Cloud Data Products. *Bull. Amer. Meteor. Soc.*, **72,** 2-20.

Roumeau S., P. Brémaud, E. Rivière, S. Baldy and J. L. Baray, 2000: Tropical cirrus clouds: a possible sink for ozone, *Geophys. Res. Lett.*, **27**, 2233-2236.

Sassen, K., 1976: Polarization diversity lidar returns from virga and precipitation: Anomalies and the bright band analogy. *J. Appl. Meteor.*, **15**, 292-300.

_____, 1991: The polarization lidar technique for cloud research: A review and current assessment. *Bull. Amer. Meteor. Soc.*, **72**, 1848-1866.

_____, 1994: Advances in polarization diversity lidar for cloud remote sensing. *Proc. IEEE*, **82,** 1907-1914

_____, 1995: Lidar cloud research. *The Review of Laser Engineer*, **23**, 148-153**.**

_____, 2000: Lidar backscatter depolarization technique for cloud and aerosol Research. *Light Scattering by Nonspherical Particles: Theory, Measurements, and Geophysical Applications*, M. L. Mishchenko, J. W. Hovenier, and L. D. Travis, Eds. Academic Press, 393-416.

_____, 2002: Cirrus clouds: A modern perspective. *Cirrus*, D. K. Lynch, K. Sassen, D. O'C. Starr, and G. Stephens, Eds., Oxford University Press, 11-40.

_____, and G. C. Dodd, 1988: Homogeneous nucleation rate for highly supercooled cirrus cloud droplets. *J. Atmos. Sci.*, **45**, 1357-1369.

_____, and B. O. Cho, 1992: Subvisual-thin cirrus lidar dataset for satellite verification and climatological research. *J. Appl. Meteor.*, **31,** 1275-1285.

_____, and T. Chen, 1995: The lidar dark band: An oddity of the radar bright band analogy. Geophys. Res. Lett., 22, 3505-3508.

_____, and J. R. Campbell, 2001: A midlatitude cirrus cloud climatology from the Facility for Atmospheric Remote Sensing. Part I: Macrophysical and synoptic properties. *J. Atmos. Sci.*, **58,** 481-496.

_____, and J. M. Comstock, 2001: A midlatitude cirrus cloud climatology from the Facility for Atmospheric Remote Sensing. Part III: Radiative properties. *J. Atmos. Sci.*, **58,**

2113-2127.

_____, and S. Benson, 2001: A midlatitude cirrus cloud climatology from the Facility for Atmospheric Remote Sensing. Part II: Microphysical propertites derived from lidar Depolarization. *J. Atmos. Sci.*, **58,** 2103-2112.

____, and G. G. Mace, 2002: Ground Based Remote Sensing of Cirrus Clouds. *Cirrus*, D. Lynch, K. Sassen, D. O'C. Starr, and G. L. Stephens, Eds. Oxford University Press, 168-195.

_____, D.O'C. Starr, and T. Uttal, 1989: Mesoscale and microscale structure of cirrus clouds: Three case studies. *J. Atmos. Sci.*, **46,** 371-396.

_____, C. J. Grund, J. D. Spinhirne, M.M. Hardesty, and J. M. Alvarez, 1990: The 27-28 October 1986 FIRE IFO cirrus case study: a five lidar overview of cloud structure and evolution. *Mon. Wea. Rev.*, **118,** 2288-2311.

_____, D.O'C. Starr, G. G. Mace, M. R. Poellot, S. H. Melfi, W. L. Eberhard, J. D. Spinhirne, E. W. Eloranta, D. E. Hagen, and J. Hallett, 1995: The 5-6 December 1991 FIRE IFO II jet stream cirrus case study: Possible influences of volcanic aerosols. *J. Atmos. Sci.*, 52, 97-123.

_____, G.G. Mace, J. Hallett, and M.R. Poellot, 1998: Corona-producing ice clouds: a case study of a cold mid-latitude cirrus layer. *Appl. Optics*, **37,** 1477-1485.

_____, J.M. Comstock, Z. Wang, and G. G. Mace, 2001: Cloud and aerosol research capabilities at FARS: The Facility for Atmospheric Remote Sensing. *Bull. Amer. Met. Soc.*, **82,** 1119-1138.

_____, J. Zhu, and S. Benson, 2003: A midlatitude cirrus cloud climatology from the Facility for Atmospheric Remote Sensing. Part III: Optical displays. *Appl. Optics*, **42,** 332-341.

_____, W. P. Arnott, D. O'C. Starr, G. G. Mace, Z. Wang, and M. R. Poellot, 2003: Midlatitude cirrus clouds derived from hurricane Nora: A case study with implication for ice crystal nucleation and shape. *J. Atmos. Sci.,* **60,** 873-891.

Schumann, U., 2002: Contrail cirrus. *Cirrus*, D. K. Lynch, K. Sassen, D. O'C. Starr, and G. Stephens, Eds., Oxford University Press, 231-255.

Scinocca, J. F., 1995: The mixing of mass and momentum by Kelvin-Helmholtz Billows. *J. Atmos. Sci.,* **52,** 2509-2530

——, and R. Ford, 2000: The Nonlinear Forcing of Large-Scale Internal Gravity Waves by Stratified Shear Instability. *J. Atmos. Sci.,* **57**, 653–672.

Scorer, R. S., 1972: *Clouds of the Worlds: A complete color Encyclopedia*. Stackpole, Books, 177 pp.

_____, 1958: Dynamics of mamma. *Sci. Prog.*, **46**, 75-82.

_____, 1997: *Dynamics of Meteorology and Climate*. John Wiley and Sons , 686 pp.

Sinha, A., and K.P. Shine, 1994: A one-dimensional study of possible cirrus cloud feedback. *J. Climate*, **7,** 158-173.

Singh, S., K. K. Mahajan, R. K. Chodhary, and O. P. Nagpal, 1999: Detection of Kelvin-Helmholtz instability with the Indian MST radar: A case study. *J. Geophys. Res.*, **104**, 3937-3945.

Smith, S. A., and P.R. Jonas, 1996: Observations of turbulence in cirrus clouds. *Atmos. Res.*, **43,** 1-29.

_____, and _____, 1997: Wavelet analysis of turbulence in cirrus clouds. *Ann. Geophys.*, **15,** 1447-1456.

Smith, W. L., P. F. Hein, and S. K. Cox, 1990: The 27–28 October 1986 FIRE cirrus case study: In situ observation of radiation and dynamic properties of cirrus cloud layer. *Mon. Wea. Rev.*, **118**.

Solomon, S., S. Borrmann, R. R. Garcia, R. Portmann, L. Thomason, L.R. Poole, D. Winker, M.P. McCormick, 1997: Heterogeneous chlorine chemistry in the tropopause region. *J. Geophys. Res.*, **102,** 21411-21429.

Starr, D. O. C., 1987: A cirrus-cloud experiment: Intensive field observations planned for FIRE. *Bull . Amer. Meteor. Soc.*, **68,** 119–124.

_____, and S. K. Cox, 1985a: Cirrus clouds, Part I: A cirrus cloud model. *J. Atmos. Sci.*, **42,** 2663-2681.

_____, and _____, 1985b: Cirrus clouds, Part II: Numerical experiments on the formation and maintenance of cirrus. *J. Atmos. Sci.*, **42,** 2682-2694.

_____, and D. P. Wylie, 1990: The 27–28 October 1986 FIRE cirrus case study: Meteorology and clouds. *Mon. Wea. Rev.*, **118,** 2259-2287.

_____, and M. Quante, 2002: Dynamical process in cirrus clouds: Concept and models.

Cirrus, D. K. Lynch, K. Sassen, D.O'C. Starr, and G. Stephens, Eds., Oxford University Press, 375-396.

_____, C. L. Korb, G. K. Schwemmer, and C. Y. Weng, 1992: Observation of height-dependent pressure structure of a strong mesoscale gravity wave. *Mon. Wea. Rev.,* **120**, 2808-2820**.**

Stephens, G. L., 1985: Reply. *Mon. Wea. Rev.,* **113**, 1834–1835.

____, 1994: *Remote sensing of the lower atmosphere: An introduction.* Oxford University Press, pp. 523.

_____, 2002: Cirrus, climate, and global change. *Cirrus*, D. K. Lynch, K. Sassen, D. O'C. Starr, and G. Stephens, Eds., Oxford University Press, 433-448.

_____, and P.J. Webster, 1981: Clouds and climate: sensitivity of simple systems. *J. Atmos. Sci.*, **38,** 235–247.

_____, S. Tsay, P. W. Stackhouse, Jr., and P. J. Flatau, 1990: The relevance of microphysical and radiative properties of cirrus clouds to climate and climate feedback. *J. Atmos. Sci.*, **47,** 1742-1753.

_____, D. G. Vane, R. Boain, G. Mace, K.Sassen, Z. Wang, A. Illingworth, E. O'Connor, W. Rossow, S.L. Durden, S. Miller, R. Austin, A. Benedetti, C. Mitrescu, and the CloudSat Science Team, 2002: The CloudSat Mission and the A-train: A new dimension of space-based observations of clouds and precipitation. *Bull. Amer. Meteor. Soc.*, **83,** 1771-1790.

Stith, J. L., 1995: In situ measurements and observations of cumulonimbus mamma. *Mon. Wea. Rev.*, **123**, 907-914.

Stokes, G. M., and S. E. Schwartz, 1994: The Atmospheric Radiation Measurement (ARM) Program: Programmatic Background and Design of the Cloud and Radiation Test Bed. *Bull. Amer. Met. Soc.*, **75,** 1201–1222.

Stubenrauch, C. J., A.D. Del Genio, and W.B. Rossow, 1997: Implementation of subgrid cloud vertical structure inside a GCM and its effect on the radiation budget. *J. Climate*, **10,** 273-287.

Stull, R. 1988: *An Introduction to Boundary Layer Metrology.* Kluwer Academic, 666 pp.

Suzuki, T., and M. Tanaka, 1993: The microphysical feedback of cirrus cloud in climate change. *J. Meteor. Soc. Japan*, **71,** 701-714.

Takayabu, I., 1992: Kelvin-helmholtz billow clouds on a frontal surface. *J. Meteor. Soc. Japan*, **70**, 733-738.

Takahashi, N., H. Uyeda, and K. Kikuchi, 1993: A Doppler radar observation on wave-like echoes generated in a strong vertical shear. *J. Meteor. Soc. Japan*, **71,** 357-365.

Taylor, G.I., 1938: Statistical theory of turbulence. *Proc. R. Soc. Lond.*, **164**, 476-90.

Teixeira, J. 2001: Cloud fraction and relative humidity in a prognostic cloud fraction scheme. *Mon. Wea. Rev.*, **129**, 1750-1753.

Tian, L., and J. A. Curry, 1989: Cloud overlap statistics. *J. Geophys. Res.,* **94**, 9925–9935.

Titov, G. A., 1998: Radiative horizontal transport and absorption in stratocumulus clouds. *J. Atmos. Soc.,* **55**, 2549–2560.

Torrence, C., and G.P. Compo, 1998: A practical guide to wavelet analysis. *Bull. Amer. Meteor. Soc.*, **79,** 61-78.

_____, and P. J. Webster, 1999: Interdecadal changes in the ENSO-Monsoon system. *J. Climate*, **12**, 2679–2690.

Thorpe, S.A., 1973: Experiments on instability and turbulence of a stratified shear flow. *J. Fluid Mech.,* **61**, 731-751.

_____, 1987: Transitional phenomena and development of turbulence in stratified fluid: A review. *J. Geophys. Res.,* **92,** 5231-5248

Thunis, P. and R. Bornstein, 1996: Hierachy of mesoscale flow assumptions and equations. *J. Atmos. Sci.*, **53**, 380-397.

Várnai T., and R. Davie, 1999: Effects of cloud heterogeneities on shortwave radiation: Comparison of cloud-top variability and internal heterogeneity. *J. Atmos. Sci.*, **5**, 1540-1548.

_____, and A. Marshak, 2001: Statistical analysis of the uncertainties in cloud optical depth retrievals caused by three-dimensional radiative effects. *J. Atmos. Sci.*, **58**, 1540-1548.

_____, and _____, 2002: Observations and analysis of three-dimensional radiative effects that influence MODIS cloud optical thickness retrievals. *J. Atmos. Sci.*, **59**, 1607-1618.

Vinnichenko, N. K., 1970: The kinetic energy spectrum in the free atmosphere – one

second to five years. *Tellus*, **22**, 158-166**.**

Wang, Z., and K. Sassen, 2001: Cloud type and macrophysical property retrieval using multiple remote sensors. *J. Appl. Meteor.*, **40**, 1665–1683.

____, and ____, 2002: Cirrus cloud microphysical property retrieval using lidar and radar measurements. Part II: Midlatitude cirrus microphysical and radiative properties. *J. Atmos. Sci.*, **59**, 2291–2302.

Warner, C., 1973: Meaurements of mamma. *Weather*, **28**, 394-397.

Welch, R. M., and B. A. Wielichi, 1984: Stratocumulus cloud filed reflected fluxes: The effect of the cloud shape. J. Atmos. Sci., **21**, 3086-3103.

Weng, H., and K.-M. Lau, 1994: Wavelets, period doubling, and time-frequency localization with application to organization of convection over the tropical western Pacific. *J. Atmos. Sci.*, **51,** 2523-2541.

Wickerhauser, M. V., 1994: *Adapted Wavelet Analysis from Theory to Software.* A. K. Peters, 504 pp

Wilks, D. S., 1995: Statistical methods in the atmospheric sciences: an Introduction. *International Geophysics Series*, Academic Press, 467pp.

Winstread, N. S., J. Verlinde, S. T. Arthur, F. Jaskiewicz, M. Jensen, N. Miles, and D.Nicosia, 2001: High-resolution airborne radar observations of mammatus. *Mon. Wea. Rev.*, **129**, 159-166.

Witt, G., 1962: Height, structure, and displacement of noctilucent clouds. *Tellus*, **14**, 1-12.

WMO, 1956: *International cloud atlas*.

Wylie, D. P., 2002: Cirrus and weather: A satellite perspective. *Cirrus*, D. K. Lynch, K. Sassen, D.O'C. Starr, and G. Stephens, Eds., Oxford University Press, 136-146.

——, and W.P. Menzel, 1999: Eight years of high clouds statistics using HIRS. *J. Climate*, **12,** 170-184.

Yagi, T., 1969: On the relationship between the shape of cirrus clouds and the static stability of the cloud level – Studies of cirrus clouds: Part IV. *J. Meteor. Soc. Japan,* **47**, 59-64.

——, T. Harimaya, and C. Magono, 1968: On the shape and movement of cirrus uncinus clouds by the trigonometric method utilizing stereophotographs – Studies of cirrus

clouds: Part II. *J. Meteor. Soc. Japan*, **46**, 266-277.

Yano, J.-I., M. W., Moncrieff, and X. Wu, 2001: Wavelet analysis of simulated tropical convective cloud Systems. Part II: Decomposition of convective-scale and mesoscale structure. *J. Atmos. Sci.*, **58**, 868-876.

Zuidema, P., and K. F. Evans, 1998: On the validity of the independent pixel approximation for boundary layer clouds observed during ASTEX *J. Geophys. Res.*, **103**, 6059-6074.